Energy Transfer Processes in the Framework of Macroscopic Quantum Electrodynamics

Dissertation for the Attainment of the Doctoral Degree
in the
Faculty of Mathematics and Physics
at the
Albert-Ludwigs University
University of Freiburg

January 30, 2023

Supervised by:

Stefan Yoshi Buhmann

Author:

Janine Franz

Co-supervised by:

Ed Grant

Dekan:

Prof. Dr. Michael Thoss

Referees:

Prof. Dr. Stefan Yoshi Buhmann

Prof. Dr. Joachim Dzubiella

Day of oral exam:

24. April 2023

Oral exam committee:

Prof. Dr. Stefan Yoshi Buhmann

Prof. Dr. Jens Timmer

Prof. Dr. Bernd von Issendorff

Abstract

Macroscopic bodies, such as surfaces, cavities or surrounding liquids and gasses, can significantly influence and thus control microscopic processes. A suitable framework to describe these effects is given by macroscopic quantum electrodynamics (QED). Inspired by the success of this theory applied to the so-called resonance energy transfer (RET), in this thesis the existing theory is on the one hand extended to related but more exotic processes and systems, and on the other hand extended to deal with collective effects and incoherent dynamics. The work is divided into three main parts.

In the first part, we investigate the competition between interatomic Coulombic decay and Auger decay and how one can change the relation of their rates to each other through their macroscopic environment, such as surfaces or cavities. In doing so, we develop a new approximate model for Auger decay that allows the dipole approximation and provides a closed-form expression for the Auger decay rate that depends on tabulated atomic data. It is shown how even a simple dielectric surface can significantly affect the competition between the two rates. The analysis is kept as general as possible, and analytical expressions are provided that can be applied to arbitrary macroscopic environment well described by its classical Green's tensor.

In the second part of this thesis, we extend the theory of RET in the framework of macroscopic QED to chiral molecules. Chiral molecules are optically active and may interact with the electromagnetic field via their magnetic transition dipole moment in addition to their electric one. As a result, new channels in the process of RET open up. The interference of some of these channels is then sensitive to the handedness of the chiral molecules: the RET rate differs between opposite-handed enantiomers and same-handed enantiomers. This makes RET a candidate for the development of a chiral discrimination technique. We show how the originally weak discriminatory power of the process can be significantly enhanced by immersing the system in a solvent. We offer a detailed discussion of a large parameter space for dielectric solvents. The importance of local-field effects is discussed and appropriate corrections are included in the calculation. We derive the local-field corrections for chiral solvents that turn out to be much more complex than those for magneto-electric media. We predict that due to these local-field effects the direction of the discrimination can be inverted inside chiral media depending on the intermolecular distance. As an opposite limit to the case of a continuous and dense macroscopic solvent, we consider possibly chiral particles surrounding the molecules

undergoing RET. We show that even a single mediating particle can have a significant impact on the discrimination depending on its position.

In the last part of the thesis, we develop a new perturbation scheme based on the master equation of the reduced atomic system in the Markov approximation and additionally extend Fermi's golden rule to density matrices. We demonstrate the applicability of Fermi's golden rule to density matrices by studying superradiant RET as a function of the initial entanglement in a collectively excited atomic pair. The new perturbation scheme modifies the splitting between perturbation and bare evolution, such that the bare evolution describes additionally incoherent dynamics such as decays. The scheme can then be used, for example, to deal with poles in the frequency domain, which are common when using perturbation theory, by a formally rigorous method.

Zusammenfassung

Makroskopische Körper wie beispielsweise Oberflächen, Resonatoren oder auch umschließende Flüssigkeiten, können mikroskopische Prozesse signifikant beeinflussen und dadurch steuern. Eine geeignete Theorie um diese Effekte zu beschreiben ist die makroskopische Quantenelektrodynamik. Inspiriert durch den Erfolg, den diese Theorie angewendet auf den sogenannten Resonanzenergietransfer (RET) erbracht hat, wird in dieser Arbeit die bestehende Theorie einerseits auf verwandte, aber exotischere Systeme ausgedehnt, und andererseits erweitert um auch kollektive Effekte und inkohärente Dynamik behandeln zu können. Die Arbeit ist in drei Hauptteile gegliedert.

Im ersten Teil untersuchen wir die Konkurrenz zwischen interatomarer Coulomb-Zerfall und Auger-Zerfall und wie man das Verhältnis ihrer Raten zueinander durch ihre makroskopische Umgebung, wie Oberflächen oder Resonatoren, verändern kann. Dabei entwickeln wir ein neues Näherungsmodell für den Auger-Zerfall, das die Dipol-Näherung erlaubt und einen geschlossenen Ausdruck für die Auger-Zerfallsrate liefert, welcher von tabellierten atomaren Daten abhängt. Es wird gezeigt, wie selbst eine einfache dielektrische Oberfläche die Konkurrenz zwischen den beiden Raten erheblich beeinflussen kann. Die Analyse ist so allgemein wie möglich gehalten, und es werden analytische Ausdrücke präsentiert, die für beliebige makroskopische Umgebung, die durch ihren klassischen Greenschen Tensor wohl beschrieben ist, angewendet werden können.

Im zweiten Teil dieser Arbeit dehnen wir die Theorie des RET im Rahmen der makroskopischen QED auf chirale Moleküle aus. Chirale Moleküle sind optisch aktiv und können mit dem elektromagnetischen Feld zusätzlich zu ihrem elektrischen auch über ihr magnetisches Übergangsdipolmoment wechselwirken. Infolgedessen eröffnen sich neue Kanäle für den RET-Prozess. Die Interferenz einiger dieser Kanäle ist dann empfindlich für die Händigkeit der chiralen Moleküle: Die Rate unterscheidet sich zwischen verschieden-händigen und gleich-händigen Enantiomeren. Damit ist RET ein Kandidat für die Entwicklung einer chiralen Diskriminierungstechnik. Wir zeigen, wie die ursprünglich schwache Diskriminierungsstärke des Prozesses durch Immersion des Systems in ein Lösungsmittel verbessert werden kann. Wir bieten eine detaillierte Diskussion eines großen Parameterraums für dielektrische Lösungsmittel. Die Bedeutung von sogenannten Lokalfeldeffekten wird diskutiert und entsprechende Korrekturen werden in die Berechnung einbezogen. Wir leiten die Lokalfeldkorrekturen für chirale Lösungsmittel

her, die sich als sehr viel komplizierter herausstellen als die entsprechenden Korrekturen für magneto-elektrische Medien. Wir leiten ab, dass aufgrund dieser Korrekturen die Richtung der Diskriminierung in einer chiralen Lösung in Abhängigkeit vom intermolekularen Abstand umgekehrt werden kann. Als entgegengesetzter Grenzfall zum Fall eines kontinuierlichen, makroskopischen Lösungsmittels betrachten wir (möglicherweise chirale) Teilchen, die das relevante System umgeben. Wir zeigen, dass selbst ein einziges mediierendes Teilchen einen signifikanten Einfluss auf die Diskriminierung haben kann.

Im letzten Teil der Arbeit entwickeln wir ein neues Schema für störungstheoretische Rechnungen, das auf der Master-Gleichung des reduzierten atomaren Systems in der Markov-Näherung basiert und dehnen zusätzlich Fermis goldene Regel auf Dichtematrizen aus. Wir demonstrieren die Anwendbarkeit von Fermis goldener Regel auf Dichtematrizen, indem wir den Superradianz-Effekte in RET als Funktion der anfänglichen Verschränkung in einem kollektiv angeregten Atompaar untersuchen. Das entwickelte Störungsschema modifiziert die Aufteilung zwischen Störung und ungestörter Zeitentwicklung, so dass die ungestörte Zeitentwicklung auch inkohärente Dynamiken wie beispielsweise Zerfälle berücksichtigt. Das Schema kann dann z. B. dazu verwendet werden, Pole im Frequenzbereich, die bei der Verwendung von Störungstheorie häufig auftreten, durch eine formal saubere Methode zu behandeln.

Acknowledgements

At this point I would like to thank the people who helped me during the time of my doctoral thesis. First and foremost, I thank my supervisor Stefan Yoshi Buhmann, who always stood by my side and helped me to persevere when I myself was in doubt. I also like to thank my graduate school, which made my time as a doctoral student exciting and varied through its wide range of scientific and social events and also brought me into contact with Ed Grant. I would like to thank my co-supervisor Ed Grant, who always made me feel confident and would have welcomed me to Vancouver had Corona not intervened. I thank Andreas Buchleitner, who gave me shelter after I was left without my supervisor in Freiburg by my own choice. I also thank the entire ninth floor of the physics high rise, past and present members and the coffee machine in particular for allowing me to spend such a wonderful time there. I would also like to thank Robert Bennett, who was part of our group in my early days and showed me that I do not always have to be so strict and doubtful with myself and my work to be a good researcher. Last but not least, I am also grateful to Philipp Leonhardt, who regularly cheered me up outside the office with words and good food, always supported me and put up with me even during my most stressful phase.

Contents

1. Introduction 1
   1.1. Excitation energy transfer processes of interest . . . 1
   1.2. Chiral molecules and their discrimination . . . 6
   1.3. Aim and structure of the thesis . . . 9

2. Theoretical Background 13
   2.1. Macroscopic quantum electrodynamics . . . 14
      2.1.1. Classical macroscopic electrodynamics . . . 14
      2.1.2. Necessary and useful properties of the medium and its fields . . . 18
      2.1.3. Quantisation in media . . . 20
      2.1.4. Extension to chiral media . . . 22
      2.1.5. Duality symmetry . . . 23
      2.1.6. Atom–field coupling . . . 25
      2.1.7. Local field correction . . . 27
   2.2. Calculation methods . . . 29
      2.2.1. Scattering theory and Dyson Series . . . 29
      2.2.2. Fermi Golden rule . . . 32
      2.2.3. Comparison to *ab initio* quantum chemistry methods . . . 33
      2.2.4. Open quantum systems . . . 34
   2.3. Previous results within (macroscopic) quantum electrodynamics . . . 36
      2.3.1. Møller formula for Auger decay . . . 36
      2.3.2. Polarisability tensor . . . 37
      2.3.3. Mediator particle as dielectric environment . . . 38
      2.3.4. Van-der-Waals force for infinitely close atoms of finite size . . . 39
      2.3.5. Spontaneous decay rate from Fermi's golden rule . . . 41
      2.3.6. Resonance energy transfer rate from Fermi's golden rule . . . 42
      2.3.7. Discrimination of chiral molecules via resonance energy transfer . . . 44

3. Auger and Interatomic Coulombic Decay 47
   3.1. General rate in the presence of a macroscopic environment . . . 47
      3.1.1. Derivation from scattering theory . . . 48
      3.1.2. Recovering the Møller formula in free space . . . 54

3.2. Rates in dipole approximation and regularisation of Auger decay 54
3.2.1. Interatomic Coulombic decay rate in dipole approximation 55
3.2.2. Regularisation of the Green's tensor and Auger decay rate 57
3.2.3. Determination of the Auger radius 60
3.3. Competing processes in an excited two-atom system 65
3.3.1. Comparison of decay channels 65
3.3.2. Impact of a surface onto decay channels 71
3.3.3. Impact of a cavity onto decay channels 76
3.3.4. Application to He–Ne dimer 78
3.4. Conclusion 83

4. Chiral Resonance Energy Transfer 87
4.1. General chiral resonance energy transfer rate 87
4.2. Local-field corrected Green's tensor in a chiral medium 92
4.2.1. Correction of a single point 93
4.2.2. Complete local-field correction of source and absorption point . . . 97
4.2.3. Consistency check for a spherical three-layer system 100
4.3. Discrimination inside a medium 104
4.3.1. Discrimination in free space 106
4.3.2. Discrimination in a magneto-electric medium 109
4.3.3. Discrimination in chiral medium 113
4.3.4. Discrimination in the presence of a chiral mediator 119
4.4. Conclusion 125

5. Open quantum systems approach to resonance energy transfer 129
5.1. Fermi's golden rule approach 130
5.2. Open quantum systems approach 133
5.2.1. General perturbative ansatz 134
5.2.2. Determination of the explicit Lindblad operator 136
5.2.3. Recovering the spontaneous decay rate 139
5.2.4. Recovering the resonance energy transfer rate 140
5.3. Incoherent perturbation scheme in the open quantum systems approach . . 143
5.3.1. Incoherent perturbation scheme 144
5.3.2. Polarisability tensor with finite linewidth 146
5.3.3. Oscillating transfer rate 149
5.4. Superradiance effects via Fermi's golden rule for mixed states 153
5.5. Conclusion 159

6. Conclusion and outlook 163

References 171

List of publications 183

A. Appendix 185
A.1. Electromagnetic fields in terms of the Green's tensor 185
A.2. Correlation functions in terms of the Green's tensor 187
A.2.1. Relating the Fermi's golden rule approach to correlation functions . 188
A.3. The Green's tensor 189
A.3.1. Planar two-layer system 192
A.3.2. Spherical layer system 194
A.4. Complex contour integration 198

Introduction

1

In 1946, Purcell proposed the modification of spontaneous emission by placing decaying atoms inside an appropriate cavity [1]. Since then the study of controlling spontaneous decay by means of the system's environment has made great advances in theory [2–9] – including for example controlled single-photon sources with applications in quantum computing [10, 11] – and experiment [12–16].

In a multi-atom system, an alternative to spontaneous decay is given by excitation energy transfer, where the excess energy is absorbed by a second particle. Inspired by the success of the Purcell effect, excitation transfer has been subject to similar studies. In this work, we extend the existing theory to a range of transfer processes not usually studied in the context of the Purcell effect, namely the excitation exchange between chiral molecules as well as interatomic Coulombic decay (ICD) and Auger decay. The aim is hereby to gain control over energy transfer processes by means of their surrounding environment as well as being able to account for the impact of realistic environments, such as macroscopic bodies, other particles or when the system is immersed in a solvent, on the process rates.

1.1. Excitation energy transfer processes of interest

Among the processes of excitation energy transfer, resonance energy transfer (RET) is the most fundamental. In RET, an initially excited donor particle relaxes and transfers its energy to an acceptor particle. For this process to take place, the emission and absorption spectra of both involved transitions need to overlap and hence be in resonance.

Already in 1922 measurements by Cario and Frank indicated that energy had been transferred between particles over a length scale exceeding the predictions of gas dynamical theories. Building on the work of Perrin and others, Förster developed the theory of what is known today as Förster or fluorescence **resonance energy transfer** (FRET) in 1946 [17, 18].

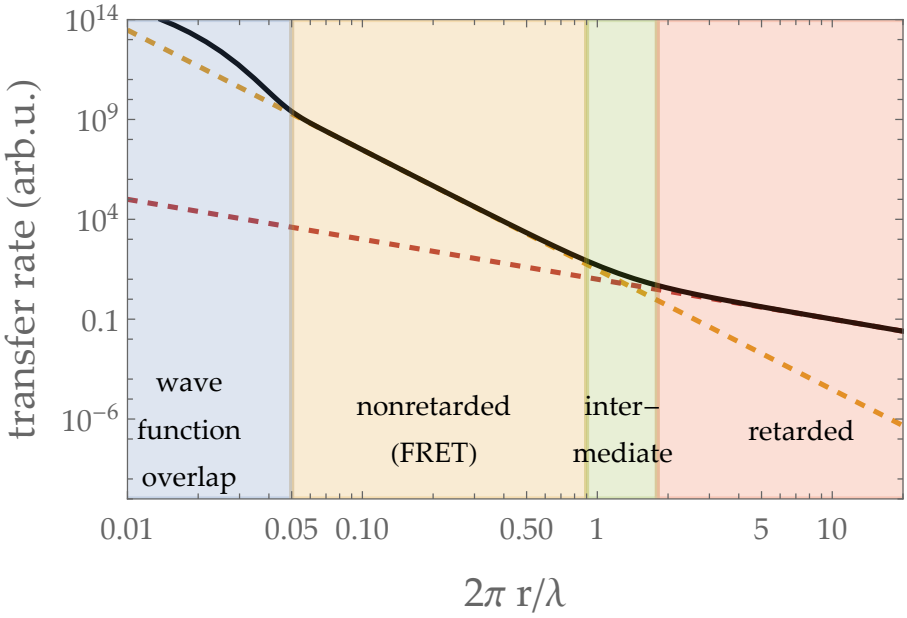

Figure 1.1.: Distance regimes for energy transfer. The solid line shows the behaviour of a typical energy transfer, the dashed lines show the respective asymptotic nonretarded and retarded behaviour.

Förster did not account for retardation effects in his theory, which is hence only valid for separation distances between donor and acceptor that are much smaller than the wavelength λ of the transferred energy $E = h/c\lambda$. In 1966 Avery extended the theory of Förster to larger separation distances by replacing the Coulomb potential used by Förster with the relativistic Breit interaction [19]. This was later improved more formally in a quantum theoretical way by Gomberoff and Power [20].

In general, the transfer can be dominantly radiative, nonradiative or a mixture of both, depending of the distance between donor and acceptor. Separation distances $r \ll \lambda$ smaller than the wavelength λ of the transferred energy we refer to as the near-zone or nonretarded limit where RET is described by FRET. The FRET rate Γ_{FRET} is famous for being extremely sensitive to the separation distance r. Its dependency is given by $\Gamma_{\text{FRET}} \propto 1/r^6$. In this limit, the transferred photon is virtual or "dressed", i.e. it is bound to the atoms during the process and does not exhibit well-defined physical properties. Due to its virtual character, the transfer efficiency can exceed the one of spontaneous emission, i.e. FRET can be faster than spontaneous decay.

In the opposite limit, $r \gg \lambda$, the retarded energy transfer process can be correctly described by spontaneous emission by the donor, propagation of a real photon and subsequent absorption by the acceptor. In contrast to FRET, the retarded or far-zone transfer is proportional to $1/r^2$. The typically rate behaviour as a function of distance is schematically plotted in Fig. 1.1.

Since its complete quantum theoretical description, Power, Craig and Thirunamachandran as well as Andrews et al. published a series papers giving insight to some physical aspects of the RET rate employing quantum electrodynamics (QED), such as reversibility of the process, the role of overlap between emission and absorption spectra together with the density of final states, the intermediate distance regime, and time-dependent analysis of the process connected to causality [21–31].

Regarding fundamental debates on the theory of RET there had historically been a long discussion on how to treat poles appearing in the frequency domain correctly which resulted in slightly different rate predictions [32]. While this debate is regarded as settled, there is still an ongoing discussion on the role of the local density of photon states [33]. Considering incoherent dynamics in the Markov approximation could give some insight to both of these questions.

Resonance energy transfer is easily accessible via experiment. It can occur between atoms, molecules, quantum dots, or even larger matter, such as nanotubes as well as naturally in biochemical processes such as photosynthesis. In the nonretarded regime, its distance sensitivity makes FRET the perfect mechanism to measure nanoscale distances leading to the "spectroscopic ruler" [34, 35] and it finds many applications as nanosensor [36]. Besides sensing, other applications have been developed based on RET; they include photovoltaic, photodynamic therapy [37, 38], light sources [39, 40] as well as manipulation of quantum information [41, 42].

The aim for control and enhancement of RET lead to the development of the field of plasmonic RET, where surface plasmons of a close-by surface can mediate the transfer. Macroscopic bodies mediating RET that have been studied include for instance nanowaveguides, nanoresonators, nano-antennas, metallic surfaces, metamaterials, graphene, Fabry-Perot-resonators and nanospheres [43–51]. A wide variety of applications using plasmonic-RET have been developed, such as detection of ions [52], enhancement of photocatalytic activity [53], and solar energy conversion [54]. Besides macroscopic bodies, the transfer can also be mediated by additional resonant particles close to the energy exchanging system [55–60]. RET has also been studied in cavities, in theory and experiment, where decoherence due to the coupling to the electromagnetic continuum can be suppressed and the strong coupling regime can be studied [61–64].

The first quantum theoretical treatment of RET with external environment was carried out microscopically via many-body QED [65]. Obviously a microscopic description of any macroscopic environment becomes infeasible due to the large number of particle involved. A solution for this problem is given by macroscopic quantum electrodynamics, where absorbing and dispersing media can be taken into account in an effective manner. In 2002 the rate for RET was first derived for general environment in the framework

of macroscopic QED [66] and since has been used to derive RET in a multitude of specific set-ups, such as in nanocavities [67], dielectric layers and microspheres [66], near wedges and wires [44], and in nonlocal media [68]. These predictions could be verified in experiment, e.g. for different cavities and a nano-cube[13, 69].

For energetically higher initial excitations the transferred energy can be sufficient to not only excite but ionise the acceptor atom. This process is called **interatomic Coulombic decay** (ICD) and was first theoretically predicted only in 1997 and experimentally verified 6 years later [70, 71]. The necessity of high initial energy in ICD implies that the donor atom requires an inner-valence vacancy. Such initial states are typically obtained after inner-valence ionisation of the donor and ICD then produces a final state with two ions in close proximity to each other, leading to a Coulomb explosion.

Although ICD and RET are equivalent processes, the difference in the amount of initial and ergo exchanged energy for both processes makes them appear fundamentally different. Compared to RET, ICD involves more complex preceding and posterior processes and occurs on shorter length scales due to the higher energies involved. The characteristic length scale of ICD makes it often essential to include wave function overlap between donor and acceptor and the resulting electron correlations as well as nuclear motion to obtain meaningful theoretical predictions. For separation distances in which the wave function overlap between donor and acceptor atom is significant the energy between donor and acceptor cannot only be transferred via a (virtual) photon but also via charge transfer. Due to the indistinguishability of the involved electrons excitation and charge transfers occur in coherence. While the photonic excitation transfer is proportional to $1/r^6$ as it is equivalent to FRET, the charge transfer, once possible, will increase exponentially with decreasing separation distance, see Fig. 1.1.

Because of the relevance of wave function overlaps in ICD as well as the scientific community in which the theory of ICD originated in, it was first treated in theory exclusively via *ab initio* quantum chemistry methods. These methods are well suited to treat effects by wave function overlap but exclude retardation effects and are not able to include the impact of dispersing and absorbing environment. After ICD was first considered in theory roughly 20 years ago and measured in experiment six years thereafter, it became more and more evident that actually *ICD is everywhere* as Ouchi et al. state in their publication [72]: ICD was not only found to occur after inner-valence ionisation [73] but also after resonant excitation [74, 75] as well as in satellite states [76–78]. In biology, it was suggested that ICD is part of a DNA repair mechanism where ICD produces a slow electron for so-called photolyases [79, 80]. It was suggested that ICD might even occur in biological tissue due to radiation therapy as it was predicted that ICD can occur in water molecules [70, 81] as well as in solutions [82]. In quantum dots ICD has so far been only considered theoretically [83–85].

A process that often occurs together with ICD is **Auger decay**. ICD may occur as a competing relaxation channel to Auger decay or as part of a decay cascade that is initialised by Auger decay. In Auger decay the initial excitation is sufficiently high such that the excess energy can be reabsorbed within the same donor atom by another electron. The electron is then emitted to the continuum leaving the donor autoionised. Accordingly, ICD is also known as interatomic Auger decay. Auger decay can involve energies even higher than those found in ICD processes. The energies involved in Auger decay can go up to the hard x-ray regime after core-shell ionisation of heavy atoms. In the overlapping energy regime of both, Auger decay and ICD can occur as competing processes. Since Auger decay requires a highly excited initial system a manifold of different processes is available as alternative relaxation channel. This includes cascade-like events where the initial inner-shell vacancy is filled not by an electron in the most outer valence shell but from another one, leading to a less excited state. Depending on its energy this transition can result in Auger or radiative decay. Following up on this further decays occur until the system ends up in its ground state. In contrast to ICD, Auger decay has been known and studied for roughly a century [86, 87].

Since its first observation the process gained importance in different fields. Auger decay rates in isolated atoms are a crucial ingredient to calculate spectra of astrophysical plasma [88]. These rates have been calculated for the past decades through elaborate *ab intio* techniques and are available as tabulated data. Two distinct applications and their respective research field based on Auger decay have developed over time: Auger electron spectroscopy and Auger decay in radiobiology. In Auger electron spectroscopy, the properties of the emitted electron, known as Auger electron are measured. After ionisation of the material under investigation the kinetic energy of the emitted Auger electron gives insight on the internal energies of the parent ion and hence on the material and its chemical bonds. In radiobiology, the Auger electron is exploited to damage biological tissue efficiently. The Auger electron typically possesses low kinetic energy and can thus destroy cancerous cells in close proximity to the Auger-decaying atom.

In 2003 it was pointed out that ICD can occur as part and in particular as terminal step of an Auger cascade. Since then, ICD as part of Auger cascades has been studied in various systems theoretically as well as seen in measurements. These studies suggested that ICD could be employed in radiobiology similar to Auger decay and is in many cases already part of the various processes triggered by radiation therapy. Unwanted ICD in the human body would lead to large damage of the surrounding tissue due to the posterior Coulomb explosion. In 2014, Cederbaum et al. suggested that resonant Auger decay, where the atom is initially excited instead of ionised can lead to a terminal ICD step where the kinetic energy of the emitted electron is tunable via the initial resonant excitation [89]. This was later verified by measurement [90–92] and subsequently further studied in theory and experiment [93], potentially leading to a scheme for radiation

therapy [94, 95].

In biological tissue and other real world systems, atoms undergoing ICD as well Auger decay are not isolated from their complex and often macroscopic surroundings. The need to study these processes in such environments is evident. Via methods of *ab initio* quantum chemistry ICD has been investigated in small water cluster and the predictions subsequently confirmed in experiment. Methods of *ab initio* quantum chemistry build up the environment microscopically and can become soon infeasible for larger systems. The framework of macroscopic QED approaches the problem from the opposite limit: it is a powerful tool to account for macroscopic and continuous matter influencing microscopic dynamics. Its predictions break partly down in the distance regime were wave function overlaps and chemical bonds between donor and acceptor play a significant role. Only recently the relation between ICD and RET has lead to the study of ICD via (macroscopic) QED methods. Hemmerich et al. showed that a perfectly reflecting surface as well as immersing the particles in a solvent such as water effects the ICD rate significantly by employing the theory of macroscopic QED [96]. In a joint work both frameworks, macroscopic QED and *ab inito* quantum chemistry, were used to investigate the impact of a third mediating particle on the ICD rate [97]. In contrast to ICD, Auger decay has never been studied via macroscopic QED. As pointed out above, the interplay of ICD and Auger decay with each other in particular in biological tissue is an important subject. The framework of macroscopic QED has much to offer to the future predictions of ICD in biological tissue and other environments. For significant progress of macroscopic QED studies in this field, it is thus necessary to include Auger decay into the framework.

1.2. Chiral molecules and their discrimination

Chiral molecules are molecules whose mirror image cannot be brought in congruence with the original by translation and rotation, see Fig. 1.2. The origin of the word *chiral* is the Greek word $\chi\varepsilon\iota\rho$ for hand. Hands are in fact a macroscopic example of chiral objects, as they are mirror images of each other but not identical. The two mirrored chiral molecules we thus refer to as left- and right-handed. They are different enantiomers of the same molecule.

In the early 1800s multiple experiments showed that certain crystals and liquids rotate the linear polarisation of transmitting light and that instances of the apparent same matter rotate light in opposite directions [98–100]. The effect was called optical activity. Finally in 1848 Pasteur separated crystals by hand under a magnifying glass into ones that showed a specific structure and their mirror images. The separated crystals showed opposite optical activity while the original racemic mixture was optically inactive [101,

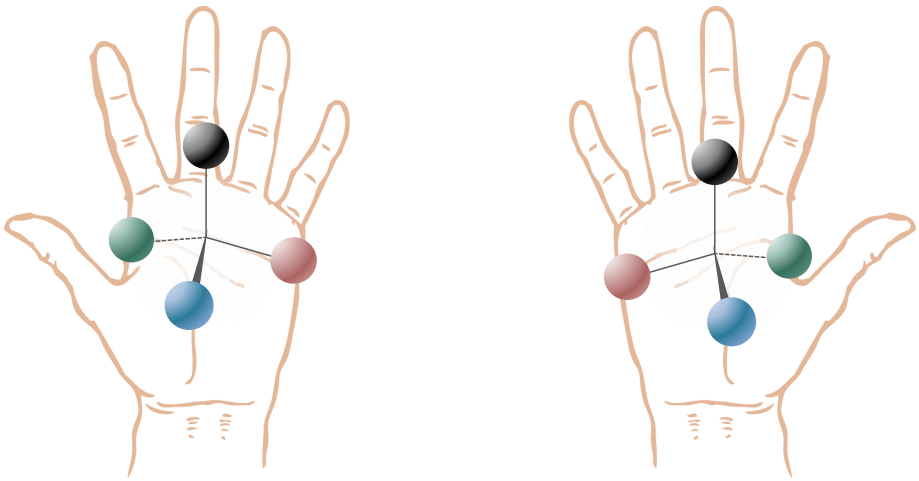

Figure 1.2.: Chiral molecules appear as different enatiomers that are nonidentical mirror images of each other, comparable to a left and right hand.

102]. While hypothesized at its time, the relation of this macroscopic chirality to the three-dimensional structure of the involved molecules was only understood decades later by the work of Le Bel and van't Hoff [103–105]. And so began the investigation of chiral molecules which is just as active today, as it turned out that chirality plays a role in many applications as well as fundamental questions across the sciences.

While different enantiomers possess identical physio-chemical properties, such as boiling and melting points, solubility and absorption spectra, they can have very different biological properties when interacting with other chiral objects. An example is given by our olfactory and gustatory system, both involving chiral receptors. Differently handed chiral molecules can hence smell and taste differently to us. For instance, the right-handed enantiomers of monoterpene carvone smells like caraway, its mirrored counterpart like spearmint, limonene smells like orange or lemon depending on the enantiomer and left-handed asparagine tastes bitter while its opposite handed version tastes sweet. As this indicates, the human body itself is made up of specifically handed chiral molecules and structures. Throughout nature one enantiomer usually appears much more often than the other, this is true e.g. for amino acids and sugars. Although this has been known since the end of the 19th century, the reason for the homochirality of nature and life is still unknown to this day.

One theory on the origin of homochirality involves parity violation due to the electroweak force. This fundamental interaction was unknown until mid 20th century and hence not considered in the study of chirality until then. The electroweak force breaks space inversion symmetry and thus there exists an incredibly small energy difference ($\sim 10^{-15}$ eV) in the internal energies of left- and right-handed chiral molecules [106]. This energy difference can be safely neglected for most purposes. However, it could be

the cause for a small initial enantiomeric excess in the origin of our world. This small imbalance then could have amplified itself by chiral catalysis, where an excess of certain handed matter gives advantage to the formation of same-handed matter [107–109]. It is to this day an open challenge to spectroscopically probe and quantify parity violation in chiral molecules [110–115].

Apart from this very fundamental interest in chiral molecules, there is just as important a reason to study them in applied science. In the pharmaceutical industry, 56% of all drugs are chiral [116] and while one enantiomer might have the desired effect the other can be either nonreactive or even harmful. For instance, is left-handed penicillamine an anti-arthritic drug while its mirror image is highly toxic. Another famous example is thalidomide, also known as Contergan, a drug that was prescribed to pregnant women in Germany as a medicine against morning sickness, anxiety and insomnia in the 1950s. While one enantiomer really acted as the desired medicine, the other was toxic and as a result, thousands of children were born with birth defects. In view of such examples, there is a high demand for measuring and controlling the excess of one handedness in a mixture of enantiomers. Advances in this regard are of such importance that several Nobel prizes have been awarded in chemistry related to the separation of different enantiomers, including Prelog in 1975 and Knowles, Nozori and Sharpless in 2001. The latest was the chemistry Nobel prize in 2021 for Benjamin List and David MacMillan for the development of asymmetric organic catalysis, i.e. a method for synthesising molecules with a preferred handedness.

Efforts to distinguish different enantiomers can be guided by the fundamental Curie symmetry principle. It states: *When certain effects show a certain asymmetry, this asymmetry must be found in the causes which gave rise to them* [117]. Applied to the task of distinguishing different enantiomers, this implies that one needs to use some chiral ingredient with known handedness in order to detect the handedness of an enantiomer. This is known as chiral discrimination. An example of such a chiral ingredient is left- and right-handed circularly polarised (LHCP/RHCP) light. And indeed one of the few differences in the behaviour of enantiomers is their optical activity: opposite handed chiral molecules interact differently with LHCP and RHCP light. This includes a difference in dispersion, leading to optical rotation and a difference in absorption, leading to circular dichroism. Many techniques for the measurement of the enantiomeric excess as well as the separation of different enantiomers have been developed based on this property [116].

Similarly, due to their optical activity, the resonance energy transfer between two chiral molecules can in principle be used to discriminate enantiomers, assuming the handedness of one of the participating molecules is known [60, 118, 119]. The discriminating effect is rather small and needs to be amplified for practical applications.

1.3. Aim and structure of the thesis

We have introduced the atomic processes of interest and outlined the current state of their respective research. In this work, we study interatomic Coulombic decay and Auger decay as decay channels appearing in the same system, and resonance energy transfer in particular between chiral molecules. As introduced, the framework of macroscopic QED was successfully used to study RET and reveal how to control the energy transfer via macroscopic environment. Its close relation to RET inspires us to transfer the analysis to the study of ICD. As discussed in the previous section, ICD might be an interesting candidate to exploit in radiation therapy. In biological tissue, the atomic system is not isolated from its macroscopic environment and studying ICD within macroscopic QED has thus a lot to offer. The most promising proposal to utilise ICD in radiation therapy involves Auger decay as well. In general, ICD and Auger decay often appear together, either in competition to or succeeding each other. To offer further insight to the ongoing research of ICD, we thus need to be able to describe Auger decay within the same framework of macroscopic QED.

We have discussed the relevance of chiral discrimination. While there are many discrimination techniques that have made their way from fundamental description to industrial application, the discriminatory power of RET has to date only been introduced in its most fundamental form in theory. It requires further investigation and the predicted effect needs to be enhanced to be utilised. One way to achieve this is to gain control over the effect by means of the macroscopic environment.

The aim of this work is two-fold. On one hand, we want to describe the introduced processes within a unified framework, i.e. macroscopic QED, that allows us to then take the impact of realistic macroscopic environments into account. On the other, we aim to extend the existing theory to be able to treat collective effects and incoherent dynamics. The latter may then be able to offer some new insights to the fundamental discussions regarding RET, such as the treatment of frequency poles and the relevance of the local density of photon states. While the resulting theory can be used to describe the introduced processes in realistic environments, such as biological tissue, we additionally study how the macroscopic environment can be used to gain control over the respective processes.

Within this work we focus on controlling the balance between ICD and Auger decay as competing processes as well as enhancing the discriminatory power of RET between chiral molecules via macroscopic environment. To this end, we first integrate Auger decay into the framework of macroscopic QED in a feasible manner, comparable to the treatment of RET and ICD. We then investigate the competition between ICD and Auger decay

in the presence of simple media. Subsequently, we look into the discrimination of chiral molecules via RET and how the degree of discrimination can be enhanced and modified by immersing the system into a solvent. By considering a solvent with chiral properties itself we can gain even more control over the discrimination. Finally, we consider the incoherent dynamics of decaying systems explicitly by developing a new perturbation scheme based on an open quantum systems approach. We show how on the level of master equations linewidths as well as energy shifts can be taken into account in perturbative calculations.

The thesis is organised as follows. Chapter 2 is dedicated to laying the theoretical groundwork which this thesis is based on. We introduce macroscopic QED and derive some useful properties of the Green's tensor and response functions in magneto-electric and chiral media. We introduce perturbative methods for calculating rates, leading to Fermi's golden rule as well as the master equation for open quantum systems in Markov approximation. We close the chapter by briefly presenting pre-existing results in free space and macroscopic QED that serve as a useful reference point throughout this thesis.

In chapter 3 we derive a new formula for the Auger decay rate based on a heuristic approximation that allows us to apply the dipole approximation to the Auger decay by regularising the respective Green's tensor. We then use this model to investigate Auger decay and ICD in competition with each other. We first derive estimations based on characteristic length scales to determine dominating decay channels in an highly excited two-atom system. We provide analytical estimations as well for the rates inside a general cavity based on its Q-factor. We then discuss in detail the modification of the balance between ICD and Auger by a close-by dielectric surface. The analysis is finally applied to the example of a HeNe-dimer.

In chapter 4 we derive the RET rate between chiral molecules in general macroscopic media. We study the degree of discrimination via RET as a function of separation distance in free space, in magneto-electric and chiral solvents. We show that local-field and screening effects should not be neglected and derive the local-field correction inside a chiral medium. We show that a chiral solvent with known handedness can be used to discriminate enantiomers. We finally study the dilute gas limit by considering a single chiral mediator molecule in close realm to the energy exchanging system.

In chapter 5 we develop a new perturbation scheme, the incoherent perturbation scheme, based on an open quantum systems approach in the Markov approximation. Here, we first introduce the master equation of the reduced atomic system and from this rederive the spontaneous decay rate as well as the RET rate via ordinary perturbation theory. We then show how the homogenous, but incoherent dynamics of the reduced system, i.e. energy shifts and decay rates, can be treated in a way that yields an alternative perturbation

scheme, we call the incoherent perturbation scheme. We show how this can be used to correct quantities derived from ordinary perturbation theory on the example of the atomic polarisability. The incoherent perturbation scheme may be used to find similar corrections to quantities of arbitrary perturbation order analogously. A comparable analysis has been done in other works to study Van-der-Waals forces between excited and ground-state atoms, yielding position-dependent oscillations only for the excited atom. In close analogy, we derive that the full decay rate of the excited donor particle, including RET, spontaneous emission and mediated emission shows position dependent oscillations. We close the chapter by extending Fermi's golden rule to density matrices where we can analyse collective effects on the rate, such as super-radiance.

Chapter 6 concludes the thesis by summarising the obtained results and outlining future prospects of the developed theories.

Theoretical Background

2

This chapter is dedicated to lay the groundwork for the thesis at hand. In the first section, the framework of macroscopic quantum electrodynamics (QED) is derived. We quantise the electromagnetic field in the presence of polarisable macroscopic media. We begin by focussing on magnetodielectric and metallic media that react either with a magnetic or electric linear response to external fields. We then extend the theory to chiral media whose response mixes electric and magnetic fields. We discuss dual symmetry, that is valid in free space but is partially broken in the presence of media. We then present two different coupling schemes between fields and atoms and finally show how emission and absorption inside a continuous medium needs to be corrected to account for screening and local field effects.

The second section derives and discusses different calculation methods to solve the atomic and molecular dynamics coupled to the electromagnetic field. We start by introducing the basic ideas of scattering theory, which relies on perturbation theory, from which we can derive Fermi's golden rule in arbitrary order. We briefly discuss the difference to *ab initio* quantum chemistry methods, whose results are used for comparison and as input parameters. We finish the section by introducing an open quantum systems approach.

The last section is dedicated to introducing some previous results obtained in free space or on the basis of macroscopic QED that either are useful throughout this thesis or serve as a consistency check in special cases of the results obtained within this thesis. We introduce the Møller scattering formula obtained from free-space QED that can be applied to calculate Auger decay rates. We derive the polarisability tensor for a single particle and show subsequently how it can be used to describe the particle as a dielectric medium via the Green's tensor. We briefly discuss a regularisation model developed for Van-der-Waals forces between infinitesimally close atoms as it serves as a justification and motivation for a similar regularisation model developed within this thesis. We then briefly sketch the derivation of the spontaneous decay rate and resonance energy transfer (RET) rate in the framework of macroscopic QED. Finally, we discuss the discriminatory power of RET between chiral molecules as it was predicted in 1998.

2.1. Macroscopic quantum electrodynamics

In this section, we will derive the fundamentals of macroscopic QED by first revisiting the classical theory from which we can already derive some useful properties and relations that also hold true in the respective quantum field theory. We then quantise the field in media by demanding several things to hold for the resulting quantum theory. While for a while this was regarded as the only way to derive macroscopic QED, field qunatisation was recently achieved in the more common canonical way. In our derivation we will mainly restrain ourselves to simple media. We subsequently extend the theory to chiral media. Furthermore, we show that electromagnetism shows duality symmetry that is useful for simplifying many results. We introduce the interaction between the field and microscopic quantum systems in minimal and multipolar coupling. Finally, we introduce a more specific concept concerning the interaction between fields and charges inside media that will be needed for the main part of the thesis, so-called local-field corrections.

2.1.1. Classical macroscopic electrodynamics

In the following, we revisit classical macroscopic electrodynamics. We derive the effect of a macroscopic medium onto the electrodynamic fields via linear response theory. The medium is characterised by means of its linear response to an applied field. We introduce the macroscopic fields, their Maxwell and constitutive equations, as well as the classical Green's tensor.

A medium consists of many charges influencing the electromagnetic fields and therefore each other according to the Maxwell equations [120]:

$$\varepsilon_0 \nabla \cdot \boldsymbol{E}(\boldsymbol{r},t) = \rho(\boldsymbol{r},t)\,, \tag{2.1}$$

$$\varepsilon_0 \nabla \cdot \boldsymbol{B}(\boldsymbol{r},t) = 0\,, \tag{2.2}$$

$$\nabla \times \boldsymbol{E}(\boldsymbol{r},t) - \dot{\boldsymbol{B}}(\boldsymbol{r},t) = \boldsymbol{0}\,, \tag{2.3}$$

$$\frac{1}{\mu_0}\nabla \times \boldsymbol{B}(\boldsymbol{r},t) - \varepsilon_0 \dot{\boldsymbol{E}}(\boldsymbol{r},t) = \boldsymbol{j}(\boldsymbol{r},t)\,. \tag{2.4}$$

Let us first consider N free charges at positions $\boldsymbol{r}_i$ and with charge q_i. The charge and current density is then given by

$$\rho(\boldsymbol{r},t) = \sum q_i \delta(\boldsymbol{r} - \boldsymbol{r}_i(t))\,, \tag{2.5}$$

$$\boldsymbol{j}(\boldsymbol{r},t) = \sum q_i \dot{\boldsymbol{r}}_i \delta(\boldsymbol{r} - \boldsymbol{r}_i(t))\,. \tag{2.6}$$

They are related to each other via the continuity equation,

$$\dot{\rho}(\boldsymbol{r},t) = -\nabla \cdot \boldsymbol{j}(\boldsymbol{r},t)\,. \tag{2.7}$$

By introducing the scalar potential ϕ and vector potential $\boldsymbol{A}$ of the electromagnetic field, such that

$$\boldsymbol{E}(\boldsymbol{r},t) = -\nabla\phi(\boldsymbol{r},t) - \dot{\boldsymbol{A}}(\boldsymbol{r},t)\,, \tag{2.8}$$

$$\boldsymbol{B}(\boldsymbol{r},t) = \nabla \times \boldsymbol{A}(\boldsymbol{r},t)\,, \tag{2.9}$$

and applying the Coulomb gauge $\nabla \cdot \boldsymbol{A} = 0$, we find the Poisson equation:

$$-\varepsilon_0 \Delta\phi(\boldsymbol{r},t) = \rho\,. \tag{2.10}$$

The Newton equations governed by the Lorentz force are then for each charge i given by

$$m_i\ddot{\boldsymbol{r}}_i = q_i\left[\boldsymbol{E}(\boldsymbol{r}_i,t) + \dot{\boldsymbol{r}}_i \times \boldsymbol{B}(\boldsymbol{r}_i,t)\right] \tag{2.11}$$

$$= \sum_{i\neq j} \frac{q_i q_j(\boldsymbol{r}_i - \boldsymbol{r}_j)}{4\pi\varepsilon_0} - q_i\dot{\boldsymbol{A}}(\boldsymbol{r}_i,t) + q_i\dot{\boldsymbol{r}} \times \left[\nabla \times \boldsymbol{A}(\boldsymbol{r}_i,t)\right]\,. \tag{2.12}$$

Obviously, it is not feasible to solve these equations for all the bound and free charges in a macroscopic medium. Instead we employ linear response theory to simplify the problem. Let us consider some continuous charge and current density inside the medium. We first have to define the response fields of the medium. Applying external fields to bound charges causes them to rearrange and separates negative and positive charges. This can be described by a polarisation field $\boldsymbol{P}$ which is a directional dipole moment density. For any volume V the total charge inside can be related to the flux of polarisation through its surface $q_V = -\iint_{\delta V} \mathrm{d}\boldsymbol{A} \cdot \boldsymbol{P}$ and the divergence theorem then gives

$$\rho(\boldsymbol{r},t) = -\nabla \cdot \boldsymbol{P}(\boldsymbol{r},t)\,. \tag{2.13}$$

The polarisation field is therefore the response of the medium to the electric field. Similarly, the magnetic field induces magnetic dipoles into the medium. Their directional density gives the magnetisation field $\boldsymbol{M}$. The charge current $\boldsymbol{J}_S = \iint_S \mathrm{d}\boldsymbol{A} \cdot \boldsymbol{j}_m$ due to these magnetic dipoles through any surface S is given by the integral over the magnetic dipoles on the surface's boundary $\boldsymbol{J}_S = \int_{\delta S} \mathrm{d}\boldsymbol{s} \cdot \boldsymbol{M}$ and with Stoke's theorem we find

$$\boldsymbol{j}_m = \nabla \times \boldsymbol{M}\,. \tag{2.14}$$

The continuity equation (2.7) together with Eq. (2.13) yields the full charge current den-

sity

$$\boldsymbol{j} = \dot{\boldsymbol{P}} + \nabla \times \boldsymbol{M} \,. \tag{2.15}$$

The magnetisation field is hence the response of the medium to the magnetic field. We can now simplify the response fields by assuming linear and causal response of the medium. With these assumptions the constitutive relations are given by the Langevin equations as

$$\boldsymbol{P}(\boldsymbol{r}, t) = \varepsilon_0 \int_{-\infty}^{\infty} \mathrm{d}\tau \int \mathrm{d}^3 r' \boldsymbol{\zeta}_e(\boldsymbol{r}, \boldsymbol{r}', \tau) \cdot \boldsymbol{E}(\boldsymbol{r}', t-\tau) + \boldsymbol{P}_N(\boldsymbol{r}, t) \,, \tag{2.16}$$

$$\boldsymbol{M}(\boldsymbol{r}, t) = \frac{1}{\mu_0} \int_{-\infty}^{\infty} \mathrm{d}\tau \int \mathrm{d}^3 r' \boldsymbol{\zeta}_m(\boldsymbol{r}, \boldsymbol{r}', \tau) \cdot \boldsymbol{B}(\boldsymbol{r}', t-\tau) + \boldsymbol{M}_N(\boldsymbol{r}, t) \,, \tag{2.17}$$

where the electric and magnetic susceptibility tensors $\boldsymbol{\zeta}_e$ and $\boldsymbol{\zeta}_m$ are retarded response functions, i.e. $|\boldsymbol{r} - \boldsymbol{r}'| < c\tau \rightarrow \boldsymbol{\zeta}_e(\boldsymbol{r}, \boldsymbol{r}', \tau) = \boldsymbol{\zeta}_m(\boldsymbol{r}, \boldsymbol{r}', \tau) = 0$, ensuring causality and $\boldsymbol{P}_N$ and $\boldsymbol{M}_N$ are noise fields due to fluctuations inside the medium, hence their statistical expectation value vanishes: $\langle \boldsymbol{P}_N \rangle = \langle \boldsymbol{M}_N \rangle = 0$. For further simplification we assume that the medium's response is local and isotropic: $\boldsymbol{\zeta}_\lambda(\boldsymbol{r}, \boldsymbol{r}', \tau) = \zeta_\lambda(\boldsymbol{r}, \tau)\delta(\boldsymbol{r} - \boldsymbol{r}')\mathbb{I}$.

The constitutive equations take a simpler form in Fourier space,

$$\boldsymbol{P}(\boldsymbol{r}, \omega) = \varepsilon_0 \varepsilon(\boldsymbol{r}, \omega) \boldsymbol{E}(\boldsymbol{r}, \omega) - \varepsilon_0 \boldsymbol{E}(\boldsymbol{r}, \omega) + \boldsymbol{P}_N(\boldsymbol{r}, \omega) \,, \tag{2.18}$$

$$\boldsymbol{M}(\boldsymbol{r}, \omega) = \frac{1}{\mu_0} \boldsymbol{B}(\boldsymbol{r}, \omega) - \frac{1}{\mu \mu_0} \boldsymbol{B}(\boldsymbol{r}, \omega) + \boldsymbol{M}_N(\boldsymbol{r}, \omega) \,, \tag{2.19}$$

where we have introduced the Fourier transformed quantities

$$f(\omega) = \mathcal{FT}\left[f(t)\right] = \frac{1}{2\pi} \int_{-\infty}^{\infty} \mathrm{d}t f(t) \mathrm{e}^{\mathrm{i}\omega t} \tag{2.20}$$

and the permittivity ε and permeability μ defined by

$$\varepsilon(\boldsymbol{r}, \omega) = 1 + \zeta_e(\boldsymbol{r}, \omega) \,, \qquad \mu(\boldsymbol{r}, \omega) = \frac{1}{1 - \zeta_m(\boldsymbol{r}, \omega)} \,. \tag{2.21}$$

Unless otherwise noted all fields and quantities are given in Fourier space from here on out . We can recast the Maxwell equations into a homogeneous form via these fields by introducing electric and magnetic excitation fields $\boldsymbol{D}$ and $\boldsymbol{H}$,

$$\boldsymbol{D} = \varepsilon_0 \boldsymbol{E} + \boldsymbol{P} = \varepsilon_0 \varepsilon \boldsymbol{E} + \boldsymbol{P}_N \,, \tag{2.22}$$

$$\boldsymbol{H} = \frac{1}{\mu_0} \boldsymbol{B} - \boldsymbol{M} = \frac{1}{\mu_0 \mu} \boldsymbol{B} - \boldsymbol{M}_N \,, \tag{2.23}$$

which are also commonly known as displacement and magnetizing fields. The macro-

scopic Maxwell equations in Fourier space then read

$$\varepsilon_0 \nabla \cdot \boldsymbol{D} = 0\,, \tag{2.24}$$

$$\varepsilon_0 \nabla \cdot \boldsymbol{B} = 0\,, \tag{2.25}$$

$$\nabla \times \boldsymbol{E} - \mathrm{i}\omega \boldsymbol{B} = \boldsymbol{0}\,, \tag{2.26}$$

$$\nabla \times \boldsymbol{H} + \mathrm{i}\omega \boldsymbol{D} = \boldsymbol{0}\,, \tag{2.27}$$

which are completed by the constitutive equations (2.22) and (2.23). From these equations we can derive the inhomogeneous Helmholtz equation for the electric field, such that

$$\left[\nabla \times \frac{1}{\mu(\boldsymbol{r},\omega)} \nabla \times - \frac{\omega^2}{c^2} \varepsilon(\boldsymbol{r},\omega)\right] \boldsymbol{E}(\boldsymbol{r},\omega) = \mathrm{i}\mu_0 \omega \boldsymbol{j}_N(\boldsymbol{r},\omega)\,, \tag{2.28}$$

where $\boldsymbol{j}_N = -\mathrm{i}\omega \boldsymbol{P}_N + \nabla \times \boldsymbol{M}_N$ is the noise charge current density. If we additionally consider free charges described by ρ and $\boldsymbol{j}$ that are not part of the medium the Gauss and Ampère law (2.24), (2.27) become again inhomogeneous and the Helmholtz equation reads

$$\left[\nabla \times \frac{1}{\mu(\boldsymbol{r},\omega)} \nabla \times - \frac{\omega^2}{c^2} \varepsilon(\boldsymbol{r},\omega)\right] \boldsymbol{E}(\boldsymbol{r},\omega) = \mathrm{i}\mu_0 \omega (\boldsymbol{j}_N(\boldsymbol{r},\omega) + \boldsymbol{j}(\boldsymbol{r},\omega))\,. \tag{2.29}$$

Formally this is solved by

$$\boldsymbol{E} = \mathrm{i}\mu_0 \omega \int \mathrm{d}^3 r' \mathbb{G}(\boldsymbol{r},\boldsymbol{r}',\omega)(\boldsymbol{j}_N(\boldsymbol{r}',\omega) + \boldsymbol{j}(\boldsymbol{r}',\omega))\,, \tag{2.30}$$

with the Green's tensor given by [121]

$$\left[\nabla \times \frac{1}{\mu(\boldsymbol{r},\omega)} \nabla \times - \frac{\omega^2}{c^2} \varepsilon(\boldsymbol{r},\omega)\right] \mathbb{G}(\boldsymbol{r},\boldsymbol{r}',\omega) = \boldsymbol{\delta}(\boldsymbol{r} - \boldsymbol{r}')\,, \tag{2.31}$$

where we call $\boldsymbol{r}'$ and $\boldsymbol{r}$ the source and absorption point, respectively. Its explicit form in free space as well as inside homogeneous media can be found in the appendix, see section A.3. When considering an environment consisting of several volumes occupied by different homogeneous media it is useful to decompose the Green's tensor in a bulk part $\mathbb{G}^{(0)}$ and scattering part $\mathbb{G}^{(1)}$, such that

$$\mathbb{G} = \mathbb{G}^{(0)} + \mathbb{G}^{(1)}\,, \tag{2.32}$$

where $\mathbb{G}^{(0)}$ is given by the solution of the Helmholtz equation inside the medium where the source is situated without considering any additional media and can be interpreted as the direct and uninfluenced propagation from source to an absorption point inside the very same medium, while the scattering Green's tensor $\mathbb{G}^{(1)}$ gives additional con-

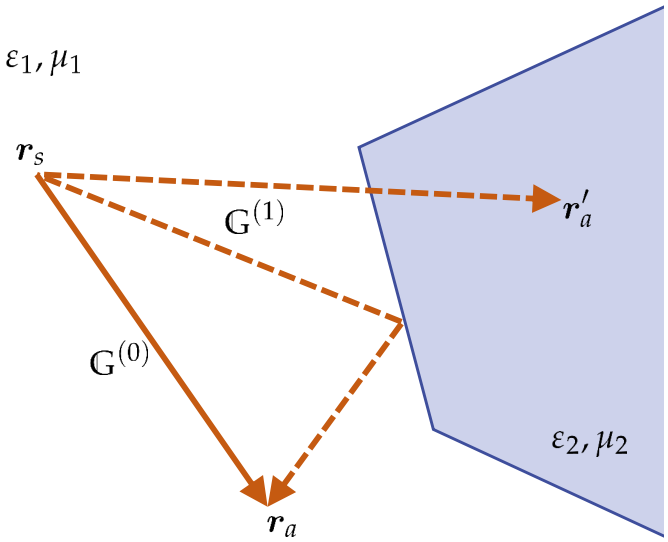

Figure 2.1.: The Green's function $\mathbb{G}(\boldsymbol{r}_a, \boldsymbol{r}_s, \omega)$ can be interpreted as the propagator of an field excitation from a source point $\boldsymbol{r}_s$ to an absorption point $\boldsymbol{r}_a$. It can be decomposed into a bulk part $\mathbb{G}^{(0)}(\boldsymbol{r}_a, \boldsymbol{r}_s, \omega)$ that describes the direct propagation through the same medium and a scattering part $\mathbb{G}^{(1)}(\boldsymbol{r}_a, \boldsymbol{r}_s, \omega)$ that takes any scattering at or transmission through secondary media into account. If the absorption point is situated in a different medium as the source the Green's tensor is given completely by the scattering part: $\mathbb{G}(\boldsymbol{r}'_a, \boldsymbol{r}_s, \omega) = \mathbb{G}^{(1)}(\boldsymbol{r}'_a, \boldsymbol{r}_s, \omega)$.

tributions due to scattering at secondary media, see Fig. 2.1. In case of absorption in a secondary media the full Green's tensor is given by $\mathbb{G}^{(1)}$.

2.1.2. Necessary and useful properties of the medium and its fields

The macroscopic fields were derived from linear response theory in the previous section. From this together with the fundamental equations for the fields we may derive some useful properties for the medium's properties, the Green's tensor and the macroscopic fields themselves.

As a consequence of causality, the response functions and hence permittivity and permeability obey the Schwarz-reflection principle [121],

$$\varepsilon^*(\omega) = \varepsilon(-\omega^*)\,, \qquad \mu^*(\omega) = \mu(-\omega^*)\,. \tag{2.33}$$

The sign of the imaginary part of $\zeta_e(\omega)$ and $\zeta_m(\omega)$ ($\omega > 0$) determines if the medium is absorbing or amplifying. We will only consider absorbing media with $\mathrm{Im}\zeta_e$, $\mathrm{Im}\zeta_m > 0$. For media with finite $\zeta_e(\tau)$ and $\zeta_m(\tau)$ that vanish for $\tau \to \infty$ the permittivity and perme-

ability $\varepsilon(\omega)$, $\mu(\omega)$ are analytic functions on the upper half of the complex plane including the real axis. This is true for magnetodielectrics, however metals feature a asymptotic behaviour of $\zeta_e(\tau \to \infty)$ due to free charges which leads to an additional pole in $\varepsilon(\omega)$ at $\omega = 0$. From these properties we can derive Kramers-Kronig relations as

$$\mathrm{Re}\varepsilon(\omega) = 1 + \frac{n}{\pi}\mathcal{P}\int_0^\infty \mathrm{d}\omega' \frac{\omega'^{n-1}}{\omega'^n - \omega^n}\mathrm{Im}\varepsilon(\omega')\,, \tag{2.34}$$

$$\mathrm{Im}\varepsilon(\omega) = \delta_{n1}\frac{\sigma_0}{\omega} - \frac{n\omega^{n-1}}{\pi}\mathcal{P}\int_0^\infty \mathrm{d}\omega' \frac{\omega'}{\omega'^n - \omega^n}(\mathrm{Re}\varepsilon(\omega') - 1)\,, \tag{2.35}$$

where $n = 2$ for a magnetodielectric medium and $n = 1$ for a metal and σ_0 is the conductivity at $\omega = 0$ of the metal's free charges. The permeability fulfils the same relation as the dielectric ε for both, dielectrics and metals.

As a consequence of these properties we can state general properties of the classical Green's tensor: it must fulfil the Schwarz reflection principle as well as the Onsager reciprocity, such that

$$\mathbb{G}^*(\boldsymbol{r}_2, \boldsymbol{r}_1, \omega) = \mathbb{G}(\boldsymbol{r}_2, \boldsymbol{r}_1, -\omega^*)\,, \tag{2.36}$$

$$\mathbb{G}^T(\boldsymbol{r}_2, \boldsymbol{r}_1, \omega) = \mathbb{G}(\boldsymbol{r}_1, \boldsymbol{r}_2, \omega)\,, \tag{2.37}$$

and we can show the very useful integral relation [121],

$$\sum_{\lambda=e,m}\int \mathrm{d}^3r'\mathbb{G}_\lambda(\boldsymbol{r}_2, \boldsymbol{r}', \omega)\cdot\mathbb{G}_\lambda^{*T}(\boldsymbol{r}_1, \boldsymbol{r}', \omega) = \frac{\hbar\mu_0}{\pi}\omega^2\mathrm{Im}\mathbb{G}(\boldsymbol{r}_2, \boldsymbol{r}_1, \omega)\,, \tag{2.38}$$

where we have defined:

$$\mathbb{G}_e(\boldsymbol{r}_2, \boldsymbol{r}_1, \omega) = \mathrm{i}\frac{\omega^2}{c^2}\sqrt{\frac{\hbar\mathrm{Im}\varepsilon(\boldsymbol{r}_1, \omega)}{\pi\varepsilon_0}}\mathbb{G}(\boldsymbol{r}_2, \boldsymbol{r}_1, \omega)\,, \tag{2.39}$$

$$\mathbb{G}_m(\boldsymbol{r}_2, \boldsymbol{r}_1, \omega) = -\mathrm{i}\frac{\omega^2}{c^2}\sqrt{\frac{\hbar\mathrm{Im}\mu(\boldsymbol{r}_1, \omega)}{\pi\varepsilon_0|\mu(r_1, \omega)|^2}}\mathbb{G}(\boldsymbol{r}_2, \boldsymbol{r}_1, \omega)\times\nabla_1\,. \tag{2.40}$$

In linear response theory the fluctuation spectrum of a field can be related to the imaginary part of its response function via the fluctuation–dissipation theorem [122, 123]. For the polarisation and magnetisation fields the theorem yields

$$\langle\Delta\boldsymbol{P}_N(\boldsymbol{r}, \omega)\Delta\boldsymbol{P}_N^*(\boldsymbol{r}', \omega')\rangle = \frac{\varepsilon_0 k_B T}{\pi\omega}\mathrm{Im}\zeta_e(\boldsymbol{r}, \omega)\boldsymbol{\delta}(\boldsymbol{r} - \boldsymbol{r}')\delta(\omega - \omega')\,, \tag{2.41}$$

$$\langle\Delta\boldsymbol{M}_N(\boldsymbol{r}, \omega)\Delta\boldsymbol{M}_N^*(\boldsymbol{r}', \omega')\rangle = \frac{k_B T}{\mu_0\pi\omega}\mathrm{Im}\zeta_m(\boldsymbol{r}, \omega)\boldsymbol{\delta}(\boldsymbol{r} - \boldsymbol{r}')\delta(\omega - \omega')\,, \tag{2.42}$$

where $\Delta f = f - \langle f\rangle$. With this we can derive the fluctuations for the electric field as well

to be

$$\langle \Delta \boldsymbol{E}_N(\boldsymbol{r},\omega) \Delta \boldsymbol{E}_N^*(\boldsymbol{r}',\omega') \rangle = \frac{\mu_0 k_B T \omega}{\pi} \mathrm{Im}\mathbb{G}(\boldsymbol{r},\boldsymbol{r}',\omega)\delta(\omega-\omega')\,, \tag{2.43}$$

where $\boldsymbol{E}_N$ is the electric field caused by the noise charge current $\boldsymbol{j}_N$ given by Eq. (2.28). This is also in accordance with the fluctuation–dissipation theorem applied to the electric field directly with $\mathbb{G}$ as linear response tensor and $\boldsymbol{E}_N$ as noise field. The classical fluctuations vanish in the limit of zero temperature.

2.1.3. Quantisation in media

Instead of canonical quantisation, we construct a quantum theory such that we reproduce free-space QED in the absence of charges and that the behaviour in the presence of charges resembles the behaviour of the classical field as close as possible. This can be achieved by fulfilling three demands: the Maxwell and constitutive equations must hold for the field operators, even inside a medium the free fields and the excitation fields have to be distinguished and the operator fluctuations must fulfil the same relations as in the classical case. However, while the fluctuations vanish for zero temperature in the classical theory we allow for ground state fluctuations of the electromagnetic quantum field. The resulting quantum theory describes media and fields as one system via collective polariton-like excitations.

We start by relating the noise polarisation and magnetisation to fundamental creation and annihilation operators [121, 124–126],

$$\hat{\boldsymbol{P}}_N(\boldsymbol{r},\omega) = \mathrm{i}\sqrt{\frac{\varepsilon_0\hbar}{\pi}\mathrm{Im}\varepsilon(\boldsymbol{r},\omega)}\hat{\boldsymbol{f}}_e(\boldsymbol{r},\omega)\,, \tag{2.44}$$

$$\hat{\boldsymbol{M}}_N(\boldsymbol{r},\omega) = \mathrm{i}\sqrt{\frac{\varepsilon_0\hbar}{\pi}\mathrm{Im}\varepsilon(\boldsymbol{r},\omega)}\hat{\boldsymbol{f}}_m(\boldsymbol{r},\omega)\,, \tag{2.45}$$

such that their fluctuation–dissipation theorem is fulfilled for operators $\hat{\boldsymbol{f}}_\lambda$ that obey the usual bosonic commutation relations,

$$\left[\hat{\boldsymbol{f}}_\lambda(\boldsymbol{r},\omega), \hat{\boldsymbol{f}}_{\lambda'}(\boldsymbol{r}',\omega')\right] = \left[\hat{\boldsymbol{f}}_\lambda^\dagger(\boldsymbol{r},\omega), \hat{\boldsymbol{f}}_{\lambda'}^\dagger(\boldsymbol{r}',\omega')\right] = \boldsymbol{0}\,, \tag{2.46}$$

$$\left[\hat{\boldsymbol{f}}_\lambda(\boldsymbol{r},\omega), \hat{\boldsymbol{f}}_{\lambda'}^\dagger(\boldsymbol{r}',\omega')\right] = \delta_{\lambda\lambda'}\boldsymbol{\delta}(\boldsymbol{r}-\boldsymbol{r}')\delta(\omega-\omega')\,. \tag{2.47}$$

Via the annihilation and creation operators we can define a Fock space for the field. Its ground state $|\{0\}\rangle$ is given by

$$\hat{\boldsymbol{f}}_\lambda(\boldsymbol{r},\omega)\,|\{0\}\rangle = \boldsymbol{0}, \qquad \forall\lambda,\boldsymbol{r},\omega\,, \tag{2.48}$$

and the field can be filled with excitations by applying the creation operator accordingly,

$$|\mathbf{1}_{\lambda_1}(\boldsymbol{r}_1,\omega_1)\dots\mathbf{1}_{\lambda_n}(\boldsymbol{r}_n,\omega_n)\rangle = \frac{1}{\sqrt{n!}}\hat{\boldsymbol{f}}^\dagger_{\lambda_1}(\boldsymbol{r}_1,\omega_1)\dots\hat{\boldsymbol{f}}^\dagger_{\lambda_n}(\boldsymbol{r}_n,\omega_n)\,|\{0\}\rangle\,. \tag{2.49}$$

With this, we can now show the validity of the fluctuation–dissipation theorem in the ground state, i.e. at zero temperature [127, 128]. We find

$$\left\langle \mathcal{S}\Big[\Delta\hat{\boldsymbol{P}}(\boldsymbol{r},\omega)\Delta\hat{\boldsymbol{P}}^\dagger(\boldsymbol{r}',\omega')\Big]\right\rangle_0 = \frac{\hbar}{2\pi}\varepsilon_0\mathrm{Im}\zeta_e(\boldsymbol{r},\omega)\boldsymbol{\delta}(\boldsymbol{r}-\boldsymbol{r}')\delta(\omega-\omega')\,, \tag{2.50}$$

$$\left\langle \mathcal{S}\Big[\Delta\hat{\boldsymbol{M}}(\boldsymbol{r},\omega)\Delta\hat{\boldsymbol{M}}^\dagger(\boldsymbol{r}',\omega')\Big]\right\rangle_0 = \frac{\hbar}{2\pi}\frac{\mathrm{Im}\zeta_m(\boldsymbol{r},\omega)}{\mu_0}\boldsymbol{\delta}(\boldsymbol{r}-\boldsymbol{r}')\delta(\omega-\omega')\,, \tag{2.51}$$

where $\mathcal{S}[\hat{a}\hat{b}] = 1/2(\hat{a}\hat{b}+\hat{b}\hat{a})$ is the symmetrised operator product. By demanding that the Maxwell and constitutive equation are still valid for the operators, i.e.

$$\varepsilon_0\nabla\cdot\hat{\boldsymbol{D}} = 0\,, \tag{2.52}$$

$$\varepsilon_0\nabla\cdot\hat{\boldsymbol{B}} = 0\,, \tag{2.53}$$

$$\nabla\times\hat{\boldsymbol{E}} - \mathrm{i}\omega\hat{\boldsymbol{B}} = \mathbf{0}\,, \tag{2.54}$$

$$\nabla\times\hat{\boldsymbol{H}} + \mathrm{i}\omega\hat{\boldsymbol{D}} = \mathbf{0}\,, \tag{2.55}$$

$$\hat{\boldsymbol{D}} = \varepsilon_0\hat{\boldsymbol{E}} + \hat{\boldsymbol{P}} = \varepsilon_0\varepsilon\hat{\boldsymbol{E}} + \hat{\boldsymbol{P}}_N\,, \tag{2.56}$$

$$\hat{\boldsymbol{H}} = \frac{1}{\mu_0}\hat{\boldsymbol{B}} - \hat{\boldsymbol{M}} = \frac{1}{\mu_0\mu}\hat{\boldsymbol{B}} - \hat{\boldsymbol{M}}_N\,, \tag{2.57}$$

we can derive the Helmholtz equation for the frequency components of the electric field operator in analogy to the classical case,

$$\left[\nabla\times\frac{1}{\mu}\nabla\times - \frac{\omega^2}{c^2}\varepsilon\right]\hat{\boldsymbol{E}}(\boldsymbol{r},\omega) = \mathrm{i}\mu_0\omega\hat{\boldsymbol{j}}_N(\boldsymbol{r},\omega)\,, \tag{2.58}$$

with $\hat{\boldsymbol{j}}_N = -\mathrm{i}\omega\hat{\boldsymbol{P}}_N + \nabla\times\hat{\boldsymbol{M}}_N$. The Helmholtz equation is formally solved by the classical Green's tensor and we find

$$\hat{\boldsymbol{E}}(\boldsymbol{r},\omega) = \sum_{\lambda=e,m}\int \mathrm{d}^3r'\mathbb{G}_\lambda(\boldsymbol{r},\boldsymbol{r}',\omega)\cdot\hat{\boldsymbol{f}}_\lambda(\boldsymbol{r}',\omega)\,, \tag{2.59}$$

where $\mathbb{G}_\lambda$ given by Eqs. (2.39) and (2.40) are the propagators for electric and magnetic field excitations. With this we can verify the fluctuation–dissipation theorem for the electric field in the ground state,

$$\left\langle \mathcal{S}\Big[\Delta\hat{\boldsymbol{E}}(\boldsymbol{r},\omega)\Delta\hat{\boldsymbol{E}}^\dagger(\boldsymbol{r}',\omega')\Big]\right\rangle_0 = \frac{\hbar}{2\pi}\mu_0\omega^2\mathrm{Im}\mathbb{G}(\boldsymbol{r},\boldsymbol{r}',\omega)\delta(\omega-\omega')\,. \tag{2.60}$$

The remaining fields are then given by the Maxwell and constitutive equations, their

explicit expressions in terms of the fundamental operators can be found in the appendix, see section A.1. In Schrödinger picture each field operator $\hat{\boldsymbol{F}}(\boldsymbol{r})$ is expressed by its frequency components via

$$\hat{\boldsymbol{F}}(\boldsymbol{r}) = \int_0^\infty \mathrm{d}\omega \hat{\boldsymbol{F}}(\boldsymbol{r},\omega) + \mathrm{H.c.}\,. \tag{2.61}$$

By construction the frequency components of each field fulfils the fundamental equations. Demanding that the time dependent frequency components in Heisenberg picture $\hat{\boldsymbol{F}}_\mathrm{H}(\boldsymbol{r},\omega,t)$ correspond to the Fourier components $e^{-\mathrm{i}\omega t}\hat{\boldsymbol{F}}(\boldsymbol{r},\omega)$ such that the Fourier transformation holds,

$$\hat{\boldsymbol{F}}_\mathrm{H}(\boldsymbol{r},t) = \int_0^\infty \mathrm{d}\omega \hat{\boldsymbol{F}}_\mathrm{H}(\boldsymbol{r},\omega,t) + \mathrm{H.c.} = \int_0^\infty \mathrm{d}\omega e^{-\mathrm{i}\omega t}\hat{\boldsymbol{F}}(\boldsymbol{r},\omega) + \mathrm{H.c.}\,, \tag{2.62}$$

we can conclude the field's Hamiltonian from Heisenberg equation of motion to be

$$\partial_t \hat{\boldsymbol{F}}_\mathrm{H}(\omega,t) = \frac{\mathrm{i}}{\hbar}\left[\hat{H}_\mathrm{F}, \hat{\boldsymbol{F}}_\mathrm{H}(\omega,t)\right]\,, \tag{2.63}$$

$$\Rightarrow \qquad \hat{H}_\mathrm{F} = \sum_\lambda \int \mathrm{d}^3 r \int_0^\infty \mathrm{d}\omega\, \hbar\omega \hat{\boldsymbol{f}}_\lambda^\dagger(\boldsymbol{r},\omega)\cdot\hat{\boldsymbol{f}}_\lambda(\boldsymbol{r},\omega)\,. \tag{2.64}$$

2.1.4. Extension to chiral media

So far, we have considered magnetodielectric as well as metallic media. The presented theory can be extended to more general media. For the framework of this thesis it is sufficient to extend the theory explicitly to reciprocal chiral media, also called Pasteur media.

A chiral medium mixes electric and magnetic fields in its linear response, i.e. Eqs. (2.16) and (2.17) now take the form (in Fourier space), such that

$$\hat{\boldsymbol{P}}(\boldsymbol{r},\omega) = \int \mathrm{d}^3 r' \left\{\varepsilon_0 \boldsymbol{\chi}_{ee}(\boldsymbol{r},\boldsymbol{r}',\omega)\cdot\hat{\boldsymbol{E}}(\boldsymbol{r}',\omega) + \sqrt{\frac{\varepsilon_0}{\mu_0}}\boldsymbol{\chi}_{em}(\boldsymbol{r},\boldsymbol{r}',\omega)\cdot\hat{\boldsymbol{B}}(\boldsymbol{r}',\omega)\right\} + \hat{\boldsymbol{P}}_N(\boldsymbol{r},\omega)\,, \tag{2.65}$$

$$\hat{\boldsymbol{M}}(\boldsymbol{r},\omega) = \int \mathrm{d}^3 r' \left\{\frac{1}{\mu_0}\boldsymbol{\chi}_{mm}(\boldsymbol{r},\boldsymbol{r}',\omega)\cdot\hat{\boldsymbol{B}}(\boldsymbol{r}',\omega) + \sqrt{\frac{\varepsilon_0}{\mu_0}}\boldsymbol{\chi}_{me}(\boldsymbol{r},\boldsymbol{r}',\omega)\cdot\hat{\boldsymbol{E}}(\boldsymbol{r}',\omega)\right\} + \hat{\boldsymbol{M}}_N(\boldsymbol{r},\omega)\,. \tag{2.66}$$

We are interested in the homogeneous, reciprocal case of a Pasteur medium where the

response tensors are given by

$$\boldsymbol{\chi}_{ee}(\boldsymbol{r},\boldsymbol{r}',\omega) = \left[\zeta_e(\omega) - \frac{\chi(\omega)^2}{\mu(\omega)}\right]\boldsymbol{\delta}(\boldsymbol{r}-\boldsymbol{r}') = \left[1-\varepsilon(\omega) - \frac{\chi(\omega)^2}{\mu(\omega)}\right]\boldsymbol{\delta}(\boldsymbol{r}-\boldsymbol{r}')\,, \tag{2.67}$$

$$\boldsymbol{\chi}_{mm}(\boldsymbol{r},\boldsymbol{r}',\omega) = \zeta_m(\omega)\boldsymbol{\delta}(\boldsymbol{r}-\boldsymbol{r}') = \left[1-\frac{1}{\mu(\omega)}\right]\boldsymbol{\delta}(\boldsymbol{r}-\boldsymbol{r}')\,, \tag{2.68}$$

$$\boldsymbol{\chi}_{em}(\boldsymbol{r},\boldsymbol{r}',\omega) = -\boldsymbol{\chi}_{me}(\boldsymbol{r},\boldsymbol{r}',\omega) = \mathrm{i}\frac{\chi(\omega)}{\mu(\omega)}\delta(\boldsymbol{r}-\boldsymbol{r}')\,, \tag{2.69}$$

where $\chi(\omega)$ is the chiral parameter and we recover the magnetodielectric relations given by Eqs. (2.21) for $\chi(\omega) = 0$. These definitions are not unique. Especially the alternative but equivalent definitions $\varepsilon' = \varepsilon - \chi^2/\mu$ and $\chi' = \chi/\mu$ are often found in the literature. With our definition we can derive the constitutive equations for a Pasteur medium as

$$\hat{\boldsymbol{D}} = \varepsilon\varepsilon_0\hat{\boldsymbol{E}} + \mathrm{i}\frac{\chi}{c}\hat{\boldsymbol{H}} + \hat{\boldsymbol{P}}_N + \mathrm{i}\frac{\chi}{c}\hat{\boldsymbol{M}}_N\,, \tag{2.70}$$

$$\hat{\boldsymbol{B}} = \mu\mu_0\hat{\boldsymbol{H}} - \mathrm{i}\frac{\chi}{c}\hat{\boldsymbol{E}} + \mu\mu_0\hat{\boldsymbol{M}}_N\,. \tag{2.71}$$

Causality still requires that the Schwarz-reflection principle holds for each response function $\boldsymbol{\chi}^*_{\lambda\lambda'}(\omega) = \boldsymbol{\chi}_{\lambda\lambda'}(-\omega^*)$ which is directly passed on to $\varepsilon(\omega)$ and $\mu(\omega)$ as in the magnetodielectric case, while we find the respective property for the chiral parameter to be: $\chi^*(\omega) = -\chi(-\omega^*)$. These properties ensure that the respective Green's tensor solving the chiral Helmholtz equation obeys the Schwarz-reflection principle. The chiral Helmholtz equation can be derived via its constitutive equations (2.70), (2.71) and the Maxwell equations (2.54) and (2.55). It reads

$$\frac{1}{\mu}\nabla\times\nabla\times\hat{\boldsymbol{E}} - 2\frac{\omega}{c}\frac{\chi}{\mu}\nabla\times\hat{\boldsymbol{E}} - \frac{\omega^2}{c^2}\left(\varepsilon - \frac{\chi^2}{\mu}\right)\hat{\boldsymbol{E}} = \mathrm{i}\omega\mu_0\hat{\boldsymbol{j}}_N\,, \tag{2.72}$$

which yields for the Green's tensor

$$\left[\frac{1}{\mu}\nabla\times\nabla\times -2\frac{\omega}{c}\frac{\chi}{\mu}\nabla\times -\frac{\omega^2}{c^2}\left(\varepsilon - \frac{\chi^2}{\mu}\right)\right]\mathbb{G}(\boldsymbol{r},\boldsymbol{r}') = \delta(\boldsymbol{r}-\boldsymbol{r}')\mathbb{1}\,. \tag{2.73}$$

Similarly, the theory can be extended to different media such as non-local or non-reciprocal media that are not governed by the presented derivation, a general approach can be found in Ref. [129].

2.1.5. Duality symmetry

In free space electric and magnetic fields obey very similar laws. In this section we introduce the concept of duality symmetry to account for this similarity. Duality symmetry and its transformation serves useful to obtain any magnetic results directly from known

electric results and vice versa. In general, a duality symmetric notation is useful to derive results in a more compact form.

We can formulate Maxwell's and the constitutive equations in a more compact form by introducing vectors of dual pairs for the fields, such that

$$\nabla \cdot \begin{pmatrix} l_0 \hat{\boldsymbol{D}} \\ \hat{\boldsymbol{B}} \end{pmatrix} = \begin{pmatrix} 0 \\ 0 \end{pmatrix}, \tag{2.74}$$

$$\nabla \times \begin{pmatrix} \hat{\boldsymbol{E}} \\ l_0 \hat{\boldsymbol{H}} \end{pmatrix} = \mathrm{i}\omega \begin{pmatrix} 0 & 1 \\ -1 & 0 \end{pmatrix} \begin{pmatrix} l_0 \hat{\boldsymbol{D}} \\ \hat{\boldsymbol{B}} \end{pmatrix}, \tag{2.75}$$

$$\begin{pmatrix} l_0 \hat{\boldsymbol{D}} \\ \hat{\boldsymbol{B}} \end{pmatrix} = \frac{1}{c} \begin{pmatrix} \varepsilon & \mathrm{i}\chi \\ -\mathrm{i}\chi & \mu \end{pmatrix} \begin{pmatrix} \hat{\boldsymbol{E}} \\ l_0 \hat{\boldsymbol{H}} \end{pmatrix} + \begin{pmatrix} 1 & \mathrm{i}\chi \\ 0 & \mu \end{pmatrix} \begin{pmatrix} l_0 \hat{\boldsymbol{P}}_N \\ \mu_0 \hat{\boldsymbol{M}}_N \end{pmatrix}, \tag{2.76}$$

where $l_0 = \sqrt{\varepsilon_0/\mu_0}$. Let us now consider the dual transformed fields $\hat{\boldsymbol{F}}^{\circledast}$, meaning that we rotate the dual space by some angle θ, such that

$$\begin{pmatrix} l_0 \hat{\boldsymbol{D}} \\ \hat{\boldsymbol{B}} \end{pmatrix}^{\circledast} = \begin{pmatrix} l_0 \hat{\boldsymbol{D}}^{\circledast} \\ \hat{\boldsymbol{B}}^{\circledast} \end{pmatrix} = D(\theta) \begin{pmatrix} l_0 \hat{\boldsymbol{D}} \\ \hat{\boldsymbol{B}} \end{pmatrix}. \tag{2.77}$$

The remaining fields are given analogously and the transformation matrix is given by

$$D(\theta) = \begin{pmatrix} \cos\theta & \sin\theta \\ -\sin\theta & \cos\theta \end{pmatrix}. \tag{2.78}$$

The Maxwell equations do not change for the transformed fields [130, 131]. However, we find that for the constitutive relations to stay invariant under dual transformation the response functions must transform as [121]

$$\begin{pmatrix} \varepsilon^{\circledast} & \mathrm{i}\chi^{\circledast} \\ -\mathrm{i}\chi^{\circledast} & \mu^{\circledast} \end{pmatrix} = D(\theta) \begin{pmatrix} \varepsilon & \mathrm{i}\chi \\ -\mathrm{i}\chi & \mu \end{pmatrix} D^T(\theta), \tag{2.79}$$

which leads to the requirement for duality symmetry: $(\varepsilon - \mu)\sin(2\theta) = 0$. It is only fulfilled for all θ if $\varepsilon = \mu$. This includes free space where $\varepsilon = \mu = 1$. However, for $\theta = n\pi/2$ Eq. (2.79) is fulfilled for arbitrary choices of ε, μ and χ. We conclude that arbitrary magneto-(di)electric and Pasteur media show so called discrete duality symmetry transforming with

$$D_n = \begin{pmatrix} 0 & 1 \\ -1 & 0 \end{pmatrix}^n. \tag{2.80}$$

2.1.6. Atom–field coupling

We have quantised the electromagnetic field in the presence of macroscopic media. However, to be able to apply our theory we need to couple the fields to atomic systems. We will employ two different coupling schemes, namely minimal and multipolar coupling throughout this thesis. The total Hamiltonian for both schemes is the same, however, the splitting into coupling and system Hamiltonian differs which can have consequences to results obtained by perturbative methods.

In the uncoupled case we find for the atomic system,

$$\hat{H}_{\mathrm{A}} = \frac{1}{2}\sum_{\alpha} m_{\alpha}\dot{\hat{\boldsymbol{r}}}_{\alpha}^{2} + \sum_{\alpha\neq\beta}\frac{q_{\alpha}q_{\beta}}{8\pi\varepsilon_{0}|\hat{\boldsymbol{r}}_{\alpha}-\hat{\boldsymbol{r}}_{\beta}|}\,, \tag{2.81}$$

where we have included the Coulomb interaction between the atomic system's charges into the atomic Hamiltonian. We divide the atomic Hamiltonian into two parts by splitting off the center of mass kinetic term,

$$\hat{H}_{\mathrm{A}} = \frac{1}{2m_{\alpha}}\dot{\hat{\boldsymbol{p}}}_{A} + \sum_{n} E_{n}\left|n\right\rangle\left\langle n\right|\,, \tag{2.82}$$

where $|n\rangle$ are the eigenstates of an atom at rest with energy E_n. The field Hamiltonian is given by Eq. (2.64). In the classical theory we can apply a minimal coupling scheme to the system's Lagrangian and derive its full Hamiltonian. The same result can be obtained by replacing $m_{\alpha}\dot{\boldsymbol{r}}_{\alpha}$ in H_A with $\boldsymbol{p}_{\alpha} - q_{\alpha}\boldsymbol{A}(\boldsymbol{r}_{\alpha})$ and adding the Coulomb interaction with the field [120, 121, 125]. An analogous procedure leads to the minimal coupling Hamiltonian $\hat{H}_{\mathrm{ia}}$ for the quantum field,

$$\hat{H} = \hat{H}_{\mathrm{A}} + \hat{H}_{\mathrm{F}} + \hat{H}_{\mathrm{ia}}\,, \tag{2.83}$$

$$\hat{H}_{\mathrm{ia}} = \sum_{\alpha} q_{\alpha}\hat{\phi}(\hat{\boldsymbol{r}}_{\alpha}) - \sum\frac{q_{\alpha}}{m_{\alpha}}\hat{\boldsymbol{p}}_{\alpha}\cdot\hat{\boldsymbol{A}}(\hat{\boldsymbol{r}}_{\alpha}) + \sum_{\alpha}\frac{q_{\alpha}^{2}}{2m_{\alpha}}\hat{\boldsymbol{A}}^{2}(\hat{\boldsymbol{r}}_{\alpha})\,, \tag{2.84}$$

where the last term in $\hat{H}_{\mathrm{ia}}$ describes elastic scattering of the field at the atom and can usually be neglected when interested in the change of internal atomic states. Equivalently, we can write the minimal coupling Hamiltonian as

$$\hat{H}_{\mathrm{ia}} = \int \mathrm{d}^{3}r\hat{\rho}(\boldsymbol{r})\hat{\phi}(\boldsymbol{r}) - \int \mathrm{d}^{3}r\hat{\boldsymbol{A}}(\boldsymbol{r})\cdot\hat{\boldsymbol{j}}(\boldsymbol{r})\,. \tag{2.85}$$

In first order of long-wavelength or dipole approximation we then find

$$\hat{H}_{\mathrm{ia}} \approx -\hat{\boldsymbol{d}}\cdot\hat{\boldsymbol{E}}^{\parallel}(\hat{\boldsymbol{r}}_{A}) - \sum\frac{q_{\alpha}}{m_{\alpha}}\hat{\boldsymbol{p}}_{\alpha}\cdot\hat{\boldsymbol{A}}(\hat{\boldsymbol{r}}_{A})\,. \tag{2.86}$$

An alternative coupling Hamiltonian can be obtained by applying the Power–Zienau–Woolley

transformation $\hat{T} = \exp\left[\mathrm{i}\hbar^{-1}\int \mathrm{d}^3 r \hat{\boldsymbol{P}}_A \cdot \hat{\boldsymbol{A}}\right]$ to all operators and expressing the minimal coupling Hamiltonian in terms of the transformed operators [132–134]. Obviously, this will not change the total Hamiltonian. The transformation leaves many relevant operators unchanged since they commute with $\hat{\boldsymbol{P}}_A$ and $\hat{\boldsymbol{A}}$. However, the electric field operator and therefore the annihilation and creation operators change under this transformation, such that

$$\hat{\boldsymbol{E}}' = \hat{\boldsymbol{E}} + \frac{1}{\varepsilon_0}\hat{\boldsymbol{P}}_A^{\perp}\,, \tag{2.87}$$

$$\hat{\boldsymbol{f}}'_\lambda(\boldsymbol{r},\omega) = \hat{\boldsymbol{f}}_\lambda(\boldsymbol{r},\omega) + \frac{1}{\hbar\omega}\int \mathrm{d}^3 s \hat{\boldsymbol{P}}_A^{\perp}(\boldsymbol{s})\cdot\mathbb{G}^*_\lambda(\boldsymbol{s},\boldsymbol{r},\omega)\,, \tag{2.88}$$

where the prime indicates the transformed operators, $\hat{O}' = \hat{T}\hat{O}\hat{T}^\dagger$. In addition, the particle's canonical momentum changes, such that

$$\hat{\boldsymbol{p}}'_\alpha = \hat{\boldsymbol{p}}_\alpha - q_\alpha \hat{\boldsymbol{A}}(\hat{\boldsymbol{r}}_\alpha) - \int \mathrm{d}^3 r \hat{\boldsymbol{\Lambda}}_\alpha \times \hat{\boldsymbol{B}} = m_\alpha \dot{\hat{\boldsymbol{r}}}_\alpha - \int \mathrm{d}^3 r \hat{\boldsymbol{\Lambda}}_\alpha \times \hat{\boldsymbol{B}}\,, \tag{2.89}$$

where $\hat{\boldsymbol{\Lambda}}_\alpha = \hat{\boldsymbol{\Lambda}}'_\alpha$ only depends on atomic operators, its lengthy expression can be found in Ref. [121]. The transformation leads to a new splitting of the Hamiltonian into atomic, field and coupling parts:

$$\hat{H}'_A = \frac{1}{2m_A}\dot{\hat{\boldsymbol{p}}}'^2_A + \sum_n E'_n \left|n'\right\rangle\left\langle n'\right|\,, \tag{2.90}$$

$$\hat{H}'_F = \sum_\lambda \int \mathrm{d}^3 r \int \mathrm{d}\omega \hbar\omega \hat{\boldsymbol{f}}'^\dagger_\lambda(\boldsymbol{r},\omega)\cdot\hat{\boldsymbol{f}}'_\lambda(\boldsymbol{r},\omega)\,, \tag{2.91}$$

$$\begin{aligned}\hat{H}'_{\mathrm{ia}} \approx -\hat{\boldsymbol{d}}\cdot\hat{\boldsymbol{E}}'(\hat{\boldsymbol{r}}_A) - \hat{\boldsymbol{m}}'\cdot\hat{\boldsymbol{B}}(\hat{\boldsymbol{r}}_A) + \sum_\alpha \frac{q_\alpha^2}{8m_\alpha}\left[\hat{\boldsymbol{r}}_\alpha \times \hat{\boldsymbol{B}}(\hat{\boldsymbol{r}}_A)\right]^2 \\ + \frac{3}{8m_A}\left[\hat{\boldsymbol{d}}\times\hat{\boldsymbol{B}}(\hat{\boldsymbol{r}}_A)\right]^2 - \frac{1}{m_A}\hat{\boldsymbol{d}}\times\hat{\boldsymbol{p}}'_A\cdot\hat{\boldsymbol{B}}(\hat{\boldsymbol{r}}_A)\,,\end{aligned} \tag{2.92}$$

where all operators have been transformed, while only the primed operators and quantities change under this transformation, and we have applied the long-wavelength approximation to the coupling Hamiltonian. In multipolar coupling the long-wavelength approximation is not identical with the dipole approximation but also contains magnetic contributions. The first two terms in the coupling Hamiltonian (2.92) describe the electric and magnetic dipole couplings, the successive two terms the diamagnetic interactions and the last term depending on the center of mass motion represents Röntgen interaction. Neglecting the center of mass motion and the typically weak diamagnetic interaction we find for the coupling Hamiltonian,

$$\hat{H}'_{\mathrm{ia}} \approx -\hat{\boldsymbol{d}}\cdot\hat{\boldsymbol{E}}'(\hat{\boldsymbol{r}}_A) - \hat{\boldsymbol{m}}'\cdot\hat{\boldsymbol{B}}(\hat{\boldsymbol{r}}_A)\,, \tag{2.93}$$

where the magnetic term vanishes for non-magnetic atoms. The interpretation of atomic

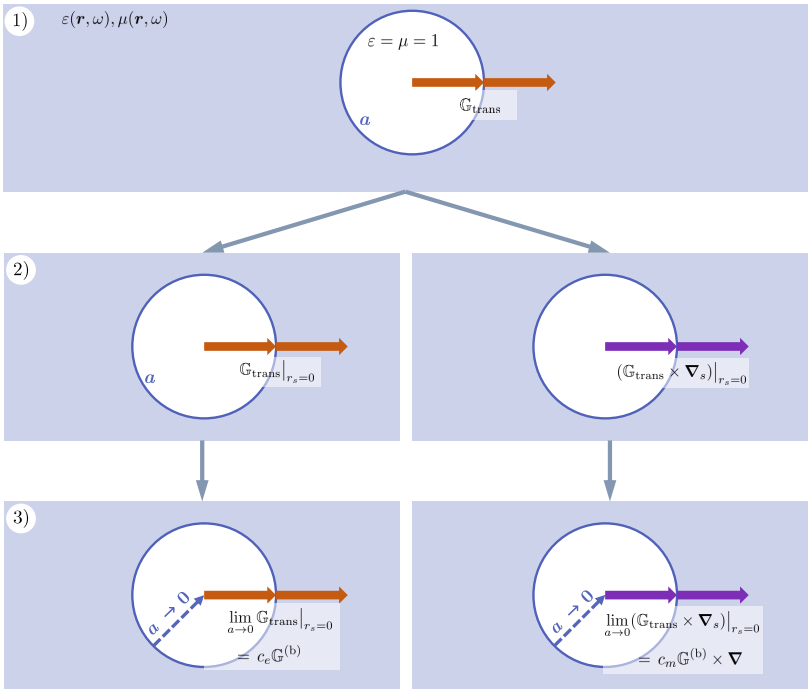

Figure 2.2.: Flow chart like sketch of local field correction derivation via Onsager real cavity model. 1.) The transmission Green's tensor from source point $\boldsymbol{r}_s$ inside to absorption point $\boldsymbol{r}_a$ outside the sphere is found by solving the Helmholtz equation and the boundary conditions at $r = a$. 2.) We apply the curl before explictly setting the source point to zero (i.e. to the center of the sphere) to receive the correction for magnetic type of excitations. 3.) We apply the limit of vanishing sphere radius and end up with source corrected bulk Green's tensors for electric (left) and magnetic (right) excitations.

as well as field states differ in the two schemes and are rotated into each other compared to the minimal coupling scheme, but are still orthogonal. However, in free space and with electric atoms the two couplings and their respective $\hat{H}_{\text{A}}$ and $\hat{H}_{\text{F}}$ coincide.

2.1.7. Local field correction

So far, we have quantised the fields in the presence of macroscopic media and derived the coupling between the macroscopic fields and atoms. However, when we want to describe atoms situated inside macroscopic media, we need to address an additional problem: so-called local field effects must be taken into account. This can be motivated by several considerations. When modelling an atom inside a macroscopic medium we should take care of the fact that the atom is not permeated by the continuous charge density that is used to describe the medium. Most importantly, any atom–field interaction should in fact be modelled to take place in free space. Without this there is an ambiguity in how to couple the field to the atomic dipoles and duality symmetry might be broken without a physical reason [9]. There are several local field models that take this into

consideration [135, 136]. While resulting in different corrections to the Green's tensor, they all restore duality symmetry. Here, we will focus on the so-called Onsager real cavity model in order to take local field effects into account. The corresponding solution for a chiral medium will be derived later as a new result within the scope of this thesis. Since we will go into full detail of the derivation in the chiral case, we only give a rough sketch of the derivation here.

To this end, we embed the source and absorption points $\boldsymbol{r}_s$ and $\boldsymbol{r}_a$ of a field excitation into a magnetodielectric medium. The propagation of excitations in a single medium is described by the bulk Green's tensor $\mathbb{G}^{(0)}$ given by Eq. (A.31). We now want to find a correction that can be applied to $\mathbb{G}^{(0)}$ to account for local fields around source and absorption. Within the Onsager real cavity model we achieve this by simply placing infinitesimal small free-space spheres around source and absorption points [137]. Because of the geometry of the problem it is difficult to find the Green's tensor for the arrangement including both free-space spheres.

Instead we first place a free space sphere with finite radius a around the source point $\boldsymbol{r}_s$ only, while the absorption point $\boldsymbol{r}_a$ is placed within the medium, see Fig. 2.2. We then solve the fields boundary conditions at the spheres surface at $|\boldsymbol{r}| = a$ for the transmitting Green's tensor, $\mathbb{G}_{\text{trans}}$ and finally find the limit for vanishing sphere radius: $\lim_{a\to 0} \mathbb{G}_{\text{trans}}$ [138, 139]. This yields the source-point corrected Green's function. For magnetic interactions at the source point we need the Green's tensor's curl at $\boldsymbol{r}_s$, see Eq. (2.40). Applying the curl before performing the limit yields the source-corrected curled Green's tensor, $\lim_{a\to 0} [\mathbb{G}_{\text{trans}} \times \boldsymbol{\nabla}]$. Comparison of both results with the original bulk Green's tensor $\mathbb{G}^{(0)}$ and its curl reveal the electric and magnetic local-field corrections. They are given by simple factors applied to the bulk Green's tensor, such that

$$\mathbb{G}^{(0)}(\boldsymbol{r}_a, \boldsymbol{r}_s, \omega) \xrightarrow{\text{source corr.}} c_{\text{e}}(\boldsymbol{r}_s, \omega)\mathbb{G}^{(0)}(\boldsymbol{r}_a, \boldsymbol{r}_s, \omega)\,, \tag{2.94}$$

$$\mathbb{G}^{(0)}(\boldsymbol{r}_a, \boldsymbol{r}_s, \omega) \times \boldsymbol{\nabla}_s \xrightarrow{\text{source corr.}} c_{\text{m}}(\boldsymbol{r}_s, \omega)\mathbb{G}^{(0)}(\boldsymbol{r}_a, \boldsymbol{r}_s, \omega) \times \boldsymbol{\nabla}_s\,, \tag{2.95}$$

$$c_{\text{e}}(\boldsymbol{r}_s, \omega) = \frac{3\varepsilon(\boldsymbol{r}_s, \omega)}{1 + 2\varepsilon(\boldsymbol{r}_s, \omega)}\,, \tag{2.96}$$

$$c_{\text{m}}(\boldsymbol{r}_s, \omega) = \frac{3}{1 + 2\mu(\boldsymbol{r}_s, \omega)}\,, \tag{2.97}$$

where because of the translation symmetry we can reintroduce a variable source point $\boldsymbol{r}_s$ into the result. The derivation steps for the source-point corrections are sketched in Fig. 2.2. Similarly, we find for the correction solely around the absorption point $\boldsymbol{r}_a$ the same correction factors $c_{\text{e/m}}(\boldsymbol{r}_a, \omega)$. From this symmetry that is related to the Onsager reciprocity we can conclude that the full local field correction for both points inside a

medium is given by [139]

$$\begin{aligned}
\mathbb{G}^{(0)} &\xrightarrow{\text{LFC}} c_e(\boldsymbol{r}_a,\omega)c_e(\boldsymbol{r}_s,\omega)\mathbb{G}^{(0)}\,,\\
\mathbb{G}^{(0)}\times\boldsymbol{\nabla}_s &\xrightarrow{\text{LFC}} c_e(\boldsymbol{r}_a,\omega)c_m(\boldsymbol{r}_s,\omega)\mathbb{G}^{(0)}\times\boldsymbol{\nabla}_s\,,\\
\boldsymbol{\nabla}_a\times\mathbb{G}^{(0)} &\xrightarrow{\text{LFC}} c_m(\boldsymbol{r}_a,\omega)c_e(\boldsymbol{r}_s,\omega)\boldsymbol{\nabla}_a\times\mathbb{G}^{(0)}\,,\\
\boldsymbol{\nabla}_a\times\mathbb{G}^{(0)}\times\boldsymbol{\nabla}_s &\xrightarrow{\text{LFC}} c_m(\boldsymbol{r}_a,\omega)c_m(\boldsymbol{r}_s,\omega)\boldsymbol{\nabla}_a\times\mathbb{G}^{(0)}\times\boldsymbol{\nabla}_s\,.
\end{aligned} \tag{2.98}$$

We will revisit this derivation in more detail for a chiral medium in chapter 4, where the local-field correction turns out to be more involved.

2.2. Calculation methods

In this section, we provide the necessary tools for calculating the process rates of interest. We start by introducing perturbative scattering theory and derive from it Fermi's Golden rule. Throughout this thesis, we will mainly used perturbation theory, including Fermi's golden rule in the dipole approximation. We then briefly compare QED in dipole approximation with *ab initio* quantum chemistry methods. While we do not use *ab initio* quantum chemistry methods throughout this thesis, we will often either compare the results obtained by out methods with results obtained by *ab initio* methods or use *ab initio* results as input parameters. Finally, we introduce open quantum systems and the master equation of a reduced system, as we will use an open quantum system approach in chapter 5.

2.2.1. Scattering theory and Dyson Series

Here, we derive the general rate of a second-order process via scattering theory, where the perturbative treatment leads to the Dyson series. We then show its application to the Auger rate in free-space QED without dipole approximation.

In scattering theory we assume that two subsystems are initially non-interactive, such that their interaction Hamiltonian H_{ia} vanishes for some time in the past, and after the interaction over a small time interval the subsystems are again left in eigenstates of the non-interacting Hamiltonian H_0. Obviously, this is true for a scattering experiment were the considered interaction is short-ranged and the two subsystems are initially separated, collide and are separated again. We want to apply scattering theory to the interaction between electrons via the electromagnetic field to describe internal atomic dynamics. While scattering theory is wildly used to describe the interaction between charges via the

electromagnetic field, the interaction is not short ranged and always present. We hence offer some remarks here for the successful application of scattering theory to our case: we assume that the atomic system is at some point in the past in an eigenstate of the full Hamiltonian that is also an eigenstate of the non-interacting Hamiltonian $\hat{H}_0$ (i.e. its ground state). The interaction is then turned on by exciting the atomic system into a state that is not an eigenstate of the full Hamiltonian. For weak coupling we may assume that the excited system is initially in a definite stationary state of the non-interacting Hamiltonian [140]. The interaction with the field then drives atomic dynamics and finally the atomic system ends up again in a state that is approximately an eigenstates of $\hat{H}_0$.

In the weak coupling regime we may apply time-dependent perturbation theory in the interaction picture and thus derive the Dyson operator for time-evolution. Let us start in Schrödinger picture where the time evolution operator $U_S(t-t_0)$ is uniquely defined by the Schrödinger equation,

$$\partial_t \hat{U}_S(t) = -\frac{i}{\hbar}\hat{H}(t)\hat{U}_S(t) \wedge \hat{U}_S(0) = 1 \quad \rightarrow \quad \hat{U}_S(t-t_0) = \mathcal{T} e^{-i\int_{t_0}^{t} d\tau \hat{H}(\tau)/\hbar}, \tag{2.99}$$

where $\mathcal{T}$ is the time-ordering operator. When splitting the Hamiltonian into system and interaction parts, $\hat{H}(t) = \hat{H}_0 + \hat{H}_{ia}$ (where we now assume for simplicity a time independent Hamiltonian), the time evolution operator $\hat{U}_S(t)$ can alternatively be written as:

$$\hat{U}_S(t) = U_0(t)U_{ia}(t), \tag{2.100}$$

$$\hat{U}_0(t) = e^{-i\hat{H}_0 t/\hbar}, \qquad \hat{U}_{ia}(t) = \mathcal{T} e^{-i\int d\tau \hat{V}(\tau)/\hbar}, \tag{2.101}$$

$$\hat{V}(t) = \hat{U}_0^\dagger(t)\hat{H}_{ia}\hat{U}_0(t). \tag{2.102}$$

This is easy to prove by taking the time derivative,

$$\begin{aligned} \partial t \left[\hat{U}_0(t)\hat{U}_{ia}(t)\right] &= -\frac{i}{\hbar}\hat{H}_0\hat{U}_0(t)\hat{U}_{ia}(t) - \frac{i}{\hbar}\hat{U}_0(t)\hat{V}(t)\hat{U}_{ia}(t) \\ &= -\frac{i}{\hbar}(\hat{H}_0 + \hat{H}_{ia})\hat{U}_0(t)\hat{U}_{ia}(t) \qquad (2.103) \\ \Leftrightarrow \qquad \hat{U}_S(t) &= \hat{U}_0(t)\hat{U}_{ia}(t), \qquad (2.104) \end{aligned}$$

and obviously $\hat{U}_0(t=0)\hat{U}_{ia}(t=0) = 1$. It is therefore an equivalent solution to the Schrödinger equation (2.99). This enables us to move to the interaction picture. Here, any operator evolves with $\hat{H}_0$ and the states evolve with $\hat{V}(t)$,

$$|\psi(t)\rangle_{ia} = \hat{U}_{ia}(t-t_0)\,|\psi_0\rangle_{ia}\,, \tag{2.105}$$

$$\hat{O}(t) = \hat{U}_0^\dagger(t-t_0)\hat{O}_0\hat{U}_0(t-t_0), \tag{2.106}$$

such that any expectation value keeps its time dependence compared to the Schrödinger

picture:

$$\langle\psi(t)|\hat{O}(t)|\psi(t)\rangle_{\text{ia}} = \langle\psi_0|\hat{U}_{\text{S}}^{\dagger}(t)\hat{O}_0\hat{U}_{\text{S}}(t)|\psi_0\rangle\ . \tag{2.107}$$

We may expand $\hat{U}_{\text{ia}}(t)$ in the Dyson series,

$$\begin{aligned}\hat{U}_{\text{ia}}(t) &= \sum_n \frac{1}{(\mathrm{i}\hbar)^n n!}\int_{t_0}^{t}\mathrm{d}t_n\cdots\int_{t_0}^{t}\mathrm{d}t_2\int_{t_0}^{t}\mathrm{d}t_1\mathcal{T}\left[\hat{V}(t_n)\ldots\hat{V}(t_2)\hat{V}(t_1)\right]\\ &= \sum_n \frac{1}{(\mathrm{i}\hbar)^n}\int_{t_0}^{t}\mathrm{d}t_n\cdots\int_{t_0}^{t_3}\mathrm{d}t_2\int_{t_0}^{t_2}\mathrm{d}t_1\hat{V}(t_n)\ldots\hat{V}(t_2)\hat{V}(t_1)\,.\end{aligned} \tag{2.108}$$

The full time evolution is then expanded by

$$\begin{aligned}\hat{U} &= \hat{U}_0(t)\hat{U}_{\text{ia}}(t) = \sum_n \hat{U}^{(n)}\\ &= \hat{U}_0(t) - \frac{\mathrm{i}}{\hbar}\int_{t_0}^{t}\mathrm{d}t_1\hat{U}_0(t)\hat{V}(t_1) + \frac{1}{\hbar^2}\int_{t_0}^{t}\mathrm{d}t_1\int_{t_0}^{t_1}\mathrm{d}t_2 U_0(t)\hat{V}(t_1)\hat{V}(t_2) + \ldots\,,\end{aligned} \tag{2.109}$$

such that $\hat{U}^{(0)} = \hat{U}_0$ and $\hat{U}^{(1)} = -\frac{\mathrm{i}}{\hbar}\int \mathrm{d}t_1\hat{U}_0(t)\hat{V}(t_1)$, and so forth. By assuming weak coupling we may use perturbation theory to truncate the series at the desired order.

The probability $P_f(t)$ to find an initial state $|\psi_0\rangle = |\psi_i\rangle$ after some interaction time t in the final state of interest $|\psi_f\rangle$ is given by

$$P_f(t) = |\,\langle\psi_f|\hat{U}_{\text{ia}}(t)|\psi_i\rangle\,|^2 = \left|S_{fi}(t)\right|^2\,, \tag{2.110}$$

where $S_{fi}(t)$ is the scattering matrix element. Here, we are interested in the process rate, which is given by the time derivative,

$$\Gamma_f = \frac{\mathrm{d}}{\mathrm{d}t}P_f(t)\,. \tag{2.111}$$

In scattering theory we usually obtain a time-independent result for the rate by assuming that the interaction only occurs in a finite, small time interval during scattering and taking the limit of $t - t_0 \to \infty$. If several final states are considered we can include them by summing over all probabilities/rates: $\Gamma = \sum_f \Gamma_f$. For second order processes the rate reads

$$\Gamma = \sum_f \frac{\mathrm{d}}{\mathrm{d}t}|S_{fi}^{(2)}(t)|^2\,, \tag{2.112}$$

$$S_{fi}^{(2)} = -\frac{1}{\hbar^2}\int_{t_0}^{t}\mathrm{d}t_2\int_{t_0}^{t_1}\mathrm{d}t_1\left\langle\psi_f\left|\hat{V}(t_2)\hat{V}(t_1)\right|\psi_i\right\rangle\,. \tag{2.113}$$

2.2.2. Fermi Golden rule

Fermi's Golden rule for transition rates serves as a starting point for many rate calculations. In this section we derive Fermi's Golden rule for second order processes from the rate expression (2.112) with help of the Dyson series.

In second order we find for the rate

$$\Gamma = \sum_f \frac{\mathrm{d}}{\mathrm{d}t} \left| \frac{1}{\hbar^2} \int_{t_0}^{t} \mathrm{d}t_2 \int_{t_0}^{t_2} \mathrm{d}t_1 \left\langle f \left| \hat{V}(t_2)\hat{V}(t_1) \right| i \right\rangle \right|^2 \tag{2.114}$$

$$= \sum_f \frac{\mathrm{d}}{\mathrm{d}t} \left| \sum_k \frac{1}{\hbar^2} \int_{t_0}^{t} \mathrm{d}t_2 \int_{t_0}^{t_2} \mathrm{d}t_1 \mathrm{e}^{\mathrm{i}\omega_{fk}t_2} \mathrm{e}^{-\mathrm{i}\omega_{ik}t_1} \left\langle f \left| \hat{H}_{\mathrm{ia}} \right| k \right\rangle \left\langle k \left| \hat{H}_{\mathrm{ia}} \right| i \right\rangle \right|^2 , \tag{2.115}$$

where we have introduced intermediate states $|k\rangle$. As we have discussed, the application of scattering theory implies that the interaction is not present at $t = t_0$. We now need to ensure explicitly that this condition holds. One way to do this is to introduce an adiabatic switch into the coupling Hamiltonian $\hat{V}(t) \to \hat{V}'(t) = \mathrm{e}^{\eta t}\hat{V}(t)$ with an arbitrarily small $\eta > 0$, such that $V'(t \to -\infty) = 0$ and then perform the limit $t_0 \to -\infty$. With this the rate yields

$$\Gamma = \sum_f \frac{1}{\hbar^4} \left| \sum_k \int_{-\infty}^{t} \mathrm{d}t_2 \int_{-\infty}^{t_2} \mathrm{d}t_1 \mathrm{e}^{\mathrm{i}\omega_{fk}t_2 + \eta t_2} \mathrm{e}^{-\mathrm{i}\omega_{ik}t_1 + \eta t_1} \left\langle f \left| \hat{H}_{\mathrm{ia}} \right| k \right\rangle \left\langle k \left| \hat{H}_{\mathrm{ia}} \right| i \right\rangle \right|^2 \tag{2.116}$$

$$= \sum_f \frac{1}{\hbar^4} \frac{d}{dt} \left| f_\eta(t) \right|^2 \left| \sum_k \frac{\left\langle f \left| \hat{H}_{\mathrm{ia}} \right| k \right\rangle \left\langle k \left| \hat{H}_{\mathrm{ia}} \right| i \right\rangle}{\omega_i - \omega_k + \mathrm{i}\eta} \right|^2 , \tag{2.117}$$

with

$$f_\eta(t) = \frac{\mathrm{e}^{\mathrm{i}(\omega_{fk} - \omega_{ik})t} \mathrm{e}^{2\eta t}}{2\eta + \mathrm{i}(\omega_{fk} - \omega_{ik})} , \tag{2.118}$$

where the limit $\eta \to 0$ after time derivation reveals a function sequence (i.e. a Lorentzian) that converges into the Dirac delta distribution for arbitrarily small η,

$$\lim_{\eta \to 0} \frac{d}{dt} \left| f_\eta(t) \right|^2 = \lim_{\eta \to 0} \frac{4\eta}{\omega_{fi}^2 + (2\eta)^2} = 2\pi\delta(\omega_f - \omega_i) . \tag{2.119}$$

We hence obtain

$$\Gamma = \sum_f \frac{2\pi}{\hbar^4} \delta(\omega_f - \omega_i) \left| \sum_k \frac{\left\langle f \left| \hat{H}_{\mathrm{ia}} \right| k \right\rangle \left\langle k \left| \hat{H}_{\mathrm{ia}} \right| i \right\rangle}{\omega_i - \omega_k} \right|^2 . \tag{2.120}$$

Fermi's Golden rule is usually applied to irreversible transitions into continuum, i.e. at least one final state's degree of freedom belongs to a continuum. In this case the sum

over these degrees of freedom is replaced by an integral: $\sum_f \to \sum_f \int \mathrm{d}\omega_f \rho(\omega_f)$, where ρ is the density of final states and $\sum_f$ sums over any remaining degrees of freedom. We finally find Fermi's Golden rule for second order transitions,

$$\Gamma = \sum_f \frac{2\pi}{\hbar^4} \rho(\omega_i) |M_{fi}|^2 , \tag{2.121}$$

with the transition matrix element,

$$M_{fi} = \sum_k \frac{\langle f \,|\, \hat{H}_{\mathrm{ia}} \,|\, k \rangle \langle k \,|\, \hat{H}_{\mathrm{ia}} \,|\, i \rangle}{\omega_i - \omega_k} \bigg|_{\omega_f = \omega_i} . \tag{2.122}$$

2.2.3. Comparison to *ab initio* quantum chemistry methods

An alternative approach for the calculation of atomic dynamics is given by *ab initio* quantum chemistry methods. We will not employ these methods in this work. However, we use results obtained via *ab initio* methods either as input parameters found as tabulated data or for comparison to results obtained via our approach. In this section we discuss the differences between these methods and (macroscopic) QED.

At the heart of all *ab initio* methods lies the Hartree–Fock method. It is used to solve the Schrödinger equation in the Born–Oppenheimer approximation numerically, iteratively and self-consistently. In the Hartree–Fock method, the many-electron problem posed by an atom or molecule is solved by identifying a dominant mean field function, the Hartree function and correcting it by single electron wave functions that are expanded as a linear combination of a finite basis set. The choice of these single electron wave functions and their finite basis set is then crucial for obtaining meaningful results. Since its invention, the Hartree–Fock method has been improved to take e.g. electron correlations and dissociation of molecules into account. These Post-Hartree–Fock methods include the Møller–Plesset perturbation theory, the configuration interaction method and the multiconfigurational self-consistent field method, to name just a few [141–143].

The results of *ab initio* methods are independent of empirical data, hence the name. In contrast, macroscopic QED leads in many cases to expressions which depend on some transition multipole moments that need to be determined either empirically or via *ab initio* methods. Another advantage of *ab initio* methods is the treatment of wave function overlap between atoms that are close to each other, e.g. in a molecule. However, *ab initio* methods do not quantise the electromagnetic field. In the post-Hartree–Fock methods the Coulomb interaction is taken into account only as an electron–electron correlation. The *ab initio* methods can hence neither account for retardation effects as QED or for the impact of macroscopic media modifying the electromagnetic vacuum as macroscopic QED

can do. Furthermore, our framework yields closed expressions that can be analytically studied, while *ab initio* methods need to be evaluated numerically.

In summary, our approach profits from *ab initio* results and for most precision calculations it would be the preferred choice to use an appropriate *ab initio* method. However, for the study of general dependencies, the inclusion of retardation effects and environment the framework of macroscopic QED is more suited.

2.2.4. Open quantum systems

Scattering theory as well as Fermi's golden rule are based on perturbation theory. An alternative treatment of weakly coupled systems is given by open quantum systems. In open quantum systems the full system is divided into a relevant system part coupled to a bath or environment. By assuming that the bath's correlations decay on a short time scale, we can find a dynamical map for the reduced system, describing its dynamics via a master equation. Its most approximative form is the Markov approximation, where the dynamics of the relevant system depend only on its state at equal times, the chosen order of bath correlations kept in the description and the bath's initial state. Within the scope of this work the bath is given by the electromagnetic field and the relevant system by the atomic system of interest.

We define the open quantum system S as a subsystem of a larger combined system $S + E$, that we refer to as full system. We assume that the full system's Hilbert space $\mathcal{H}$ is given by the tensor product of the individual systems' Hilbert spaces, such that the set of tensor products of the eigenstates of the individual Hilbert space form a basis of $\mathcal{H}$. We can then extend any observable $\hat{O}_S$ of the open system S to the full system as $\hat{O} = \hat{O}_S \otimes \mathbb{1}_E$. The expectation value of $\hat{O}_S$ in a state given by the density matrix $\rho(t)$ is then given by

$$\hat{O}_S = \mathrm{Tr}\left[\hat{O}\rho(t)\right] = \mathrm{Tr}_S\left[\hat{O}_S\rho_S(t)\right] , \tag{2.123}$$

where $\mathrm{Tr}_S[\cdot]$ is the partial trace over the system's basis set and $\rho_S(t) = \mathrm{Tr}_E[\rho(t)]$ is the reduced density matrix for the open quantum system. We hence find that the reduced density matrix $\rho_S(t)$ contains all necessary information for the system's observables. The problem then boils down to finding a dynamical map for $\rho_S(t)$, such that we may evolve ρ_S in time without evolving the full state $\rho(t)$.

The system's evolution is governed by the Liouville-von Neumann equation. In interaction picture it reads

$$\dot{\tilde{\rho}}(t) = -\frac{\mathrm{i}}{\hbar}\left[\hat{V}(t), \tilde{\rho}(t)\right] , \tag{2.124}$$

where $\tilde{\rho}$ and $\hat{V}(t)$ denote the density matrix and the interaction Hamiltonian, see Eq. (2.102), in interaction picture. Formal integration yields

$$\dot{\tilde{\rho}}(t) = \rho_0 - \frac{\mathrm{i}}{\hbar}\int_{t_0}^{t} \mathrm{d}t_1 \left[\hat{V}(t_1), \rho(t_1)\right] , \tag{2.125}$$

where $\rho_0 = \rho(t_0)$. Substituting this back into Eq. (2.124) gives the differential equation

$$\dot{\tilde{\rho}}(t) = -\frac{\mathrm{i}}{\hbar}\left[\hat{V}(t), \rho_0\right] - \frac{1}{\hbar^2}\int_{t_0}^{t} \mathrm{d}t_1 \left[\hat{V}(t), \left[\hat{V}(t_1), \tilde{\rho}(t_1)\right]\right] , \tag{2.126}$$

and hence

$$\dot{\tilde{\rho}}_S(t) = -\frac{\mathrm{i}}{\hbar}\,\mathrm{Tr}_E\left\{\left[\hat{V}(t), \rho_0\right]\right\} - \frac{1}{\hbar^2}\int_{t_0}^{t} \mathrm{d}t_1\,\mathrm{Tr}_E\left\{\left[\hat{V}(t), \left[\hat{V}(t_1), \tilde{\rho}(t_1)\right]\right]\right\} , \tag{2.127}$$

which is still exact. Next we treat the correlations building up in the environment perturbatively via the Born approximation. We assume that only correlations up to second order are relevant to the evolution of the open system. We have already cast the master equation (2.127) explicitly into a second-order form. We may hence apply the approximation by factorising the full system's density matrix inside the master equation as $\tilde{\rho}(t) = \tilde{\rho}_S(t) \otimes \rho_E(t_0)$ and find

$$\dot{\tilde{\rho}}_S(t) = -\frac{\mathrm{i}}{\hbar}\,\mathrm{Tr}_E\left\{\left[\hat{V}(t), \rho_0\right]\right\} - \frac{1}{\hbar^2}\int_{t_0}^{t} \mathrm{d}t_1\,\mathrm{Tr}_E\left\{\left[\hat{V}(t), \left[\hat{V}(t_1), \tilde{\rho}_S(t_1) \otimes \rho_E(t_0)\right]\right]\right\} . \tag{2.128}$$

Let us additionally assume that odd moments of the interaction Hamiltonian with the environment's initial state vanishes. The Born-approximated master equation (2.128) can then be simplified to read

$$\dot{\tilde{\rho}}_S(t) = -\frac{1}{\hbar^2}\int_{t_0}^{t} \mathrm{d}t_1\,\mathrm{Tr}_E\left\{\left[\hat{V}(t), \left[\hat{V}(t_1), \tilde{\rho}_S(t_1) \otimes \rho_E(t_0)\right]\right]\right\} . \tag{2.129}$$

For an open system S weakly coupled to a large environment E whose excitations and correlations decay quickly compared to the time scale in which the open system evolves the Markov approximation is justified. In a Markov process the time evolution of the system is independent of its past. We hence apply the replacement $\tilde{\rho}_S(t_1) \to \tilde{\rho}_S(t)$, yielding

$$\dot{\tilde{\rho}}_S(t) = -\frac{1}{\hbar^2}\int_{t_0}^{t} \mathrm{d}t_1\,\mathrm{Tr}_E\left\{\left[\hat{V}(t), \left[\hat{V}(t_1), \tilde{\rho}_S(t) \otimes \rho_E(t_0)\right]\right]\right\} , \tag{2.130}$$

which still is not truly Markovian since it depends on the system's state at time t_0. It is called the Redfield equation [144, 145]. Alternatively it can be derived via time-convolutionless projection operator method in second order [146]. Assuming that the time scale at which the open system varies is much larger than the time scale at which

the environments correlations decay we may put $t - t_0 \to \infty$ and obtain the Markov master equation [146]

$$\dot{\tilde{\rho}}_S(t) = -\frac{1}{\hbar^2}\int_{-\infty}^{t} \mathrm{d}t_1 \,\mathrm{Tr}_E \left\{ \left[\hat{V}(t), \left[\hat{V}(t_1), \tilde{\rho}_S(t_1) \otimes \rho_E(t_0)\right]\right]\right\} . \tag{2.131}$$

2.3. Previous results within (macroscopic) quantum electrodynamics

In this section, we will present and discuss some known results from the introduced framework of macroscopic QED as well as free-space QED. We will use these results in the main part of this thesis to either build new results upon or to compare our results to. We start by presenting the Møller formula for Auger decay, where we skip a full derivation here since we will revisit its derivation in the framework of macroscopic QED in chapter 3. We then derive the polarisability tensor for a non-polar atom as it serves useful for many applications throughout this thesis and we will build upon this derivation in chapter 5. We also discuss a successful regularisation model for Van-der-Waals forces between very close atoms. We will use this model as inspiration and its success as justification to develop a similar model in chapter 3 for Auger decay. We then briefly sketch the derivation of the spontaneous decay rate in the framework of macroscopic QED as a fundamental process highly related to the processes studied in this work and subsequently provide similarly the derivation of the resonance energy transfer rate, both derivations are revisited in detail in chapter 5. Finally, we discuss the discriminatory power of RET as it was studied theoretically within free-space QED.

2.3.1. Møller formula for Auger decay

We start by presenting the Møller formula for Auger decay obtained via scattering theory as presented in section 2.2.1 in free-space QED. The resulting formula will be rederived as a special case of our theory in chapter 3.

Let us consider two electrons bound in the same atom that scatter at each other. Each electron is initially thought of in some eigenstate $|i\rangle = |n, m\rangle$ of their non-interacting Hamiltonian $\hat{H}_0$ at time t_0. We are interested in the scattering process where the electrons end up to be in a non-interacting final state $|f\rangle = |k, p\rangle$, where k is an energetically lower level than n and m and p denotes a continuum state. In the usual formalism of Auger

decay we couple the electrons to the fields via minimal coupling, see Eq. (2.84),

$$\hat{H}_{\mathrm{ia}} = \int \mathrm{d}^3 r \hat{\rho}(\boldsymbol{r})\hat{\phi}(\boldsymbol{r}) - \int \mathrm{d}^3 r \hat{\boldsymbol{j}}(\boldsymbol{r}) \cdot \hat{\boldsymbol{A}}(\boldsymbol{r}) \,. \tag{2.132}$$

Using the general rate formula for second order transitions obtained via scattering theory, see Eq. (2.112), and the fields quantised via free-space QED, the derivation yields

$$\lim_{t,t_0\to\pm\infty} S^{(2)}_{fi}(t) = \lim_{t,t_0\to\pm\infty} \left(S^{(2)}_{\mathrm{dir}}(t) - S^{(2)}_{\mathrm{exch}}(t) \right) , \tag{2.133}$$

$$\begin{aligned} \lim_{t,t_0\to\pm\infty} S^{(2)}_{\mathrm{dir}}(t) = \frac{1}{2\mathrm{i}} \delta(\omega_{kn} - \omega_{mp}) \iint \mathrm{d}^3 r_1 \mathrm{d}^3 r_2 \frac{\mathrm{e}^{\mathrm{i}\omega_{kn}|\boldsymbol{r}_1 - \boldsymbol{r}_2|/c}}{|\boldsymbol{r}_1 - \boldsymbol{r}_2|} \\ \times \left(\rho_{kn}(\boldsymbol{r}_1)\rho_{mp}(\boldsymbol{r}_2) - \boldsymbol{j}_{kn}(\boldsymbol{r}_1)\boldsymbol{j}_{mp}(\boldsymbol{r}_2) \right) , \end{aligned} \tag{2.134}$$

where S_{dir} and S_{exch} label the direct and exchange term for the two indistinguishable electrons and $\rho_{ab} = \langle a|\hat{\rho}|b\rangle$ and $\boldsymbol{j}_{ab} = \langle a|\hat{\boldsymbol{j}}|b\rangle$ are the transition charge and transition charge current densities, respectively. The exchange term can be obtained from the direct term by exchanging its labels $n \leftrightarrow m$. This is known as Møller formula for electron–electron-scattering that includes retardation effects. It will emerge from our framework in the special case of free space, where we will revisit its derivation in detail.

2.3.2. Polarisability tensor

A helpful quantity for describing atom–field interactions within macroscopic quantum electrodynamics that can be calculated via perturbative methods is the polarisability tensor. The polarisability is classically known for many macroscopic objects. A variety of results can be represented in compact form by using the polarisability tensor. Its microscopical counterpart shall be briefly derived here. We present the derivation within in the framework of macroscopic QED; note that free-space QED yields the same result.

The electric polarisability $\boldsymbol{\alpha}$ of a macroscopic object is defined as the proportionality between an external electric field $\boldsymbol{E}$ and its induced dipole in Fourier space, such that

$$\mathcal{FT}\left[\langle \hat{\boldsymbol{d}}(t)\rangle\right] = \boldsymbol{\alpha}_n(\boldsymbol{r}_{\mathrm{A}},\omega) \cdot \boldsymbol{E}(\boldsymbol{r}_{\mathrm{A}},\omega) \,. \tag{2.135}$$

Let us consider an atom at position $\boldsymbol{r}_{\mathrm{A}}$ in one of its eigenstates $|n\rangle$ such that $\langle n|\hat{\boldsymbol{d}}|n\rangle = 0$, and let us consider for simplicity a coherent state $|\boldsymbol{E}(\boldsymbol{r},\omega)\rangle$ as external field , such that $\hat{\boldsymbol{E}}(\boldsymbol{r},\boldsymbol{\omega})\,|\boldsymbol{E}(\boldsymbol{r},\omega)\rangle = \boldsymbol{E}(\boldsymbol{r},\boldsymbol{\omega})\,|\boldsymbol{E}(\boldsymbol{r},\omega)\rangle$. The expectation value of the dipole operator then gives the induced dipole moment. We can calculate this expectation value up to the first

order in the electric field by applying perturbation theory

$$\left\langle \hat{\boldsymbol{d}}(t) \right\rangle = \sum_{ij} \boldsymbol{d}_{ij} \left\langle \hat{A}_{ij}(t) \right\rangle = \sum_{ij} \boldsymbol{d}_{ij} \left(\left\langle n, \boldsymbol{E} \left| \hat{U}^{(1)\dagger}(t) \hat{A}_{ij} \hat{U}^{(0)}(t) \right| n \right\rangle + \left\langle n \left| \hat{U}^{(0)\dagger}(t) \hat{A}_{ij} \hat{U}^{(1)}(t) \right| n, \boldsymbol{E} \right\rangle \right) , \tag{2.136}$$

where $\hat{A}_{ij} = |i\rangle \langle j|$ are atomic flip operators and $\hat{U}^{(n)}$ is the nth order of the time evolution operator in Schrödinger picture in terms of the Dyson series, see Eq (2.109).

With this and the interaction in dipole approximation $\hat{H}_{\mathrm{ia}} = -\hat{\boldsymbol{d}} \cdot \hat{\boldsymbol{E}}(\boldsymbol{r}_{\mathrm{A}})$ we find

$$\mathcal{FT}\left[\left\langle \hat{\boldsymbol{d}}(t) \right\rangle\right] = \frac{\mathrm{i}}{\hbar} \sum_k \mathcal{FT}\Bigg[\int \mathrm{d}t_1 \Big\{ \mathrm{e}^{\mathrm{i}\omega_{nk}(t_1 - t_0)} \boldsymbol{d}_{nk} \otimes \boldsymbol{d}_{kn} \cdot \boldsymbol{E}(\boldsymbol{r}_{\mathrm{A}}, t_1) - \mathrm{e}^{-\mathrm{i}\omega_{nk}(t_1 - t_0)} \boldsymbol{d}_{kn} \otimes \boldsymbol{d}_{nk} \cdot \boldsymbol{E}(\boldsymbol{r}_{\mathrm{A}}, t_1) \Big\} \Bigg] . \tag{2.137}$$

With the Fourier decomposition of the electric field,

$$\boldsymbol{E}(\boldsymbol{r}_{\mathrm{A}}, t) = \int_0^\infty \mathrm{d}\omega \left(\mathrm{e}^{-\mathrm{i}\omega(t - t_0)} \boldsymbol{E}(\boldsymbol{r}, \omega) + \mathrm{e}^{\mathrm{i}\omega(t - t_0)} \boldsymbol{E}^*(\boldsymbol{r}, \omega) \right) , \tag{2.138}$$

we can carry out the t_1-integration and with $\mathcal{FT}[\exp(\mathrm{i}\omega t)] = \delta(\omega)$ we get for the polarisability tensor,

$$\boldsymbol{\alpha}_n(\boldsymbol{r}_{\mathrm{A}}, \omega) = \frac{1}{\hbar} \sum_k \left[\frac{\boldsymbol{d}_{nk} \otimes \boldsymbol{d}_{kn}}{\omega_{kn} - \omega} + \frac{\boldsymbol{d}_{kn} \otimes \boldsymbol{d}_{nk}}{\omega_{kn} + \omega} \right] . \tag{2.139}$$

The polarisability tensor derived in this way diverges in cases of resonance, where $\omega = \omega_{kn}$. As we will show in chapter 5, by adopting results of an open quantum system approach into the derivation, one can derive imaginary corrections to the resonance case, such that the corrected polarisability reads

$$\boldsymbol{\alpha}_n(\boldsymbol{r}_{\mathrm{A}}, \omega) = \frac{1}{\hbar} \sum_k \left[\frac{\boldsymbol{d}_{nk} \otimes \boldsymbol{d}_{kn}}{\omega_{kn} - \omega - \mathrm{i}\gamma_{kn}} + \frac{\boldsymbol{d}_{kn} \otimes \boldsymbol{d}_{nk}}{\omega_{kn} + \omega + \mathrm{i}\gamma_{kn}} \right] , \tag{2.140}$$

with the damping constants γ_{kn} given by the respective transition line width.

2.3.3. Mediator particle as dielectric environment

The polarisability tensor for a single atom or molecule derived in the previous section serves useful in the framework of macroscopic QED. In close analogy to the permittivity of a macroscopic dielectric, the polarisability acts as linear response of a particle to an external field. In this section we include a single particle as dielectric media into the Green's tensor. We assume that the electric response of the particle is small and use a

Born-series as well as the Clausius–Mossotti law to find the scattering Green's tensor for a mediating particle.

The Helmholtz equation in the presence of a dielectric reads

$$\left[\nabla \times \nabla \times -\frac{\omega^2}{c^2}\boldsymbol{\varepsilon}(\boldsymbol{r},\omega)\right]\mathbb{G}(\boldsymbol{r},\boldsymbol{r}') = \delta(\boldsymbol{r}-\boldsymbol{r}')\mathbb{1}\,, \tag{2.141}$$

where $\boldsymbol{\varepsilon}$ can be tensor-valued. Let us assume that the deviation of $\boldsymbol{\varepsilon}(\boldsymbol{r},\omega) = \mathbb{I} + \boldsymbol{\zeta}(\boldsymbol{r},\omega)$ from its vacuum value is small. The free space solution (i.e. $\varepsilon = \mathbb{I}$) is given by $\mathbb{G}^{(0)}$, we can hence formally solve Eq. (2.141) by

$$\mathbb{G}(\boldsymbol{r},\boldsymbol{r}') = \mathbb{G}^{(0)}(\boldsymbol{r},\boldsymbol{r}') + \int \mathrm{d}^3 s\, \mathbb{G}^{(0)}(\boldsymbol{r},\boldsymbol{s}) \cdot \left(\frac{\omega^2}{c^2}\boldsymbol{\zeta}(\boldsymbol{r},\omega)\right) \cdot \mathbb{G}(\boldsymbol{s},\boldsymbol{r})\,, \tag{2.142}$$

and in lowest order of $\boldsymbol{\zeta}$ we find

$$\mathbb{G}(\boldsymbol{r},\boldsymbol{r}') = \mathbb{G}^{(0)}(\boldsymbol{r},\boldsymbol{r}') + \int \mathrm{d}^3 s\, \mathbb{G}^{(0)}(\boldsymbol{r},\boldsymbol{s}) \cdot \left(\frac{\omega^2}{c^2}\boldsymbol{\zeta}(\boldsymbol{r},\omega)\right) \cdot \mathbb{G}^{(0)}(\boldsymbol{s},\boldsymbol{r}) + \mathcal{O}(\boldsymbol{\zeta}^2)\,. \tag{2.143}$$

We may apply the Clausius–Mossotti law in the dilute gas limit to find the electric response $\boldsymbol{\zeta}$ of a single particle in lowest order to be

$$\boldsymbol{\zeta}(\boldsymbol{r},\omega) = \eta(\boldsymbol{r})\frac{\boldsymbol{\alpha}(\omega)}{\varepsilon_0}\,, \tag{2.144}$$

where $\eta(\boldsymbol{r})$ is the atom's density distribution in position space and $\boldsymbol{\alpha}(\omega) = \boldsymbol{\alpha}_0(\omega)$ is the ground state polarisability tensor, see Eq. (2.140). We assume further that the position distribution $\eta(\boldsymbol{r})$ of the second atom at position $\boldsymbol{r}_\mathrm{M}$ is well described by a delta distribution and hence get

$$\mathbb{G}(\boldsymbol{r},\boldsymbol{r}') = \mathbb{G}^{(0)}(\boldsymbol{r},\boldsymbol{r}') + \mathbb{G}^{\mathrm{M}}(\boldsymbol{r},\boldsymbol{r}')\,, \tag{2.145}$$

$$\mathbb{G}^{\mathrm{M}}(\boldsymbol{r},\boldsymbol{r}') = \frac{\omega^2}{c^2}\mathbb{G}^{(0)}(\boldsymbol{r},\boldsymbol{r}_\mathrm{M}) \cdot \frac{\boldsymbol{\alpha}(\omega)}{\varepsilon_0} \cdot \mathbb{G}^{(0)}(\boldsymbol{r}_\mathrm{M},\boldsymbol{r}')\,, \tag{2.146}$$

where $\mathbb{G}^{\mathrm{M}}$ is the mediator Green's tensor.

2.3.4. Van-der-Waals force for infinitely close atoms of finite size

When deriving the rate of Auger decay, we will find that the approach involving dipole approximation leads to a diverging result. A similar problem has previously been encountered when deriving Van-der-Waals forces between close atoms and energy shifts in the presented framework of macroscopic QED. We hence revisit the problem and its

solution here to prepare for an analogue regularisation model of the Auger decay rate.

Van-der-Waals forces between two atoms derived in the framework of macroscopic QED are given via the Van-der-Waals potential [121],

$$U(\boldsymbol{r}_1, \boldsymbol{r}_2) = -\frac{\hbar\mu_0^2}{2\pi}\int \mathrm{d}\xi\xi^4 \,\mathrm{Tr}\left[\boldsymbol{\alpha}^{(1)}(\mathrm{i}\xi)\cdot\mathbb{G}(\boldsymbol{r}_1,\boldsymbol{r}_2,\mathrm{i}\xi)\cdot\boldsymbol{\alpha}^{(2)}(\mathrm{i}\xi)\cdot\mathbb{G}(\boldsymbol{r}_2,\boldsymbol{r}_1,\mathrm{i}\xi)\right], \tag{2.147}$$

where the subscripts 1 and 2 label the two atoms and $\boldsymbol{\alpha}$ is their respective polarisability tensor. This potential diverges for $r \to 0$, where $r = |\boldsymbol{r}_1 - \boldsymbol{r}_2|$ is the interatomic separation. In these calculations the atoms are modelled as point dipoles. While taking higher multipoles into account can improve the results obtained for small separations, the divergence remains. At very small distances, numerical *ab initio* quantum chemistry methods may take wave function overlap between both atoms into account and electrostatic repulsion leads to a minimum potential at finite distances. Alternatively, Ninham and Mahanty suggested in 1975 that the finite size of atoms can be taken into account heuristically by introducing a finite size density profile to the atomic polarisability α_n, distributing it into a polarisability cloud. This then leads to a finite result for the force in the limit of $r \to 0$.

The polarisability tensor of an atom in state n is given by its transition dipole moments,

$$\boldsymbol{\alpha}_n(\omega) = \frac{1}{\hbar}\sum_k \left(\frac{\langle k|\hat{\boldsymbol{d}}|n\rangle \otimes \langle n|\hat{\boldsymbol{d}}|k\rangle}{\omega+\omega_k} - \frac{\langle n|\hat{\boldsymbol{d}}|k\rangle \otimes \langle k|\hat{\boldsymbol{d}}|n\rangle}{\omega-\omega_k}\right), \tag{2.148}$$

which is proportional to the identity for isotropic transition dipole moments $\langle k|\hat{\boldsymbol{d}}|n\rangle$. The polarisability's position independence is a direct consequence of the assumption of point-like atoms. We now introduce a Gaussian profile with size a_n to the polarisability to reintroduce the spatial volume of the atom,

$$\boldsymbol{\alpha}_n(\boldsymbol{r},\omega) = \frac{\mathrm{e}^{-r^2/a_n^2}}{\pi^{3/2}a_n^3}\boldsymbol{\alpha}_n(\omega), \tag{2.149}$$

where a_n is the atom's size in state $|n\rangle$. The Van-der-Waals potential between two ground state atoms can then be written as

$$U(\boldsymbol{r}_1, \boldsymbol{r}_2) = -\frac{\hbar\mu_0^2}{2\pi}\int \mathrm{d}\xi\xi^4 \,\mathrm{Tr}\left[\mathbb{F}_1(\boldsymbol{r}_1,\boldsymbol{r}_2,\mathrm{i}\xi)\cdot\mathbb{F}_2(\boldsymbol{r}_2,\boldsymbol{r}_1,\mathrm{i}\xi)\right], \tag{2.150}$$

$$\mathbb{F}_i(\boldsymbol{r}_1,\boldsymbol{r}_2,\mathrm{i}\xi) = \int \mathrm{d}^3r'\boldsymbol{\alpha}_0^{(i)}(\boldsymbol{r}'-\boldsymbol{r}_1,\mathrm{i}\xi)\cdot\mathbb{G}(\boldsymbol{r}',\boldsymbol{r}_2,\mathrm{i}\xi). \tag{2.151}$$

Alternatively, the regularisation can equivalently be applied to the Green's tensor instead

of the polarisability,

$$\tilde{\mathbb{G}}^{(i)}(\boldsymbol{r}_1,\boldsymbol{r}_2,\omega)=\int \mathrm{d}^3r'\frac{\mathrm{e}^{-(r_1-r')^2/a_{\mathrm{gs},i}^2}}{\pi^{3/2}a_{\mathrm{gs},i}^3}\mathbb{G}(\boldsymbol{r}',\boldsymbol{r}_2,\omega)\,, \tag{2.152}$$

where $a_{\mathrm{gs},i}$ is the ith atom's ground state radius. $\mathbb{F}_i$ is then given by

$$\mathbb{F}_i(\boldsymbol{r}_1,\boldsymbol{r}_2,\mathrm{i}\xi)=\boldsymbol{\alpha}_0(\omega)\cdot\tilde{\mathbb{G}}^{(i)}(\boldsymbol{r}_1,\boldsymbol{r}_2,\mathrm{i}\xi)\,. \tag{2.153}$$

This is similar to local field effects that can also either be accounted for by correcting the respective Green's tensor, see section 2.1.7 or the polarisability tensor [135]. By using the regularised Green's tensor $\tilde{\mathbb{G}}$ we obtain finite potentials even in the limit of $|\boldsymbol{r}_2-\boldsymbol{r}_1|\to 0$,

$$\lim_{\boldsymbol{r}_1\to\boldsymbol{r}_2}\mathbb{G}(\boldsymbol{r}_1,\boldsymbol{r}_2,\omega)\to\infty\,, \tag{2.154}$$

$$\lim_{\boldsymbol{r}_1\to\boldsymbol{r}_2}\tilde{\mathbb{G}}(\boldsymbol{r}_1,\boldsymbol{r}_2,\omega)\approx-\frac{c^2}{3\pi^{3/2}\omega^2a_{\mathrm{gs}}^3},\qquad a_{\mathrm{gs}}\ll\omega/c\,, \tag{2.155}$$

where we have assumed free space for simplicity. Ninham and Mahanty applied their approach to the potential between two atoms at vanishing separation limit as well as for the dispersion self-energy of a single atom. In the former case they derived energies in the order of magnitude of the molecular binding energy of the two atoms while in the latter case they obtained a self-energy of hydrogen in the order of magnitude of the electrons binding energy. In chapter 3 we will use these ideas to regularise the Green's tensor in the calculation of transition probabilities instead of potentials.

2.3.5. Spontaneous decay rate from Fermi's golden rule

We outline here the derivation of the spontaneous decay rate in the framework of macroscopic QED via Fermi's golden rule. The resulting rate is given in terms of the Green's tensor for arbitrary environment. From this we then derive the isotropic free space decay rate. A detailed derivation is presented in the main part of this thesis, see chapter 5.

Spontaneous decay is a first order process on the level of transition matrix elements for a single excited particle, where we only consider electric coupling to the atom, such that $\hat{H}_{\mathrm{ia}}=-\hat{\boldsymbol{d}}\cdot\hat{\boldsymbol{E}}$, see Eq. (2.93). According to Fermi's golden rule, see section 2.2.2 the spontaneous decay rate can be calculated via

$$\Gamma=\sum_f\frac{2\pi}{\hbar^4}\delta(\omega_f-\omega_i)\left|M_{fi}^{(1)}\right|^2,\qquad M_{fi}^{(1)}=\langle f\,|\,\hat{H}_{\mathrm{is}}\,|\,i\rangle \tag{2.156}$$

where $M_{fi}^{(1)}$ is the transition matrix element in first order, and $|i\rangle$ and $|f\rangle$ are the initial and final state, respectively. They are given by

$$|i\rangle = |e\rangle_{\mathrm{A}} \, |\{0\}\rangle_{\mathrm{F}} \,, \tag{2.157}$$

$$|f\rangle = |g\rangle_{\mathrm{A}} \, |\mathbf{1}_\lambda(\boldsymbol{r},\omega)\rangle_{\mathrm{F}} \,, \tag{2.158}$$

where $|\cdot\rangle_{\mathrm{A/F}}$ is the atomic/field state. Using the properties of the field's fundamental operators, see Eqs. (2.46)–(2.48), the Onsager reciprocity (2.37) and the integral relation (2.38) we find for the spontaneous emission rate

$$\Gamma_{\mathrm{s}} = \frac{2\mu_0}{\hbar}\omega_{eg}^2 \boldsymbol{d}_{eg} \cdot \mathrm{Im}\mathbb{G}(\boldsymbol{r}_{\mathrm{A}}, \boldsymbol{r}_{\mathrm{A}}, \omega_{eg}) \cdot \boldsymbol{d}_{ge} \,, \tag{2.159}$$

where $\boldsymbol{d}_{eg} = \langle e|\hat{\boldsymbol{d}}|g\rangle$ is the transition dipole moment. Using the free space Green's tensor, Eq. (A.32) we obtain

$$\Gamma_{\mathrm{s}}^{(0)} = \frac{\omega_{eg}^3 |\boldsymbol{d}_{eg}|^2}{3\pi\varepsilon_0\hbar c^3} \,, \tag{2.160}$$

for the free space spontaneous decay rate. The free space spontaneous decay rate serves as atomic parameter in many rate formulas. When we use it as such we will refer to it as γ_{eg}. It is known as tabulated atomic data for many systems from experiment and numerical *ab initio* calculations.

2.3.6. Resonance energy transfer rate from Fermi's golden rule

Here, we outline the derivation of the RET rate in the framework of macroscopic QED. We provide the rate in terms of the Green's tensor, in general as well as in the isotropic case and the free space rate. We waive a detailed derivation at this point, since we will revisit it in detail in chapter 5. We discuss the approach via Fermi's golden rule and interpret its result.

Resonance energy transfer is a second order process, involving the emission and absorption of field excitation at two different particles. Coupling the atomic system and the field via the electric multipolar coupling $\hat{H}_{\mathrm{ia}} = -\hat{\boldsymbol{d}} \cdot \hat{\boldsymbol{E}}$, see Eq. (2.93) and using Fermi's golden rule we find for the RET rate

$$\Gamma = \sum_f \frac{2\pi}{\hbar^4} \delta(\omega_f - \omega_i) \left| M_{fi}^{(2)} \right|^2 \,, \qquad M_{fi}^{(2)} = \sum_k \frac{\langle f \,|\, \hat{H}_{\mathrm{ia}} \,|\, k\rangle \, \langle k \,|\, \hat{H}_{\mathrm{ia}} \,|\, i\rangle}{\omega_i - \omega_k} \,, \tag{2.161}$$

where M_{fi}^2 is the second order transition matrix element and $|i\rangle$, $|f\rangle$ and $|k\rangle$ are the initial,

final and intermediate state, respectively. They are given by

$$|i\rangle = |e, 0, \{0\}\rangle \ , \tag{2.162}$$

$$|f\rangle = |g, 1, \{0\}\rangle \ , \tag{2.163}$$

$$|k\rangle \in \left\{ |g, 0, \mathbf{1}_\lambda(\boldsymbol{r}, \omega)\rangle \ , |e, 1, \mathbf{1}_\lambda(\boldsymbol{r}, \omega)\rangle \,\middle|\, \forall \lambda, \boldsymbol{r}, \omega \right\} \ , \tag{2.164}$$

where $|n, m, l\rangle = |n\rangle_\mathrm{D} |m\rangle_\mathrm{A} |l\rangle_\mathrm{F}$ is the product state of donor, acceptor and field state. Using the properties of the field's fundamental operators, see Eqs. (2.46)–(2.48), the Onsager reciprocity (2.37), the integral relation Eq. (2.38) and applying some algebra we find for the rate:

$$\Gamma_\mathrm{ret} = \sum_f \delta(\omega_{eg} - \omega_{10}) \frac{2\pi\mu_0\omega_{10}^2}{\hbar^2} \left| \boldsymbol{d}_{10} \cdot \mathbb{G}(\boldsymbol{r}_\mathrm{A}, \boldsymbol{r}_\mathrm{D}, \omega_{10}) \cdot \boldsymbol{d}_{ge} \right|^2 \ , \tag{2.165}$$

where $\boldsymbol{d}_{ij} = \langle i|\hat{\boldsymbol{d}}|j\rangle$ are transition dipole moments. We may further simplify this result by assuming isotropic dipole moments. The isotropy can be either the result from so called isotropic averaging, where we assume that the two interacting particle do not have a specific orientation to each other or from isotropic degenerate states in the sum over all final states. In both cases we find that isotropic transition dipoles can be approximated by $\boldsymbol{d} \otimes \boldsymbol{d} = |\boldsymbol{d}|^2 \mathbb{I}/3$. With this we can simplify the RET rate further, such that

$$\Gamma_\mathrm{ret} = \sum_f \delta(\omega_{eg} - \omega_{10}) \frac{2\pi\mu_0\omega_{10}^2 |\boldsymbol{d}_{eg}|^2 |\boldsymbol{d}_{10}|^2}{9\hbar^2} \operatorname{Tr}\left[\mathbb{G}(\boldsymbol{r}_\mathrm{A}, \boldsymbol{r}_\mathrm{D}, \omega_{10}) \cdot \mathbb{G}^*(\boldsymbol{r}_\mathrm{D}, \boldsymbol{r}_\mathrm{A}, \omega_{10}) \right] \ , \tag{2.166}$$

where we used the cyclic property of the trace and the Onsager reciprocity (2.37). The derived rate expression (2.166) is proportional to the delta-distribution, i.e. the rate either vanishes completely for $\omega_{eg} \neq \omega_{10}$ or diverges in case of resonance. Fermi's golden rule is applicable to irreversible processes. Considering the assumed system, its Hamiltonian as well as the final state of the process, there is no reason to assume irreversibility. However, this is only true in isolated systems that are truly described by the assumed Hamiltonian. Usually, RET is not observed between two isolated atoms in free space but atoms that are bound within a larger molecular compound. The resulting splitting of each energy level into e.g. several vibrational levels can then be regarded as a level broadening, since the splitting is very small compared to the transition energy. We may approximately take this into account by introducing an integral over the possible final states $\sum_f \to \int \mathrm{d}\omega_f \rho(\omega_f)$, where $\rho(\omega_f)$ is the density of final states at energy $\hbar\omega_f$. Its width is related to the linewidth of the transition. With this we find the finite result:

$$\Gamma_\mathrm{ret} = \rho(\omega_{eg}) \frac{2\pi\mu_0\omega_{10}^2 |\boldsymbol{d}_{eg}|^2 |\boldsymbol{d}_{10}|^2}{9\hbar^2} \operatorname{Tr}\left[\mathbb{G}(\boldsymbol{r}_\mathrm{A}, \boldsymbol{r}_\mathrm{D}, \omega_{10}) \cdot \mathbb{G}^*(\boldsymbol{r}_\mathrm{D}, \boldsymbol{r}_\mathrm{A}, \omega_{10}) \right] \ . \tag{2.167}$$

Using Eq. (A.32) for the Green's tensor, this yields in free space

$$\Gamma_{\text{ret}}^{(0)} = \frac{\gamma_{eg}\sigma_{01}(\omega_{eg})}{4\pi k^4 r^6}\left(k^4r^4 + k^2r^2 + 3\right), \tag{2.168}$$

where $r = |r_{\text{A}} - r_{\text{D}}|$ is the donor–acceptor separation distance and we introduced the free spontaneous decay rate $\gamma_{eg} = \Gamma_{\text{s}}^{(0)}$ for the donor, see Eq. (2.160) as well as the photoabsorption cross section σ_0 for the acceptor's ground state. The photoabsorption cross section is given in terms of transition dipole moments by [147]

$$\sigma_{01}(\omega) = \rho(\omega)\frac{\pi\omega_{10}|\boldsymbol{d}_{01}|^2}{3\varepsilon_0 c\hbar}. \tag{2.169}$$

2.3.7. Discrimination of chiral molecules via resonance energy transfer

In principle, resonance energy transfer between chiral molecules may be used to distinguish left- and right-handed molecules. In this section we briefly present and discuss the discriminatory part of the RET rate involving chiral molecules as it was suggested in free-space QED [118].

Let us consider the exchange of a photon between two optically active chiral molecules, i.e. resonance energy transfer between a donor D and an acceptor molecule A. Assuming that the chiral molecules at hand are indeed optical active we may use the multipolar expanded interaction Hamiltonian (2.93) to take magnetic interactions into account,

$$\hat{H}_{\text{ia}} = -\sum_{\alpha=\text{D,A}}\left(\hat{\boldsymbol{d}}^{\alpha}\cdot\hat{\boldsymbol{E}}(\boldsymbol{r}_{\alpha}) + \hat{\boldsymbol{m}}^{\alpha}\cdot\hat{\boldsymbol{B}}(\boldsymbol{r}_{\alpha})\right), \tag{2.170}$$

where we have neglected diamagnetic interactions as well as center of mass velocities. The rate can be calculated via Fermi's golden rule in second order (2.121). The initial, final and intermediate state for RET are given by Eqs. (2.162)–(2.164). In contrast to the purely electric coupled RET rate discussed in section 2.3.6, we gain additional process channels as a consequence of the possible magnetic interaction between molecules and field. Each channel consists of two interactions with the field and each interaction might either be electric or magnetic. We can hence label each transition matrix element by the type of interactions that are involved in emission and absorption of the respective channel,

$$M_{fi} = M_{\text{ee}} + M_{\text{em}} + M_{\text{mm}}. \tag{2.171}$$

In free-space QED the transition matrix elements are then given by [118]

$$M_{\mathrm{ee}} = \frac{1}{4\pi\varepsilon_0} d_i^{\mathrm{A}} d_j^{\mathrm{D}} \left[\nabla^2 \delta_{ij} - \nabla_i \nabla_j\right] \frac{e^{\mathrm{i}kr}}{r}\,, \tag{2.172}$$

$$M_{\mathrm{em}} = \frac{\mathrm{i}k}{4\pi\varepsilon_0 c} \left(d_i^{\mathrm{D}} m_j^{\mathrm{A}} - m_i^{\mathrm{D}} d_j^{\mathrm{A}}\right) \epsilon_{ijk} \nabla_k \frac{e^{\mathrm{i}kr}}{r}\,, \tag{2.173}$$

$$M_{\mathrm{mm}} = \frac{1}{4\pi\varepsilon_0 c^2} m_i^{\mathrm{A}} m_j^{\mathrm{D}} \left[\nabla^2 \delta_{ij} - \nabla_i \nabla_j\right] \frac{e^{\mathrm{i}kr}}{r}\,, \tag{2.174}$$

where r is the intermolecular distance and $k = \omega/c$ with $\hbar\omega$ is the transition energy. When considering the interference between different transition matrix elements we find that some contributions are proportional to $\boldsymbol{d}^{\alpha} \cdot \boldsymbol{m}^{\alpha}$ for $\alpha = \mathrm{D}, \mathrm{A}$. For chiral molecules this scalar product is related to the so-called rotatory strength,

$$R = \mathrm{Im}\left[\langle g|\boldsymbol{d}|e\rangle \cdot \langle e|\boldsymbol{m}|g\rangle\right]\,. \tag{2.175}$$

Its sign depends on the handedness and hence may be used to discriminate left- and right-handed enantiomers. The total rate given by Fermi's golden rule can then be split into two parts, one whose sign is insensitive to handedness and one that is handedness-depend and hence potentially discriminatory, Γ_{disc}. In free-space QED the discriminatory part associated with terms M_{em} and M_{me} is then given by

$$\Gamma_{\mathrm{disc}} = \frac{\rho(\omega)}{18\pi\varepsilon_0 \hbar c^2 r^6} R^{\mathrm{A}} R^{\mathrm{D}} \left(3 + 2k^2 r^2 + 2k^4 r^4\right)\,, \tag{2.176}$$

which is proportional to the product of the donor's and acceptor's rotatory strength. In conclusion the sign of Γ_{disc} is actually not determined by individual left- or right-handedness but by same or opposite handedness of donor and acceptor. In agreement with the Curie symmetry principle one of the participant's handedness needs to be known to determine the other's and if one of the participants is achiral, i.e. its rotatory strength is zero, the discriminatory part of the rate vanishes.

Auger and Interatomic Coulombic Decay

3

In this chapter, we study Auger decay and interatomic Coulombic decay (ICD) as two competing relaxation processes and show how macroscopic media can modify their ratio. We start by deriving the rates of Auger decay and ICD as special cases of electron–electron scattering where the two electrons are initially in some bound states and scatter into an unbound continuum state and an energetically lower state. As an intermediate result we obtain a rate formula where macroscopic effects could be introduced into *ab initio* calculation methods. We prove consistency with free-space QED by deriving the Møller formula for Auger decay. Subsequently, we introduce the dipole approximation to obtain a closed expression circumventing numerical integration. For Auger decay we develop a novel regularisation method to regain a finite result in the form of a closed expression in dipole approximation. This requires to introduce a new quantity, namely the Auger radius into the Auger decay rate. We provide a model for the Auger radius and compare the rate obtained by our model to results from *ab initio* methods, where we find good agreement. We then study both competing processes, ICD and Auger decay in the presence of dispersing and absorbing media. In doing so, we first give a general estimation for the relative magnitude of all possible decay channels in free space. We then show that the ratio of the rates to each other can be modified by the environment. We study the presence of a surface quantitatively, while giving a qualitative estimation for the rates inside a cavity. We finally apply the derived theory to the example of a He–Ne dimer. The results of this chapter were partly published in Refs. [JF1, JF2].

3.1. General rate in the presence of a macroscopic environment

In this section, we derive the general rate formulas for Auger decay and ICD from scattering theory. Both processes are second-order transitions, where two bound electrons scatter into an unbound continuum state and an energetically lower state. Their main difference is that in ICD the two involved electrons belong to different atoms while in Auger they belong to the same atom.

We derive a rate formula beyond dipole approximation in the framework of macroscopic QED that could be used to consider macroscopic environments while still treating the atoms as complex many-electron systems via involved numerical methods. From this rate formula we show consistency with free-space QED by recovering the Møller formula for electron–electron scattering. Finally we apply the dipole approximation to circumvent numerical integration and many-electron methods.

3.1.1. Derivation from scattering theory

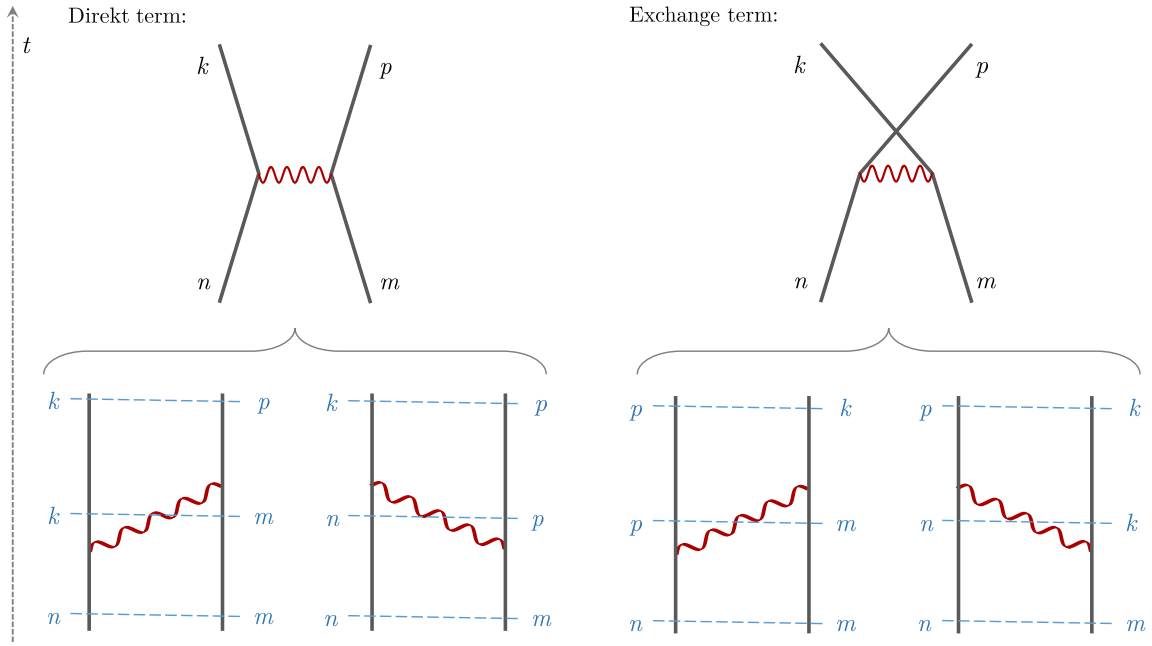

Figure 3.1.: Feynman diagrams for electron–electron scattering. Because of their indistinguishability we need to include the exchange term. The direct and exchange term can be each divided into two Feynman diagrams where the main difference are the intermediate states.

We start by deriving the general rate formula for a second-order transition beyond dipole approximation. We couple the atomic system to the electromagnetic field via the coupling Hamiltonian (2.85),

$$\hat{H}_{\mathrm{ia}} = \int \mathrm{d}^3 r \hat{\rho}(\boldsymbol{r})\hat{\phi}(\boldsymbol{r}) - \int \mathrm{d}^3 r \hat{\boldsymbol{A}}(\boldsymbol{r}) \cdot \hat{\boldsymbol{j}}(\boldsymbol{r}) \,. \tag{3.1}$$

The electron–electron scattering involves two interactions with the electromagnetic field, that is assumed to be initially excitation-less. The possible second-order channels are displayed in the form of Feynman diagrams in Fig. 3.1. The transition is described by the

scattering matrix in second order, see Eq. (2.113) and the rate is given by Eq. (2.112),

$$\Gamma = \sum_f \frac{\mathrm{d}}{\mathrm{d}t} |\langle f| \hat{S}^{(2)}(t) |i\rangle|^2 , \tag{3.2}$$

with the product states $|i\rangle = |n,m\rangle_\mathrm{A} |\{0\}\rangle_\mathrm{F}$ and $|f\rangle = |k,p\rangle_\mathrm{A} |\{0\}\rangle_\mathrm{F}$, where $|\cdot\rangle_{\mathrm{A/F}}$ are eigenstates of the respective uncoupled Hamiltonian $\hat{H}_\mathrm{A}/\hat{H}_\mathrm{F}$. From this point forward, we will drop the index notations A and F for the atomic and field states. The product state $|n,m\rangle = |n\rangle_a |m\rangle_b$ labels two bound states n and m for the two electrons involved in the transition, while the product state $|k,p\rangle$ labels an energetically lower and initially vacant state k and a continuum state p for each electron. The scattering operator can be divided into three contributions that are treated separately,

$$\hat{S}^{(2)}(t) = -\frac{1}{\hbar^2}\left(\hat{A}(t) + \hat{B}(t) + \hat{C}(t)\right), \tag{3.3}$$

$$\hat{A}(t) = \int_{t_0}^{t}\mathrm{d}t_a \int_{t_0}^{t_a}\mathrm{d}t_b \int\mathrm{d}^3 r_a \int\mathrm{d}^3 r_b\, \hat{\rho}_a\hat{\phi}_a\, \hat{\rho}_b\hat{\phi}_b , \tag{3.4}$$

$$\hat{B}(t) = \int_{t_0}^{t}\mathrm{d}t_a \int_{t_0}^{t_a}\mathrm{d}t_b \int\mathrm{d}^3 r_a \int\mathrm{d}^3 r_b\, \hat{\boldsymbol{j}}_a\cdot\hat{\boldsymbol{A}}_a\, \hat{\boldsymbol{j}}_b\cdot\hat{\boldsymbol{A}}_b , \tag{3.5}$$

$$\hat{C}(t) = -\int_{t_0}^{t}\mathrm{d}t_a \int_{t_0}^{t_a}\mathrm{d}t_b \int\mathrm{d}^3 r_a \int\mathrm{d}^3 r_b \left(\hat{\rho}_a\hat{\phi}_a\, \hat{\boldsymbol{j}}_b\cdot\hat{\boldsymbol{A}}_b + \hat{\boldsymbol{j}}_a\cdot\hat{\boldsymbol{A}}_a\, \hat{\rho}_b\hat{\phi}_b\right), \tag{3.6}$$

where we have introduced the shorthand notation $\hat{O}_x = \hat{O}(\boldsymbol{r}_x, t_x)$ for any operator $\hat{O}$. Additionally, because of the indistinguishability of the involved electrons the transition involves a direct term $n \to k$, $m \to p$ and an exchange term $m \to k$, $n \to p$, see Fig. 3.1, such that

$$\langle f|\hat{S}^{(2)}(t)|i\rangle = = \underbrace{S^{(2)}_{n\to k}(t)}_{\text{direct term}} - \underbrace{S^{(2)}_{n\to p}(t)}_{\text{exchange term}} , \tag{3.7}$$

where the sign is a consequence of the antisymmetric nature of the fermionic electrons under exchange. We focus on the direct term for the derivation and obtain the exchange term in the end by simply exchanging the respective state labels. We start by deriving the first contribution (3.4) of the direct term

$$A_{n\to k}(t) = \int_{t_0}^{t}\mathrm{d}t_a \int_{t_0}^{t_a}\mathrm{d}t_b \int\mathrm{d}^3 r_a \int\mathrm{d}^3 r_b \Big\{\rho_{nk}(\boldsymbol{r}_a, t_a)\, \langle\{0\}|\, \hat{\phi}_a\hat{\phi}_b\, |\{0\}\rangle\, \rho_{mp}(\boldsymbol{r}_b, t_b) + \rho_{mp}(\boldsymbol{r}_a, t_a)\, \langle\{0\}|\, \hat{\phi}_a\hat{\phi}_b\, |\{0\}\rangle\, \rho_{nk}(\boldsymbol{r}_b, t_b)\Big\}, \tag{3.8}$$

where the two summands represent different ordering of emission and absorption, according to the lower Feynman diagrams in Fig. 3.1, and we have introduced the transition quantities $\rho_{nm} = \langle n|\hat{\rho}|m\rangle$ and $\boldsymbol{j}_{nm} = \langle n|\hat{\boldsymbol{j}}|m\rangle$. Formally, both processes (first emission, then absorption and vice versa) need to be taken into account even though one of them

violates energy conservation. We will see later that the latter term does not appear in the resulting rate. The time evolution for the transition charge and current densities in interaction picture are given by

$$\rho_{nk}(\boldsymbol{r}_a, t_a) = e^{\mathrm{i}\omega_{kn}t}\rho(\boldsymbol{r}_a)\,, \tag{3.9}$$

$$\boldsymbol{j}_{nk}(\boldsymbol{r}_a, t_a) = e^{\mathrm{i}\omega_{kn}t}\rho(\boldsymbol{r}_a)\,, \tag{3.10}$$

where $\hbar\omega_{kn} = E_k - E_n$ is the energy difference between the involved orbitals. As a consequence we can write the continuity equation (2.7) as

$$\rho(\boldsymbol{r}_a) = \frac{\mathrm{i}}{\omega_{kn}}\nabla\cdot\boldsymbol{j}_{nk}(\boldsymbol{r}_a)\,. \tag{3.11}$$

To simplify the following calculation, we will already take into account the different signs of the transition frequencies. For the downward transition from $|n\rangle$ to $|k\rangle$ one finds $\hbar\omega_{kn} = E_k - E_n < 0$, we therefore define the positive frequency $\omega_{nk} = (E_n - E_k)/\hbar = -\omega_{kn} > 0$. In case of the second transition ($|m\rangle \to |p\rangle$) the transition energy is positive, $\omega_{pm} = (E_p - E_m)/\hbar > 0$. Combining Eqs. (3.8) – (3.11) we obtain

$$\begin{aligned} A_{n\to k}(t) &= \int_{t_0}^{t}\mathrm{d}t_a\int_{t_0}^{t_a}\mathrm{d}t_b\int\mathrm{d}^3r_a\int\mathrm{d}^3r_b\,\frac{1}{\omega_{nk}\omega_{pm}}\Big\{\boldsymbol{\nabla}\cdot\boldsymbol{j}_{nk}(\boldsymbol{r}_a,t_a)\,\langle\{0\}|\,\hat{\phi}_a\hat{\phi}_b\,|\{0\}\rangle\,\boldsymbol{\nabla}\cdot\boldsymbol{j}_{mp}(\boldsymbol{r}_b,t_b) \\ &\qquad + \boldsymbol{\nabla}\cdot\boldsymbol{j}_{mp}(\boldsymbol{r}_a,t_a)\,\langle\{0\}|\,\hat{\phi}_a\hat{\phi}_b\,|\{0\}\rangle\,\boldsymbol{\nabla}\cdot\boldsymbol{j}_{nk}(\boldsymbol{r}_b,t_b)\Big\} \\ &= \int_{-\infty}^{t}\mathrm{d}t_a\int_{-\infty}^{t_a}\mathrm{d}t_b\int\mathrm{d}^3r_a\int\mathrm{d}^3r_b\,\frac{1}{\omega_{nk}\omega_{pm}}\Big\{\boldsymbol{j}_{nk}(\boldsymbol{r}_a,t_a)\cdot\langle\{0\}|\,\hat{\boldsymbol{E}}_a^{\parallel}\hat{\boldsymbol{E}}_b^{\parallel}\,|\{0\}\rangle\cdot\boldsymbol{j}_{mp}(\boldsymbol{r}_b,t_b) \\ &\qquad + \boldsymbol{j}_{mp}(\boldsymbol{r}_a,t_a)\cdot\langle\{0\}|\,\hat{\boldsymbol{E}}_a^{\parallel}\hat{\boldsymbol{E}}_b^{\parallel}\,|\{0\}\rangle\cdot\boldsymbol{j}_{nk}(\boldsymbol{r}_b,t_b)\Big\}\,, \end{aligned} \tag{3.12}$$

where we have integrated by parts in the last step and used that in Coulomb gauge $\hat{\boldsymbol{E}}^{\parallel} = -\nabla\phi$, see Eq. (A.7). We introduce the Green's tensor into the equation by evaluating

the vacuum fluctuations, see Eqs. (A.15)

$$\begin{aligned} A_{n\to k}(t) = \int_{-\infty}^{t}\mathrm{d}t_a\int_{-\infty}^{t_a}\mathrm{d}t_b\int\mathrm{d}^3r_a\int\mathrm{d}^3r_b\int\mathrm{d}\omega\ \frac{1}{\omega_{nk}\omega_{pm}}\frac{\hbar\omega^2}{\pi c^2\varepsilon_0}e^{-\mathrm{i}\omega(t_a-t_b)} \\ \times\Big\{\boldsymbol{j}_{nk}(\boldsymbol{r}_a,t_a)\cdot\mathrm{Im}^{\parallel}\mathbb{G}^{\parallel}(\boldsymbol{r}_a,\boldsymbol{r}_b,\omega)\cdot\boldsymbol{j}_{mp}(\boldsymbol{r}_b,t_b) \\ +\boldsymbol{j}_{mp}(\boldsymbol{r}_a,t_a)\cdot\mathrm{Im}^{\parallel}\mathbb{G}^{\parallel}(\boldsymbol{r}_a,\boldsymbol{r}_b,\omega)\,|\{0\}\rangle\,\boldsymbol{j}_{nk}(\boldsymbol{r}_b,t_b)\Big\} \\ = \int\mathrm{d}^3r_a\int\mathrm{d}^3r_b\int\mathrm{d}\omega\ \frac{\omega^2}{\omega_{nk}\omega_{pm}}\frac{\hbar}{\pi c^2\varepsilon_0}h(t,\omega)\boldsymbol{j}_{nk}(\boldsymbol{r}_a)\cdot\mathrm{Im}^{\parallel}\mathbb{G}^{\parallel}(\boldsymbol{r}_a,\boldsymbol{r}_b,\omega)\cdot\boldsymbol{j}_{mp}(\boldsymbol{r}_b) \end{aligned} \tag{3.13}$$

$$h(t,\omega) = \int_{-\infty}^{t}\mathrm{d}t_a\int_{-\infty}^{t_a}\mathrm{d}t_b\,e^{-\mathrm{i}\omega(t_a-t_b)}\left(e^{-\mathrm{i}\omega_{nk}t_a}e^{\mathrm{i}\omega_{pm}t_b}+e^{\mathrm{i}\omega_{pm}t_a}e^{-\mathrm{i}\omega_{nk}t_b}\right), \tag{3.14}$$

where we have used the Onsager reciprocity (2.37) and the fact that the position integrations are symmetric in $\boldsymbol{r}_a$ and $\boldsymbol{r}_b$. The superscripts denote transverse and longitudinal parts of the respective vector or tensor and are defined by Eqs. (A.8)–(A.13). The second and third contributions can be treated similarly, such that

$$\begin{aligned} B_{n\to k}(t) =& \int_{-\infty}^{t}\mathrm{d}t_a\int_{-\infty}^{t_a}\mathrm{d}t_b\int\mathrm{d}^3r_a\int\mathrm{d}^3r_b\Big\{\boldsymbol{j}_{nk}(\boldsymbol{r}_a,t_a)\cdot\langle\{0\}|\,\hat{\boldsymbol{A}}_a{\otimes}\hat{\boldsymbol{A}}_b\,|\{0\}\rangle\cdot\boldsymbol{j}_{mp}(\boldsymbol{r}_b,t_b) \\ &+\boldsymbol{j}_{mp}(\boldsymbol{r}_a,t_a)\cdot\langle\{0\}|\,\hat{\boldsymbol{A}}_a{\otimes}\hat{\boldsymbol{A}}_b\,|\{0\}\rangle\cdot\boldsymbol{j}_{nk}(\boldsymbol{r}_b,t_b)\Big\} \\ =& \int\mathrm{d}^3r_a\int\mathrm{d}^3r_b\int\mathrm{d}\omega\frac{\hbar}{\pi c^2\varepsilon_0}h(t,\omega)\boldsymbol{j}_{nk}(\boldsymbol{r}_a)\cdot\mathrm{Im}^{\perp}\mathbb{G}^{\perp}(\boldsymbol{r}_a,\boldsymbol{r}_b,\omega)\cdot\boldsymbol{j}_{mp}(\boldsymbol{r}_b)\,, \end{aligned} \tag{3.15}$$

$$\begin{aligned} C_{n\to k}(t) =& \int_{-\infty}^{t}\mathrm{d}t_a\int_{-\infty}^{t_a}\mathrm{d}t_b\int\mathrm{d}^3r_a\int\mathrm{d}^3r_b\Big\{\frac{\mathrm{i}}{\omega_{nk}}\boldsymbol{j}_{nk}(\boldsymbol{r}_a,t_a)\cdot\langle\{0\}|\,\hat{\boldsymbol{E}}_a^{\parallel}{\otimes}\hat{\boldsymbol{A}}_b\,|\{0\}\rangle\cdot\boldsymbol{j}_{mp}(\boldsymbol{r}_b,t_b) \\ &-\frac{\mathrm{i}}{\omega_{pm}}\boldsymbol{j}_{mp}(\boldsymbol{r}_a,t_a)\cdot\langle\{0\}|\,\hat{\boldsymbol{E}}_a^{\parallel}{\otimes}\hat{\boldsymbol{A}}_b\,|\{0\}\rangle\cdot\boldsymbol{j}_{nk}(\boldsymbol{r}_b,t_b) \\ &-\frac{\mathrm{i}}{\omega_{pm}}\boldsymbol{j}_{nk}(\boldsymbol{r}_a,t_a)\cdot\langle\{0\}|\,\hat{\boldsymbol{A}}_a{\otimes}\hat{\boldsymbol{E}}_b^{\parallel}\,|\{0\}\rangle\cdot\boldsymbol{j}_{mp}(\boldsymbol{r}_b,t_b) \\ &+\frac{\mathrm{i}}{\omega_{nk}}\boldsymbol{j}_{mp}(\boldsymbol{r}_a,t_a)\cdot\langle\{0\}|\,\hat{\boldsymbol{A}}_a{\otimes}\hat{\boldsymbol{E}}_b^{\parallel}\,|\{0\}\rangle\cdot\boldsymbol{j}_{nk}(\boldsymbol{r}_b,t_b)\Big\} \\ =& \int\mathrm{d}^3r_a\int\mathrm{d}^3r_b\int\mathrm{d}\omega\frac{\hbar}{\pi\varepsilon_0c^2}h(t,\omega)\Big\{\frac{\omega}{\omega_{nk}}\boldsymbol{j}_{nk}(\boldsymbol{r}_a)\cdot\mathrm{Im}^{\parallel}\mathbb{G}^{\perp}(\boldsymbol{r}_a,\boldsymbol{r}_b,\omega)\cdot\boldsymbol{j}_{mp}(\boldsymbol{r}_b) \\ &+\frac{\omega}{\omega_{pm}}\boldsymbol{j}_{nk}(\boldsymbol{r}_a)\cdot\mathrm{Im}^{\perp}\mathbb{G}^{\parallel}(\boldsymbol{r}_a,\boldsymbol{r}_b,\omega)\cdot\boldsymbol{j}_{mp}(\boldsymbol{r}_b)\Big\}\,, \end{aligned} \tag{3.16}$$

where we have expressed the vacuum fluctuations in terms of the Green's tensor, see Eqs. (A.14)–(A.17), and used the time dependency (3.10) as well as the continuity equation (3.11).

The time integration inside $h(t,\omega)$ can be carried out, yielding poles in the frequency

domain. As in the derivation of Fermi's golden rule, see section 2.2.2, we need to ensure that the coupling vanishes at $t_0 \to -\infty$. We analogously include an infinitesimal parameter $\eta > 0$ into the coupling Hamiltonian to ensure this, $\hat{V}(t) \to \hat{V}'(t) = e^{\eta t}\hat{V}(t)$. The time integrations of the three contributions then leads to

$$\begin{aligned} h(t,\omega) = \int_{-\infty}^{t} \mathrm{d}t_a \int_{-\infty}^{t_a} \mathrm{d}t_b \, e^{\eta(t_a+t_b)} e^{\mathrm{i}\omega(t_b-t_a)} \left\{ e^{\mathrm{i}\omega_{pm}t_a} e^{-\mathrm{i}\omega_{nk}t_b} \pm e^{-\mathrm{i}\omega_{nk}t_a} e^{\mathrm{i}\omega_{pm}t_b} \right\} \\ = f_\eta(t) \left\{ \frac{1}{\mathrm{i}(\omega - \omega_{nk} - \mathrm{i}\eta)} \pm \frac{1}{\mathrm{i}(\omega + \omega_{pm} - \mathrm{i}\eta)} \right\}, \end{aligned} \tag{3.17}$$

with $f_\eta(t)$ defined by Eq. (2.118),

$$f_\eta(t) = \frac{\mathrm{e}^{\mathrm{i}(\omega_{nk}-\omega_{pm})t} \mathrm{e}^{2\eta t}}{2\eta + \mathrm{i}(\omega_{nk} - \omega_{pm})} \,. \tag{3.18}$$

Analogously to Eq. (2.119), we obtain for the rate

$$\Gamma \propto \mathrm{d}/\mathrm{d}t |f_\eta(t)|^2 \quad \xrightarrow[\eta \to 0]{} \quad 2\pi\delta(\omega_{pm} - \omega_{nk}) \,, \tag{3.19}$$

which ensures energy conservation. As a consequence, we use $\omega_{pm} = \omega_{nk}$ explicitly from here on. The time integration has introduced poles in the frequency domain. The complex frequency integral can be performed in general for all terms. Due to the resonance constraint, Eq. (3.19), they yield the same result

$$-\mathrm{i}\int_0^\infty \mathrm{d}\omega \left\{ \frac{p(\omega)}{\omega - (\omega_{nk} + \mathrm{i}\eta)} + \frac{p(-\omega)}{\omega + \omega_{nk} - \mathrm{i}\eta} \right\} \mathrm{Im}\,\mathbb{G}(\omega) = -\mathrm{i}\pi \mathbb{G}(\omega_{nk}) \,, \tag{3.20}$$

with

$$p(\omega) = \begin{cases} \frac{\omega^2}{\omega_{nk}^2} & \text{for } A_{n\to k} \\ 1 & \text{for } B_{n\to k} \\ \frac{\omega}{\omega_{nk}} & \text{for } C_{n\to k} \end{cases} \tag{3.21}$$

and $p(\omega_{nk}) = 1$. The contour integration is carried out in detail in the appendix, see section A.4. The second (positive) pole is due to the second summand of Eq. 3.8, i.e. results from the energy-violating term. It is cancelled out by a contribution of the first pole, see

section A.4. With this the contributions simplify to

$$A_{n\to k}(t) = \frac{\hbar}{c^2\varepsilon_0} f_\eta(t) \int \mathrm{d}^3 r_a \int \mathrm{d}^3 r_b \left\{ \boldsymbol{j}_{nk}(\boldsymbol{r}_a) \cdot {}^{\parallel}\mathbb{G}^{\parallel}(\boldsymbol{r}_a, \boldsymbol{r}_b, \omega) \cdot \boldsymbol{j}_{mp}(\boldsymbol{r}_b) \right\}, \tag{3.22}$$

$$B_{n\to k}(t) = \frac{\hbar}{c^2\varepsilon_0} f_\eta(t) \int \mathrm{d}^3 r_a \int \mathrm{d}^3 r_b \left\{ \boldsymbol{j}_{nk}(\boldsymbol{r}_a) \cdot {}^{\perp}\mathbb{G}^{\perp}(\boldsymbol{r}_a, \boldsymbol{r}_b, \omega) \cdot \boldsymbol{j}_{mp}(\boldsymbol{r}_b) \right\}, \tag{3.23}$$

$$\begin{aligned} C_{n\to k}(t) = \frac{\hbar}{c^2\varepsilon_0} f_\eta(t) \int \mathrm{d}^3 r_a \int \mathrm{d}^3 r_b \Big\{ & \boldsymbol{j}_{nk}(\boldsymbol{r}_a) \cdot {}^{\parallel}\mathbb{G}^{\perp}(\boldsymbol{r}_a, \boldsymbol{r}_b, \omega) \cdot \boldsymbol{j}_{mp}(\boldsymbol{r}_b) \\ & + \boldsymbol{j}_{nk}(\boldsymbol{r}_a) \cdot {}^{\perp}\mathbb{G}^{\parallel}(\boldsymbol{r}_a, \boldsymbol{r}_b, \omega) \cdot \boldsymbol{j}_{mp}(\boldsymbol{r}_b) \Big\}, \end{aligned} \tag{3.24}$$

where we have omitted the redundant phase factor $1/\mathrm{i}$. The sum over all contributions then simply yields

$$S_{n\to k}(t) = f_\eta(t) M_{n\to k}, \tag{3.25}$$

$$M_{n\to k} = \frac{\mu_0}{\hbar} \int \mathrm{d}^3 r_a \int \mathrm{d}^3 r_b \, \boldsymbol{j}_{nk}(\boldsymbol{r}_a) \cdot \mathbb{G}(\boldsymbol{r}_a, \boldsymbol{r}_b, \omega) \cdot \boldsymbol{j}_{mp}(\boldsymbol{r}_b), \tag{3.26}$$

where we have used that by definition $\mathbb{G} = \sum_{i,j=\perp,\parallel} {}^{i}\mathbb{G}^{j}$. The exchange term follows directly by exchanging the respective state labels

$$S_{n\to p}(t) = f_\eta(t) M_{n\to p}, \tag{3.27}$$

$$M_{n\to p} = \frac{\mu_0}{\hbar} \int \mathrm{d}^3 r_a \int \mathrm{d}^3 r_b \, \boldsymbol{j}_{mk}(\boldsymbol{r}_a) \cdot \mathbb{G}(\boldsymbol{r}_a, \boldsymbol{r}_b, \omega) \cdot \boldsymbol{j}_{np}(\boldsymbol{r}_b). \tag{3.28}$$

The rate is then given by

$$\begin{aligned} \Gamma &= \sum_f \frac{d}{dt} |\, \langle f |\, \hat{S}^{(2)}(t)\, | i \rangle \,|^2 \\ &= \sum_f 2\pi \delta(\omega_{pm} - \omega_{nk}) \left| M_{n\to k} - M_{n\to p} \right|^2 \\ &= 2\pi \sum_{m,n} \int \mathrm{d}\omega_p \rho(\omega_p) \delta(\omega_{pm} - \omega_{nk}) \left| M_{n\to k} - M_{n\to p} \right|^2 \\ &= 2\pi \sum_{m,n} \rho(\omega_p) \left| M_{n\to k} - M_{n\to p} \right|^2, \end{aligned} \tag{3.29}$$

where we have replaced the sum over all final continuum states $|p\rangle$ by an integral and introduced the density of final states for the continuum electron $\rho(\omega_p)$ at energy $\hbar\omega_p$. The same result can be obtained by applying Fermi's golden rule. The calculation of the process rate has now boiled down to the calculation of the transition matrix elements

$$M_{n\to k} = -\frac{\mathrm{i}\mu_0}{\hbar} \int \mathrm{d}^3 r_a \int \mathrm{d}^3 r_b \, \boldsymbol{j}_{nk}(\boldsymbol{r}_a) \cdot \mathbb{G}(\omega_{nk}) \cdot \boldsymbol{j}_{mp}(\boldsymbol{r}_b). \tag{3.30}$$

This formula can serve as a new starting point including macroscopic media into *ab initio*

quantum chemistry methods that are suited to deal with many-electron problems and wave-function overlaps between different atoms.

3.1.2. Recovering the Møller formula in free space

To prove consistency with free-space QED, we briefly rederive the Møller-formula for Auger decay here, see section 2.3.1 from the macroscopic QED result (3.29).

The Green's tensor consists of a bulk part and scattering part. In free space the bulk part corresponds to the well-known photon propagator and one can rederive the famous Møller-formula for electron–electron scattering. The free-space Green's tensor is given by

$$\mathbb{G}^{(0)}(\boldsymbol{r}_a, \boldsymbol{r}_b, \omega_{nk}) = \frac{1}{4\pi}\left[\mathbb{1} + \frac{c^2}{\omega_{nk}^2}\boldsymbol{\nabla}_a \otimes \boldsymbol{\nabla}_a\right] \frac{e^{\mathrm{i}\omega_{nk}|\boldsymbol{r}_a - \boldsymbol{r}_b|/c}}{|\boldsymbol{r}_a - \boldsymbol{r}_b|}\,. \tag{3.31}$$

We hence find in free space that the transition matrix element (3.30) is given by

$$\begin{aligned} M_{n\to k} &= -\frac{\mathrm{i}\mu_0}{4\pi\hbar}\int \mathrm{d}^3 r_a \int \mathrm{d}^3 r_b\, \boldsymbol{j}_{nk}(\boldsymbol{r}_a)\cdot\left[\mathbb{1} - \frac{c^2}{\omega_{nk}^2}\boldsymbol{\nabla}_a \otimes \boldsymbol{\nabla}_b\right] \frac{e^{\mathrm{i}\omega_{nk}|\boldsymbol{r}_a - \boldsymbol{r}_b|/c}}{|\boldsymbol{r}_a - \boldsymbol{r}_b|}\cdot \boldsymbol{j}_{mp}(\boldsymbol{r}_b) \\ &= -\frac{\mathrm{i}\mu_0}{4\pi\hbar}\int \mathrm{d}^3 r_a \int \mathrm{d}^3 r_b\, \frac{e^{\mathrm{i}\omega_{nk}|\boldsymbol{r}_a - \boldsymbol{r}_b|/c}}{|\boldsymbol{r}_a - \boldsymbol{r}_b|}\left\{\boldsymbol{j}_{nk}(\boldsymbol{r}_a)\cdot\boldsymbol{j}_{mp}(\boldsymbol{r}_b) - c^2\rho_{nk}(\boldsymbol{r}_a)\rho_{mp}(\boldsymbol{r}_b)\right\}, \end{aligned} \tag{3.32}$$

where we have integrated by parts and used the continuity equation (3.11). Using the rate formular (3.29) this results in the free space rate

$$\begin{aligned} \Gamma^{(0)} = \rho(\omega_p)\frac{\mu_0^2}{8\pi\hbar^2}\Bigg| \iint \mathrm{d}^3 r_a \mathrm{d}^3 r_b\, \frac{e^{\mathrm{i}\omega|\boldsymbol{r}_a - \boldsymbol{r}_b|/c}}{|\boldsymbol{r}_a - \boldsymbol{r}_b|}\Big\{ &\boldsymbol{j}_{nk}(\boldsymbol{r}_a)\cdot\boldsymbol{j}_{mp}(\boldsymbol{r}_b) - c^2\rho_{nk}(\boldsymbol{r}_a)\rho_{mp}(\boldsymbol{r}_b) \\ &- \left[\boldsymbol{j}_{np}(\boldsymbol{r}_a)\cdot\boldsymbol{j}_{mk}(\boldsymbol{r}_b) - c^2\rho_{np}(\boldsymbol{r}_a)\rho_{mk}(\boldsymbol{r}_b)\right]\Big\}\Bigg|^2, \end{aligned}$$

where $\omega = \omega_{nk} = \omega_{pm}$. This is the generalised Møller formula for electron–electron scattering as introduced in section 2.3.1 [148, 149].

3.2. Rates in dipole approximation and regularisation of Auger decay

While the derived rate formula (3.29) can be used directly to calculate ICD and Auger decay rates in the presence of media, we circumvent the numerical effort to solve the

many-electron problem in this section by applying the dipole approximation and focus on the influence of macroscopic media. For the ICD rate this immediately yields a closed expression in the presence of macroscopic media. However, for Auger decay a more involved treatment is necessary: The dipole approximation is justified if the electromagnetic field does not change significantly on the length scale of the atom. Even though this is valid for our cases of interest, we find that the Auger decay rate diverges in the dipole approximation. We identify the root of the divergence in the dipole approximation and develop a regularisation model based on a successful approach that was originally developed for Van-der-Waals forces, see section 2.3.4. In this model, we reintroduce the finite spatial distribution of the electrons in their respective state. We apply the regularisation model to find a closed expression for the Auger decay rate in free space. We estimate the size of the electron distribution via Slater's rule for orbital radii and compare the obtained result with known rates, finding good agreement when accounting for a missing overall factor.

3.2.1. Interatomic Coulombic decay rate in dipole approximation

In this section we apply the dipole approximation to our derived rate formula (3.29). This yields the transfer rate as it is well-known in the resonance energy transfer community. We then apply the approximation to ICD. We obtain from this a rate for ICD that includes retardation effects as well as the impact of surrounding dispersing and absorbing macroscopic bodies, but excludes effects from wave function overlap.

In the dipole approximation the transition charge current densities can be simplified, such that

$$\boldsymbol{j}_{nk}(\boldsymbol{r}) = \sum_{\alpha} \frac{q_\alpha}{m\alpha} \langle k|\hat{\boldsymbol{p}}_\alpha \delta(\boldsymbol{r} - \hat{\boldsymbol{R}})|n\rangle = \sum \frac{q_\alpha}{m_\alpha} \langle k|\hat{\boldsymbol{p}}_\alpha|n\rangle \, \delta(\boldsymbol{r} - \boldsymbol{R}) \,, \tag{3.33}$$

where $\hat{\boldsymbol{p}}_\alpha$ is the momentum operator, m_α the mass of electron α and $\boldsymbol{R}_\alpha$ is the center of mass/nucleus position belonging to electron α for all α. Using both expressions for the atomic Hamiltonian, Eqs. (2.82) and (2.81) with the usual commutation relation $[\hat{\boldsymbol{r}}_\alpha, \hat{\boldsymbol{p}}_\beta] = \mathrm{i}\hbar\delta_{\alpha\beta}$, we find for the commutator with $\hat{\boldsymbol{d}} = \sum_{n,k} \boldsymbol{d}_{nk} |n\rangle \langle k| = \sum_\alpha q_\alpha \hat{\boldsymbol{r}}_\alpha$:

$$\begin{aligned}
\left[\hat{H}_A, \hat{\boldsymbol{d}}\right] = \sum_{n,k} (E_k - E_n) \boldsymbol{d}_{nk} |k\rangle \langle n| &= \sum_{\alpha,\beta} \frac{q_\beta}{2m_\alpha} \left[\hat{\boldsymbol{p}}_\alpha^2, \hat{\boldsymbol{r}}_\alpha\right] \\
\Rightarrow \qquad \sum_{n,k} \hbar\omega_{kn} \boldsymbol{d}_{nk} |k\rangle \langle n| &= -\mathrm{i}\hbar \sum_\alpha \frac{q_\alpha}{m_\alpha} \hat{\boldsymbol{p}}_\alpha \qquad (3.34) \\
\Rightarrow \qquad \mathrm{i}\omega_{kn} \boldsymbol{d}_{nk} &= \sum \frac{q_\alpha}{m_\alpha} \langle k|\hat{\boldsymbol{p}}_\alpha|n\rangle \,, \qquad (3.35)
\end{aligned}$$

such that in dipole approximation we get the relations

$$\boldsymbol{j}_{nk}(\boldsymbol{r}_a) = -\mathrm{i}\omega_{nk}\boldsymbol{d}_{nk}\delta(\boldsymbol{r}_a - \boldsymbol{R}_a), \qquad \boldsymbol{j}_{mp}(\boldsymbol{r}_b) = \mathrm{i}\omega_{pm}\boldsymbol{d}_{mp}\delta(\boldsymbol{r}_b - \boldsymbol{R}_b)\,. \tag{3.36}$$

These are related to the Thomas–Reiche–Kuhn sum rule [150–152]. Introducing this into Eq. (3.30), we obtain the transition matrix element in dipole approximation,

$$M_{n\to k} = \frac{\mu_0\omega_{nk}^2}{\hbar}\boldsymbol{d}_{nk}\cdot\mathbb{G}(\boldsymbol{R}_a,\boldsymbol{R}_b,\omega_{nk})\cdot\boldsymbol{d}_{mp}\,. \tag{3.37}$$

For electrons that belong to different atoms, $\boldsymbol{R}_a \neq \boldsymbol{R}_b$ we may calculate the transition rate from this formula. However, in Auger decay both electrons belong to the same atom and hence $\boldsymbol{R}_a = \boldsymbol{R}_b$. The propagator $\mathbb{G}$ diverges in this case. To be able to use the dipole approximation we need to find a regularisation model.

Assuming that donor and acceptor are well separated, such that wave function overlaps are negligible, the dipole approximation is an appropriate simplification for the rate of ICD. Applying the dipole approximation (3.37) to the derived rate equation (3.29) leads then to the ICD rate,

$$\Gamma_{\mathrm{ICD}} = \sum_f \frac{2\pi\mu_0^2}{\hbar^2}\rho(\omega_p)\omega_{nk}^4\left|\boldsymbol{d}_{mp}\cdot\mathbb{G}(\boldsymbol{r}_{\mathrm{A}},\boldsymbol{r}_{\mathrm{D}},\omega_{nk})\cdot\boldsymbol{d}_{nk}\right|^2 . \tag{3.38}$$

where $\boldsymbol{r}_{\mathrm{A/D}}$ is the acceptor's/donor's position. The exchange term vanishes here, $M_{n\to p} = 0$, since the two atoms are well separated, i.e. $\langle k|\hat{\boldsymbol{d}}|m\rangle = 0$. Alternatively, this expression can be derived from multipolar coupling in dipole approximation and Fermi's golden rule [96]. Assuming that the involved atoms are not aligned to each other in any specific way we may use the isotropic average, i.e. $\boldsymbol{d}_{ij}\otimes\boldsymbol{d}_{ji} = \frac{1}{3}|\boldsymbol{d}_{ij}|^2\mathbb{I}$ [153]. This yields for the isotropic ICD rate

$$\begin{aligned}\Gamma_{\mathrm{ICD}} &= \frac{2\pi\mu_0^2}{9\hbar^2}\rho(\omega_p)\omega_{nk}^4|\boldsymbol{d}_{nk}|^2|\boldsymbol{d}_{mp}|^2\,\mathrm{Tr}\left[\mathbb{G}_{ab}(\omega_{nk})\cdot\mathbb{G}_{ba}^*(\omega_{nk})\right]\\ &= 2\pi\gamma_{nk}\sigma_m(\omega_{nk})\,\mathrm{Tr}\left[\mathbb{G}(\boldsymbol{r}_{\mathrm{A}},\boldsymbol{r}_{\mathrm{D}},\omega_{nk})\cdot\mathbb{G}^{*T}(\boldsymbol{r}_{\mathrm{A}},\boldsymbol{r}_{\mathrm{D}},\omega_{nk})\right],\end{aligned} \tag{3.39}$$

where we have related the respective transition dipole moments to the photoionisation cross section $\sigma_m(\omega_{nk})$, see Eq. (2.169) and similarly replaced the transition dipole moments of the bound states with the respective spontaneous decay rate γ_{nk}, see Eq. (2.160). They are related via

$$\gamma_{nk} = \frac{\omega_{nk}^3|\boldsymbol{d}_{nk}|^2}{3\pi\varepsilon_0\hbar}\,, \tag{3.40}$$

$$\sigma_m(\omega_{pm}) = \frac{\pi\omega_{pm}\rho(\omega_p)\left|\boldsymbol{d}_{mp}\right|^2}{3\varepsilon_0 c\hbar}\,. \tag{3.41}$$

To obtain the ICD rate $\Gamma_{\mathrm{ICD},0}$ in free space we use the free space Green's tensor (A.32) in Eq. (3.39). The free-space ICD rate is then given by

$$\Gamma_{\mathrm{ICD},0} = \frac{\gamma_{nk}\sigma_m(\omega_{nk})c^4}{4\pi\omega_{nk}^4 r_{\mathrm{DA}}^6}\left(3 + \frac{\omega_{nk}^2 r_{\mathrm{DA}}^2}{c^2} + \frac{\omega_{nk}^4 r_{\mathrm{DA}}^4}{c^4}\right), \tag{3.42}$$

where $r_{\mathrm{DA}} = |\boldsymbol{r}_{\mathrm{A}} - \boldsymbol{r}_{\mathrm{D}}|$. For separation distances that are smaller than the wavelength of the transition energy, i.e. $\omega_{nk} r_{\mathrm{DA}}/c \ll 1$ the rate is dominated by its nonretarded contribution and yields

$$\Gamma_{\mathrm{ICD},0} \approx \frac{3\gamma_{nk}\sigma_m(\omega_{nk})c^4}{4\pi\omega_{nk}^4 r_{\mathrm{DA}}^6}. \tag{3.43}$$

The nonretarded free-space rate (3.43) is known in the ICD community as asymptotic formula [154]. It is valid for the distance regime, where wave function overlap and hence charge transfer are negligible. While this denotes a long-distance limit for said community it is also the short-distance limit (near-zone) for the RET community and neglects retardation effects. Interatomic Coulombic decay in dipole approximation has been recently studied in the framework of macroscopic QED [96].

3.2.2. Regularisation of the Green's tensor and Auger decay rate

We have introduced the dipole approximation into the transition matrix element. As a consequence, the Green's tensor in Eq. (3.37) describes a propagation from the position of the nucleus binding electron b to that binding electron a. In the case of Auger decay the participating electrons however belong to the same nucleus and we find that the propagator diverges in the limit of same–point–propagation. In this section we first develop a regularisation model for Auger decay by reintroducing the finite size of the atom on the level of the Green's tensor in a similar manner as it was already successfully done for Van-der-Waals forces, recall section 2.3.4. With the regularised Green's tensor we then obtain a simple closed expression for the Auger decay rate, similarly to the ICD rate. We finally show how to evaluate the sum over final degenerate states by use of the Wigner–Eckart theorem. We apply the Wigner-Eckart theorem to obtain some general rate formulas for the special cases of free space and isotropic transitions.

The propagation of electromagnetic fields is described by the Green's tensor. It consists of a bulk part $\mathbb{G}^{(0)}$ and scattering part $\mathbb{G}^{(1)}$. While the bulk part contains the direct propagation from source to absorption point, the scattering part describes the scattering at secondary media. As a consequence the divergence of the Green's tensor only stems

from the bulk part

$$\lim_{\boldsymbol{R}_a \to \boldsymbol{R}_b} \mathbb{G}^{(0)}(\boldsymbol{R}_a, \boldsymbol{R}_b, \omega) \to \infty\,, \tag{3.44}$$

while the scattering part stays finite in this limit. We assume the bulk medium to be free space throughout the chapter for simplicity. We want to find a regularised free space Green's tensor that stays finite in this limit. Let us replace the delta-distributions in Eq. (3.33) by Gaussian distributions $g_{1/2}(\boldsymbol{r})$ for electron a and b. This leads to

$$M_{n\to k} = \int \mathrm{d}^3 r_a \int \mathrm{d}^3 r_b \frac{\mu_0 \omega_{nk}^2}{\hbar} \boldsymbol{d}_{nk} \cdot \mathbb{G}^{(0)}(\boldsymbol{r}_a, \boldsymbol{r}_b, \omega_{nk}) \cdot \boldsymbol{d}_{mp} g_1(\boldsymbol{r}_a - \boldsymbol{R}_a) g_2(\boldsymbol{r}_b - \boldsymbol{R}_b)\,. \tag{3.45}$$

In free space as well as in isotropic media the Green's tensor only depends on the relative position of the two electrons, $\mathbb{G}^{(0)}(\boldsymbol{r}_a, \boldsymbol{r}_b, \omega_{nk}) = \mathbb{G}^{(0)}(\boldsymbol{r}_{ab}, \omega_{nk})$ with $\boldsymbol{r}_{ab} = \boldsymbol{r}_a - \boldsymbol{r}_b$. We hence find

$$M_{n\to k} = \int \mathrm{d}^3 r_{ab} \frac{\mu_0 \omega_{nk}^2}{\hbar} \boldsymbol{d}_{nk} \cdot \mathbb{G}^{(0)}(\boldsymbol{r}_{ab}, \omega_{nk}) \cdot \boldsymbol{d}_{mp} g_{12}(\boldsymbol{r}_{ab} - \boldsymbol{R}_{ab})\,, \tag{3.46}$$

where g_{12} is the convolution of two Gaussians, yielding another Gaussian

$$g_{12}(\boldsymbol{r}) = \frac{1}{(2\pi)^{3/2} a_{12}^3} \mathrm{e}^{r^2/2a_{12}^2}\,, \tag{3.47}$$

$$a_{12} = \sqrt{a_1^2 + a_2^2}\,. \tag{3.48}$$

The atomic property of finite spatial distribution can then be defined into a regularised free space Green's tensor $\tilde{\mathbb{G}}^{(0)}$. It is given by

$$\begin{aligned}
\tilde{\mathbb{G}}^{(0)}(\omega_{nk}) &= \int \mathrm{d}^3 r_{ab} \mathbb{G}^{(0)}(\boldsymbol{r}_{ab}, \omega_{nk}) g_{12}(\boldsymbol{r}_{ab} - \boldsymbol{R}_{ab}) \\
&= -\frac{\mathbb{1}}{6\sqrt{2}\pi^{3/2} a^3 k^2} \left\{ 1 - 2a^2k^2 + \sqrt{2\pi} a^3 k^3 e^{-\frac{1}{2}a^2k^2} \left(\mathrm{erfi}\left(\frac{ak}{\sqrt{2}}\right) - i \right) \right\} \\
&\approx -\frac{\mathbb{1}}{6\sqrt{2}\pi^{3/2} a^3 k^2}\,,
\end{aligned} \tag{3.49}$$

where $k = \omega_{nk}/c$ is the wave number, $a = a_{12}$ is the size of the convoluted Gaussian, $\mathrm{erfi}(z) = -\mathrm{ierf}(\mathrm{i}z)$ is the imaginary error function and we approximated $ak \ll 1$ in the last step. The Gaussian size a is an atomic property that depends on the involved transitions. From here on out we will call this new parameter *Auger radius*. The transition matrix element can now be recast into the familiar dipole approximated form (3.37) using

the regularised Green's tensor

$$M_{n\to k} = \frac{\mu_0 \omega_{nk}^2}{\hbar} \boldsymbol{d}_{nk} \cdot \tilde{\mathbb{G}}(\omega_{nk}) \cdot \boldsymbol{d}_{mp} \,, \tag{3.50}$$

$$\tilde{\mathbb{G}}(\omega_{nk}) = \tilde{\mathbb{G}}^{(0)}(\omega_{nk}) + \mathbb{G}^{(1)}(\boldsymbol{R}, \boldsymbol{R}, \omega_{nk}) \,, \tag{3.51}$$

where $\boldsymbol{R}$ is the position of the atom and $\mathbb{G}^{(1)}$ is the scattering Green's tensor.

We can now return to the Auger rate in the dipole approximation. The Auger rate (3.29) can written as

$$\Gamma = \Gamma_{\text{dir}} + \Gamma_{\text{exch}} + \Gamma_{\text{intf}} \,, \tag{3.52}$$

$$\Gamma_{\text{dir}} = 2\pi \sum_{m,n} \rho(\omega_p) \left| M_{n\to k} \right|^2 \,, \tag{3.53}$$

$$\Gamma_{\text{exch}} = 2\pi \sum_{m,n} \rho(\omega_p) \left| M_{n\to p} \right|^2 \,, \tag{3.54}$$

$$\Gamma_{\text{intf}} = -2\pi \sum_{m,n} \rho(\omega_p) 2\text{Re}\left[M_{n\to k} M_{n\to p}^* \right] \,, . \tag{3.55}$$

with the transition element $M_{i\to j}$ given in dipole approximation by Eq. (3.50). Let us focus on the direct term first,

$$\Gamma_{\text{dir}} = \sum_{m,n} \frac{2\pi \mu_0^2 \omega_{nk}^4}{\hbar^2} \rho(\omega_p) \left| \boldsymbol{d}_{nk} \cdot \tilde{\mathbb{G}}(\omega_{nk}) \cdot \boldsymbol{d}_{mp} \right|^2 \,, \tag{3.56}$$

which has the same form as the ICD rate (3.38) except for the replacement of $\mathbb{G}$ with $\tilde{\mathbb{G}}$. The sum over all final states includes possible degeneracies. The sum over any degenerate levels can be evaluated via the Wigner–Eckart theorem:

Let an electron state be denoted as $|NLM\rangle$ where N is the principal quantum number, L denotes the angular momentum, M its projection onto the quantisation axis and let $\hat{T}_q$ denote the qth component of a spherical tensor operator $\hat{\mathbb{T}}$ with rank κ, i.e. $q \in \{-1, 0, 1\}$. The Wigner–Eckart theorem then yields the relation

$$\left\langle NLM \left| \hat{T}_q \right| N'L'M' \right\rangle = \langle L'\kappa; M'q | LM \rangle \left\langle NL \left\| \hat{T}_q \right\| N'L' \right\rangle \,, \tag{3.57}$$

where $\left\langle NL \left\| \hat{T}_q \right\| N'L' \right\rangle$ is the reduced matrix element and $\langle L'\kappa; M'q | LM \rangle$ denotes a Clebsch–Gordan coefficient. Assuming that there exists no directional preference, i.e. a definite M, for either electronic state in the transition, the Wigner–Eckart theorem effectively results in isotropic averaging.

In most cases it is advisable to evaluate the rate given by Eq. (3.56) via the Wigner–Eckart theorem for the specific system directly. For some special cases the Wigner–Eckart theorem yields general results, such as free space and isotropic transitions. In free space

$\tilde{\mathbb{G}} = \tilde{\mathbb{G}}^{(0)} \propto \mathbb{I}$ and we thus may perform the sum over the M-degeneracy to obtain in general

$$\begin{aligned}\Gamma_{\text{dir}} &= \frac{2\pi\mu_0^2\omega_{nk}^4}{\hbar^2}\sum_{m,n}\rho(\omega_p)\,\text{Tr}\left\{\boldsymbol{d}_{nk}\otimes\boldsymbol{d}_{kn}\cdot\tilde{\mathbb{G}}^{(0)}(\omega_{nk})\cdot\boldsymbol{d}_{mp}\otimes\boldsymbol{d}_{pm}\cdot\tilde{\mathbb{G}}^{(0)*}(\omega_{nk})\right\}] \\ &= \sum_{m,n}\frac{2\pi\mu_0^2\omega_{nk}^4}{\hbar^2}\rho(\omega_p)c_{\text{dir}}|\boldsymbol{d}_{nk}|^2|\boldsymbol{d}_{mp}|^2\,\text{Tr}\left\{\tilde{\mathbb{G}}^{(0)}(\omega_{nk})\cdot\tilde{\mathbb{G}}^{(0)*}(\omega_{nk})\right\}, \qquad (3.58)\end{aligned}$$

$$\Gamma_{\text{exch}} = \sum_{m,n}\frac{2\pi\mu_0^2\omega_{km}^4}{\hbar^2}\rho(\omega_p)c_{\text{exch}}|\boldsymbol{d}_{mk}|^2|\boldsymbol{d}_{np}|^2\,\text{Tr}\left\{\tilde{\mathbb{G}}^{(0)}(\omega_{km})\cdot\tilde{\mathbb{G}}^{(0)*}(\omega_{km})\right\}, \qquad (3.59)$$

$$\Gamma_{\text{intf}} = -\sum_{m,n}\frac{4\pi\mu_0^2\omega_{nk}^4}{\hbar^2}\rho(\omega_p)\text{Re}\left\{\mathbb{D}::\left[\tilde{\mathbb{G}}^{(0)}(\omega_{nk})\otimes\tilde{\mathbb{G}}^{(0)*}(\omega_{nk})\right]\right\}, \qquad (3.60)$$

where the remaining sum excludes these evaluated degeneracies, we have introduced the fourth rank tensor $\mathbb{D} = \boldsymbol{d}_{nk}\otimes\boldsymbol{d}_{mp}\otimes\boldsymbol{d}_{mk}^*\otimes\boldsymbol{d}_{np}^*$, and the factors c_{dir} and c_{exch} stem from the Wigner–Eckart theorem. The specific prefactors $c_{\text{dir/exch}}$ of the pure terms $\Gamma_{\text{dir/exch}}$ as well as the dipole tensor $\mathbb{D}$ can then be determined for the specific transitions.

In general these expressions only hold for free space. An exception to this is given by isotropic transitions. Here we find that $c_{\text{dir}} = c_{\text{exch}} = 1/9$, as expected for isotropic averaging and that Eqs. (3.58) and (3.59) still hold for arbitrary Green's tensors $\tilde{\mathbb{G}} \neq \tilde{\mathbb{G}}^{(0)}$. We may hence write the isotropic direct rate in arbitrary macroscopic media as

$$\Gamma_{\text{dir}} = 2\pi\gamma_{nk}\sigma_m(\omega_{nk})\,\text{Tr}\left\{\tilde{\mathbb{G}}(\omega_{nk})\cdot\tilde{\mathbb{G}}^{*T}(\omega_{nk})\right\}, \qquad (3.61)$$

where we have introduced again the photoionisation cross section $\sigma_m(\omega_{nk})$ and the spontaneous decay rate γ_{nk}, see Eqs. (3.41) and (3.40). The rate is completely governed by Eq. (3.61) for vanishing exchange terms, e.g. for dipole forbidden transitions $m \to k$.

3.2.3. Determination of the Auger radius

So far, we have regularised the free space Green's tensor for Auger decay by introducing a new quantity, the Auger radius. In this section we first discuss how to estimate the Auger radius for a given system. By comparison with free-space Auger decay rates obtained in other works we discuss the quality of our estimation. The Auger radius plays a significant role in the determination of the correct rate. While we demonstrate that the Auger radius can be roughly estimated by the size of the vacancy orbital, even small derivations from the correct Auger radius leads to large errors in the rate. We hence present a more general model for the Auger radius based on Slater rules and fit it to the available data.

We want to compare our model to known Auger rates. We choose the KLL-Auger decay in the isoelectronic sequence of F-like ions, i.e. Ne^+, Na^{2+}, Mg^{3+}, ..., Zn^{21+}. They

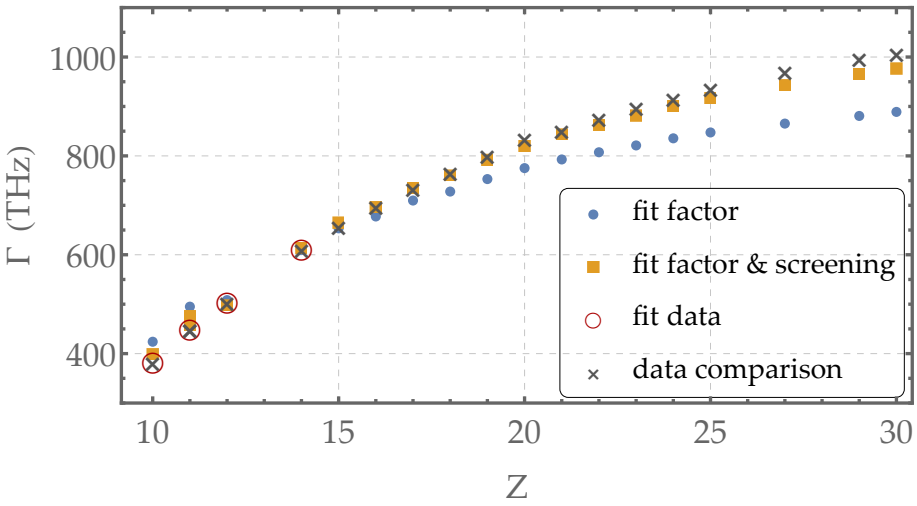

Figure 3.2.: Comparison of our model to numerically obtained rates from tabulated data [155, 156] as function of the number of protons Z. Using the first four data points (red circled) to fit an additional prefactor onto the vacancy orbital radius $a = c_{\text{fit}} a_{1s}$ (blue dots) gives already good agreement with the numerical values (black crosses) with $c_{\text{fit}} = 1.8$. Fitting additionally the screening factor of the radius model gives almost perfect agreement to the numerical data with $a = 1.77 a_0/(Z - 0.77)$(yellow squares).

are ions with nine bound electrons where the vacancy is in the 1s-orbital. Their electronic structure is then given by: $1s2s^2 2p^6$. Since we are interested in the total shell KLL-Auger rate we may neglect coupling effects [157]. The vacant state $|k\rangle$, bound states $|n\rangle$ and $|m\rangle$ and the continuum state $|p\rangle$ are then given by

$$|k\rangle = |1s m_s \uparrow\downarrow\rangle\,, \qquad m_s = 0\,, \tag{3.62}$$

$$|n\rangle = |2p m_p \uparrow\downarrow\rangle\,, \qquad m_p \in \{-1, 0, 1\}\,, \tag{3.63}$$

$$|m\rangle \in \left\{|2p m_p \uparrow\downarrow\rangle\,, |2s m_s \uparrow\downarrow\rangle\right\}\,, \tag{3.64}$$

$$|p\rangle = |E_p l_c m_c \uparrow\downarrow\rangle\,, \qquad E_p = \hbar\omega_p,\ l_c \in \{0, 1, 2\},\ m_c \in [-l_c, l_c]\,. \tag{3.65}$$

The vacancy state is determined by the initial state. The transition 2s $\to$ 1s is dipole forbidden, hence only electrons from state $|2p\rangle$ can fill the vacancy. The possible decay channels are then:

$$\begin{aligned} &\text{direct channel:} && |n\rangle = |2p m_p \uparrow\downarrow\rangle \longrightarrow |k\rangle = |1s m_s \uparrow\downarrow\rangle\,, \\ &&& |m\rangle \in \{|2p m_p \uparrow\downarrow\rangle\,, |2s m_s \uparrow\downarrow\rangle\} \longrightarrow |p\rangle = |E_p l_c m_c \uparrow\downarrow\rangle\,. \end{aligned} \tag{3.66}$$

$$\begin{aligned} &\text{exchange channel:} && |m\rangle = |2p m_p \uparrow\downarrow\rangle \longrightarrow |k\rangle = |1s m_s \uparrow\downarrow\rangle\,, \\ &&& |n\rangle = |2p m_p \uparrow\downarrow\rangle \longrightarrow |p\rangle = |E_p l_c m_c \uparrow\downarrow\rangle\,. \end{aligned} \tag{3.67}$$

Since in free space the regularised Green's tensor $\tilde{\mathbb{G}}^{(0)}$ (3.49) is proportional to the iden-

Z	fit factor $a = 1.84a_0/(Z-0.3)$ in THz (%)	fit screening $a = 1.77a_0/(Z-0.77)$ in THz (%)	data in THz
10	423 (110)	391 (102)	385
11	494 (110)	469 (104)	450
12	508 (100)	493 (97)	506
14	609 (99)	614 (100)	613
15	652 (99)	667 (101)	660
16	676 (97)	700 (100)	699
17	709 (96)	742 (101)	736
18	727 (95)	768 (100)	769
19	752 (94)	802 (100)	802
20	774 (92)	832 (99)	837
21	792 (93)	857 (100)	853
22	806 (92)	878 (100)	877
23	820 (91)	898 (100)	900
24	834 (91)	919 (100)	919
25	846 (90)	937 (100)	938
27	864 (89)	965 (99)	972
29	880 (88)	989 (99)	1000
30	888 (88)	1002 (99)	1010

Table 3.1.: Comparison of the Auger rate calculated by the analytic formula (3.73) with two different Auger radius models for a and the numerically calculated rates found in [155]. The obtained rate is additionally given in percentage relative to the numerical value in braces.

tity Eqs. (3.58)–(3.60) hold. Additionally the transitions are isotropic, i.e. for each state $|\phi\rangle$ we find $\sum_{m_\phi} m_\phi = 0$ for its degenerate states. Because of this the coefficients in Eqs. (3.58) and (3.59) are given by $c_{\text{dir}} = c_{\text{exch}} = 1/9$. For the chosen system the interference term (3.60) yields similarly

$$\sum_{m_p, m_p', m_c} \operatorname{Re}\left\{\mathbb{D} :: \left[\tilde{\mathbb{G}}^{(0)} \otimes \tilde{\mathbb{G}}^{(0)*}\right]\right\} = \frac{1}{9}\left|\langle 2p \uparrow\downarrow ||\hat{\boldsymbol{d}}||E_p l_c \uparrow\downarrow\rangle\right|^2 \left|\langle 2p \uparrow\downarrow ||\hat{\boldsymbol{d}}||1s \uparrow\downarrow\rangle\right|^2 \operatorname{Tr}\left\{\tilde{\mathbb{G}}^{(0)} \cdot \tilde{\mathbb{G}}^{(0)*}\right\} \quad (3.68)$$

with

$$\mathbb{D} = \big[\, \langle 2pm_p \uparrow\downarrow |\hat{\boldsymbol{d}}| 1sm_s \uparrow\downarrow\rangle \otimes \langle 2pm_p' \uparrow\downarrow |\hat{\boldsymbol{d}}| E_p l_c m_c \uparrow\downarrow\rangle \otimes \langle 2pm_p' \uparrow\downarrow |\hat{\boldsymbol{d}}| 1sm_s \uparrow\downarrow\rangle^* \otimes \langle 2pm_p \uparrow\downarrow |\hat{\boldsymbol{d}}| E_p l_c m_c \uparrow\downarrow\rangle^* \,\big]\,. \quad (3.69)$$

Using the Wigner–Eckart theorem for the m-degeneracies in this way, summing over the remaining degrees of freedom, taking selection rules into account and normalising the

initial state classically, we find for the Auger rate (3.52)

$$\Gamma = \frac{2\pi\mu_0^2\omega_{nk}^4}{9\hbar^2}\left|\langle 1s||\hat{\boldsymbol{d}}||2p\rangle\right|^2 \sum_{l_c} 2\rho(\omega_p)\left(\left|\langle\omega_p l_c||\hat{\boldsymbol{d}}||2p\rangle\right|^2 + \left|\langle\omega_p l_c||\hat{\boldsymbol{d}}||2s\rangle\right|^2\right) \times \mathrm{Tr}\left\{\tilde{\mathbb{G}}^{(0)}(\omega_{nk})\cdot\tilde{\mathbb{G}}^{(0)*}(\omega_{nk})\right\}. \quad (3.70)$$

We can relate the remaining reduced transition dipoles to the spontaneous decay rate $\gamma_{nk} = \gamma_{2p\to 1s}$, see Eq. (3.40) and the photoionisation cross section σ_m, given by

$$\sigma_{2s}(\omega_p) = 2\sum_{l_c}\frac{\pi\omega_{pm}\rho(\omega_p)\left|\langle\omega_p l_c||\hat{\boldsymbol{d}}||2s\rangle\right|^2}{3\varepsilon_0 c\hbar}, \quad (3.71)$$

$$\sigma_{2p}(\omega_p) = 2\sum_{l_c}\frac{\pi\omega_{pm}\rho(\omega_p)\left|\langle\omega_p l_c||\hat{\boldsymbol{d}}||2p\rangle\right|^2}{3\varepsilon_0 c\hbar}, \quad (3.72)$$

where the additional factor compared to Eq. (3.41) stems from the spin degree of freedom. With this the KLL-Auger rate for F-like ions finally yields

$$\begin{aligned}\Gamma &= 2\pi\gamma_{2p\to 1s}\sigma_{\mathrm{tot}}(\omega_{nk})\,\mathrm{Tr}\left\{\tilde{\mathbb{G}}^{(0)}(\omega_{nk})\cdot\tilde{\mathbb{G}}^{(0)*}(\omega_{nk})\right\}\\ &= \frac{c^2}{12\pi^2\omega_{nk}^2 a^6}\gamma_{2p\to 1s}\sigma_{\mathrm{tot}}(\omega_{nk}),\end{aligned} \quad (3.73)$$

where $\sigma_{\mathrm{tot}} = \sigma_{2s} + \sigma_{2p}$ is the total L-shell photoionisation cross section and we have evaluated the trace with $\tilde{\mathbb{G}}^{(0)}$ given by Eq. (3.49). Here, we made use of the fact that the transition probability of the total shell is independent of the chosen coupling scheme (e.g. *LS*-coupling, *jj*-coupling or no coupling) [157].

When we want to estimate the spatial distribution of transition charge current densities of two electron states, see Eq. (3.33), it is easy to see that the overlap between two wave functions is dominated by the smallest orbital. However, the dominant term in $\mathbb{G}^{(0)}$ and hence in $\tilde{\mathbb{G}}^{(0)}$ is given by a delta-distribution, see Eq. (A.32). In this case we find that the transition element M does not depend on the overlap of two wave functions but rather on the overlap of all four involved wave functions, i.e.

$$M_{n\to k} \propto \int \mathrm{d}^3 r\, \boldsymbol{j}_{nk}(\boldsymbol{r}-\boldsymbol{R}_a)\boldsymbol{j}_{mp}(\boldsymbol{r}-\boldsymbol{R}_b). \quad (3.74)$$

We hence assume that the Auger radius a behaves itself like an orbital radius and its magnitude is dominated by the vacancy orbital's radius. We can approximate the size of an electron's orbital with main quantum number n by its Slater radius

$$a_n = \frac{n^2 a_0}{(Z-S)}, \quad (3.75)$$

where a_0 is the Bohr radius, Z is the number of protons in the nucleus and S is the screening due to other electrons in the atom. For the vacancy orbital $|k\rangle = |1s\rangle$ in our example Slater's rules yield $n = 1$ and $S = 0.3$. Using this as Auger radius in our formula overestimates the rates in comparison to the ones reported by Palmeri et al. [155, 156] by a factor of roughly 40. However, if we allow for an additional factor c_{fit}, such that

$$a = c_{\text{fit}} a_{1s}, \qquad a_{1s} = \frac{a_0}{Z - 0.3}. \tag{3.76}$$

We find good agreement with the numerically calculated KLL-Auger rates for $c_{\text{fit}} = 1.80$. This additional factor can stem from several uncertainties in our model: the chosen Gaussian distribution is not unique and other distributions would lead to the same result as obtained for $a\omega_{kn}/c \ll 1$ but with a different prefactor. Additionally, we approximated the four wave function overlap with only the smallest orbital size. It is expected that the remaining wave functions broaden the distribution.

The Auger rates obtained by Eq. (3.76) together with Eq. (3.73) in comparison with the rates reported by Palmeri et al. [155, 156] for the different ions are plotted in Fig. 3.2 as a function of their proton number Z as well as given in table 3.1. To demonstrate the predictive power of our model we only used four reported numerical rates with the lowest $Z \in \{10, 11, 12, 14\}$ to fit our model. The fit was done by using the reported KLL-Auger decay rates for F-like ions by Palmeri et al. [155, 156] together with our formula, Eq. (3.73) as well as tabulated data for the spontaneous decay rates [155, 156] and the respective photoionisation cross sections [158, 159] to calculate the Auger radii predicted by the rate data. We then used these radii as fitting data to optimise the respective model for a.

The Auger radius given by the vacancy orbital but adjusted with a factor yields rates that fit the data quite well. However, as we can see in Fig. 3.2 the slope of the two curves do not fit perfectly with each other. The deviation is very small on the level of the Auger radius, but the strong sensitivity of the rate to a, i.e. $\Gamma \propto 1/a^6$ leads to a magnified relative error on the rate itself. If we allow for the screening to be fitted as well, i.e. we use a general radius model for the Auger radius given by

$$a = \frac{c_{\text{fit}} a_0}{Z - S_{\text{fit}}}, \tag{3.77}$$

we find almost perfect agreement with $c_{\text{fit}} = 1.77$ and $S_{\text{fit}} = 0.77$. The rates obtained by using Eq. (3.77) for the Auger radius are plotted as well in Fig. 3.2 and are given in table 3.1.

With this we conclude that the Auger rate indeed depends on an Auger radius a in the predicted way. The derived formulas can be used in three different ways. Firstly, one can use the provided model for the Auger radius together with tabulated radiative decay rates

and cross sections to calculate Auger decay rates directly. For this the provided Auger radius model should be further studied and improved. Secondly, one can use the derived Auger rate formula to estimate free-space Auger rates from known and related Auger rates, e.g. Auger rates with varied proton number, different cross section or different vacancy orbital from known rates. And most importantly, we can use known free-space Auger rates, conclude from them the appropriate Auger radius and apply our framework to take the impact of macroscopic environment into account. By simply introducing the respective scattering Green's tensor into the calculation, we may now study the effects of surrounding media, such as surfaces or cavities. With this we are now able to study Auger decay together with other competing processes, such as the spontaneous emission or ICD in a joint framework and in arbitrary environment.

3.3. Competing processes in an excited two-atom system

Now that ICD and Auger decay can be described within the same framework we consider in this section an excited two-atom system where both processes appear as competing relaxation channels. We first compare all possible relaxation channels in the bare two-atom system by relating them to their characteristic length scales. In this comparison we also consider the effect of a second atom on single-particle decay rates. The length scale comparison reveals the dominating channels. As we will see, Auger decay usually dominates the relaxation process. We then show in the framework of macroscopic QED how nearby surfaces may influence the ratio between the competing rates. We will focus on the enhancement of the weaker ICD process compared to the dominant Auger decay. We derive analytical expressions for the rate in the case of isotropic transitions close to a dielectric surface. We discuss the surface's influence onto the competition between the rates for general systems and show the impact of anisotropic transition dipoles onto the surface-modified rate. Subsequently, we offer a discussion on the expected enhancement inside an appropriate cavity and derive a simple analytical formula to estimate the necessary properties of such a cavity for a given molecular system. Finally, we demonstrate applicability of the provided expressions by applying our results to the example of a doubly excited He–Ne dimer. We compare our results in free space with *ab initio* data reported in other works.

3.3.1. Comparison of decay channels

In this section we compare the possible relaxation channels of an excited two-atom system in free space to each other, namely spontaneous decay, Auger decay and ICD. They are

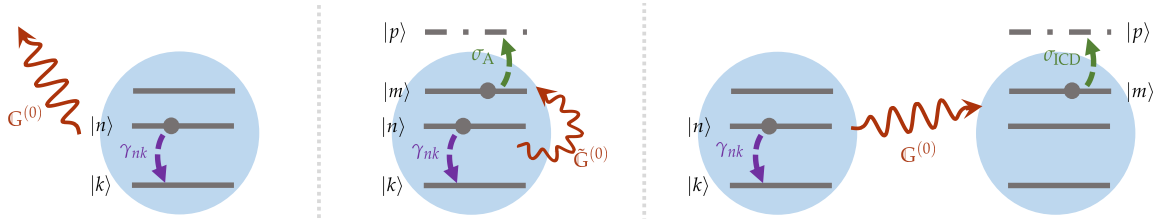

Figure 3.3.: Possible decay channels shown schematically including the chosen labelling scheme. Spontaneous decay and Auger decay are single-atom processes, while ICD is only possible with a nearby acceptor atom. The spontaneous decay rate γ_{nk} in the rate formulas, Eq. (3.39) and Eq. (3.81) are hence the same, while the photoionisation cross section $\sigma_m(\omega_{nk}) \in \{\sigma_A, \sigma_{ICD}\}$ refers to different transitions in ICD and Auger decay.

schematically shown in Fig. 3.3. Even for single-atom processes, the presence of a second atom can have an impact onto the rate. In these cases we include the second atom into the rate via its polarisability tensor. We determine characteristic length scales for each rate and discuss their typical order of magnitude. By comparison of the respective length scales to each other we can determine the most and least dominant relaxation channels.

The most fundamental relaxation channel of a single atom is spontaneous or radiative decay. In terms of the Green's tensor it is given by Eq. (2.159)[3]

$$\Gamma_s = \frac{2\mu_0}{\hbar} \sum \omega_{nk}^2 \boldsymbol{d}_{nk} \cdot \operatorname{Im} \mathbb{G}(\boldsymbol{r}, \boldsymbol{r}, \omega_{nk}) \cdot \boldsymbol{d}_{kn} \,, \tag{3.78}$$

where the sum runs over all degeneracies. We assume for simplicity that the process is isotropic and focus on relaxation via a single transition, such that

$$\Gamma_s = \frac{2\mu_0}{3\hbar} |\boldsymbol{d}_{nk}|^2 \omega_{nk}^2 \operatorname{Tr} \operatorname{Im} \mathbb{G}(\boldsymbol{r}, \boldsymbol{r}, \omega_{nk}) \,. \tag{3.79}$$

In free space this gives the spontaneous decay rate, see Eq. (2.160),

$$\Gamma_{s,0} = \gamma_{nk} = \frac{\omega_{nk}^3 |\boldsymbol{d}_{nk}|^2}{3\pi\varepsilon_0\hbar} \,, \tag{3.80}$$

where we have used $\mathbb{G} = \mathbb{G}^{(0)}$, see Eq. (A.32). For a sufficiently high initial excitation Auger decay becomes available as an additional decay channel. For simplicity we assume that the exchange term $m \to k$ is dipole forbidden and that the process is isotropic. Following the derivation of section 3.2.2, the Auger rate is then given by Eq. (3.61),

$$\Gamma_A = 2\pi\gamma_{nk}\sigma_A(\omega_{nk}) \operatorname{Tr} \left\{ \tilde{\mathbb{G}}(\omega_{nk}) \cdot \tilde{\mathbb{G}}(\omega_{nk}) \right\} \,, \tag{3.81}$$

where we relabelled $\sigma_m \to \sigma_\mathrm{A}$ and by using the regularised free-space Green's tensor $\tilde{\mathbb{G}}^{(0)}$, see Eq. (3.49) we find the free space rate to be

$$\Gamma_{\mathrm{A},0} = \frac{c^2}{12\pi^2\omega_{nk}^2 a^6}\gamma_{nk}\sigma_\mathrm{A}(\omega_{nk})\,. \tag{3.82}$$

Typically, once the Auger decay is energetically allowed it is much faster than the spontaneous decay rate by a factor of

$$\frac{\Gamma_{\mathrm{A},0}}{\Gamma_{\mathrm{s},0}} = \frac{2\pi^2}{3}\left(\frac{\lambda_{nk}}{4\pi^{3/2}a}\right)^4 \times \left(\frac{a_\sigma}{2\pi^{1/2}a}\right)^2, \tag{3.83}$$

where $\lambda_{nk} = 2\pi c/\omega_{nk}$ is the wavelength of the downward transition and we have defined the photoionisation radius $\pi a_\sigma^2 = \sigma(\omega_{nk})$.

The two ratios in Eq. (3.83) determine how much the Auger decay dominates over spontaneous decay. Let us discuss their magnitude. The photoionisation cross section $\sigma_\mathrm{A}(\omega) = \sigma_m(\omega)$ decreases with some order of ω, depending on the orbital quantum number l of state $|m\rangle$ (e.g. for an s-state σ decreases with $\omega^{-11/2}$, for a p-state with $\omega^{-15/2}$ [160]) and is typically in the order of $\sim 10^{-2} - 10^{1}$ Mb. The photoionisation radius a_σ is hence in a regime of $a_\sigma \sim 10^{-2} - 10^{-1}$ Å, which is comparable to the regime covered by the Auger radius a ($2\pi^{\frac{1}{2}}a \sim 10^{-2} - 10^{-1}$ Å, see sec. 3.2.3). The ratio of these length scales could hence be either in favour of Auger or spontaneous decay. However, the transition wavelength λ_{nk} can be found somewhere in the xray to XUV regime, and it holds that $\lambda_{nk} \gg 4\pi^{\frac{3}{2}}a$, which decides the ratio (3.83) in favour of Auger decay.

The presence of a second atom may influence these rates. Even at interatomic distances where the wave function overlap may be neglected the second atom passively manipulates the electromagnetic vacuum and serves as a mediator for the radiative rate as well as the Auger decay rate. The mediator Green's tensor is given by Eq. (2.146) and reads

$$\mathbb{G}^\mathrm{M}(\boldsymbol{r},\boldsymbol{r}',\omega) = \frac{\omega^2}{c^2}\mathbb{G}^{(0)}(\boldsymbol{r},\boldsymbol{r}_\mathrm{M},\omega)\cdot\frac{\boldsymbol{\alpha}(\omega)}{\varepsilon_0}\cdot\mathbb{G}^{(0)}(\boldsymbol{r}_\mathrm{M},\boldsymbol{r}',\omega)\,, \tag{3.84}$$

where $\boldsymbol{r}_\mathrm{M}$ is the mediator atom's position and $\boldsymbol{\alpha}$ is its polarisabilty tensor, see section 2.3.2. We assume an isotropic polarisability, such that $\boldsymbol{\alpha} = \alpha\mathbb{I}$. It is given by

$$\alpha(\omega_{nk}) = \frac{2}{3\hbar}\sum_i \frac{\omega_i|\boldsymbol{d}_{in}|^2}{\omega_i^2 - \omega_{nk}^2 - \mathrm{i}\omega_{nk}\gamma_i}\,, \tag{3.85}$$

with resonances at ω_i each with a width of γ_i and we used that $\gamma_i \ll \omega_i$ to simplify the expression. Let us introduce the polarisability volume $\tilde{\alpha} = \alpha/4\pi\varepsilon_0$. Depending on ω_{nk}

the polarisability volume $\tilde{\alpha}$ can be estimated in three different regimes:

$$\begin{aligned} &\text{for } \omega_{nk} \ll \omega_i : && \tilde{\alpha} \approx \frac{\alpha_0}{4\pi\varepsilon_0} \propto \sum_i \frac{|\boldsymbol{d}_{in}|^2}{\omega_i} \\ &\text{for } \omega_{nk} = \omega_i : && \tilde{\alpha} \propto \mathrm{i}\frac{|\boldsymbol{d}_{in}|^2}{\gamma_i} \\ &\text{for } \omega_{nk} \gg \omega_i : && \tilde{\alpha} \propto \sum_i \left(\frac{\omega_i}{\omega_{nk}}\right)^2 \times \frac{|\boldsymbol{d}_{in}|^2}{\omega_i} \end{aligned} \tag{3.86}$$

where α_0 is known as static polarisability and $\tilde{\alpha}$ only possesses a significant imaginary part when close to a resonance. Considering the energy regime we are interested in, we will exclude cases $\omega_{nk} \ll \omega_i$ from the discussion. Using the mediator Green's tensor, Eq. (3.84) as scattering Green's tensor together with the respective rate formulas, Eqs. (3.81) and (3.79) we obtain the rates in the presence of a second atom. In the nonretarded limit of small interatomic distances they are given by

$$\Gamma_\mathrm{s} = \Gamma_{\mathrm{s},0} + \Delta\Gamma_\mathrm{s}\,, \tag{3.87}$$

$$\Delta\Gamma_\mathrm{s} \approx 3\Gamma_{\mathrm{s},0}\left(\frac{\lambda_{nk}}{2\pi r}\right)^3 \frac{\mathrm{Im}\tilde{\alpha}}{r^3}\,, \tag{3.88}$$

$$\Gamma_\mathrm{A} = \Gamma_{\mathrm{A},0} + \Delta\Gamma_\mathrm{A}\,, \tag{3.89}$$

$$\Delta\Gamma_\mathrm{A} \approx -24\sqrt{\pi}\Gamma_{\mathrm{A},0}\left[\frac{a^3\mathrm{Re}\,\tilde{\alpha}}{r^6} - 9\sqrt{\pi}\frac{a^6|\tilde{\alpha}|^2}{r^{12}}\right]\,, \tag{3.90}$$

where r is the separation distance between the decaying atom and the second, mediating one. Only for a resonance in the mediator atom, i.e. $\omega_{nk} \approx \omega_i$ the spontaneous decay rate is significantly enhanced. The magnitude of $\tilde{\alpha}$ on a resonance is determined by its line width γ_i and can be of several orders of magnitude. For transition energies ω_{nk} larger than the mediator's resonances ω_i the polarisability $\tilde{\alpha}$ decreases with ω_{nk}, see Eq. (3.86). In this energy regime we find that typically $\tilde{\alpha} \lesssim 10^{-1}$ Å^3. We define a length scale a_α for the polarisability volume $\tilde{\alpha} = \pm a_\alpha^3$. With this we find for the Auger rate in lowest order

$$\frac{\Delta\Gamma_\mathrm{A}}{\Gamma_{\mathrm{A},0}} \approx \mp 4\left(\frac{2\sqrt{\pi}a}{r}\right)^3 \times \left(\frac{a_\alpha}{r}\right)^3\,, \tag{3.91}$$

which is usually much smaller than one and negative for $\omega_{nk} \gg \omega_i$.

By introducing a second atom into the system we also open up another relaxation channel, i.e. ICD. The isotropic free-space ICD rate in the nonretarded limit is given by Eq. (3.43) and reads

$$\Gamma_\mathrm{ICD} \approx \frac{3\gamma_{nk}\sigma_\mathrm{ICD}(\omega_{nk})c^4}{4\pi\omega_{nk}^4 r_\mathrm{DA}^6}\,, \tag{3.92}$$

	$\Gamma_{s,0}$	$\Gamma_{A,0}$	Γ_{ICD}	$\Delta\Gamma_s$
$\Gamma_{s,0}$				
$\Gamma_{A,0}$	$\frac{2\pi^2}{3}\left(\frac{\lambda_{nk}}{4\pi^{3/2}a}\right)^4\left(\frac{a_\sigma}{2\pi^{\frac{1}{2}}a}\right)^2$			
Γ_{ICD}	$\frac{3}{4}\left(\frac{\lambda_{nk}}{2\pi r}\right)^4\left(\frac{a_\sigma}{r}\right)^2$	$\frac{9}{8\pi^2}\left(\frac{\sigma_{ICD}}{\sigma_A}\right)\left(\frac{2\pi^{\frac{1}{2}}a}{r}\right)^6$		
$\Delta\Gamma_s$	$3\left(\frac{\lambda_{nk}}{2\pi r}\right)^3\frac{\mathrm{Im}\tilde{\alpha}}{r^3}$	$12\left(\frac{2\pi^{\frac{1}{2}}a}{r}\right)^6\left(\frac{\mathrm{Im}\tilde{\alpha}}{a_\sigma^2\lambda}\right)^2$	$\frac{32\pi}{3}\left(\frac{\mathrm{Im}\tilde{\alpha}}{a_\sigma^2\lambda}\right)^2$	
$\Delta\Gamma_A$	$\mp 2\pi\left(\frac{\lambda_{nk}}{2\pi r}\right)^4\left(\frac{a_\sigma}{r}\right)^2\left(\frac{a_\alpha}{2\pi^{\frac{1}{2}}a}\right)^2$	$\mp\frac{3}{\pi}\left(\frac{a_\alpha}{r}\right)^3\left(\frac{2\pi^{\frac{1}{2}}a}{r}\right)^3$	$\mp\frac{8\pi}{3}\left(\frac{\sigma_A}{\sigma_{ICD}}\right)\left(\frac{a_\alpha}{2\pi^{\frac{1}{2}}a}\right)^3$	$\mp\frac{1}{2}\left(\frac{a_\alpha}{\mathrm{Im}\tilde{\alpha}}\right)^3\left(\frac{a_\sigma}{2\pi^{\frac{1}{2}}a}\right)^2\left(\frac{\lambda_{nk}}{4\pi^{\frac{3}{2}}a}\right)$
$\mathrm{Im}\tilde{\alpha}=0\,,\quad \lambda_{nk}/2\pi > r > 2\pi^{\frac{1}{2}}a \sim a_\sigma \gtrsim a_\alpha \quad\Rightarrow\quad \Gamma_{A,0} > \Gamma_{ICD} \gtrsim \Delta\Gamma_A \gtrsim \Gamma_{s,0} > \Delta\Gamma_s \sim 0$				

Table 3.2.: Comparison of different relaxation rates for an excited atom in close proximity to a second atom (via one-photon-exchange). In the presence of a second atom, the one-atom decay rates $\Gamma_{s/A}$ gain a contribution $\Delta\Gamma_{s/A}$. The ratios are defined by the ratio of the length scales: transition wavelength λ_{nk}, atom separation r, Auger-radius a, photoionisation radius $\pi a_\sigma^2 = \sigma$ and polarisability radius $a_\alpha^3 = \tilde{\alpha}$. The ratio between the two involved photoionisation cross sections σ_A and σ_{ICD} typically range from 10^{-2} to 10^2 and there is no general preference in favour of either process. If the involved length scales obey their typical relation to each other, we can sort the rates by their magnitude. For the given hierarchy we have excluded the case of $\omega_{nk} \approx \omega_i$, which would lead to a significantly high $\mathrm{Im}\alpha$ and hence large $\Delta\Gamma_s$, $\Delta\Gamma_A$.

where we relabelled $\sigma_m \to \sigma_{ICD}$ which is not the same photoionsation cross section as σ_A in the Auger decay, see the process schemes in Fig. 3.3. The ratio between ICD and Auger rate is given by

$$\frac{\Gamma_A}{\Gamma_{ICD}} \approx \frac{\Gamma_{A,0}}{\Gamma_{ICD}} + \frac{\Delta\Gamma_A}{\Gamma_{ICD}}\,, \tag{3.93}$$

$$\frac{\Delta\Gamma_A}{\Gamma_{ICD}} = \mp\frac{32\pi^2}{9}\left(\frac{\sigma_A}{\sigma_{ICD}}\right)\left(\frac{a_\alpha}{2\sqrt{\pi}a}\right)^3\,, \tag{3.94}$$

$$\frac{\Gamma_{A,0}}{\Gamma_{ICD}} = \frac{8\pi^2}{9}\left(\frac{\sigma_A}{\sigma_{ICD}}\right)\left(\frac{r}{2\sqrt{\pi}a}\right)^6\,. \tag{3.95}$$

The ratio of the different photoionisation cross sections σ_A/σ_{ICD} can vary around unity typically from 10^{-2} to 10^2. The free-space ratio $\Gamma_{A,0}/\Gamma_{ICD}$ is usually much larger than unity as a result of $r/a \gg 1$. The different ratios are given in a compact form in table 3.2, together with an estimation of the typical hierarchy of the rates, where we have assumed that $\omega_{nk} \gg \omega_i$, i.e. that $\mathrm{Im}\alpha \ll 1$.

Assuming that the transition frequency ω_{nk} is much larger than the atomic resonances of the system, the hierarchy of the characteristic length scales is typically given by

$$\lambda_{nk}/2\pi > r > 2\pi^{\frac{1}{2}} a \sim a_\sigma \gtrsim a_\alpha \,, \tag{3.96}$$

and $\mathrm{Im}\tilde{\alpha} = 0$, from which we may conclude the hierarchy of the rates to be

$$\Gamma_{\mathrm{A},0} > \Gamma_{\mathrm{ICD}} \gtrsim \Delta\Gamma_{\mathrm{A}} \gtrsim \Gamma_{\mathrm{s},0} > \Delta\Gamma_{\mathrm{s}} \sim 0 \,. \tag{3.97}$$

Auger decay, once energetically allowed will dominate the decay process and spontaneous decay is usually negligible in comparison to other decay channels. From this analysis it becomes evident that it is rather impossible to find a system, where ICD dominates over Auger decay in free space. For an acceptor polarisability $\alpha(\omega_{nk}) > 2\sqrt{\pi}a$, where $a \sim 10^{-1}$ Å is the Auger radius, the Auger rate can be suppressed by the presence of the second atom. A system where ICD is similarly fast as Auger should chosen such that $\sigma_{\mathrm{ICD}} \gg \sigma_{\mathrm{A}}$, the donor–acceptor distance r should be as small as possible, ω_{nk} should be small and rather close to the atomic transition frequencies ω_i such that the acceptor's polarisability at this frequency is non negligible and the vacancy orbital should be chosen as large as possible, e.g. small proton number Z of the donor.

The presented treatment can easily be adapted to account for multiple atoms. For the single atomic relaxation channels, spontaneous decay and Auger decay, additional neighbouring atoms passively influence the rates, similar as shown for the single neighbouring atom. This can be easily taken into account by introducing multiple polarisability tensors $\boldsymbol{\alpha}_i$ for the respective neighbouring atom at position $\boldsymbol{r}_i$. The Born series for N mediators simply yields a sum, such that

$$\mathbb{G}^{N\mathrm{M}}(\boldsymbol{r}, \boldsymbol{r}', \omega) = \sum_i^N \mathbb{G}^{\mathrm{M}_i}(\boldsymbol{r}, \boldsymbol{r}', \omega) \,, \tag{3.98}$$

$$\mathbb{G}^{\mathrm{M}_i}(\boldsymbol{r}, \boldsymbol{r}', \omega) = \frac{\omega}{c^2} \mathbb{G}^{(0)}(\boldsymbol{r}, \boldsymbol{r}_i, \omega) \cdot \frac{\boldsymbol{\alpha}_i(\omega)}{\varepsilon_0} \cdot \mathbb{G}^{(0)}(\boldsymbol{r}_i, \boldsymbol{r}', \omega) \,. \tag{3.99}$$

Each mediator Green's tensor $\mathbb{G}^{\mathrm{M}_i}$ highly depends on the respective distance between the mediating neighbour and the decaying atom. Close mediators have a larger impact onto the rates than farther ones. Assuming that the distances as well as the polarisabilities are comparable to each other, such that $\mathbb{G}^{\mathrm{M}_i} \approx \mathbb{G}^{\mathrm{M}_j}$ for all i, j, the scattering Green's tensor scales linearly with the number of mediators: $\mathbb{G}^{N\mathrm{M}} \approx N\mathbb{G}^{\mathrm{M}}$. The rate depends quadratically on the sum of the free space Green's tensor and the mediator one. It hence scales linearly with the number of mediators in first order of α and quadratically in its second order. The same holds for ICD, however here we have to account for only $N - 1$ mediators since the process itself occurs between two atoms already.

Furthermore, in ICD the rate scales linearly with the number of possible acceptors. This can be taken into account via the sum over final states in the rate (3.38). Explicitly in the isotropic case this would lead to an additional sum in the ICD rate (3.39), where the positions $\boldsymbol{r}_{b_i}$ of the acceptors and their respective photoionisation cross section σ_{m_i} are summed over. This discussion neglects superradiance effects where the initial state must include shared excitations between several donor atoms.

3.3.2. Impact of a surface onto decay channels

So far, we have shown that Auger decay typically dominates over ICD, while in the donor–acceptor distance regime we are interested in the spontaneous decay rate is negligible compared to ICD. In this section we determine the impact of a close-by surface onto the excitation-propagation for the two dominating process rates, ICD and Auger decay. We show that even a simple dielectric surface can alter the ratio between the two rates. General analytic formulas to describe the modification of their ratio are provided. We show that ICD is in general more strongly effected by macroscopic bodies due to its larger characteristic length scale introduced in the previous section and we further consider anisotropic transitions and show that anisotropy can have large effect on the impact of the surface.

As before, we limit ourselves for the discussion to cases were the relaxing electron transitions from the same energy level for both processes, Auger and ICD. In this case ω_{nk} as well as γ_{nk} are the same for each process, while the photoionisation cross section $\sigma_m(\omega_{nk})$ differs for the two rates, see Fig. 3.3. We will refer to the photoionisation cross section appearing in the Auger decay rate and ICD rate as σ_{A} and σ_{ICD}, respectively.

Let us consider a macroscopic surface close to the atomic system. The influence of the second atom on the Auger decay rate as it was considered in the previous section will be neglected in this section, such that we concentrate the following study on the modification of the rates via the surface. The scattering Green's tensor $\mathbb{G}^{(1)}$ for a magnetodielectric half space is given in the appendix, see Eq. (A.48). For non cavity-like

index	reflection coeff. r_{NR}	permittivity ε	refraction index n_r
1	-2	-0.33	$0.58\mathrm{i}$
2	$2\mathrm{i}$	$-0.60+0.80\mathrm{i}$	$0.45+0.90\mathrm{i}$
3	$1.41+1.41\mathrm{i}$	$-1.38+1.30\mathrm{i}$	$0.51+1.28\mathrm{i}$
4	2	-3	$1.73\mathrm{i}$

Table 3.3.: Chosen values for the material parameters at $\omega = \omega_{nk}$. The parameters are related by: $r_{\mathrm{NR}} = (\varepsilon-1)/(\varepsilon+1)$ and $n_r = \sqrt{\varepsilon}$.

geometries the nonretarded regime of very small distances $\Delta r \ll c/\omega_{nk}$ to the surface achieves the strongest effects. Let us consider a homogeneous dielectric surface with permittivity ε and a nonretarded reflection coefficient of $r_{\mathrm{NR}} = (\varepsilon - 1)/(\varepsilon + 1)$. In the nonretarded limit the scattering Green's tensor can be approximated by Eq. (A.55) and reads

$$\begin{aligned} \mathbb{G}^{(1)}_{\mathrm{surface}}(\boldsymbol{r}_b, \boldsymbol{r}_a, \omega) &= -\frac{r_{\mathrm{NR}} c^2}{4\pi\omega^2 \bar{r}_{ab}^3} (\mathbb{I} - 3\bar{\boldsymbol{e}}_{ab} \otimes \bar{\boldsymbol{e}}_{ab}) \cdot \mathbb{M}\,, \\ \mathbb{M} &= \mathbb{I} - 2\boldsymbol{e}_{\Delta r} \otimes \boldsymbol{e}_{\Delta r}\,, \\ \bar{\boldsymbol{r}}_{ab} &= \mathbb{M} \cdot \boldsymbol{r}_{ab} - 2\Delta\boldsymbol{r}, \quad \bar{\boldsymbol{e}}_{ab} = \bar{\boldsymbol{r}}_{ab}/\bar{r}_{ab}\,, \end{aligned} \tag{3.100}$$

where $\boldsymbol{r}_{ab} = \boldsymbol{r}_b - \boldsymbol{r}_a$ and $\bar{\boldsymbol{r}}_{ab}$ is its mirror point, behind the surface and $\boldsymbol{e}_x = \boldsymbol{r}_x/|r_x|$ is the respective unit vector. The full Green's tensor for Auger decay and ICD close to a surface is then given by

$$G_{\mathrm{A}} = \tilde{\mathbb{G}}^{(0)}(\omega_{nk}) + \mathbb{G}^{(1)}_{\mathrm{surface}}(\boldsymbol{r}_{\mathrm{D}}, \boldsymbol{r}_{\mathrm{D}}, \omega_{nk})\,, \tag{3.101}$$

$$G_{\mathrm{ICD}} = \mathbb{G}^{(0)}(\boldsymbol{r}_{\mathrm{A}}, \boldsymbol{r}_{\mathrm{D}}, \omega_{nk}) + \mathbb{G}^{(1)}_{\mathrm{surface}}(\boldsymbol{r}_{\mathrm{A}}, \boldsymbol{r}_{\mathrm{D}}, \omega_{nk})\,, \tag{3.102}$$

where $\boldsymbol{r}_{\mathrm{D/A}}$ are the positions of the excited (donor) atom D and the ground-state (acceptor) atom A. Using these Green's tensors in the respective rate equation for isotropic transitions, see Eq. (3.39) for ICD and Eq. (3.61) for Auger decay, yields the rates in the presence of a surface as a function of the atoms' positions. For the isotropic Auger decay rate we find

$$\Gamma_{\mathrm{A}} = \Gamma_{\mathrm{A},0} \left(1 - \frac{2\sqrt{\pi}\mathrm{Re}\left[r_{\mathrm{NR}}\right] a^3}{\Delta r^3} + \frac{9\pi |r_{\mathrm{NR}}|^2 a^6}{8\Delta r^6} \right)\,, \tag{3.103}$$

where $\Gamma_{\mathrm{A},0}$ is given by the isotropic free space Auger rate, Eq. (3.82). Although we have restricted ourselves so far to isotropic processes, ICD still possesses a preferred direction due to the atoms' position relative to each other. Depending on the orientation of the donor–acceptor separation vector relative to the surface, the effect onto the process rate varies. The two extremes are given by perpendicular and parallel separation vector $\boldsymbol{r}_{\mathrm{DA}} = \boldsymbol{r}_{\mathrm{A}} - \boldsymbol{r}_D$ to the surface, see the inset schemes in Fig. 3.4. The ICD rates for these extreme cases read

$$\Gamma^{\parallel}_{\mathrm{ICD}} = \Gamma_{\mathrm{ICD},0} \left(1 - \frac{\mathrm{Re}\left[r_{\mathrm{NR}}\right] \left(\Delta r^2/r_{\mathrm{DA}}^2 + 4 \right)}{3\left(\Delta r^2/r_{ab}^2 + 1 \right)^{5/2}} + \frac{|r_{\mathrm{NR}}|^2}{\left(\Delta r^2/r_{\mathrm{DA}}^2 + 1 \right)^3} \right)\,, \tag{3.104}$$

$$\Gamma^{\perp}_{\mathrm{ICD}} = \Gamma_{\mathrm{ICD},0} \left(1 + \frac{2\mathrm{Re}\left[r_{\mathrm{NR}}\right] r_{\mathrm{DA}}^3}{3\left(2\Delta r + r_{\mathrm{DA}}\right)^3} + \frac{|r_{\mathrm{NR}}|^2 r_{\mathrm{DA}}^6}{\left(2\Delta r + r_{\mathrm{DA}}\right)^6} \right)\,, \tag{3.105}$$

where $\Gamma_{\mathrm{ICD},0}$ is the isotropic free space ICD rate in the nonretarded limit given by

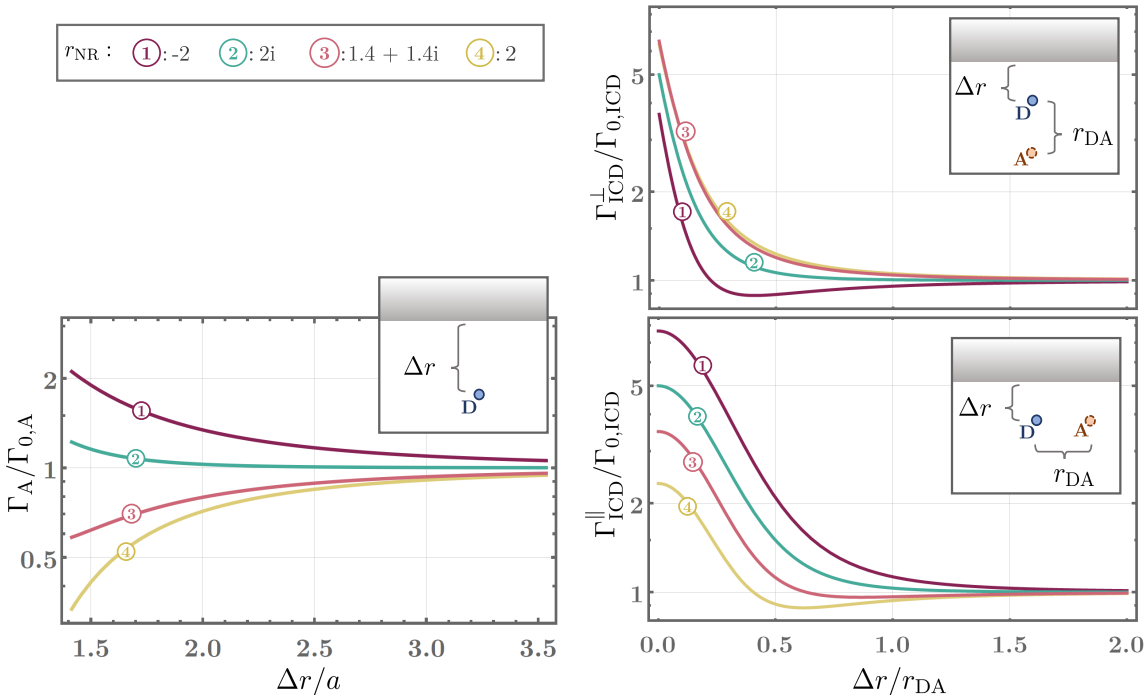

Figure 3.4.: The relative Auger rate $\Gamma_A/\Gamma_{A,0}$ and the relative ICD rate $\Gamma_{ICD}/\Gamma_{0,ICD}$ close to a surface as a function of surface distance Δr. For ICD two geometries are presented: $\Gamma^{\perp}_{ICD}$ with a donor–acceptor-separation $\boldsymbol{r}_{DA}$ perpendicular to the surface and $\Gamma^{\parallel}_{ICD}$ with $\boldsymbol{r}_{DA}$ parallel to the surface. Each rate is given for four different reflection coefficients $r_{NR} \in \{-2, 2i, 1.4 + 1.4i, 2\}$ indicated in the curves by their respective index, see Table 3.3.

Eq. (3.43).

In Fig. 3.4 these rates are plotted relatively to their free-space rate for different complex values of $r_{NR} \in \{-2, 2i, 1.4 + 1.4i, 2\}$, such that $|r_{NR}| = 2$. In Table 3.3 the respective permittivity and complex refractive index $n_r = \sqrt{\varepsilon}$ for these values are given. The length scale that determines how much the surface influences the process is the interatomic separation r_{DA} in ICD, while in Auger this length scale is given by the Auger-radius a. The Auger-radius can be determined via known free-space Auger rates or be roughly estimated by using Slater rules for the vacancy orbital as shown in section 3.2.3 and is of the order of the Bohr radius $a_0 \approx 0.5\,\text{Å}$. Therefore $a \ll r_{DA}$ and as a consequence there is a large range of surface-atom distances Δr, at which the Auger rate is effectively the free-space rate, while the ICD rate is modified by the surface. For the chosen permittivities the nonretarded effect of the surface vanishes in case of ICD for separations $\Delta r > 2r_{DA}$, while the effect onto the Auger rate vanishes for separations $\Delta r > 4a$.

The parallel geometry for the ICD rate is influenced more strongly by the surface. This can be easily understood. In the nonretarded limit the impact of the surface is comparable to that of an mirrored acceptor-dipole. For a donor distance Δr the distance

to the mirrored acceptor dipole is larger in the perpendicular case than for the parallel case, its impact hence smaller. From the point of view of surface polaritons it is also clear that the parallel geometry profits from surface waves mediating the energy transfer. The two real reflection coefficients $r_{\mathrm{NR}} \in \{-2, 2\}$, i.e. the extreme cases of complex phases of r_{NR} give the most different behaviour per process and geometry. Every curve belonging to a reflection coefficient with $|r_{\mathrm{NR}}| = 2$ is between these two extremes. For larger values of $|r_{\mathrm{NR}}|$ the respective impact of the surface onto the rate would be amplified.

Since ICD is often studied inside of a dimer or larger molecule, the sum in Eq. (3.38) over the involved transition dipoles $\boldsymbol{d}_{nk} = \langle k|\hat{\boldsymbol{d}}|n\rangle$, with $|n\rangle = |E_n, L_n, M_n\rangle$ is not necessarily isotropic. If we introduce transition dipole orientations, we find that specific orientations are stronger influenced by a simple close-by surface than others, depending on the geometry. We illustrate this in the example, where the initial $|n\rangle$-state of the donor only involves angular momentum $\boldsymbol{L}_n$ with $L_n = |\boldsymbol{L}_n| = 1$ that are either parallel ($M_n \in \{-L_n, L_n\}$) or perpendicular ($M_n = 0$) to the quantisation axes, i.e. the separation axes between donor and acceptor, see Fig. 3.5c).

We want to focus on the modification of the competition between Auger and ICD rate. For this we define the ratio between the competing rates as a branching ratio:

$$B = \Gamma_{\mathrm{ICD}}/\Gamma_{\mathrm{A}} \tag{3.106}$$

and the free-space branching ratio $B_0 = \Gamma_{\mathrm{ICD},0}/\Gamma_{\mathrm{A},0}$, that is constant in Δr. The larger the branching ratio, the faster ICD becomes compared to Auger. As discussed in section 3.3.1, Auger is typically faster than ICD, and we expect $B_0 < 1$. The branching ratio itself depends on the ratio of the photoionisation cross sections $\sigma_{\mathrm{ICD}}/\sigma_{\mathrm{A}}$, which can be of several orders of magnitude. The environment's impact onto the branching ratio, given by B/B_0 however depends only on the surface properties and the geometry, including the relation between r_{DA} and a.

In Fig. 3.5, the branching ratio B is given for $a = 7r_{\mathrm{DA}}$ compared to the free space branching ratio B_0 as a function of the donor's distance to the surface Δr. Both extreme complex phases of the reflection coefficient $r_{\mathrm{NR}} \in \{-2, 2\}$ are presented for each introduced dipole orientation as well as for the isotropic case. For the perpendicular geometry the branching ratio $B^{\perp} = \Gamma^{\perp}_{\mathrm{ICD}}/\Gamma_{\mathrm{A}}$ shows a simple behaviour as function of the surface distance Δr, see Fig. 3.5a: for $M_n \in \{-1, 1\}$ as well as for the isotropic case a positive reflection coefficient $r_{\mathrm{NR}} > 0$ enhances the branching ratio in favour of ICD for all distances, while $r_{\mathrm{NR}} < 0$ suppresses the ICD compared to the Auger decay. For $M_n = 0$ the situation is roughly inversed. In the parallel geometry, see Fig. 3.5b a negative reflection coefficient $r_{\mathrm{NR}} < 0$ leads in all cases to an enhanced branching ratio $B^{\parallel}/B_0 > 1$. While a positive reflection coefficient can shift the branching ratio in either direction and achieves

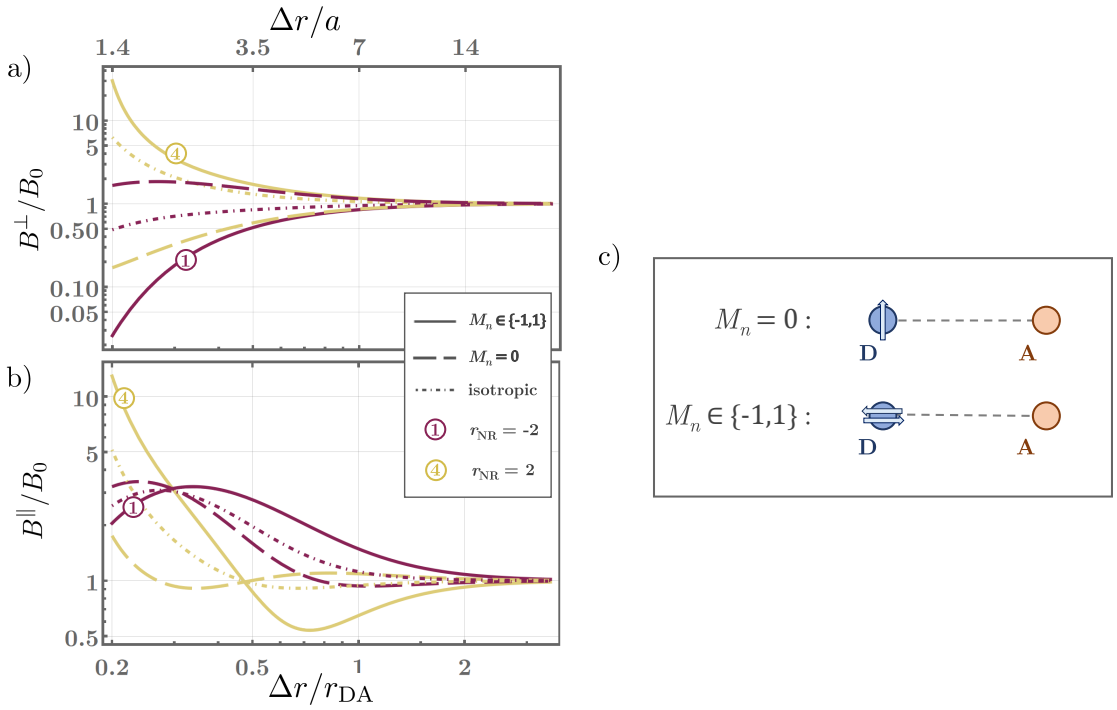

Figure 3.5.: The relative branching ratio B/B_0 (see Eq. 3.106) close to a surface in the **a)** perpendicular and **b)** parallel ICD-geometries (see Fig. 3.4) and for the two extreme complex phases of the reflection coefficient $r_{\mathrm{NR}} \in \{-2, 2\}$. **c)** In addition to the isotropic case, we also considered specific orientations of the transition dipole as a consequence of specific angular momentum projections M_n of the initial state $|n\rangle$. For the plots we chose the characteristic length scale ratio of the two processes to be $r_{\mathrm{DA}}/a = 7$.

in very small surface distances an higher enhancement than the negative reflection coefficient. For each geometry the isotropic case plotted in Fig. 3.5 is always given by a weighted average of the respective two anisotropic results.

In Fig. 3.6, the distance between the two atoms is not fixed. Instead we fix the position of the acceptor atom at the origin with a distance to the surface of $\Delta r = 3.5a$, where a is again the Auger-radius and hence the fundamental scale for Auger decay. The donor's position is varied. We choose a refractive index of $r_{\mathrm{NR}} = -2$, since this choice revealed itself to be most favourable for enhancing ICD compared to Auger decay in the geometries considered so far. The contours give the branching ratio B (3.106) between ICD and Auger for a donor at the respective position in terms of the photoionisation cross section ratio, if e.g. the ratio of the respective photoionisation cross sections is given by $\sigma_{\mathrm{ICD}}/\sigma_{\mathrm{A}} = 100$ then the contour at $B/(\sigma_{\mathrm{ICD}}/\sigma_{\mathrm{A}}) = 0.01$ yields the donor position at which Auger and ICD are equally fast. The dashed contours give the respective branching ratio B_0 in free space. The colormap shows the modification of the branching ratio by the surface, i.e. B/B_0. The surface has a stronger impact onto the branching ratio the larger the donor–acceptor distance r_{DA} is. However, the larger r_{DA} the lower is the free space branching

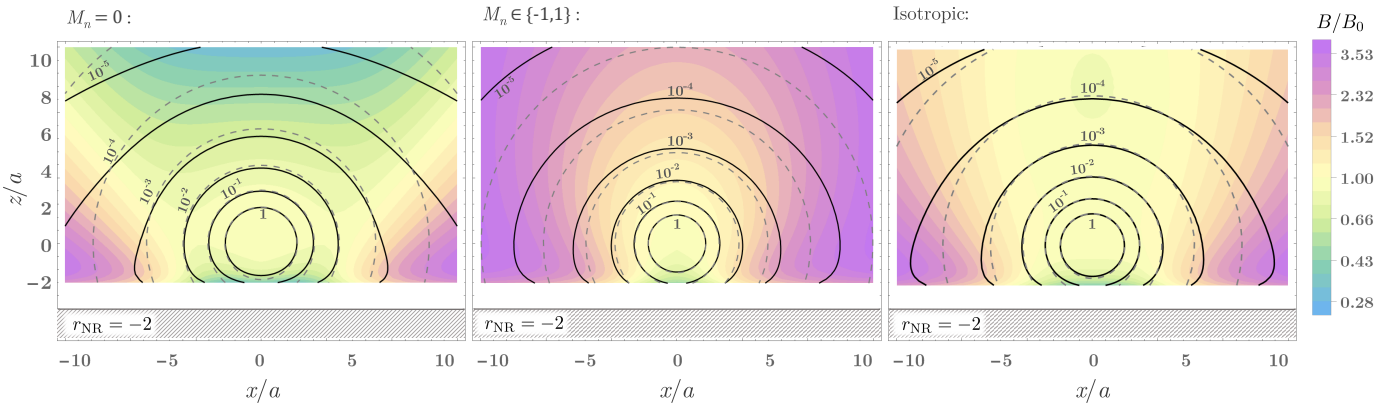

Figure 3.6.: Contour plots for the two different non-isotropic cases as well as the isotropic case for a surface reflection coefficient $r_{NR} = -2$. The acceptor atom's position is fixed at the origin while we vary the position of the donor. The surface is considered at $z = 3.5a$. The black contours show the absolute branching ratio in terms of the cross section ratio $B/(\sigma_{ICD}/\sigma_A)$ in the presence of the surface, while the dashed contours show the respective value for the branching ratio in free space $B_0/(\sigma_{ICD}/\sigma_A)$. The color plot shows the comparison B/B_0 of the branching ratios with and without the surface.

ratio B_0. A system were the photoionsiation cross section of the ICD process is much larger than the one of Auger gives hence a preferable initial condition, since it yields a higher free space branching ratio B_0. The impact of the surface becomes stronger with larger $|r_{NR}|$. The strongest effect can be achieved if the involved transition dipoles are parallel to the surface. In case of $M_n = 0$ we find suppression of ICD compared to Auger (i.e. $B/B_0 < 1$) for the surface–parallel transition dipole moment and for $M_n \in \{-1, 1\}$ we find enhancement of ICD compared to Auger (i.e. $B/B_0 > 1$) for the surface–parallel transition dipole moments.

With the simple dielectric surface chosen here we can already achieve an enhancement of ICD compared to Auger by a factor of roughly 3.5. However, depending on the magnitude of its reflection coefficient $|r_{NR}|$ the distances at which a surface shows significant influence onto the rates can become quite small compared to the atomic size. At such distances there may occur additional effects, due to the breakdown of the dipole approximation, possible wave function overlap and the possible breakdown of the surface being experienced by the atomic system as a continuum. The discussed results should still serve as a good approximation.

3.3.3. Impact of a cavity onto decay channels

The impact of a surface was discussed in detail in the previous section. As shown a surface only has an impact onto rates in the nonretarded limit of very small distances. In

cavities, this restriction does not apply. For specific set ups the rates of interest can be calculated explicitly by solving for the respective cavity Green's tensor. Here however, we want to keep the analysis as general as possible. Based on the cavity's Q-factor and some general properties of the cavity Green's tensor in the retarded limit, we may estimate the general effect of a cavity on ICD and Auger decay. This can then be used to either predict the maximum enhancement one can expect inside a given cavity or to determine the required properties of an appropriate cavity for a given atomic system.

The Q-factor of a cavity is defined by the relation between the spontaneous decay rate in free space $\Gamma_{s,0}$ and the one enhanced by the cavity Γ_s via

$$Q = \frac{\Gamma_s}{s\Gamma_{s,0}}, \qquad \text{with: } s = \frac{3\lambda^3}{4\pi^2 V} \tag{3.107}$$

$$\Rightarrow \qquad sQ - 1 = \frac{|\mathrm{Im}\,\mathbb{G}^{(1)}(\boldsymbol{r},\boldsymbol{r})|}{|\mathrm{Im}\,\mathbb{G}^{(0)}(\boldsymbol{r},\boldsymbol{r})|}, \tag{3.108}$$

where $\boldsymbol{r}$ is the position of the atom. Cavity QED usually assumes the opposite distance limit of the one applied in the previous section, namely the retarded limit in the surface-system distance $\Delta r\omega_{nk}/c \gg 1$. In the retarded limit the scattering Green's tensor describes propagating waves and we may approximate: $|\mathbb{G}^{(1)}(\boldsymbol{r},\boldsymbol{r})| \approx |\mathrm{Im}\,\mathbb{G}^{(1)}(\boldsymbol{r},\boldsymbol{r})|$. This can be seen in the example of a spherical cavity analytically, see the appendix A.3.2. We assume that a system undergoing ICD in the cavity has a donor–acceptor separation r_{DA} that is much smaller than the surface-system separation Δr. The scattering Green's tensor for ICD, can hence be approximated by: $\mathbb{G}^{(1)}(\boldsymbol{r}_{\mathrm{A}},\boldsymbol{r}_{\mathrm{D}}) \approx \mathbb{G}^{(1)}(\boldsymbol{r}_{\mathrm{A}} = \boldsymbol{r}_{\mathrm{D}})$, i.e. the same scattering Green's tensor as for spontaneous decay appearing in Eq. (3.108). We also use that the nonretarded bulk Green's tensor $\mathbb{G}^{(0)}(r_{\mathrm{A}}, r_{\mathrm{D}})$ and the regularised bulk $\tilde{\mathbb{G}}$ are real. Let us summarise these approximations and assumptions:

$$r_{\mathrm{DA}} \ll \Delta r \quad \Rightarrow \quad \mathbb{G}^{(1)}(r_{\mathrm{A}}, r_{\mathrm{D}}) \approx \mathbb{G}^{(1)}(r_{\mathrm{D}}, r_{\mathrm{D}}) \tag{3.109a}$$

$$\omega_{nk}\Delta r/c \gg 1 \quad \Rightarrow \quad \mathbb{G}^{(1)}(r_{\mathrm{D}}, r_{\mathrm{D}}) \approx \mathrm{Im}\,\mathbb{G}^{(1)}(r_{\mathrm{D}}, r_{\mathrm{D}}) \approx \mathrm{Re}\,\mathbb{G}^{(1)}(r_{\mathrm{D}}, r_{\mathrm{D}}) \tag{3.109b}$$

$$\omega_{nk} r_{\mathrm{DA}}/c \ll 1 \quad \Rightarrow \quad \mathbb{G}^{(0)}(r_{\mathrm{A}}, r_{\mathrm{D}}) \approx \mathrm{Re}\,\mathbb{G}^{(0)}(r_{\mathrm{A}}, r_{\mathrm{D}}) \tag{3.109c}$$

$$\omega_{nk} a/c \ll 1 \quad \Rightarrow \quad \tilde{\mathbb{G}}^{(0)} \approx \mathrm{Re}\,\tilde{\mathbb{G}}^{(0)} \tag{3.109d}$$

In addition, we define the ratio between the imaginary part of the free space Green's tensor and the real part of the free space Green's tensor for ICD and Auger, respectively:

$$b_{\mathrm{icd}} = \frac{|\mathrm{Im}\,\mathbb{G}^{(0)}(r_{\mathrm{D}}, r_{\mathrm{D}})|}{|\mathrm{Re}\,\mathbb{G}^{(0)}(r_{\mathrm{A}}, r_{\mathrm{D}})|} = \frac{\omega_{nk}^3 r_{\mathrm{DA}}^3}{3c^3} \ll 1\,, \tag{3.110a}$$

$$b_{\mathrm{a}} = \frac{|\mathrm{Im}\,\mathbb{G}^{(0)}(r_{\mathrm{D}}, r_{\mathrm{D}})|}{|\mathrm{Re}\,\tilde{\mathbb{G}}^{(0)}|} = 4\sqrt{\pi}\frac{\omega_{nk}^3 a^3}{c^3} \ll 1\,. \tag{3.110b}$$

By using Eqs. (3.109a)–(3.109c) and the definitions of b_{icd}, Eq. (3.110a) and Q, Eq. (3.108) we can estimate the maximum possible enhancement for ICD in a cavity,

$$\begin{aligned}
\Gamma_{\mathrm{ICD}}^{(\mathrm{cav})} &= \Gamma_{\mathrm{ICD},0}\left(\frac{|\mathbb{G}^{(0)}(\boldsymbol{r}_{\mathrm{A}}, \boldsymbol{r}_D) + \mathbb{G}^{(1)}(\boldsymbol{r}_{\mathrm{A}}, \boldsymbol{r}_D)|^2}{|\mathbb{G}^{(0)}(\boldsymbol{r}_{\mathrm{A}}, \boldsymbol{r}_D)|^2}\right) \\
&\approx \Gamma_{\mathrm{ICD},0}\left(1 + 2\frac{\mathrm{Re}\,\mathbb{G}^{(1)}(\boldsymbol{r}_{\mathrm{D}}, \boldsymbol{r}_D)}{\mathrm{Re}\,\mathbb{G}^{(0)}(\boldsymbol{r}_{\mathrm{A}}, \boldsymbol{r}_D)} + \left[\frac{\mathrm{Im}\,\mathbb{G}^{(1)}(\boldsymbol{r}_{\mathrm{D}}, \boldsymbol{r}_D)}{\mathrm{Re}\,\mathbb{G}^{(0)}(\boldsymbol{r}_{\mathrm{A}}, \boldsymbol{r}_D)}\right]^2\right) \\
&= \Gamma_{\mathrm{ICD},0}\left(1 + 2(sQ-1)b_{\mathrm{icd}} + (sQ-1)^2 b_{\mathrm{icd}}^2\right) \\
&\approx \Gamma_{\mathrm{ICD},0}\left(1 + 2sb_{\mathrm{icd}}Q + s^2 b_{\mathrm{icd}}^2 Q^2\right)\,,
\end{aligned} \tag{3.111}$$

where we have approximated $b \ll 1$, while $sbQ \sim 1$. Similarly, by using Eq. (3.109d) and Eq. (3.110b) we find for the maximum enhanced Auger decay rate in a cavity

$$\Gamma_{\mathrm{A}}^{(\mathrm{cav})} \approx \Gamma_{\mathrm{A},0}\left(1 + 2sb_{\mathrm{a}}Q + s^2 b_{\mathrm{a}}^2 Q^2\right)\,. \tag{3.112}$$

The estimation is based on the assumption that $sbQ \sim 1$, i.e. an appropriate cavity has to have a Q-factor, such that $sQ \geq 1/b$ for the respective process, where s is a factor determined by the cavities geometry, see Eq. (3.107). We have discussed the maximum enhancement possible in a cavity for both, ICD and Auger decay. To achieve maximum difference between ICD and Auger decay, i.e. to modify their ratio by a cavity most efficiently, one would need to take advantage of the maximum enhancement and maximum suppression inside the cavity simultaneously. Depending on the acceptor's position relative to the donor it should possible to enhance ICD while suppressing Auger. However, it is easier to enhance ICD than Auger due to $b_{\mathrm{icd}} > b_{\mathrm{a}}$, i.e. Auger requires a larger Q factor to obtain the same enhancement as ICD. Therefore even if both processes are maximally enhanced by the same cavity their ratio is modified in favour of ICD.

3.3.4. Application to He–Ne dimer

So far, we have discussed the modification of ICD and Auger decay as competing processes via macroscopic environment in general. In this section, we offer an example system and evaluate the derived formulas to demonstrate their applicability to specific systems. A doubly excited He–Ne dimer, with both He electrons excited may undergo

Auger decay or ICD to relax. This system has been treated in free space theoretically via *ab initio* calculation methods by Jabbari et al. [161]. We use their results to verify our free-space limit and extract the correct Auger radius before predicting the possible influence of a macroscopic environment. We first introduce the system and determine its parameters as they appear in our formulas. We then calculate the free space rate for ICD and compare it for verification with the one reported by Jabbari et al. We then use their Auger decay rates to determine the Auger radius. We finally apply the results of the previous sections to the system.

In their ground state (before excitation), the two atoms in the dimer have an equilibrium separation of $r_{\mathrm{DA}} = 3$ Å[161]. The dimer exists in two possible molecular state, Σ and Π. For sufficiently large separation distances each molecule state maps to the product of the atomic ground state of neon and the $M_\Sigma = 0$ and $M_\Pi \in \{-1, 1\}$ doubly excited state for helium, respectively. We will consider the system in this limit and compare our results with the results obtained by Jabbari et al.

When exciting helium, there are several possible doubly excited states. The two dominating ones are 2s2p and 23sp+, with $|23\mathrm{sp}+\rangle = 2^{-1/2}\left(|2\mathrm{p3s}\rangle + |2\mathrm{s3p}\rangle\right)$[161]. We choose to apply our formalism to the dimer consisting of 23sp+ helium. We therefore need to determine the involved single atom properties ω_{nk}, γ_{nk} and $\sigma_{\mathrm{A}}/\sigma_{\mathrm{ICD}}$ appearing in the rate formulas of the respective process:

$$
\begin{aligned}
\text{ICD:} \qquad \mathrm{He}^{**}(23\mathrm{sp}+) &\xrightarrow[\gamma_{nk}]{} \mathrm{He}^{*}(1\mathrm{s3s}) + \hbar\omega_{nk} \\
\mathrm{Ne} + \hbar\omega_{nk} &\xrightarrow[\sigma_{\mathrm{ICD}}]{} \mathrm{Ne}^{+} + \mathrm{e}^{-} \\
\text{Auger:} \qquad \mathrm{He}^{**}(23\mathrm{sp}+) &\xrightarrow[\gamma_{nk}]{} \mathrm{He}^{*}(1\mathrm{s3s}) + \hbar\omega_{nk} \\
\mathrm{He}^{*}(1\mathrm{s3s}) + \hbar\omega_{nk} &\xrightarrow[\sigma_{\mathrm{A}}]{} \mathrm{He}^{+} + \mathrm{e}^{-}
\end{aligned}
$$

as in the general discussion of previous sections we find that γ_{nk} is the same in both processes, while the photoionisation cross sections refer to different transitions. The photoionisation cross section σ_{A} in the Auger decay describes an emission of the 3s-electron of the double excited helium, while the one for ICD, σ_{ICD} describes the emission of an electron in the most outer shell of neon. Furthermore, we find that alternative transitions are dipole forbidden, such that the exchange term in the Auger decay vanishes.

From tabulated data, we find the atomic properties to be given by: $\omega_{nk} = 40.94$ eV [161], $\sigma_{\mathrm{ICD}} = 9.28$ Mb [158], $\sigma_{\mathrm{A}} = 0.35$ Mb [162], $\gamma_{nk} = 5.65 \times 10^{9}\ \mathrm{s}^{-1}$ [163]. According to the model suggested in section 3.2.3 the Auger-radius would be given by $a_{\mathrm{model}} \approx 1.80 a_{\mathrm{vac}} = 0.45$ Å with the vacancy orbital given by $a_{\mathrm{vac}} = a_0/2$ according to Slater rules. Unfortunately, this yields an Auger decay rate that differs from reported data from numerical calculations [163–165]. The additional factor of 1.8 was found in section 3.2.3

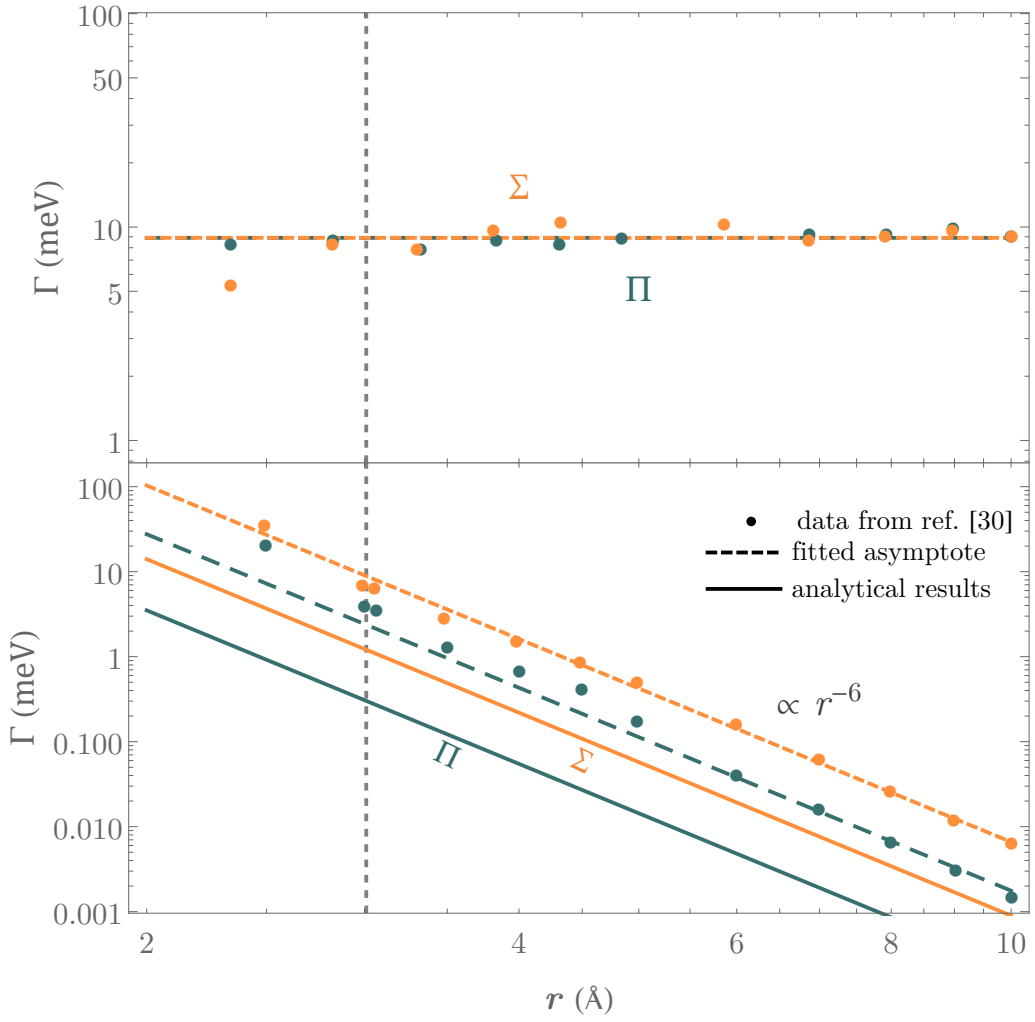

Figure 3.7.: The free-space Auger decay rate (upper plot) and ICD rate (lower plot) as function of dimer separation distance r for both molecule states Σ and Π. Neglecting wave function overlap, Auger decay rates are constant as a function of separation distance r, while ICD rates decrease with r^{-6} (asymptotic behaviour). We compare the ICD decay obtained in our framework (solid lines) with ones calculated by Jabbari et al. [161]. The dashed lines illustrate the asymptotic behaviour of the *ab initio* ICD rates. The discrepancy to our result is discussed in the main text. The deviation from constant lines in the *ab initio* Auger decay rates and from the r^{-6}-behaviour in the *ab initio* ICD rates is negligible at the equilibrium distance of $r = 3$ Å.

by a fit to available data of the isoelectronic sequence of Fluor-like ions. This electronic structure differs from the one in doubly excited helium. It was hence to be expected that the found model parameters cannot be transferred without adjustment to doubly excited helium. Using the known Auger rate from Jabbari et al. we may calculate the appropriate Auger radius. The Auger decay rate in free space in our model is given by

$$\Gamma_{\mathrm{A}} = 2\pi\gamma_{2p\to 1s}\sigma_{\mathrm{A}}\,\mathrm{Tr}\left\{\tilde{\mathbb{G}}(\omega_{nk})\cdot\tilde{\mathbb{G}}(\omega_{nk})\right\} \tag{3.113}$$

for both molecule state, Σ and Π. Using the regularised free-space Green's tensor (3.49) and demanding that Eq. (3.82) yields the Auger rate of 8.1 meV reported by Jabbari et al. we obtain an Auger radius of $a = 0.65$ Å. While the Auger radius obtained from the fitted parameters (0.45 Å) is as expected not sufficiently exact to use for the He-Ne dimer, it still possesses the correct order of magnitude.

Let us first discuss the possible impact of neon onto the spontaneous decay rate and Auger decay rate and the characteristic length scale hierarchy according to the results of section 3.3.1. The polarisability α_{Ne} of neon itself is negligible at $\omega_{nk} = 43.84$ eV ($\alpha_{\mathrm{Ne}}(43.84\text{ eV}) \sim \mathcal{O}(10^{-6})$) and hence neither mediates the radiative nor Auger decay [166]. The characteristic length scales are given by

$$\lambda_{nk}/2\pi \approx 48\,\text{Å} \gg r \approx 3\,\text{Å} > 2\pi^{\frac{1}{2}}a \approx 2.3\,\text{Å} > a_\sigma^{\mathrm{ICD}} \approx 0.17\,\text{Å} > a_\sigma^{\mathrm{A}} = 0.03\,\text{Å}\,. \tag{3.114}$$

It immediately follows from $\lambda_{nk} \gg r > 2\pi^{1/2}a$ that the spontaneous decay rate is negligible as a decay channel compared to Auger. The chosen system shows many features that favours ICD as a competing processes: the photoionisation cross section for ICD $\sigma_{\mathrm{ICD}} = \pi(a_\sigma^{\mathrm{ICD}})^2$ is larger than the one for Auger, $\sigma_{\mathrm{A}} = \pi(a_\sigma^{\mathrm{A}})^2$ and the Auger radius a is too small compared to the donor–acceptor distance $r \approx 5a$. We hence expect that in the chosen system – albeit slower – ICD is not negligible compared to Auger decay.

For ICD the two different molecular states, determining directions of the involved transition dipole moments yield different free space rates. In the nonretarded limit we find

$$\Gamma_{\mathrm{ICD},\Pi} = \frac{3c^4\gamma_{2p\to 1s}\sigma_{\mathrm{ICD}}}{8\pi\omega_{nk}^4 r_{\mathrm{DA}}^6}\,, \tag{3.115}$$

$$\Gamma_{\mathrm{ICD},\Sigma} = \frac{3c^4\gamma_{2p\to 1s}\sigma_{\mathrm{ICD}}}{2\pi\omega_{nk}^4 r_{\mathrm{DA}}^6} = 4\Gamma_{\mathrm{ICD},\Pi}\,. \tag{3.116}$$

When comparing the resulting ICD rates as a function of the separation distance r_{DA} with the ones reported by Jabbari et al., we find that the relative magnitude between the two ICD rates matches the ones obtained in Ref. [161] but their overall magnitude is smaller by a factor of roughly 7 for all distances and both considered molecule states,

see Fig. 3.7. The *ab initio* quantum chemistry method used by Jabbari et al. goes beyond the dipole approximation and includes wave function overlaps between donor and acceptor. However, this cannot be the source of the observed discrepancy: in the limit of larger distances the rates obtained by *ab initio* methods converge to the ones obtained in dipole approximation, i.e. our formalism. An indicator of when this limit is reached is the behaviour of the obtained rate as a function of the donor–acceptor distance r_{DA}: At distances where the rate shows a r_{DA}^{-6} behaviour the asymptotic limit which is well described by the dipole approximation is achieved. As one can see in Fig. 3.7 the discrepancy between the *ab initio* rates and the one obtained in the dipole approximation is independent of the distance.

We have reached out to the authors of Ref [161] to discuss the discrepancy obtained by the different frameworks. It can in fact be traced back to a less accurate representation of the transition dipoles in the method employed by Jabbari et al. as compared with the values used in our approach [167]. A discussion of the behaviour of the *ab initio* decay widths at large interatomic separations can be found for Ne–H_2O clusters in reference [168]. While we conclude that the reported ICD rates by Jabbari et al. are off by a factor of 7, the source of this error does not affect their Auger rate calculation. Their Auger rates are in good agreement with measurement and numerical rates obtained in other works [163–165].

Even at the equilibrium distance of 3 Å, the r^{-6}- behaviour of the *ab initio* ICD rate implies that wave function overlap between neon and helium do not play a significant role for the rates, instead we may use atomic data to approximate the rates at the equilibrium distance in our framework. We conclude that our approach, including the dipole approximation is suited to treat ICD at the equilibrium distance of $r_{\mathrm{DA}} = 3$ Å. The free space ratio between ICD and Auger decay at the equilibrium distance is hence $B_{0,\Sigma} \approx 0.15$ and $B_{0,\Pi} \approx 0.04$.

Next we apply the results of our study of a close-by surface obtained in section 3.3.2 to the example of the He–Ne dimer. At the equilibrium distance we find a ratio of $r_{\mathrm{DA}}/a = 4.64$ between the characteristic length scales of ICD and Auger decay, which is smaller than the one we assumed for the plot given in Fig. 3.5. Adapting the ratio accordingly and replotting the graph for the case of the He–Ne dimer gives the plot shown in Fig. 3.8, where the two molecular states, Σ and *Pi* correspond to the angular momentum projection numbers $M_\Sigma = 0$ and $M_\Pi \in \{-1, 1\}$, respectively. The strongest influence of the plate in favour of ICD can be found for the Π-dimer. For a negative reflection coefficient $r_{\mathrm{NR}} = -2$ one can reach an enhancement of the branching ratio $B/B_0 = 2$ at a 2 Å distance from the surface, while a positive reflection coefficient shifts the ratio in favour of Auger to $B/B_0 \approx 1/2$ at the same surface distance. At very close distances the ICD process can be enhanced for $r_{\mathrm{NR}} = -2$ significantly. In this realm however, it would be appropriate to exploit local field methods that resolve the structure

of the specific material by using its density and the polarisability of its constituents as well as take effects from wave function overlap into account.

At arbitrary donor–acceptor distances in the presence of the considered surface with a nonretarded reflection coefficient $r_{\mathrm{NR}} = -2$ we can use the known photoionisation cross section ratio $\sigma_{\mathrm{ICD}}/\sigma_{\mathrm{A}} = 26.76$ to label the contours in Fig. 3.6 accordingly, e.g. when placing the donor at the $B/(\sigma_{\mathrm{ICD}}/\sigma_{\mathrm{A}}) = 10^{-2}$ contour we expect a branching ratio of $B = 0.27$, i.e. the ICD rate with a donor at this position is roughly a quarter of the Auger rate. Depending on the molecule state the 10^{-2} contour can be found closer to or farther from the acceptor's position, see Fig. 3.6.

Lastly, we consider the possible enhancement inside a cavity using the estimation obtained in section 3.3.3. We can determine the necessary Q-factor for each process by determining the defined b-factors, see Eqs. (3.110a) and (3.110b). We find for the He–Ne dimer

$$b_{\mathrm{icd}} = 7.99 \times 10^{-5}, \qquad b_{\mathrm{a}} = 5.78 \times 10^{-6}. \tag{3.117}$$

To achieve a significant effect via a cavity its Q-factor for a transition frequency of $\omega_{nk} = 40.94$ eV hence needs to be at least of the order of $sQ \sim \mathcal{O}(10^4)$ and $\sim \mathcal{O}(10^5)$ for ICD and Auger decay, respectively. For a Q-factor of $sQ = 6.25 \times 10^3$, ICD can be enhanced by a factor of 2.25 inside the cavity, while Auger decay would experience a maximum enhancement of only additional 7%, such that $B/B_0 \approx 2.25$.

3.4. Conclusion

We have presented a novel model for the Auger decay rate based on the dipole approximation by regularising the free space Green's tensor via the size of the involved atomic orbitals. The derived rate formula is a closed expression where tabulated atomic data can be used to evaluate the rate for a given process including the impact of surrounding media via the Green's tensor. We have been able to verify that the introduced Auger radius is dominated by the vacancy orbital size and behaves in fact like an atomic radius. As presented here, our model can be used to include the effects of surrounding macroscopic media if the free-space Auger rate is known. We demonstrated this for the example of Auger decay in doubly excited helium. Free-space Auger rates are available as tabulated data, numerical as well as experimental, for several systems and atoms.

By including Auger decay in this manner into our framework of macroscopic QED we were able to treat ICD and Auger decay simultaneously in systems were they compete with each other. We identified characteristic length scales for each possible decay of an

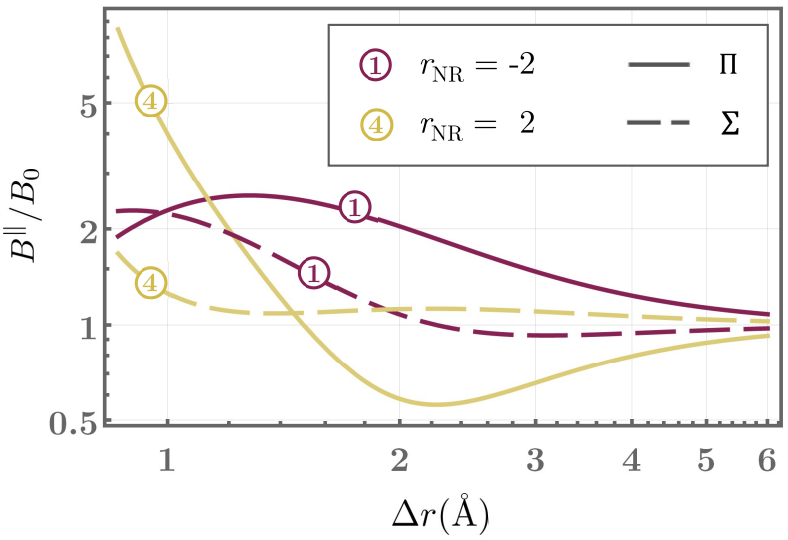

Figure 3.8.: The relative branching ratio when placing a He–Ne dimer with a donor–acceptor distance of 3 Å in front of a surface with a reflection coefficient of $r_{\mathrm{NR}} \in \{-2, 2\}$. The He–Ne dimer can either be in a Π- or Σ-state, leading to different branching ratios in the presence of a surface. The chosen initial state of the doubly-excited helium corresponds to the 23sp+ single-atom state. The characteristic length-scale for the Auger decay in 23sp+ helium is $a = 0.431$Å. We chose $\boldsymbol{r}_{\mathrm{DA}}$ to be parallel to the surface.

excited two–atom system, including radiative decay and by comparison of these length scales deduced the least and most dominant process. We showed that typically Auger decay dominates over ICD.

We have studied the impact of a close-by surface in detail and showed that ICD can be modified more easily by the macroscopic environment compared to Auger due to its larger characteristic length scale. The presented formulas can be used to generally include the impact of a dielectric surface onto each rate. As shown, even such a simple environment may enhance ICD compared to Auger decay significantly. We demonstrated that anisotropic transitions have a significant effect on the environment's influence: for surface-dimer separation and transition dipoles parallel to each other we find the strongest surface induced effect. Furthermore, we have presented a general estimation of the expected enhancement of Auger decay and ICD, respectively in a cavity based on the cavity's Q-factor.

We finally applied the derived formulas to the example of a doubly excited He–Ne dimer. We compared our free space result with rates obtained by *ab initio* methods and illustrated how the derived general formulas may be applied to obtain results for specific systems in the studied environments.

Our framework can alternatively be used to consider cascades of several decays includ-

ing the individual decay channel's interferences with each other. Further studies could lead to a more precise model for the Auger radius. The presented treatment of a cavity was kept general and only based on the cavity's Q-factor. For a specific cavity, the exploited framework can be used to offer a quantitative rate calculation. Additionally, as a side product of our fundamental derivation we obtained a rate equation that might be used with usual *ab initio* methods to go beyond dipole approximation, account for wave function overlap and also include the scattering at macroscopic media.

Chiral Resonance Energy Transfer 4

In this chapter, we derive the RET rate between two chiral molecules. We focus on its power to discriminate between different enantiomers and introduce a degree of discrimination that quantifies this effect. We show that in order to discriminate chiral molecules of unknown handedness one needs to use a chiral object with known handedness. In the first part of this chapter, we focus on the donor molecule to be said object. We show that an appropriate medium that surrounds the system may enhance the degree of discrimination and demonstrate the importance of local field effects for the quantitative prediction of discrimination. The enhancement can lead in theory to optimum discrimination. We derive the necessary requirements for optimum discrimination. In the second part, we introduce a new chiral object, namely a chiral medium. In preparation of this study we derive the local-field correction (LFC) inside a chiral medium, which proves to be more involved than in its achiral counterpart. We derive the degree of discrimination in this conceptionally different setup and discuss the impact of local-field effects. Its name, local-field *correction* is misleading as LFC does not result in a minor correction of quantities obtained without LFC, but may change them significantly. In the case of a chiral medium LFC even results in new terms to the degree of discrimination that dominate the discrimination in certain regimes. We close the study by considering the limit of dilute gases as surrounding medium, where the gas is more appropriately described as individual mediator molecules surrounding donor and acceptor. We consider the transfer and its degree of discrimination in the presence of a single mediator that may itself be chiral. The results presented in this chapter are partially published in Ref. [JF3].

4.1. General chiral resonance energy transfer rate

As shown in section 2.3.7 resonance energy transfer between chiral molecules depends on the relative handedness of donor and acceptor molecule. The discriminatory rate contribution results either in constructive (same handedness) or destructive (opposite handedness) interference terms to the total rate. We first derive the rate for a general setup involving chiral molecules in the framework of macroscopic QED.

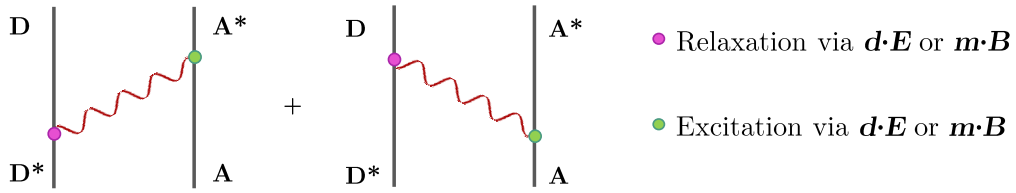

Figure 4.1.: Feynman diagrams for RET between chiral donor (D) and acceptor (A) molecule: the donor is initially excited, its energy is transferred via the field to the acceptor. Each interaction (vertex) can either be carried out via electric or magnetic coupling. The possible intermediate states consist of two conceptionally different states.

The multipolar coupling Hamiltonian (2.170) in long-wavelength approximation is given by

$$\hat{H}_{\mathrm{ia}} = -\sum_{\alpha=\mathrm{D,A}}\sum_{\lambda=\mathrm{e,m}} \hat{\boldsymbol{d}}^{\alpha}_{\lambda}\cdot\hat{\boldsymbol{E}}_{\lambda}(\boldsymbol{r}_{\alpha}) = -\int \mathrm{d}\omega' \sum_{\alpha,\lambda}\left(\hat{\boldsymbol{d}}^{\alpha}_{\lambda}\cdot\hat{\boldsymbol{E}}_{\lambda}(\omega',\boldsymbol{r}_{\alpha}) + \hat{\boldsymbol{d}}^{\alpha}_{\lambda}\cdot\hat{\boldsymbol{E}}^{\dagger}_{\lambda}(\omega',\boldsymbol{r}_{\alpha})\right), \quad (4.1)$$

where we have introduced the dual symmetric notation: $\hat{\boldsymbol{E}}_{\mathrm{m}} = c\hat{\boldsymbol{B}}$ and $\hat{\boldsymbol{d}}_{\mathrm{m}} = \hat{\boldsymbol{m}}/c$, while $\hat{\boldsymbol{E}}_{\mathrm{e}} = \hat{\boldsymbol{E}}$ and $\hat{\boldsymbol{d}}_{\mathrm{e}} = \hat{\boldsymbol{d}}$ and D/A label the donor/acceptor molecule. The rate can be calculated via Fermi's golden rule (2.121) with the transition matrix element in second order,

$$M = \sum_{\phi} \frac{\langle f|\hat{H}_{\mathrm{ia}}|\phi\rangle\,\langle\phi|\hat{H}_{\mathrm{ia}}|i\rangle}{E_i - E_{\phi}}\Big|_{\omega_i=\omega_f}, \quad (4.2)$$

with an initially excited donor, ground-state acceptor and the field in its vacuum state, $|i\rangle = |e,0,\{0\}\rangle$ and a final state where the excitation was transferred to the acceptor, $|f\rangle = |g,1,\{0\}\rangle$, with $\omega_{g/0} < \omega_{e/1}$. We use here e,g to label the donor's excited and ground state and $0,1$ for the states of the acceptor. The intermediate states are given by $|\phi_1\rangle = |g,0,\mathbf{1}_{\lambda'}(\boldsymbol{r}',\omega')\rangle$ and $|\phi_2\rangle = |e,1,\mathbf{1}_{\lambda'}(\boldsymbol{r}',\omega')\rangle$ with energies $E_{\phi_{1/2}} = \hbar\omega_{g/e} + \hbar\omega_{0/1} + \hbar\omega'$. The feynman diagrams of the process are given in Fig. 4.1. The transition matrix element then reads

$$\begin{aligned} M = -\int \mathrm{d}\omega' \int \mathrm{d}^3 r' \sum_{\{\lambda\}} \Big[&\langle g|\hat{\boldsymbol{d}}^{\mathrm{D}}_{\lambda_1}|e\rangle_{\mathrm{D}} \cdot \frac{\langle\{0\}|\hat{\boldsymbol{E}}_{\lambda_1}(\boldsymbol{r}_{\mathrm{D}})|\mathbf{1}'\rangle_{\mathrm{F}}\,\langle\mathbf{1}'|\hat{\boldsymbol{E}}_{\lambda_2}(\boldsymbol{r}_{\mathrm{A}})|\{0\}\rangle_{\mathrm{F}}}{\hbar\omega' + \hbar\omega_{10}} \cdot \langle e|\hat{\boldsymbol{d}}^{\mathrm{A}}_{\lambda_2}|g\rangle_{\mathrm{A}} \\ &+ \langle e|\hat{\boldsymbol{d}}^{\mathrm{A}}_{\lambda_1}|g\rangle_{\mathrm{A}} \cdot \frac{\langle\{0\}|\hat{\boldsymbol{E}}_{\lambda_1}(\boldsymbol{r}_{\mathrm{A}})|\mathbf{1}'\rangle_{\mathrm{F}}\,\langle\mathbf{1}'|\hat{\boldsymbol{E}}_{\lambda_2}(\boldsymbol{r}_{\mathrm{D}})|\{0\}\rangle_{\mathrm{F}}}{\hbar\omega' - \hbar\omega_{eg}} \cdot \langle g|\hat{\boldsymbol{d}}^{\mathrm{D}}_{\lambda_2}|e\rangle_{\mathrm{D}} \Big], \end{aligned} \quad (4.3)$$

where $|\mathbf{1}'\rangle = |\mathbf{1}_{\lambda'}(\omega',\boldsymbol{r}')\rangle$ and $\omega_{xy} = \omega_x - \omega_y$ and because of $\omega_i = \omega_f$ it follows that

$\omega_{eg} = \omega_{10}$. With the relation (see proof in appendix A.2.1),

$$\int \mathrm{d}\omega' \int \mathrm{d}^3 r' \sum_{\lambda'} \frac{\langle \{0\}|\hat{\boldsymbol{E}}_{\lambda_1}(\boldsymbol{r}_\alpha)|\mathbf{1}'\rangle \langle \mathbf{1}'|\hat{\boldsymbol{E}}_{\lambda_2}(\boldsymbol{r}_\beta)|\{0\}\rangle}{\hbar\omega' + \hbar\omega_{10}} = \iint \mathrm{d}\omega_1 \mathrm{d}\omega_2 \frac{\langle \hat{\boldsymbol{E}}_{\lambda_1}(\omega_1, \boldsymbol{r}_\alpha)\hat{\boldsymbol{E}}^\dagger_{\lambda_2}(\omega_2, \boldsymbol{r}_\beta)\rangle}{\hbar\omega_2 + \hbar\omega_{10}}, \quad (4.4)$$

we find

$$\begin{aligned} M = &- \sum_{\lambda_1,\lambda_2} \iint \mathrm{d}\omega_1 \mathrm{d}\omega_2 \, \boldsymbol{d}^{\mathrm{D}}_{\lambda_1} \cdot \frac{\langle \hat{\boldsymbol{E}}_{\lambda_1}(\omega_1, \boldsymbol{r}_{\mathrm{D}})\hat{\boldsymbol{E}}^\dagger_{\lambda_2}(\omega_2, \boldsymbol{r}_{\mathrm{A}})\rangle}{\hbar\omega_2 + \hbar\omega_{10}} \cdot \boldsymbol{d}^{\mathrm{A}}_{\lambda_2} \\ &+ \boldsymbol{d}^{\mathrm{A}}_{\lambda_1} \cdot \frac{\langle \hat{\boldsymbol{E}}_{\lambda_1}(\omega_1, \boldsymbol{r}_{\mathrm{A}})\hat{\boldsymbol{E}}^\dagger_{\lambda_2}(\omega_2, \boldsymbol{r}_{\mathrm{D}})\rangle}{\hbar\omega_2 - \hbar\omega_{10}} \cdot \boldsymbol{d}^{\mathrm{D}}_{\lambda_2} \quad (4.5) \\ = &- \iint \mathrm{d}\omega_1 \mathrm{d}\omega_2 \left(\frac{1}{\hbar\omega_2 - \hbar\omega_{10}} + \frac{1}{\hbar\omega_2 + \hbar\omega_{10}} \right) \\ &\times \boldsymbol{d}^{\mathrm{A}}_{\lambda_1} \cdot \left[\langle \hat{\boldsymbol{E}}_e(\omega_1, \boldsymbol{r}_{\mathrm{A}})\hat{\boldsymbol{E}}^\dagger_e(\omega_2, \boldsymbol{r}_{\mathrm{D}})\rangle + \langle \hat{\boldsymbol{E}}_m(\omega_1, \boldsymbol{r}_{\mathrm{A}})\hat{\boldsymbol{E}}^\dagger_m(\omega_2, \boldsymbol{r}_{\mathrm{D}})\rangle \right] \cdot \boldsymbol{d}^{\mathrm{D}}_{\lambda_2} \\ &- \iint \mathrm{d}\omega_1 \mathrm{d}\omega_2 \left(\frac{1}{\hbar\omega_2 - \hbar\omega_{10}} - \frac{1}{\hbar\omega_2 + \hbar\omega_{10}} \right) \\ &\times \boldsymbol{d}^{\mathrm{A}}_{\lambda_1} \cdot \left[\langle \hat{\boldsymbol{E}}_e(\omega_1, \boldsymbol{r}_{\mathrm{A}})\hat{\boldsymbol{E}}^\dagger_m(\omega_2, \boldsymbol{r}_{\mathrm{D}})\rangle + \langle \hat{\boldsymbol{E}}_m(\omega_1, \boldsymbol{r}_{\mathrm{A}})\hat{\boldsymbol{E}}^\dagger_e(\omega_2, \boldsymbol{r}_{\mathrm{D}})\rangle \right] \cdot \boldsymbol{d}^{\mathrm{D}}_{\lambda_2}, \quad (4.6) \end{aligned}$$

where we have defined the transition dipole moment for the acceptor $\boldsymbol{d}^{\mathrm{A}}_\lambda = \langle 1|\hat{\boldsymbol{d}}^{\mathrm{A}}_\lambda|0\rangle$, which describes an upward transition and the donor $\boldsymbol{d}^{\mathrm{D}}_\lambda = \langle g|\hat{\boldsymbol{d}}^{\mathrm{A}}_\lambda|e\rangle$, which describes a downward transition and we used that for any tensor $\mathbb{M}$ one has $\boldsymbol{v} \cdot \mathbb{M} \cdot \boldsymbol{w} = \boldsymbol{w} \cdot \mathbb{M}^T \cdot \boldsymbol{v}$ and

$$\langle \boldsymbol{E}_\lambda(\boldsymbol{r}_1)\boldsymbol{E}^\dagger_\lambda(\boldsymbol{r}_2)\rangle^T = \langle \boldsymbol{E}_\lambda(\boldsymbol{r}_2)\boldsymbol{E}^\dagger_\lambda(\boldsymbol{r}_1)\rangle, \quad (4.7)$$

$$\langle \boldsymbol{E}_\lambda(\boldsymbol{r}_1)\boldsymbol{E}^\dagger_{\lambda'}(\boldsymbol{r}_2)\rangle^T = -\langle \boldsymbol{E}_{\lambda'}(\boldsymbol{r}_2)\boldsymbol{E}^\dagger_\lambda(\boldsymbol{r}_1)\rangle, \quad \text{for } \lambda \neq \lambda' \quad (4.8)$$

to summarize the terms. The vacuum correlation functions are calculated and given explicitly in the appendix, see Eqs. (A.18)–(A.21). Inserting them into Eq. (4.6) leads to

$$M = \frac{\mu_0 c^2}{\pi} \sum_{\lambda_1\lambda_2} \int \mathrm{d}\omega \left(\frac{1}{\omega - \omega_{10}} \pm \frac{1}{\omega + \omega_{10}} \right) \boldsymbol{d}^{\mathrm{A}}_{\lambda_1} \cdot [\mathrm{Im}\mathbb{G}(\boldsymbol{r}_{\mathrm{A}}, \boldsymbol{r}_{\mathrm{D}}, \omega)]_{\lambda_1\lambda_2} \cdot \boldsymbol{d}^{\mathrm{D}}_{\lambda_2}, \quad (4.9)$$

where the positive sign applies for $\lambda_1 = \lambda_2$ terms, while the negative sign applies for

$\lambda_1 \neq \lambda_2$ and we have used the shorthand notation:

$$[\mathrm{Im}\mathbb{G}(\boldsymbol{r}_\mathrm{A}, \boldsymbol{r}_\mathrm{D}, \omega)]_{\lambda_1\lambda_2} = \begin{cases} -\frac{\omega^2}{c^2}\mathrm{Im}\mathbb{G}(\boldsymbol{r}_\mathrm{A}, \boldsymbol{r}_\mathrm{D}, \omega) & (\lambda_1\lambda_2) = (\mathrm{e},\mathrm{e}) \\ \mathrm{i}\frac{\omega}{c}\mathrm{Im}\mathbb{G}(\boldsymbol{r}_\mathrm{A}, \boldsymbol{r}_\mathrm{D}, \omega) \times \nabla_\mathrm{D} & (\lambda_1, \lambda_2) = (\mathrm{e},\mathrm{m}) \\ \mathrm{i}\frac{\omega}{c}\nabla_\mathrm{A} \times \mathrm{Im}\mathbb{G}(\boldsymbol{r}_\mathrm{A}, \boldsymbol{r}_\mathrm{D}, \omega) & (\lambda_1, \lambda_2) = (\mathrm{m},\mathrm{e}) \\ \nabla_\mathrm{A} \times \mathrm{Im}\mathbb{G}(\boldsymbol{r}_\mathrm{A}, \boldsymbol{r}_\mathrm{D}, \omega) \times \nabla_\mathrm{D} & (\lambda_1, \lambda_2) = (\mathrm{m},\mathrm{m}) \end{cases} \tag{4.10}$$

The frequency pole-integrals in Eq. (4.9) are of the form:

$$\int \mathrm{d}\omega \left(\frac{f(\omega)}{\omega - \omega_{10}} + \frac{f(-\omega)}{\omega + \omega_{10}} \right) \mathrm{Im}\mathbb{G} \qquad \text{with:} \quad f(\omega) = \omega^n, \quad n \in \{0, 1, 2\}\,. \tag{4.11}$$

The first term of the integrand contains a pole on the real axis and hence divergences. However, the pole stems from the time-independent perturbation treatment, revisiting its derivation one can regularise the pole and finds (see proof in appendix A.4):

$$\int \mathrm{d}\omega \left(\frac{f(\omega)}{\omega - (\omega_{10} + \mathrm{i}\epsilon)} + \frac{f(-\omega)}{\omega + \omega_{10}} \right) \mathrm{Im}\mathbb{G} = \pi f(\omega_{10})\mathbb{G}(\omega_{10})\,. \tag{4.12}$$

This finally leads to the dual transition matrix elements

$$M = \sum_{\lambda_1\lambda_2} M_{\lambda_1\lambda_2}\,, \tag{4.13}$$

$$M_{\lambda_1\lambda_2} = \mu_0 c^2 \boldsymbol{d}^\mathrm{A}_{\lambda_1} \cdot \mathbb{G}_{\lambda_1\lambda_2}(\boldsymbol{r}_\mathrm{A}, \boldsymbol{r}_\mathrm{D}, \omega_{10}) \cdot \boldsymbol{d}^\mathrm{D}_{\lambda_2}\,, \tag{4.14}$$

with the dual Green's tensor defined as:

$$\mathbb{G}_{\lambda_1\lambda_2}(\boldsymbol{r}_\mathrm{A}, \boldsymbol{r}_\mathrm{D}, \omega) = \begin{cases} -\frac{\omega^2}{c^2}\mathbb{G}(\boldsymbol{r}_\mathrm{A}, \boldsymbol{r}_\mathrm{D}, \omega) & (\lambda_1\lambda_2) = (\mathrm{e},\mathrm{e}) \\ \mathrm{i}\frac{\omega}{c}\mathbb{G}(\boldsymbol{r}_\mathrm{A}, \boldsymbol{r}_\mathrm{D}, \omega) \times \nabla_\mathrm{D} & (\lambda_1, \lambda_2) = (\mathrm{e},\mathrm{m}) \\ \mathrm{i}\frac{\omega}{c}\nabla_\mathrm{A} \times \mathbb{G}(\boldsymbol{r}_\mathrm{A}, \boldsymbol{r}_\mathrm{D}, \omega) & (\lambda_1, \lambda_2) = (\mathrm{m},\mathrm{e}) \\ \nabla_\mathrm{A} \times \mathbb{G}(\boldsymbol{r}_\mathrm{A}, \boldsymbol{r}_\mathrm{D}, \omega) \times \nabla_\mathrm{D} & (\lambda_1, \lambda_2) = (\mathrm{m},\mathrm{m}) \end{cases} \tag{4.15}$$

The total rate is hence given by

$$\Gamma = \sum \Gamma_{\lambda_1\lambda_2\lambda_3\lambda_4}\,, \tag{4.16}$$

$$\Gamma_{\lambda_1\lambda_2\lambda_3\lambda_4} = \frac{2\pi\mu_0^2\rho}{\hbar^2} \left(\boldsymbol{d}^\mathrm{A}_{\lambda_1} \cdot \mathbb{G}_{\lambda_1\lambda_4}(\boldsymbol{r}_\mathrm{A}, \boldsymbol{r}_\mathrm{D}, \omega_{10}) \cdot \boldsymbol{d}^\mathrm{D}_{\lambda_4} \right) \left(\boldsymbol{d}^\mathrm{A}_{\lambda_2} \cdot \mathbb{G}_{\lambda_2\lambda_3}(\boldsymbol{r}_\mathrm{A}, \boldsymbol{r}_\mathrm{D}, \omega_{10}) \cdot \boldsymbol{d}^\mathrm{D}_{\lambda_3} \right)^*\,, \tag{4.17}$$

where $\rho = \rho(\omega_{10})$ is the density of final states. For isotropic transition dipoles we may

use that on average: $\boldsymbol{d}_1 \otimes \boldsymbol{d}_2 = \boldsymbol{d}_1 \cdot \boldsymbol{d}_2 \mathbb{I}/3$. This simplifies the rate to

$$\begin{aligned}\Gamma_{\lambda_1\lambda_2\lambda_3\lambda_4} &= \frac{2\pi\mu_0^2\rho}{9\hbar^2}(\boldsymbol{d}^{\mathrm{A}}_{\lambda_1}\cdot\boldsymbol{d}^{\mathrm{A}*}_{\lambda_2})(\boldsymbol{d}^{\mathrm{D}*}_{\lambda_3}\cdot\boldsymbol{d}^{\mathrm{D}}_{\lambda_4})\,\mathrm{Tr}\left[\mathbb{G}_{\lambda_1\lambda_4}(\boldsymbol{r}_{\mathrm{A}},\boldsymbol{r}_{\mathrm{D}},\omega_{10})\cdot\mathbb{G}^{*T}_{\lambda_2\lambda_3}(\boldsymbol{r}_{\mathrm{A}},\boldsymbol{r}_{\mathrm{D}},\omega_{10})\right]\\ &= \frac{2\pi c^4}{\omega_{10}^4}\sigma^{\mathrm{A}}_{\lambda_1\lambda_2}\gamma^{\mathrm{D}}_{\lambda_3\lambda_4}\,\mathrm{Tr}\left[\mathbb{G}_{\lambda_1\lambda_4}(\boldsymbol{r}_{\mathrm{A}},\boldsymbol{r}_{\mathrm{D}},\omega_{10})\cdot\mathbb{G}^{*T}_{\lambda_2\lambda_3}(\boldsymbol{r}_{\mathrm{A}},\boldsymbol{r}_{\mathrm{D}},\omega_{10})\right]\,,\end{aligned} \tag{4.18}$$

with

$$\sigma_{\lambda_1\lambda_2} = \frac{\pi\omega_{10}\rho}{3\varepsilon_0 c\hbar}\boldsymbol{d}^{\mathrm{A}}_{\lambda_1}\cdot\boldsymbol{d}^{\mathrm{A}*}_{\lambda_2} \qquad \text{and} \qquad \gamma_{\lambda_1\lambda_2} = \frac{\omega_{10}^3}{3\pi\varepsilon_0 c^3\hbar}\boldsymbol{d}^{\mathrm{D}*}_{\lambda_1}\cdot\boldsymbol{d}^{\mathrm{D}}_{\lambda_2}\,, \tag{4.19}$$

which give for $\lambda_1 = \lambda_2$ the (electric/magnetic) photoabsorption cross section and spontaneous decay rate, respectively. For chiral molecules the mixed electric-magnetic quantities with $\lambda_1 \neq \lambda_2$ contain the so-called rotatory strength,

$$R_{10} = \mathrm{Im}[\langle 0|\hat{\boldsymbol{d}}|1\rangle\cdot\langle 1|\hat{\boldsymbol{m}}|0\rangle]\,. \tag{4.20}$$

In our notational convention, where $\boldsymbol{d}^{\mathrm{D}}_{\lambda} = \langle g|\hat{\boldsymbol{d}}_{\lambda}|e\rangle$ describes a downward transition and $\boldsymbol{d}^{\mathrm{A}}_{\lambda} = \langle 1|\hat{\boldsymbol{d}}_{\lambda}|0\rangle$ an excitation, the respective rotatory strengths are given by

$$R_{\mathrm{D}}/c = \mathrm{Im}[\boldsymbol{d}^{\mathrm{D}}_{\mathrm{e}}\cdot\boldsymbol{d}^{\mathrm{D}*}_{\mathrm{m}}] = -\mathrm{i}\boldsymbol{d}^{\mathrm{D}}_{\mathrm{e}}\cdot\boldsymbol{d}^{\mathrm{D}*}_{\mathrm{m}} \qquad \text{and} \qquad R_{\mathrm{A}}/c = \mathrm{i}\boldsymbol{d}^{\mathrm{A}}_{\mathrm{e}}\cdot\boldsymbol{d}^{\mathrm{A}*}_{\mathrm{m}}\,, \tag{4.21}$$

where we have assumed that the electric transition dipoles are purely real while the magnetic ones are purely imaginary. The sign of the rotatory strength depends on the molecule's handedness.

Here, we adapted a dual notation to simplify the expressions. The notation mirrors the discrete duality symmetry that is fulfilled in dielectric media as well as reciprocal, chiral media, as shown in section 2.1.5. When coupling the fields to a magnetic dipole inside a medium, duality symmetry appears to be broken without physical reasons [9]. The symmetry can be restored by considering local-field corrections via one of the available models, for example the Onsager real cavity model that was introduced in section 2.1.7.

With this we have derived the total RET rate (4.16) between two chiral molecules in arbitrary absorbing and dispersing media, given by the sum over its dual rate contributions (4.18). We may now apply the theory to different set-ups, including the case of an acceptor with unknown handedness in free space, magentodielectric and chiral media.

4.2. Local-field corrected Green's tensor in a chiral medium

As preparation for section 4.3.3, we need to work out the LFC for a chiral medium. There exist several models for LFC. We choose here the Onsager real cavity model. All available models have in common that the interaction points are placed inside free space instead of the macroscopic medium. In Onsager real cavity model both, source and absorption point are modelled inside infinitesimal vacuum spheres. The geometry of this problem does not allow for an analytical derivation for both points at once. In magneto-electric media this obstacle is circumvented by the convenient result that the correction of a single point leads to a mere correction factor, which is different for electric and magnetic interactions. Hence one can conclude that the product of the respective factors results in the correct LFC for magneto-electrics, see section 2.1.7. For chiral media we start with correcting one interaction point as well and will see that the necessary correction for a single point will not result into a factor but is more involved. We present a method for constructing the Green's tensor based on the multiplication of transmission and reflection matrices. This method helps us then to obtain the correction of both, source and absorption point simultaneously. We finally show its validity for a special example, where the specific geometry allows for an exact calculation for comparison.

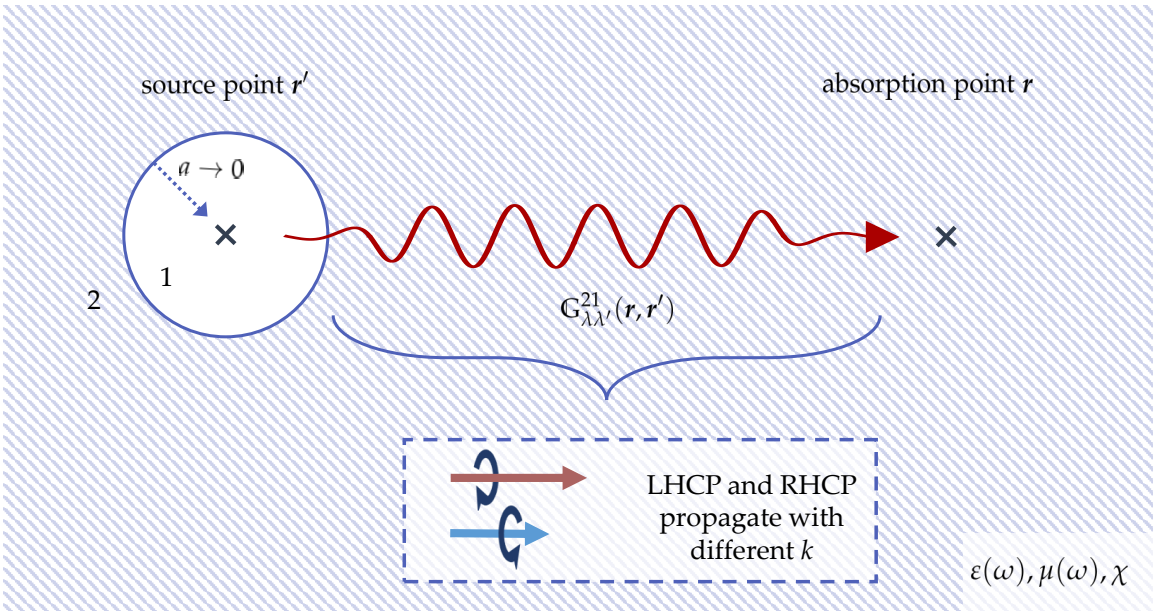

Figure 4.2.: Scheme for local-field correction of the source point. The source point r' is placed inside a free space sphere with radius a (region 1), surrounded by chiral medium (region 2). We solve the transmitting Green's tensor for magnetic and electric interactions inside the free-space sphere. Inside the chiral medium left- and right-handed circularly polarised (LHCP/RHCP) light propagates differently.

4.2.1. Correction of a single point

We first derive the Green's tensor for a vacuum sphere in a chiral bulk medium, where the source point sits in the center of said sphere, see Fig. 4.2, analogously to the derivation in Ref. [169]. The referenced paper uses slightly different conventions: $\xi_c = \chi/\mu$, $\varepsilon' = \varepsilon - \chi^2/\mu$ and the propagator $\mathbf{\Gamma}_c = \mathbb{G}/\mu$. The limit of infinitesimal free-space sphere radius reveals then the Green's tensor including LFC of the source point. The derivation hence follows the same steps as the derivation of LFC for a magneto-electric medium, see section 2.1.7.

In our chosen convention the constitutive relations in a chiral medium are given by Eqs. (2.70) and (2.71) which lead to the Helmholtz equation (2.73) for a chiral medium. To solve it we choose as a basis set a symmetric and antisymmetric combination of the spherical vector wave functions $\boldsymbol{M}_{\substack{\mathrm{e}\\\mathrm{o}}mn}(\boldsymbol{r})$ and $\boldsymbol{N}_{\substack{\mathrm{e}\\\mathrm{o}}mn}(\boldsymbol{r})$, which read

$$\boldsymbol{V}_{\substack{\mathrm{e}\\\mathrm{o}}mn}(\boldsymbol{r},k) = \frac{\boldsymbol{M}_{\substack{\mathrm{e}\\\mathrm{o}}mn}(\boldsymbol{r}) + \boldsymbol{N}_{\substack{\mathrm{e}\\\mathrm{o}}mn}(\boldsymbol{r})}{\sqrt{2}}\,, \tag{4.22}$$

$$\boldsymbol{W}_{\substack{\mathrm{e}\\\mathrm{o}}mn}(\boldsymbol{r},k) = \frac{\boldsymbol{M}_{\substack{\mathrm{e}\\\mathrm{o}}mn}(\boldsymbol{r}) - \boldsymbol{N}_{\substack{\mathrm{e}\\\mathrm{o}}mn}(\boldsymbol{r})}{\sqrt{2}}\,, \tag{4.23}$$

where e,o denote here even and odd vector wave functions, and should not be confused with $\lambda \in \{\mathrm{e},\mathrm{m}\}$ when denoting electric and magnetic components when using dual symmetric notations. Their full expressions are given in the appendix A.3.2. They form an orthogonal basis set and by construction fulfil

$$\nabla \times \boldsymbol{V}_{\substack{\mathrm{e}\\\mathrm{o}}mn}(\boldsymbol{r},k) = k\boldsymbol{V}_{\substack{\mathrm{e}\\\mathrm{o}}mn}(\boldsymbol{r},k), \qquad \nabla \times \boldsymbol{W}_{\substack{\mathrm{e}\\\mathrm{o}}mn}(\boldsymbol{r},k) = -k\boldsymbol{W}_{\substack{\mathrm{e}\\\mathrm{o}}mn}(\boldsymbol{r},k)\,. \tag{4.24}$$

With this, we find for the chiral bulk Green's tensor,

$$\begin{aligned}\mathbb{G}^{(0)}(\boldsymbol{r},\boldsymbol{r}') = \frac{\mathrm{i}\mu}{2\pi(k_+ + k_-)} \sum_n^\infty \sum_m^n \Big[(2-\delta_{m0})\frac{(2n+1)(n-m)!}{n(n+1)(n+m)!} \\ \times \left(k_+^2 \boldsymbol{V}^{(1)}_{\substack{\mathrm{e}\\\mathrm{o}}mn}(\boldsymbol{r},k_+)\boldsymbol{V}_{\substack{\mathrm{e}\\\mathrm{o}}mn}(\boldsymbol{r}',k_+) + k_-^2 \boldsymbol{W}^{(1)}_{\substack{\mathrm{e}\\\mathrm{o}}mn}(\boldsymbol{r},k_-)\boldsymbol{W}_{\substack{\mathrm{e}\\\mathrm{o}}mn}(\boldsymbol{r}',k_-)\right)\Big]\,,\end{aligned} \tag{4.25}$$

where $|\boldsymbol{r}| > |\boldsymbol{r}'|$ and the superscript (1) on the vector functions indicates the substitution of the spherical Bessel functions j_n with the spherical Hankel functions of the first kind $h_n^{(1)}$ inside the vector wave functions definitions (A.57) and (A.59) and we have defined

$$k_\pm = \sqrt{\epsilon\mu}\omega \pm \omega\chi\,. \tag{4.26}$$

Note that the free-space Green's tensor (A.32) can be obtained by setting χ to 0.

The chiral bulk Green's tensor is invariant under translation. We may hence assume

the source to be at the origin $\boldsymbol{r}' = \boldsymbol{0}$ without loss of generality to obtain a more compact result,

$$\mathbb{G}^{(0)}(\boldsymbol{r}, \boldsymbol{r}' = \boldsymbol{0}) = \mathbb{G}^{(vv)}(\boldsymbol{r}) + \mathbb{G}^{(ww)}(\boldsymbol{r}), \tag{4.27}$$

$$\mathbb{G}^{(vv)}(\boldsymbol{r}) = \frac{\mathrm{i}3\mu}{4\pi(k_+ + k_-)} \sum_{m=0}^{1} k_+^2 \boldsymbol{V}^{(1)}_{\substack{\mathrm{e}\\\mathrm{o}}m1}(\boldsymbol{r}, k_+) \boldsymbol{V}_{\substack{\mathrm{e}\\\mathrm{o}}m1}(\boldsymbol{0}) \tag{4.28}$$

$$\mathbb{G}^{(ww)}(\boldsymbol{r}) = \frac{\mathrm{i}3\mu}{4\pi(k_+ + k_-)} \sum_{m=0}^{1} k_-^2 \boldsymbol{W}^{(1)}_{\substack{\mathrm{e}\\\mathrm{o}}m1}(\boldsymbol{r}, k_-) \boldsymbol{W}_{\substack{\mathrm{e}\\\mathrm{o}}m1}(\boldsymbol{0}), \tag{4.29}$$

where we used that $\boldsymbol{V}/\boldsymbol{W}_{\substack{\mathrm{e}\\\mathrm{o}}mn}(\boldsymbol{r}' = 0) = \boldsymbol{0}, \forall n > 1$ and introduced the Green's tensors for left- and right-handed circularly polarised light $\mathbb{G}^{(vv)}$ and $\mathbb{G}^{(ww)}$. In this form of the Green's tensor it is obvious that inside the medium, differently circularly polarised light exhibits different wave numbers $k_\pm$.

We may give the chiral bulk Green's tensor in a dual notation. According to the definition given by Eq. (4.15) we find

$$\mathbb{G}^{(0)}_{\lambda\lambda'}(\boldsymbol{r}, \boldsymbol{r}' = \boldsymbol{0}) = \mathbb{G}^{(vv)}_{\lambda\lambda'}(\boldsymbol{r}) + \mathbb{G}^{(ww)}_{\lambda\lambda'}(\boldsymbol{r}), \tag{4.30}$$

with $\lambda, \lambda' \in \{\mathrm{e}, \mathrm{m}\}$ and

$$\mathbb{G}^{(vv)/(ww)}_{\lambda_1\lambda_2} = \begin{cases} -\dfrac{\omega^2}{c^2}\mathbb{G}^{(vv)/(ww)} & (\lambda_1\lambda_2) = (\mathrm{e},\mathrm{e}) \\ \mp\mathrm{i}\dfrac{k_\pm\omega}{c}\mathbb{G}^{(vv)/(ww)} & (\lambda_1,\lambda_2) = (\mathrm{e},\mathrm{m}) \\ \pm\mathrm{i}\dfrac{k_\pm\omega}{c}\mathbb{G}^{(vv)/(ww)} & (\lambda_1,\lambda_2) = (\mathrm{m},\mathrm{e}) \\ k_\pm^2\mathbb{G}^{(vv)/(ww)} & (\lambda_1,\lambda_2) = (\mathrm{m},\mathrm{m}) \end{cases}, \tag{4.31}$$

where we omitted the position argument for readability and evaluated the curls with Eqs. (4.24).

Next, we introduce a free-space sphere around the origin with radius a. We are then interested in the propagation from a source situated at $\boldsymbol{r}'$ inside the sphere to a point $\boldsymbol{r}$ outside of the sphere, i.e. into the chiral medium, see Fig. 4.2. The Green's tensor has to fulfil the boundary conditions:

$$\boldsymbol{e}_r \times \mathbb{G}(\boldsymbol{r} \to \boldsymbol{a}^-, \boldsymbol{r}') = \boldsymbol{e}_r \times \mathbb{G}(\boldsymbol{r} \to \boldsymbol{a}^+, \boldsymbol{r}'), \tag{4.32}$$

$$\boldsymbol{e}_r \times \nabla \times \mathbb{G}(\boldsymbol{r} \to \boldsymbol{a}^-, \boldsymbol{r}') = -\frac{\chi\omega}{\mu}\boldsymbol{e}_r \times \mathbb{G}(\boldsymbol{r} \to \boldsymbol{a}^+, \boldsymbol{r}') + \frac{1}{\mu}\boldsymbol{e}_r \times \nabla \times \mathbb{G}(\boldsymbol{r} \to \boldsymbol{a}^+, \boldsymbol{r}'), \tag{4.33}$$

where $\boldsymbol{a}$ is an arbitrary vector pointing to the sphere's surface, i.e. $|\boldsymbol{a}| = a$. For the source

point $\boldsymbol{r}'$ inside the sphere we choose the ansatz:

$$r < a: \quad \mathbb{G}^{11}(\boldsymbol{r},\boldsymbol{r}') = \mathbb{G}^{(0)}_{\mathrm{vac}} + \frac{\mathrm{i}}{4\pi k_0}\sum_n^\infty\sum_m^n (2-\delta_{m0})\frac{(2n+1)(n-m)!}{n(n+1)(n+m)!} \times \Big\{ \left[c_n^v \boldsymbol{V}_{\substack{\mathrm{e}\\\mathrm{o}}mn}(\boldsymbol{r},k_0) + c_n^w \boldsymbol{W}_{\substack{\mathrm{e}\\\mathrm{o}}mn}(\boldsymbol{r},k_0)\right]\boldsymbol{V}_{\substack{\mathrm{e}\\\mathrm{o}}mn}(\boldsymbol{r}',k_0) + \left[d_n^v \boldsymbol{V}^{(1)}_{\substack{\mathrm{e}\\\mathrm{o}}mn}(\boldsymbol{r},k_0) + d_n^w \boldsymbol{W}^{(1)}_{\substack{\mathrm{e}\\\mathrm{o}}mn}(\boldsymbol{r},k_0)\right]\boldsymbol{W}_{\substack{\mathrm{e}\\\mathrm{o}}mn}(\boldsymbol{r}',k_0)\Big\}, \tag{4.34}$$

$$r > a: \quad \mathbb{G}^{21}(\boldsymbol{r},\boldsymbol{r}') = \frac{\mathrm{i}}{4\pi k_0}\sum_n^\infty\sum_m^n (2-\delta_{m0})\frac{(2n+1)(n-m)!}{n(n+1)(n+m)!} \times \Big\{ \left[a_n^v \boldsymbol{V}^{(1)}_{\substack{\mathrm{e}\\\mathrm{o}}mn}(\boldsymbol{r},k_+) + a_n^w \boldsymbol{W}^{(1)}_{\substack{\mathrm{e}\\\mathrm{o}}mn}(\boldsymbol{r},k_-)\right]\boldsymbol{V}_{\substack{\mathrm{e}\\\mathrm{o}}mn}(\boldsymbol{r}',k_0) + \left[b_n^v \boldsymbol{V}^{(1)}_{\substack{\mathrm{e}\\\mathrm{o}}mn}(\boldsymbol{r},k_+) + b_n^w \boldsymbol{W}^{(1)}_{\substack{\mathrm{e}\\\mathrm{o}}mn}(\boldsymbol{r},k_-)\right]\boldsymbol{W}_{\substack{\mathrm{e}\\\mathrm{o}}mn}(\boldsymbol{r}',k_0)\Big\}, \tag{4.35}$$

where $k_0 = \omega/c$ is the field's vacuum wave number, $\mathbb{G}^{(0)}_{\mathrm{vac}}$ is the free-space Green's tensor and the superscripts in $\mathbb{G}^{ij}$ denote the region of the source (j) and region of the absorption (i) point as labelled in Fig. 4.2. The full solution of these boundary conditions is given in the appendix, see section A.3.2. We obtain the local-field correction for the source point by considering the limit of vanishing sphere radius, i.e. $a \to 0$. In this limit the coefficients for the transmitting Green's tensor (4.35) become

$$\lim_{a\to 0} a_v^n = a_v = \frac{1}{D_k} 3k_+^3(2k_- + k)(1+l), \tag{4.36}$$

$$\lim_{a\to 0} a_w^n = a_w = \frac{1}{D_k} 3k_-^3(k - 2k_+)(l-1), \tag{4.37}$$

$$\lim_{a\to 0} b_v^n = b_v = \frac{1}{D_k} 3k_+^3(k - 2k_-)(l-1), \tag{4.38}$$

$$\lim_{a\to 0} b_w^n = b_w = \frac{1}{D_k} 3k_-^3(2k_+ + k)(1+l), \tag{4.39}$$

$$D = 2(4k_+k_-l + k^2 l + (k_+ + k_-)k(1+l^2)), \qquad l = \frac{\sqrt{\varepsilon\mu}}{\mu}. \tag{4.40}$$

Comparing the transmitting Green's tensor to the chiral bulk Green's tensor (4.27) and casting it into a similar form yields

$$\mathbb{G}^{21}(\boldsymbol{r},0) = \frac{\mathrm{i}\mu}{2\pi(k_+ + k_-)}\sum_{m=0}^{1}\frac{3}{2}\left(c_{ev}k_+^2 \boldsymbol{V}^{(1)}_{\substack{\mathrm{e}\\\mathrm{o}}m1}(\boldsymbol{r},k_+)\boldsymbol{V}_{\substack{\mathrm{e}\\\mathrm{o}}m1}(0) + c_{ew}k_-^2 \boldsymbol{W}^{(1)}_{\substack{\mathrm{e}\\\mathrm{o}}m1}(\boldsymbol{r},k_-)\boldsymbol{W}_{\substack{\mathrm{e}\\\mathrm{o}}m1}(0)\right), \tag{4.41}$$

where we have exploited that for $\boldsymbol{r}' = 0 \Rightarrow \boldsymbol{W}(\boldsymbol{r}') = -\boldsymbol{V}(\boldsymbol{r}')$. The introduced correction

factors are given by

$$c_{\mathrm{e}v} = \frac{[a_v - b_v](k_+ + k_-)}{2\mu k k_+^2} = \frac{3(n_r + \chi)(-2\mu\chi + 2\mu n_r + n_r)}{\mu\left(2\mu - 4\chi^2 + 1\right) + (4\mu + 2)n_r^2}\,, \tag{4.42}$$

$$c_{\mathrm{e}w} = \frac{[b_w - a_w](k_+ + k_-)}{2\mu k k_-^2} = c_{\mathrm{e}v}\big|_{\chi\to-\chi}\,, \tag{4.43}$$

with $n_r = \sqrt{\varepsilon\mu}$ being the refractive index. These give the known corrections for a dielectric medium, see section 2.1.7 when setting $\chi = 0$,

$$c_{\mathrm{e}v}\big|_{\chi\to0} = c_{\mathrm{e}w}\big|_{\chi\to0} = c_{\mathrm{e}} = \frac{3\varepsilon}{1 + 2\varepsilon}\,. \tag{4.44}$$

Magnetic interactions at the source point are governed by the curl of $\mathbb{G}$ acting on $\boldsymbol{r}'$, see Eq. (4.15). The source point curl of the transmitting Green's tensor $\mathbb{G}^{21}(\boldsymbol{r}, \boldsymbol{r}')$ at the source point $\boldsymbol{r}' = \boldsymbol{0}$ is given by

$$\mathbb{G}^{21}(\boldsymbol{r}, \boldsymbol{r}') \times \nabla'\Big|_{\boldsymbol{r}'=0} = \frac{\mathrm{i}}{4\pi}\sum_{m=0}^{1}\frac{3}{2}\Big(- c_{\mathrm{m}v}k_+^3 \boldsymbol{V}^{(1)}(\boldsymbol{r}, k_+)\boldsymbol{V}(0) + c_{\mathrm{m}w}k_-^3 \boldsymbol{W}^{(1)}(\boldsymbol{r}, k_-)\boldsymbol{W}(0)\Big)\,, \tag{4.45}$$

where we have used Eqs. (4.24) and again made use of $\boldsymbol{V}(0) = -\boldsymbol{W}(0)$ to reorder the terms and recast the expression into a similar form as the chiral bulk Green's tensor. The introduced magnetic correcting factors are given by

$$c_{\mathrm{m}v} = (a_v + b_v)\frac{k_+ + k_-}{2\mu k_+^3} = \frac{3\left(\mu + 2n_r^2 - 2n_r\chi\right)}{\mu\left(2\mu - 4\chi^2 + 1\right) + (4\mu + 2)n_r^2}\,, \tag{4.46}$$

$$c_{\mathrm{m}w} = (a_w + b_w)\frac{k_+ + k_-}{2\mu k_-^3} = c_{\mathrm{m}v}\big|_{\chi\to-\chi}\,, \tag{4.47}$$

where we can again find the known magentic correction, see section 2.1.7 for achiral media,

$$c_{\mathrm{m}v}\Big|_{\chi=0} = c_{\mathrm{m}w}\Big|_{\chi=0} = c_{\mathrm{m}} = \frac{3}{1 + 2\mu}\,. \tag{4.48}$$

In the limit of small χ we can write the correction terms as

$$c_{\mathrm{e}v} \approx c_{\mathrm{e}} + \chi c_{\mathrm{e}\chi}\,, \qquad c_{\mathrm{e}w} \approx c_{\mathrm{e}} - \chi c_{\mathrm{e}\chi}\,, \qquad c_{\mathrm{e}\chi} = \frac{c_{\mathrm{e}}}{n_r(1 + 2\mu)}\,, \tag{4.49}$$

$$c_{\mathrm{m}v} \approx c_{\mathrm{m}} - \chi c_{\mathrm{m}\chi}\,, \qquad c_{\mathrm{m}w} \approx c_{\mathrm{m}} + \chi c_{\mathrm{m}\chi}\,, \qquad c_{\mathrm{m}\chi} = \frac{2n_r c_{\mathrm{m}}}{\mu + 2n_r^2}\,, \tag{4.50}$$

where it is interesting to note that the terms linear in χ are almost the same for $c_{\mathrm{e/m}}$ and

are closely related to the product of the nonchiral corrections,

$$c_{\mathrm{e}\chi} = \frac{1}{2} c_{\mathrm{m}\chi} = \frac{1}{3n_r} c_{\mathrm{e}} c_{\mathrm{m}} \,. \tag{4.51}$$

In dual notation the single-point corrected Green's tensor can now be given by

$$\mathbb{G}^{(\mathrm{single})}_{\lambda\mathrm{e}} = c_{\mathrm{e}v}\mathbb{G}^{(vv)}_{\lambda\mathrm{e}} + c_{\mathrm{e}w}\mathbb{G}^{(ww)}_{\lambda\mathrm{e}}\,, \tag{4.52}$$

$$\mathbb{G}^{(\mathrm{single})}_{\lambda\mathrm{m}} = c_{\mathrm{m}v}\mathbb{G}^{(vv)}_{\lambda\mathrm{m}} + c_{\mathrm{m}w}\mathbb{G}^{(ww)}_{\lambda\mathrm{m}}\,, \tag{4.53}$$

with $\lambda \in \{\mathrm{e},\mathrm{m}\}$ and the $\mathbb{G}^{(vv)/(ww)}_{\lambda\lambda'}$ are defined by Eqs. (4.31). The same corrections are found when correcting solely around the absorption point analogously. This is in agreement with $\mathbb{G}^T(\boldsymbol{r},\boldsymbol{r}') = \mathbb{G}(\boldsymbol{r}',\boldsymbol{r})$ for any Green's tensor in reciprocal media.

We have followed the analogous steps as were done for magneto-electric media, see section 2.1.7. For achiral media we find $c_{\lambda v} = c_{\lambda w} = c_\lambda$ and hence obtain one overall correction factor applied to the bulk Green's tensor. The simplicity of this result enables one then to conclude the simultaneous correction of source and absorption point. In contrast, for chiral media we have a more complicated situation, since we have to divide the bulk Green's tensor into two different parts $\mathbb{G}^{(vv)}$ and $\mathbb{G}^{(ww)}$ that are then differently corrected. We can conclude that as a consequence of their different k-vectors inside chiral media the propagator for left- and right-handed circularly polarised light needs to be differently local-field corrected.

4.2.2. Complete local-field correction of source and absorption point

We have derived the local-field correction of a single point inside chiral media, obtaining different correction factors for the propagation of left- and right-handed circularly polarised light. As a consequence, the simultaneous correction of both points is not obvious. In this section, we introduce a new notation and formalism for the Green's tensor, where each boundary is represented by a transmission and reflection matrix in the basis of spherical vector wave functions. Similarly, any Green's tensor and operation on a Green's tensor can be cast into this matrix form. In this formalism, the full Green's tensor can be obtained by multiplying the appropriate reflection, transmission and other matrices with each other. From this formalism we can conclude the full local-field correction of source and absorption points inside a chiral medium.

We may expand any Green's tensor via tensor products of $\boldsymbol{V}^{(1)}_{\sigma mn}(\boldsymbol{r},k_+)/\boldsymbol{W}^{(1)}_{\sigma mn}(\boldsymbol{r},k_-)$ and $\boldsymbol{V}_{\sigma mn}(\boldsymbol{r}',k_+)/\boldsymbol{W}_{\sigma mn}(\boldsymbol{r}',k_-)$, with $\sigma \in \{\mathrm{e},\mathrm{o}\}$. In this basis we adapt a matrix notation

and write any Green's tensor as

$$\mathbb{G}(\boldsymbol{r},\boldsymbol{r}') = \bigoplus_{n,m,\sigma} \begin{pmatrix} g_{vv}(n,m) & g_{vw}(n,m) \\ g_{wv}(n,m) & g_{ww}(n,m) \end{pmatrix}_{nm\sigma}, \tag{4.54}$$

where

$$\begin{pmatrix} 1 \\ 0 \end{pmatrix}_{nm\sigma} = \boldsymbol{V}_{\sigma mn}(\boldsymbol{r}', k_+), \qquad \begin{pmatrix} 0 \\ 1 \end{pmatrix}_{nm\sigma} = \boldsymbol{W}_{\sigma mn}(\boldsymbol{r}', k_-), \tag{4.55}$$

$$\begin{pmatrix} 1 & 0 \end{pmatrix}_{nm\sigma} = \boldsymbol{V}^{(1)}_{\sigma mn}(\boldsymbol{r}, k_+), \qquad \begin{pmatrix} 0 & 1 \end{pmatrix}_{nm\sigma} = \boldsymbol{W}^{(1)}_{\sigma mn}(\boldsymbol{r}, k_-), \tag{4.56}$$

with $\sigma \in \{\mathrm{e},\mathrm{o}\}$ and $m \leq n$. The chiral bulk Green's tensor is then given by the diagonal matrix,

$$\mathbb{G}^{(0)}(\boldsymbol{r},\boldsymbol{r}') = \frac{\mathrm{i}3\mu}{4\pi(k_+ + k_-)} \bigoplus_{n,m,\sigma} (2-\delta_{m0}) \frac{(2n+1)(n-m)!}{n(n+1)(n+m)!} \begin{pmatrix} k_+^2 & 0 \\ 0 & k_-^2 \end{pmatrix}, \tag{4.57}$$

where we have omitted the subscript $nm\sigma$ on the matrix-notation for better readability. The Green's tensor for an achiral bulk medium ($k_+ = k_-$) is hence proportional to the identity. The bulk Green's tensor is invariant under translation transformation. We may therefore choose to put $\boldsymbol{r}' = \boldsymbol{0}$ without loss of generality. We also adapt a dual notation, see Eq. (4.15). The dual bulk Green's tensor's are then given by

$$\mathbb{G}^{(0)}_{\mathrm{ee}}(\boldsymbol{r}) = f_{\mathrm{ee}} \begin{pmatrix} k_+^2 & 0 \\ 0 & k_-^2 \end{pmatrix}, \qquad \mathbb{G}^{(0)}_{\mathrm{em}}(\boldsymbol{r}) = f_{\mathrm{em}} \begin{pmatrix} -k_+^3 & 0 \\ 0 & k_-^3 \end{pmatrix}, \tag{4.58}$$

$$\mathbb{G}^{(0)}_{\mathrm{me}}(\boldsymbol{r}) = f_{\mathrm{em}} \begin{pmatrix} k_+^3 & 0 \\ 0 & -k_-^3 \end{pmatrix}, \qquad \mathbb{G}^{(0)}_{\mathrm{mm}}(\boldsymbol{r}) = f_{\mathrm{mm}} \begin{pmatrix} k_+^4 & 0 \\ 0 & k_-^4 \end{pmatrix}, \tag{4.59}$$

where we have omitted the direct sum over $m \leq n = 1$ and $\sigma \in \{\mathrm{e},\mathrm{o}\}$ in our notation and the prefactors are given by

$$f_{\mathrm{ee}} = -\frac{\mathrm{i}3\mu\omega^2}{4\pi c^2(k_+ + k_-)}, \qquad f_{\mathrm{em}} = -\frac{3\mu\omega}{4\pi c(k_+ + k_-)}, \qquad f_{\mathrm{mm}} = -\frac{\mathrm{i}3\mu}{4\pi(k_+ + k_-)}. \tag{4.60}$$

The derived transmission Green's tensor (4.35) for a source situated inside a vacuum sphere with radius a is given in the new notation by

$$\mathbb{G}^{21}_{\mathrm{ee}}(\boldsymbol{r},\boldsymbol{r}') = -\frac{\mathrm{i}k_0}{2\pi} f_{nm} \begin{pmatrix} a_n^v & b_n^v \\ a_n^w & b_n^w \end{pmatrix}, \qquad f_{nm} = (2-\delta_{m0}) \frac{(2n+1)(n-m)!}{n(n+1)(n+m)!}, \tag{4.61}$$

$$\mathbb{G}^{21}_{\mathrm{em}}(\boldsymbol{r},\boldsymbol{r}') = -\frac{1}{2\pi} f_{nm} \begin{pmatrix} a_n^v & b_n^v \\ a_n^w & b_n^w \end{pmatrix} \diamond \begin{pmatrix} -k_0 & 0 \\ 0 & k_0 \end{pmatrix}, \tag{4.62}$$

where $k_0 = \omega/c$, the coefficients are given by Eqs. (A.65)–(A.68), the matrix product on

level of the introduced matrices is denoted by $\diamond$ and the diagonal matrix in (4.62) results from the curl from the right.

From the non-vanishing off-diagonal elements in Eqs. (4.61) and (4.62) we can see that transmission through the surface mixes left- and right-handed circularly polarised light. However, when performing the limit of $a \to 0$, we implicitly force the source to sit at the origin, $\boldsymbol{r}' \to 0$. We can then map Eq. (4.61) onto a diagonal matrix without loss of generality, such that

$$\mathbb{G}^{21}_{\mathrm{ee}}(\boldsymbol{r},0)\Big|_{a\to 0} = -\frac{\mathrm{i}3k_0}{4\pi}\begin{pmatrix} a_v - b_v & 0 \\ 0 & -a_w + b_w \end{pmatrix}, \tag{4.63}$$

$$\mathbb{G}^{21}_{\mathrm{em}}(\boldsymbol{r},0)\Big|_{a\to 0} = -\frac{3}{4\pi}\begin{pmatrix} a_v + b_v & 0 \\ 0 & a_w + b_w \end{pmatrix} \diamond \begin{pmatrix} -k_0 & 0 \\ 0 & k_0 \end{pmatrix}, \tag{4.64}$$

where the coefficients are given by Eqs. (4.36) – (4.39). Finally, we can extract a local-field correction matrix C_λ that, when applied to the chiral bulk, yields the Green's tensor with single-point correction,

$$\text{correction of source point:} \qquad \mathbb{G}^{(0)}_{\lambda\lambda'}(\boldsymbol{r}) \diamond C_{\lambda'} \tag{4.65}$$

$$\text{correction of absorption point:} \qquad C_\lambda \diamond \mathbb{G}^{(0)}_{\lambda\lambda'}(\boldsymbol{r}) \tag{4.66}$$

with the LFC-matrix,

$$C_\lambda = \begin{pmatrix} c_{\lambda v} & 0 \\ 0 & c_{\lambda w} \end{pmatrix}. \tag{4.67}$$

From this we may conclude the simultaneous correction of both points,

$$\mathbb{G}^{\mathrm{lfc}}_{\lambda\lambda'}(\boldsymbol{r}) = C_\lambda \diamond \mathbb{G}^{(0)}_{\lambda\lambda'}(\boldsymbol{r}) \diamond C_{\lambda'} \tag{4.68}$$

$$= c_{\lambda v} c_{\lambda' v} \mathbb{G}^{(vv)}_{\lambda\lambda'}(\boldsymbol{r}) + c_{\lambda w} c_{\lambda' w} \mathbb{G}^{(ww)}_{\lambda\lambda'}(\boldsymbol{r}). \tag{4.69}$$

This is the fully local-field corrected bulk Green's tensor. The correction matrix becomes proportional to the identity in the limit of $\chi \to 0$ and hence reproduces the known solution for a magneto-electric medium, see Eqs. (4.48) and (4.44).

The introduced formalism also proves useful when solving transmission and reflection at several interfaces. For this some additional normalisations need to be considered and we do not present its general application here. The resulting method however is comparable to the on developed in Ref. [170] for planar-layered systems. In the next section we use this formalism only to verify the local-field correction method given by Eq. (4.68) in a specific example that allows for an analytical derivation of the local-field correction.

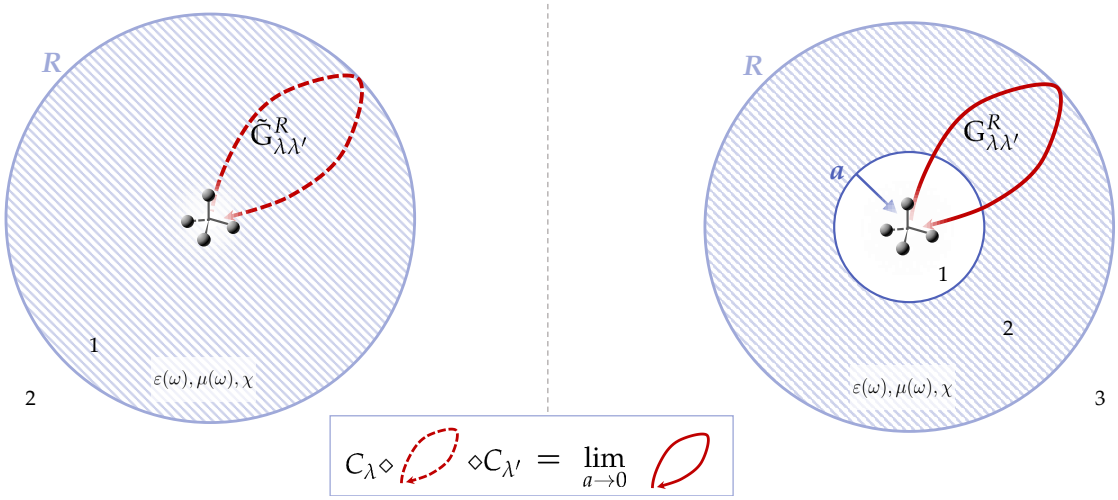

Figure 4.3.: Scheme of the validity check: we apply our method for LFC inside a chiral medium to the reflecting Green's tensor inside a chiral sphere (left) and we derive the Green's tensor for reflection at the outer boundary in a three-layer system (right). In the limit of vanishing inner free-space sphere, $a \to 0$, this yields the exact local-field corrected Green's tensor. We verify that both derivations give the same result.

4.2.3. Consistency check for a spherical three-layer system

We want to verify our method for LFC in a chiral medium, given by Eq. (4.68) for an example where we can calculate the simultaneous correction of source and absorption exactly. For this we consider spherically layered systems, where the special case of source and absorption at the origin allows for an exact calculation of the local-field corrected Green's tensor. We start by outlining the necessary calculations in detail, where we introduce the special spherical layered case that is then local-field correct via our method, and next introduce the system that yields the exact local-field corrected Green's tensor via an analytical calculation. Then follow the respective calculations and finally we show that the analytically obtained result for this special case is the same as the one obtained by our LFC method given by Eq. (4.68).

The special case that allows to be treated by both, our LFC method as well as an analytical and exact approach is the two-layer system where the inner layer is filled with chiral medium and source and absorption are placed at the origin. We hence consider such a spherical two-layer system where the inner layer with radius R is filled with a chiral medium and the outer layer is considered to be free space. Neglecting multiple scattering, the Green's tensor $\mathbb{G}^{11}$ for source and absorption inside the inner layer then consists of the known chiral bulk Green's tensor $\mathbb{G}_c^{(0)}$ (4.25) and the Green's tensor $\tilde{\mathbb{G}}^R$ resulting from single reflection at the interface at $r = R$, see Fig. 4.3. We are here only interested in the latter part $\tilde{\mathbb{G}}^R$. We then first obtain the local-field corrected version of

this Green's tensor by applying our method, i.e. the derived LFC-matrices (4.68) to $\tilde{\mathbb{G}}^R$.

As a second ingredient we need the exact local-field corrected Green's tensor for this system. For this we consider a three-layer system, were we added an inner layer with its boundary at $r = a < R$ that is filled with free space compared to the two-layer system, see Fig. 4.3. Neglecting again multiple scattering events, the Green's tensor $\mathbb{G}^{11}$ for source and absorption inside the inner layer consists now of three parts: $\mathbb{G}^{11} = \mathbb{G}^{(0)} + \mathbb{G}^a + \mathbb{G}^R$, where $\mathbb{G}^{(0)}$ is the known free space Green's tensor that describes the direct propagation from source to absorption, $\mathbb{G}^a$ results from a single reflection at the boundary at $r = a$ and $\mathbb{G}^R$ from a single reflection at the most outer boundary at $r = R$. These Green's tensors are sketched in Fig. 4.4. We are again only interested in the latter part $\mathbb{G}^R$, resulting from a single reflection at the outer interface. We may then perform the limit of vanishing inner layer radius $\lim_{a\to 0} \mathbb{G}^R(\boldsymbol{r}, \boldsymbol{r}')$. This result is then the exact local-field corrected version $\tilde{\mathbb{G}}^R$. After we calculated then both, $\tilde{\mathbb{G}}^R$ with the local-field correction via our method and the analytically derived local-field corrected result $\lim_{a\to 0} \mathbb{G}^R(\boldsymbol{r}, \boldsymbol{r}')$, we can verify that they yield the same result. This comparison is schematically sketched in Fig. 4.3.

Solution for a three-layer chiral system

We start by solving the more involved three-layer system. The derivation for the two-layer system then follows similar steps. For a source inside the inner layer we choose the ansatz:

$$\begin{aligned} 0 < r < a: \quad \mathbb{G}^{11}(\boldsymbol{r}, \boldsymbol{r}') = \mathbb{G}^{(0)}(\boldsymbol{r}, \boldsymbol{r}') + \frac{\mathrm{i}}{4\pi k} \sum_n^\infty \sum_m^n (2 - \delta_{m0}) \frac{(2n+1)(n-m)!}{n(n+1)(n+m)!} \\ \times \Big\{ \left[c_n^v \boldsymbol{V}_{\substack{\mathrm{e}\\\mathrm{o}}mn}(\boldsymbol{r}, k) + c_n^w \boldsymbol{W}_{\substack{\mathrm{e}\\\mathrm{o}}mn}(\boldsymbol{r}, k) \right] \boldsymbol{V}_{\substack{\mathrm{e}\\\mathrm{o}}mn}(\boldsymbol{r}', k) \\ + \left[d_n^v \boldsymbol{V}_{\substack{\mathrm{e}\\\mathrm{o}}mn}(\boldsymbol{r}, k) + d_n^w \boldsymbol{W}_{\substack{\mathrm{e}\\\mathrm{o}}mn}(\boldsymbol{r}, k) \right] \boldsymbol{W}_{\substack{\mathrm{e}\\\mathrm{o}}mn}(\boldsymbol{r}', k) \Big\} \end{aligned} \tag{4.70}$$

$$\begin{aligned} a < r < R: \quad \mathbb{G}^{21}(\boldsymbol{r}, \boldsymbol{r}') = \frac{\mathrm{i}}{4\pi k} \sum_n^\infty \sum_m^n (2 - \delta_{m0}) \frac{(2n+1)(n-m)!}{n(n+1)(n+m)!} \\ \times \Big\{ \left[a_n^v \boldsymbol{V}^{(1)}_{\substack{\mathrm{e}\\\mathrm{o}}mn}(\boldsymbol{r}, k_+) + a_n^w \boldsymbol{W}^{(1)}_{\substack{\mathrm{e}\\\mathrm{o}}mn}(\boldsymbol{r}, k_-) \right] \boldsymbol{V}_{\substack{\mathrm{e}\\\mathrm{o}}mn}(\boldsymbol{r}', k) \\ + \left[b_n^v \boldsymbol{V}^{(1)}_{\substack{\mathrm{e}\\\mathrm{o}}mn}(\boldsymbol{r}, k_+) + b_n^w \boldsymbol{W}^{(1)}_{\substack{\mathrm{e}\\\mathrm{o}}mn}(\boldsymbol{r}, k_-) \right] \boldsymbol{W}_{\substack{\mathrm{e}\\\mathrm{o}}mn}(\boldsymbol{r}', k) \\ + \left[\tilde{a}_n^v \boldsymbol{V}_{\substack{\mathrm{e}\\\mathrm{o}}mn}(\boldsymbol{r}, k_+) + \tilde{a}_n^w \boldsymbol{W}_{\substack{\mathrm{e}\\\mathrm{o}}mn}(\boldsymbol{r}, k_-) \right] \boldsymbol{V}_{\substack{\mathrm{e}\\\mathrm{o}}mn}(\boldsymbol{r}', k) \\ + \left[\tilde{b}_n^v \boldsymbol{V}_{\substack{\mathrm{e}\\\mathrm{o}}mn}(\boldsymbol{r}, k_+) + \tilde{b}_n^w \boldsymbol{W}_{\substack{\mathrm{e}\\\mathrm{o}}mn}(\boldsymbol{r}, k_-) \right] \boldsymbol{W}_{\substack{\mathrm{e}\\\mathrm{o}}mn}(\boldsymbol{r}', k) \Big\} \end{aligned} \tag{4.71}$$

$$r > R: \quad \mathbb{G}^{31}(\boldsymbol{r},\boldsymbol{r}') = \frac{\mathrm{i}}{4\pi k}\sum_{n}^{\infty}\sum_{m}^{n}(2-\delta_{m0})\frac{(2n+1)(n-m)!}{n(n+1)(n+m)!} \times \Big\{\big[e_n^v \boldsymbol{V}^{(1)}_{\substack{\mathrm{e}\\\mathrm{o}}mn}(\boldsymbol{r},k) + e_n^w \boldsymbol{W}^{(1)}_{\substack{\mathrm{e}\\\mathrm{o}}mn}(\boldsymbol{r},k)\big]\boldsymbol{V}_{\substack{\mathrm{e}\\\mathrm{o}}mn}(\boldsymbol{r}',k) + \big[f_n^v \boldsymbol{V}^{(1)}_{\substack{\mathrm{e}\\\mathrm{o}}mn}(\boldsymbol{r},k) + f_n^w \boldsymbol{W}^{(1)}_{\substack{\mathrm{e}\\\mathrm{o}}mn}(\boldsymbol{r},k)\big]\boldsymbol{W}_{\substack{\mathrm{e}\\\mathrm{o}}mn}(\boldsymbol{r}',k)\Big\} \quad (4.72)$$

where $\mathbb{G}^{(0)}$ is here the free space bulk Green's tensor (A.32). We find the coefficients by solving the boundary conditions at each interface, see Eqs. (4.32) and (4.33) where we find that $a_n^{v/w}$ and $b_n^{v/w}$ are given by the same expressions as in the single-point correction derivation, see Eq. (4.35).

When neglecting multiple scattering, the Green's tensor $\mathbb{G}^{11}$ consists of three parts: (1) the direct propagation from source to absorption $\mathbb{G}^{(0)}$, (2) the reflection at the inner interface at $r = a$, $\mathbb{G}^a$ and (3) the reflection at the outer interface $r = R$ and transmission through the inner interface, $\mathbb{G}^R$, see Fig. 4.4. For our comparison we are only interested in this latter part of the Green's tensor. It is easy to identify this term: (1) is already explicitly known and (2) consists only of terms that diverge in the limit of inner radius $a \to 0$. So by using $\mathbb{G}^{11} - \mathbb{G}^{(0)}$, dismissing any term that diverges with $a \to 0$ and keeping only the lowest order in R (such that higher order scattering at $r = R$ are neglected), we end up with the desired propagator $\mathbb{G}^R$. It is given by

$$\lim_{a\to 0}\mathbb{G}^R = \sum_{n,m}\frac{3\mathrm{i}}{8\pi k}\Big(\tilde{c}_v \boldsymbol{V}_{\substack{\mathrm{e}\\\mathrm{o}}mn}(\boldsymbol{r},k)\boldsymbol{V}_{\substack{\mathrm{e}\\\mathrm{o}}mn}(\boldsymbol{r}',k) + \tilde{c}_w \boldsymbol{W}_{\substack{\mathrm{e}\\\mathrm{o}}mn}(\boldsymbol{r},k)\boldsymbol{V}_{\substack{\mathrm{e}\\\mathrm{o}}mn}(\boldsymbol{r}',k) + \tilde{d}_v \boldsymbol{V}_{\substack{\mathrm{e}\\\mathrm{o}}mn}(\boldsymbol{r},k)\boldsymbol{W}_{\substack{\mathrm{e}\\\mathrm{o}}mn}(\boldsymbol{r}',k) + \tilde{d}_w \boldsymbol{W}_{\substack{\mathrm{e}\\\mathrm{o}}mn}(\boldsymbol{r},k)\boldsymbol{W}_{\substack{\mathrm{e}\\\mathrm{o}}mn}(\boldsymbol{r}',k)\Big), \quad (4.73)$$

or in matrix notation, see Eqs. (4.55)–(4.56),

$$\lim_{a\to 0}\mathbb{G}^R = \bigoplus_{n=1,m\le 1,\sigma}\frac{3\mathrm{i}}{8\pi k}\begin{pmatrix}\tilde{c}_v & \tilde{d}_v\\ \tilde{c}_w & \tilde{d}_w\end{pmatrix}_{nm\sigma}, \quad (4.74)$$

with

$$\begin{aligned}\tilde{c}_v = -\Big(&27\mathrm{i}\mu(-\mu^2(\mu^2(4\chi^2+2)+\mu(4\chi^4-8\chi^3+3\chi^2+4\chi-2)\\ &-2\chi(1-2\chi)^2(\chi^2-3\chi+2)) - n_r^4(-8\mu^2(\chi-3)+4\mu^3\\ &+\mu(-8\chi^2+8\chi-3)+4\chi^2+2)+\mu n_r^2(\mu^2(8\chi^2-8\chi+3)+4\mu^3\\ &-2\mu(8\chi^3-28\chi^2+21\chi-9)-4\chi^4+8\chi^3-3\chi^2-4\chi+2)-4(\mu-1)n_r^6\Big)/D,\end{aligned} \quad (4.75)$$

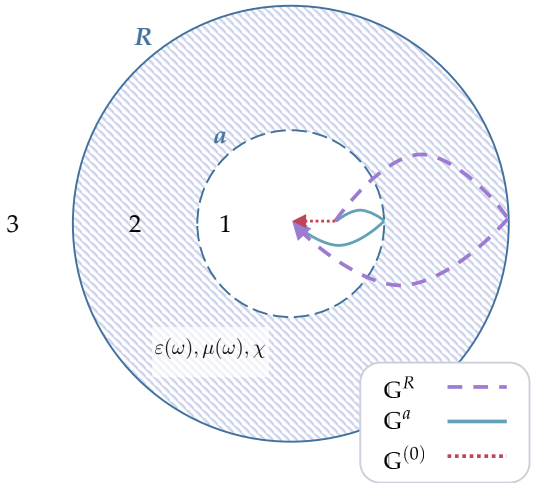

Figure 4.4.: Scheme for the considered three-layer system: the second layer consists of chiral medium, while the other two are considered to be free space. For source and absorption inside the inner layer, the Green's tensor consists of three parts: direct propagation in free space $\mathbb{G}^{(0)}$, reflection at the inner surface $\mathbb{G}^a$ and finally reflection at the outer surface $\mathbb{G}^R$.

$$\tilde{c}_w = 27\mathrm{i}\mu(\mu^2 - n_r^2)\Big(-\mu(\mu(4\chi^2-2)+4\chi^4+21\chi^2+2) + n_r^2(4\mu^2+\mu(8\chi^2+21)-4\chi^2+2)-4(\mu-1)n_r^4\Big)/D\,, \tag{4.76}$$

$$D = 2kR^3\left(\mu\left(2\mu-4\chi^2+1\right)+(4\mu+2)n_r^2\right)^2\left(\mu\left(2\mu-\chi^2+4\right)+(\mu+2)n_r^2\right)\,, \tag{4.77}$$

$$\text{and} \qquad \tilde{d}_v = \tilde{c}_w\Big|_{\chi\to-\chi}\,, \qquad \tilde{d}_w = \tilde{c}_v\Big|_{\chi\to-\chi}\,. \tag{4.78}$$

The result $\lim_{a\to 0}\mathbb{G}^R$ is the exact local-field corrected Green's tensor in a chiral sphere for a single reflection at a the boundary and with source and absorption at $\boldsymbol{r} = \boldsymbol{r}' = \boldsymbol{0}$.

Solution for a chiral sphere in free space

Next, we derive the Green's tensor for a similar system, without the inner free space layer, see Fig. 4.3. As the derivation follows exactly the same steps as the more complicated preceding three-layer version we do without a detailed calculation here. Analogously as before, we may form an ansatz for a source inside the chiral sphere and absorption in the two different layers, then solve the boundary conditions and neglect higher order scattering at R by keeping only its lowest order. With this we obtain the Green's tensor for single reflection at R as

$$\tilde{\mathbb{G}}^R = \bigoplus_{n=1,m\le 1,\sigma} \frac{\mathrm{i}3\mu}{4\pi c^2(k_+ + k_-)} \begin{pmatrix} c'_v & d'_v \\ c'_w & d'_w \end{pmatrix}_{nm\sigma}\,. \tag{4.79}$$

The remaining coefficients are given by

$$c_v' = -\frac{9\mu\left(3\mu^2\chi + (2\mu+1)n_r^3 + 3n_r^2\chi + \mu n_r\left(\mu - 2\left(\chi^2+2\right)\right)\right)}{16\pi n_r R^3\omega^4(n_r+\chi)^3\left((\mu+2)n_r^3 + \mu n_r\left(2\mu-\chi^2+4\right)\right)}, \tag{4.80}$$

$$c_w' = \frac{27\mu\left(n_r^2-\mu^2\right)}{16\pi n_r^2 R^3\omega^4(n_r-\chi)(n_r+\chi)\left(\mu\left(2\mu-\chi^2+4\right)+(\mu+2)n_r^2\right)}, \tag{4.81}$$

$$d_{v/w}' = c_{w/v}'\Big|_{\chi\to-\chi}. \tag{4.82}$$

The Green's tensor $\tilde{\mathbb{G}}^R$ describes a single reflection at a the boundary inside a chiral sphere and with source and absorption at $\boldsymbol{r} = \boldsymbol{r}' = \mathbf{0}$.

Comparison

We may correct the two-layer solution $\tilde{G}^R_{\lambda\lambda'}$ via C_λ and find that this results into the same local-field corrected Green's tensor as the analytical calculation given by Eq. (4.74), i.e. we find that

$$C_\lambda \diamond \tilde{G}^R_{\lambda\lambda'} \diamond C_{\lambda'} = \lim_{a\to 0}\mathbb{G}^R_{\lambda\lambda'}, \quad \forall\lambda,\lambda' \in \{\mathrm{e},\mathrm{m}\} \tag{4.83}$$

where the subscripts λ, λ' denote the respective dual Green's tensor, defined by Eq. (4.15). This verifies the suggested method for local-field correction in a chiral medium in this special case. At the same time, when applying the LFC matrices to the bulk Green's tensor we find the known megneto-electric corrections in the limit of $\chi \to 0$. While there exist alternative suggestions for LFC matrices that seem intuitive from the way we derived them in this section, none of them passes all the validity checks that one can do. Summarised, these validity checks are: hold for all $\lambda, \lambda' \in \{\mathrm{e},\mathrm{m}\}$ when applied to the bulk Green's tensor in the limit of $\chi \to 0$ and hold for all $\lambda, \lambda' \in \{\mathrm{e},\mathrm{m}\}$ when applied to the special case of a chiral spherical layered system. We conclude that the diagonal correction matrices can be interpreted as transmission matrices through infinitesimal free-space spheres which can be applied to any Green's tensor with source and/or absorption inside a chiral medium to find its local-field corrected version.

4.3. Discrimination inside a medium

We are now equipped to look into the RET rate involving chiral molecules inside different media, including chiral materials. We restrict ourselves to the task of distinguishing left- and right-handed acceptors. All considered schemes are illustrated in Fig. 4.5. We first

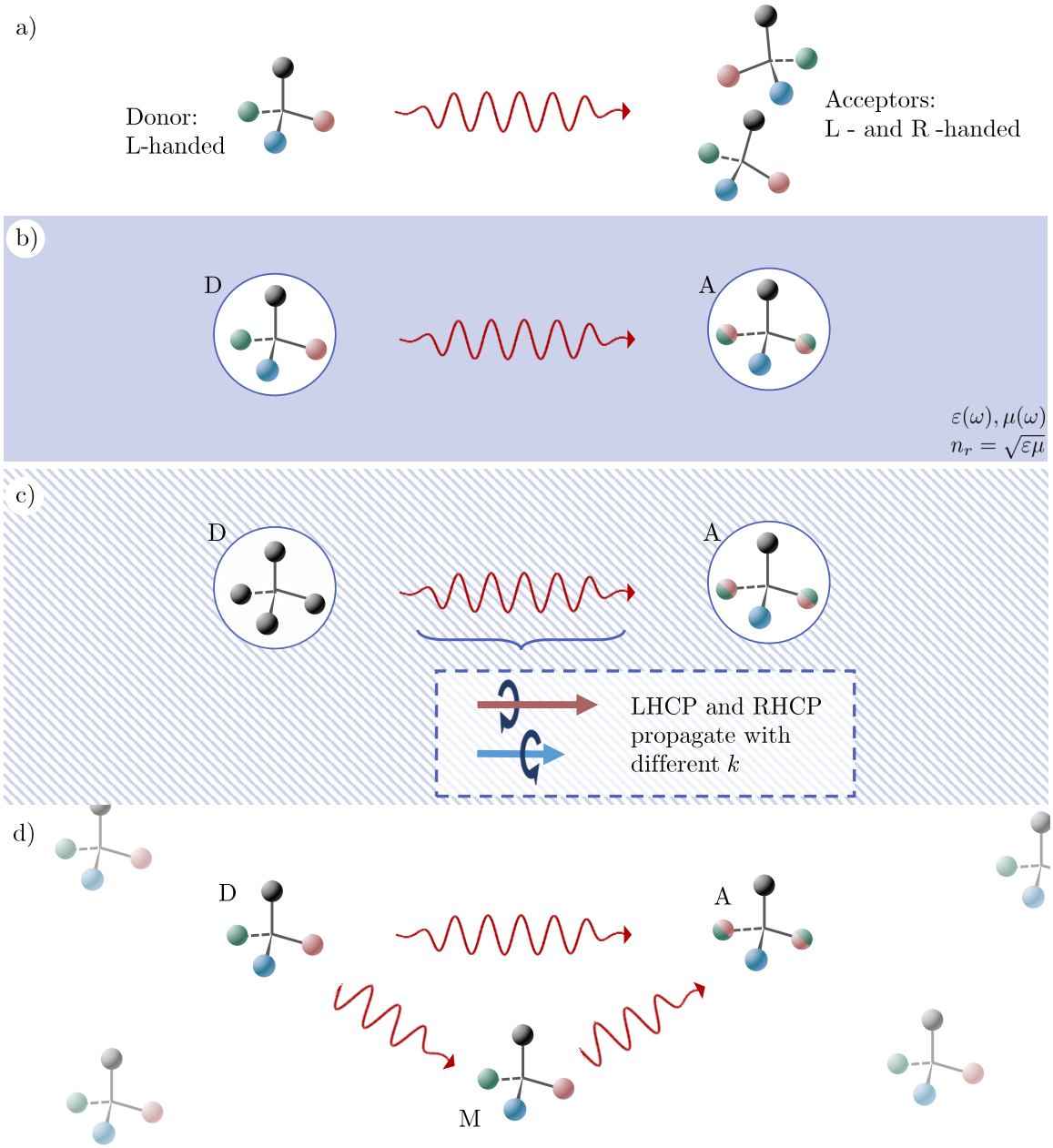

Figure 4.5.: Schemes of the considered setups for discrimination: **a)** We consider a donor molecule D with known handedness and an acceptor A with unknown handedness in free space. **b)** We consider a local-field corrected magneto-electric medium surrounding the system of a). **c)** We introduce chirality into the medium itself. The medium can hence actively discriminate the acceptor's enantiomers and the donor may be achiral. **d)** Finally, we model a very dilute medium by just considering a single, possibly chiral mediator molecule M as environment.

revisit the free-space case, where we introduce a measure for the degree of discrimination and discuss what is necessary to distinguish the acceptor's enantiomers in general. We then place our system into a magneto-electric medium and derive the medium's properties necessary to enhance the degree of discrimination. We derive analytic functions for the rates inside different media, which enables us to predict properties leading to maximum discrimination. We analyse absorbing dielectric media with complex permittivity in detail. Next a LFC-corrected chiral medium that surrounds the system is considered. The chiral property of the medium can be used to actively discriminate unknown enantiomers and we discuss the most beneficial set-up for successful discrimination of the acceptor's enantiomers. We conclude by considering a single chiral molecule in close proximity to the donor and acceptor pair as a limit of very dilute gases surrounding the system.

4.3.1. Discrimination in free space

We first revisit the RET process in free space, see Fig. 4.5a. We demonstrate consistency between our framework and free-space QED. We then characterise the degree of discrimination of RET by determining the discriminatory and nondiscriminatory contributions to the total rate. In free space this degree is completely determined by the involved molecular transition dipoles. We show that in contrast to the overall rate the discrimination benefits from large separation distance. We then introduce a suitable concrete example of chiral molecules to apply our theory.

Let us start by verifying the consistency of our framework with the rates derived in [118], see section 2.3.7. In free space the Green's tensor is given by

$$\mathbb{G}^{(0)} = \left[\mathbb{I} + \frac{\nabla\nabla}{k^2}\right] \frac{e^{\mathrm{i}k\rho}}{4\pi\rho}, \tag{4.84}$$

with $\rho = |\boldsymbol{r}_A - \boldsymbol{r}_B|$ and $k = \omega_{01}/c$. Inserting this into the derived matrix elements (4.14) and using the definition of the dual Green's tensor (4.15) yields

$$M_{\mathrm{ee}} = -\mu_0 c^2 \sum d_i^{\mathrm{A}} \left[k^2\delta_{ij} + \nabla_i\nabla_j\right] \frac{e^{\mathrm{i}k\rho}}{4\pi\rho} d_j^{\mathrm{D}} = \frac{1}{4\pi\varepsilon_0} \sum d_i^{\mathrm{A}} d_j^{\mathrm{D}} \left[\nabla^2\delta_{ij} - \nabla_i\nabla_j\right] \frac{e^{\mathrm{i}k\rho}}{\rho}. \tag{4.85}$$

With $\nabla \times \nabla\nabla = 0$, we find for the magnetic contributions:

$$\begin{aligned} M_{\mathrm{mm}} &= -\mu_0 \sum m_i^{\mathrm{A}} m_j^{\mathrm{D}} \left[\nabla \times \mathbb{I} \times \nabla\right]_{ij} \frac{e^{\mathrm{i}k\rho}}{4\pi\rho} \\ &= \frac{1}{4\pi\varepsilon_0 c^2} \sum m_i^{\mathrm{A}} m_j^{\mathrm{D}} \left[\nabla^2\delta_{ij} - \nabla_i\nabla_j\right] \frac{e^{\mathrm{i}k\rho}}{\rho}. \end{aligned} \tag{4.86}$$

And with

$$\left[\nabla_B \times \mathbb{G}^{(BA)}\right]_{ij} = -\sum_k \epsilon_{ijk}\nabla_k \frac{e^{\mathrm{i}k\rho}}{4\pi\rho} \qquad \text{and} \qquad \left[\mathbb{G}^{(BA)} \times \nabla_A\right]_{ij} = \sum_k \epsilon_{ijk}\nabla_k \frac{e^{\mathrm{i}k\rho}}{4\pi\rho}\,, \quad (4.87)$$

we find

$$M_{\mathrm{em}} + M_{\mathrm{me}} = \sum \frac{\mathrm{i}k}{4\pi\varepsilon_0 c}\left(d_i^{\mathrm{D}} m_j^{\mathrm{A}} - m_i^{\mathrm{D}} d_j^{\mathrm{A}}\right)\epsilon_{ijk}\nabla_k \frac{e^{\mathrm{i}k\rho}}{\rho}\,. \quad (4.88)$$

The matrix elements (4.85), (4.86) and (4.88) for free space are the same as the ones derived in [118] from free-space QED, recall section 2.3.7.

The total rate for an isotropic system is given by Eq. (4.18). The only quantity that is sensitive to the acceptor's handedness is its rotatory strength R_{A}. Its sign depends on the enantiomer. We hence find that in principle any rate contributions $\Gamma_{\mathrm{em}\lambda\lambda'} \propto R_{\mathrm{A}}$ and $\Gamma_{\mathrm{me}\lambda\lambda'} \propto R_{\mathrm{A}}$ are sensitive to the acceptor's handedness as well. These contributions are of two different forms,

$$\Gamma_{\mathrm{em}\lambda\lambda} \propto R^{\mathrm{A}} |\boldsymbol{d}_\lambda^{\mathrm{D}}|^2 \,\mathrm{Tr}\left[\mathbb{G}_{\mathrm{e}\lambda} \cdot \mathbb{G}_{\mathrm{m}\lambda}^{*T}\right]\,, \quad (4.89)$$

$$\Gamma_{\mathrm{em}\lambda_1\lambda_2} \propto R^{\mathrm{A}} R^{\mathrm{D}} \,\mathrm{Tr}\left[\mathbb{G}_{\mathrm{e}\lambda_1} \cdot \mathbb{G}_{\mathrm{m}\lambda_2}^{*T}\right]\,, \quad (4.90)$$

with $\lambda_1 \neq \lambda_2$ and analogously for $\Gamma_{\mathrm{me}\lambda\lambda'}$.

In agreement with the Curie symmetry principle [117] contributions of the first kind vanish in free space, $\mathrm{Tr}\left[\mathbb{G}_{\mathrm{e}\lambda} \cdot \mathbb{G}_{\mathrm{m}\lambda}^{*T}\right] = \mathrm{Tr}\left[\mathbb{G}_{\mathrm{m}\lambda} \cdot \mathbb{G}_{\mathrm{e}\lambda}^{*T}\right] = 0$, $\forall\lambda$. Only contributions that emerge from the chiral properties of both, donor and acceptor, i.e. that are proportional to $R_{\mathrm{A}}R_{\mathrm{D}}$, can discriminate the acceptor's enantiomers. We hence do not distinguish between left- and right-handed acceptors but between same- and opposite-handed acceptors relative to the donor. In conclusion we need to know the donor's handedness (i.e. the sign of R_{D}) to distinguish between left- and right-handed acceptors.

We assume from here on out that the donor's handedness is known and without loss of generality we assume that the donor is left-handed. The total discriminatory contribution is given by

$$\Gamma_{\mathrm{disc}} = \Gamma_{\mathrm{emme}} + \Gamma_{\mathrm{meme}} + \Gamma_{\mathrm{emem}} + \Gamma_{\mathrm{meem}}\,, \quad (4.91)$$

and the remaining non-vanishing terms add up the nondiscriminatory rate contribution,

$$\Gamma_{\mathrm{nd}} = \sum_{\lambda_1\lambda_2} \Gamma_{\lambda_1\lambda_1\lambda_2\lambda_2}\,, \quad (4.92)$$

yielding the total rate for left- and right-handed acceptor's via $\Gamma_{\mathrm{L/R}} = \Gamma_{\mathrm{nd}} \pm |\Gamma_{\mathrm{disc}}|$.

By using the free-space Green's tensor (A.32), we find for the rate contributions

$$\Gamma_{\text{disc}} = \rho \frac{R_{\text{D}} R_{\text{A}}}{18\pi c^2 \epsilon_0^2 \hbar^2 r^6} \left(3 + 2\frac{r^2\omega^2}{c^2} + 2\frac{r^4\omega^4}{c^4}\right), \tag{4.93}$$

$$\begin{aligned}\Gamma_{\text{nd}} = \frac{\rho}{36\pi\epsilon_0^2\hbar^2 r^6} \Bigg\{ & 3\left(|\boldsymbol{d}_{\text{e}}^{\text{A}}|^2 |\boldsymbol{d}_{\text{e}}^{\text{D}}|^2 + |\boldsymbol{d}_{\text{m}}^{\text{A}}|^2 |\boldsymbol{d}_{\text{m}}^{\text{D}}|^2\right) \\ & + \left(|\boldsymbol{d}_{\text{e}}^{\text{A}}|^2 + |\boldsymbol{d}_{\text{m}}^{\text{A}}|^2\right)\left(|\boldsymbol{d}_{\text{e}}^{\text{D}}|^2 + |\boldsymbol{d}_{\text{m}}^{\text{D}}|^2\right)\left[\frac{\omega^2 r^2}{c^2} + \frac{\omega^4 r^4}{c^4}\right]\Bigg\},\end{aligned} \tag{4.94}$$

where $r = |\boldsymbol{r}_D - \boldsymbol{r}_{\text{A}}|$ and $\omega = \omega_{01}$. We define the degree of discrimination S as the relative difference between the two rates,

$$S = \frac{\Gamma_{\text{L}} - \Gamma_{\text{R}}}{\Gamma_{\text{L}} + \Gamma_{\text{R}}} = \frac{\Gamma_{\text{disc}}}{\Gamma_{\text{nd}}}. \tag{4.95}$$

The rotatory strength is given by $|R_x|/c = \text{Im}\left[\boldsymbol{d}_{\text{e}}^x \cdot \boldsymbol{d}_{\text{m}}^x\right] = \cos(\theta_x)|\boldsymbol{d}_{\text{e}}^x||\boldsymbol{d}_{\text{m}}^x|$. The contributions relative to each other are hence determined by the angle θ_x and the ratio $|\boldsymbol{d}_{\text{m}}^x|/|\boldsymbol{d}_{\text{e}}^x|$, $x \in \{\text{A}, \text{D}\}$. Let us for simplicity assume that donor and acceptor are the same molecule, such that

$$\Gamma_{\text{disc}} = \frac{|\boldsymbol{d}_{\text{e}}|^4 \rho}{18\pi\epsilon_0^2\hbar^2 r^6} \cos^2\theta \frac{|\boldsymbol{d}_{\text{m}}|^2}{|\boldsymbol{d}_{\text{e}}|^2} \left(3 + 2\frac{r^2\omega^2}{c^2} + 2\frac{r^4\omega^4}{c^4}\right), \tag{4.96}$$

$$\Gamma_{\text{nd}} = \frac{|\boldsymbol{d}_{\text{e}}|^4 \rho}{36\pi\epsilon_0^2\hbar^2 r^6} \left\{3\left(1 + \frac{|\boldsymbol{d}_{\text{m}}|^4}{|\boldsymbol{d}_{\text{e}}|^4}\right) + \left(1 + \frac{|\boldsymbol{d}_{\text{m}}|^2}{|\boldsymbol{d}_{\text{e}}|^2}\right)^2 \left[\frac{\omega^2 r^2}{c^2} + \frac{\omega^4 r^4}{c^4}\right]\right\}. \tag{4.97}$$

Usually the magnetic transition dipole moment is much smaller than the electric one, $|\boldsymbol{d}_{\text{m}}| \ll |\boldsymbol{d}_{\text{e}}|$. We may use this to approximate the degree of discrimination,

$$S \approx 2\cos^2\theta \frac{|\boldsymbol{d}_{\text{m}}|^2}{|\boldsymbol{d}_{\text{e}}|^2} \frac{3 + 2k^2r^2 + 2k^4r^4}{3 + k^2r^2 + k^4r^4}, \tag{4.98}$$

where we can identify that S assumes its lower bound in the nonretarded and its upper one in the retarded limit. They are given by

$$S_{r\to 0} = \frac{2R_{\text{D}}R_{\text{A}}}{c^2|\boldsymbol{d}_{\text{e}}^{\text{D}}|^2|\boldsymbol{d}_{\text{e}}^{\text{A}}|^2} = 2\cos^2\theta \frac{|\boldsymbol{d}_{\text{m}}|^2}{|\boldsymbol{d}_{\text{e}}|^2}, \qquad S_{r\to\infty} \approx 2S_{r\to 0}. \tag{4.99}$$

Although the absolute rates rapidly decrease with the separation distance ($\sim r^{-6}$) the discrimination is stronger by a factor of approximately 2 in the retarded regime, see Fig. 4.6.

To provide plots for the presented analysis of chiral discrimination via resonance energy transfer, we choose the example of 3-methylcyclopentanone (3MCP) [171–174]. It

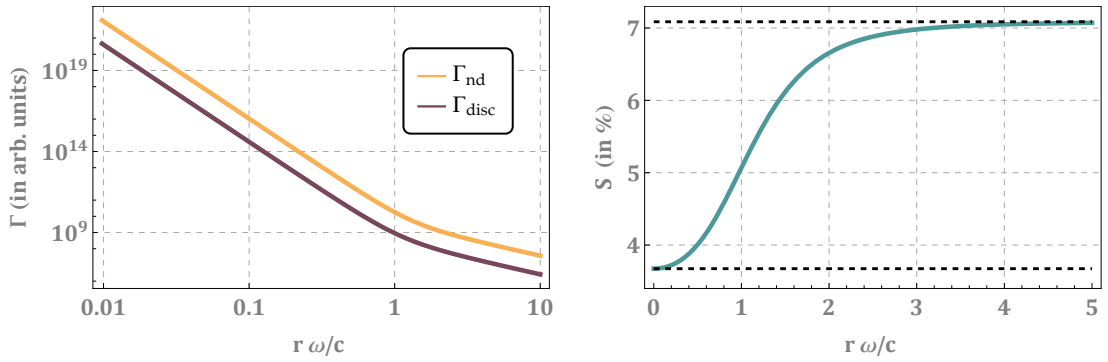

Figure 4.6.: **a)** The nondiscriminatory and discriminatory rate contributions for the example of 3MCP in free space as a function of separation distance r. In 3MCP the transition frequency is given by $\omega/c = 2.15 \times 10^{-7}$ m^{-1}. The rates rapidly decrease as a function of the separation distance. **b)** The free space degree of discrimination as a function of the separation distance r in the example of 3MCP. While the rate itself decreases with distance, the discrimination increases. The dashed lines mark the nonretarded and retarded asymptotes.

features a transition with a rather large magnetic transition dipole ($|\boldsymbol{d}_m| = 3.31 \times 10^{-32}$ Cm) compared to its electric transition dipole ($|\boldsymbol{d}_e| = 7.9|\boldsymbol{d}_m| = 2.44 \times 10^{-31}$ Cm). This leads to a relatively large rotatory strength $R/c = \cos\theta |\boldsymbol{d}_e||\boldsymbol{d}_m|$, where $\cos\theta = 0.98 \approx 1$. The transition frequency is at $\omega_{01} = 6.44 \times 10^{15}$ s^{-1}, which corresponds to a wave number in free space of $k_0 = \omega/c = 2.15 \times 10^{7}$ m^{-1}. In this example we find that the asymptotes are given by $S_{r\to 0} \approx 3.7\%$ and $S_{r\to\infty} \approx 7.4\%$. This means that the relative difference between left- and right-handed excited acceptors after RET took place is only roughly 4% to 8%, depending on the separation distance. The RET rates as well as the full degree of discrimination as functions of separation distance are shown in Fig. (4.6).

4.3.2. Discrimination in a magneto-electric medium

We have seen that in free space RET can in principle be used to discriminate chiral molecules. However, the effect is quite small and in free space completely determined by the involved molecules. We want to enhance and gain control over the degree of discrimination by considering a medium surrounding the system, see Fig. 4.5b. We show the impact of the LFC on an example to demonstrate its importance. The optimal dielectric property of the medium for discrimination is derived, additionally we show that even commercially available liquids may improve the degree of discrimination significantly. The general theory is applied to the introduced example of 3MCP.

Placing the system inside a magneto-electric medium with a relative permittivity ε and permeability μ, the discriminatory and nondiscriminatory rate contributions consist of

the same terms as in free space,

$$\Gamma_{\text{disc}} = \Gamma_{\text{emme}} + \Gamma_{\text{meme}} + \Gamma_{\text{emem}} + \Gamma_{\text{meem}}\,, \tag{4.100}$$

$$\Gamma_{\text{nd}} = \sum_{\lambda_1\lambda_2} \Gamma_{\lambda_1\lambda_1\lambda_2\lambda_2}\,. \tag{4.101}$$

By using the appropriate local-field corrected Green's tensor for a source and absorption point inside a magneto-electric medium, see Eq. (2.98) we find the rate contributions to be given by

$$\begin{aligned}\Gamma_{\text{nd}} = \frac{|\mu|^2|\boldsymbol{d}_{\text{e}}^{\text{A}}|^2|\boldsymbol{d}_{\text{e}}^{\text{D}}|^2 e^{-2kr(\text{Im}n_r)}}{36\pi r^6\varepsilon_0^2\hbar^2|n_r|^4}\Big\{&|c_{\text{e}}|^4\Big(|n_r|^4k^4r^4 + |n_r|^2k^2r^2(2\text{Im}n_rkr+1)\\ &\qquad + 4\text{Im}n_r^2k^2r^2 + 6\text{Im}n_rkr + 3\Big)\\ &+ |c_{\text{e}}|^2|n_rc_{\text{m}}|^2\Big(\frac{|\boldsymbol{d}_{\text{m}}^{\text{D}}|^2}{|\boldsymbol{d}_{\text{e}}^{\text{D}}|^2} + \frac{|\boldsymbol{d}_{\text{m}}^{\text{A}}|^2}{|\boldsymbol{d}_{\text{e}}^{\text{A}}|^2}\Big)\Big(2|n_r|^4k^4r^4 + |n_r|^2k^2r^2(2\text{Im}n_rkr+1)\Big)\\ &+ |n_rc_{\text{m}}|^4\frac{|\boldsymbol{d}_{\text{m}}^{\text{D}}|^2|\boldsymbol{d}_{\text{m}}^{\text{A}}|^2}{|\boldsymbol{d}_{\text{e}}^{\text{D}}|^2|\boldsymbol{d}_{\text{e}}^{\text{A}}|^2}\Big(|n_r|^2k^2r^2(2\text{Im}n_rkr+1) + |n_r|^4k^4r^4 + 4\text{Im}n_r^2k^2r^2 + 6\text{Im}n_rkr + 3\Big)\Big\}\,,\end{aligned} \tag{4.102}$$

$$\begin{aligned}\Gamma_{\text{disc}} = \frac{R_{\text{A}}R_{\text{D}}\omega^2|\mu|^2e^{-2\text{Im}n_rkr}}{18\pi c^4k^2r^6\varepsilon_0^2\hbar^2|n_r|^4}\Big\{&k^2r^2|c_{\text{e}}|^2|c_{\text{m}}|^2|n_r|^4\left(k^2r^2|n_r|^2 + 2kr\text{Im}n_r + 1\right)\\ &+ \text{Re}\left[c_{\text{e}}^{*2}c_{\text{m}}^2n_r^2\right]\left(k^2r^2|n_r|^2(2kr\text{Im}n_r+1) + k^4r^4|n_r|^4 + k^2r^2\text{Im}n_r^2 + 6kr\text{Im}n_r + 3\right)\Big\}\,,\end{aligned} \tag{4.103}$$

where $n_r = \sqrt{\varepsilon\mu}$ and c_λ are the LFC-factors given by Eqs. (2.96) and (2.97). They read

$$c_{\text{e}} = \frac{3\varepsilon}{1+2\varepsilon}\,, \qquad c_{\text{m}} = \frac{3}{1+2\mu}\,. \tag{4.104}$$

The rates without LFC can be obtained by setting $c_{\text{e}} = c_m = 1$, the free-space case can be obtained by additionally setting $n_r = \mu = 1$.

From this we can calculate the degree of discrimination S in the presence of a medium. In the nonretarded and retarded limits, they are given by

$$S_{r\to 0} = \frac{6R_{\text{A}}R_{\text{D}}\text{Re}\left[c_{\text{e}}^{*2}c_{\text{m}}^2n_r^2\right]}{c^2(3|c_{\text{e}}|^4|\boldsymbol{d}_{\text{e}}^{\text{A}}|^2|\boldsymbol{d}_{\text{e}}^{\text{D}}|^2 + 3|n_rc_{\text{m}}|^4|\boldsymbol{d}_{\text{m}}^{A}|^2|\boldsymbol{d}_{\text{m}}^{\text{D}}|^2)}\,, \tag{4.105}$$

$$S_{r\to\infty} = \frac{2R_{\text{A}}R_{\text{D}}\left(|c_{\text{e}}|^2|n_rc_{\text{m}}|^2 + \text{Re}\left[c_{\text{e}}^{*2}c_{\text{m}}^2n_r^2\right]\right)}{c^2\left(|c_{\text{e}}|^2|\boldsymbol{d}_{\text{e}}^{\text{A}}|^2 + |n_rc_{\text{m}}|^2|\boldsymbol{d}_{\text{m}}^{A}|^2\right)\left(|c_{\text{e}}|^2|\boldsymbol{d}_{\text{e}}^{\text{D}}|^2 + |n_rc_{\text{m}}|^2|\boldsymbol{d}_{\text{m}}^{\text{D}}|^2\right)}\,. \tag{4.106}$$

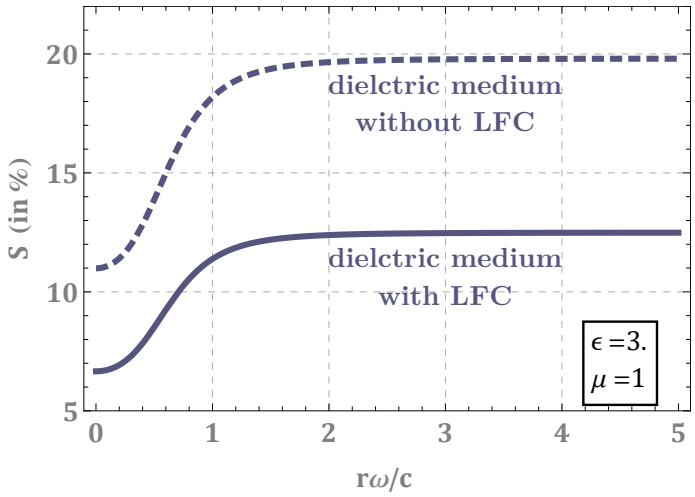

Figure 4.7.: The degree of discrimination in a surrounding medium as a function of the separation distance r in the example of 3MCP with and without LFC: Without local-field corrections the degree of discrimination is overestimated. We chose $\mu = 1$ and $\varepsilon = 3$, i.e. $n_r \approx 1.7$ for the medium. The separation distance is given in units of $c/\omega_{01} = \lambda_{01}/2\pi \approx 47$ nm.

Assuming that $|\boldsymbol{d}_m| \ll |\boldsymbol{d}_e|$ and that the medium is nonabsorbing (ε, $\mu \in \mathbb{R}$) the local-field corrected degree of discrimination, see Eq. (4.105) differs by a factor of roughly c_m^2/c_e^2 to the uncorrected result, see Eq. (4.105) with $c_\mathrm{e} = c_\mathrm{m} = 1$. For $\mu = 1$ the following applies: $c_m^2/c_\mathrm{e}^2 < 1 \Leftrightarrow |\varepsilon| > 1$. In conclusion in most cases the medium's impact onto the degree of discrimination would be overestimated without LFC.

This is illustrated for the example of 3MCP in Fig. 4.7, where the degree of discrimination is plotted with and without correction for a dielectric medium with real permittivity $\varepsilon(\omega) = 3$ and trivial permeability $\mu(\omega) = 1$. The impact by local-field correction is of similar magnitude as the impact of the medium itself compared to its free-space case, see Fig. 4.6.

However, despite local-field effects an appropriate medium can enhance the degree of discrimination in general up to $S = \prod_x \mathrm{Im}[\boldsymbol{m}_x \cdot \boldsymbol{d}_x]/(|\boldsymbol{m}_x||\boldsymbol{d}_x|) = \prod_x \cos\theta_x \leq 100\%$, where x =A,D. We can predict the optimum refractive indices $n_{r,\mathrm{opt}}$ at which $S = \cos^2\theta$ for any two chiral molecules of the same type as a function of the ratio $|\boldsymbol{d}_\mathrm{e}|/|\boldsymbol{d}_\mathrm{m}|$. If we limit ourselves to positive real permittivities $\varepsilon > 0$ and trivial permeabilities $\mu = 1$, we find that $S = \cos^2\theta$ for

$$n_{r,\mathrm{opt}} = \frac{1}{4}\left(3\frac{|\boldsymbol{d}_e|}{|\boldsymbol{d}_m|} \pm \sqrt{9\frac{|\boldsymbol{d}_e|^2}{|\boldsymbol{d}_m|} - 8}\right). \tag{4.107}$$

The optimum refractive indices as functions of the transition dipole moments ratio are plotted in Fig. 4.8. They each diverge from unity with increasing ratio $|\boldsymbol{d}_\mathrm{e}|/|\boldsymbol{d}_\mathrm{m}|$.

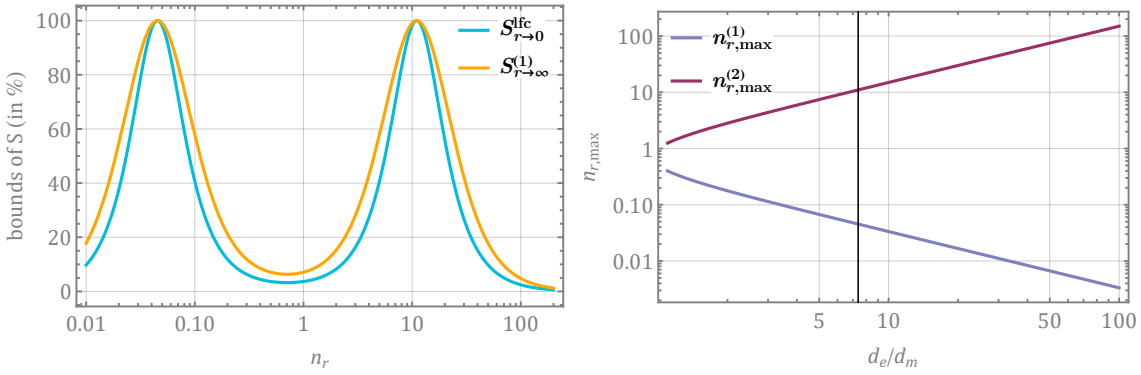

Figure 4.8.: **Left:** The two asymptotes for the degree of discrimination are plotted as a function of the refractive index $n_r = \sqrt{\varepsilon}$ of a dielectric medium for the example of 3MCP. One can identify two maxima where the discrimination is 100% independent of the separation distance. **Right:** For arbitrary but identical donor and acceptor molecules we can predict the real refractive indices at which the degree of discrimination is maximal, they diverge further and further from the free space refractive index $n_r = 1$ for increasing ratio $|\boldsymbol{d}_{\mathrm{e}}|/|\boldsymbol{d}_m|$. The vertical line shows the ratio $|\boldsymbol{d}_{\mathrm{e}}|/|\boldsymbol{d}_m|$ for the example of 3MCP.

A maximum degree of discrimination of 100% can only be achieved if the angle θ between magnetic and electric transition dipole is zero. It corresponds to vanishing excitation transfer to the right-handed acceptor ($\Gamma_R = 0$) independent of the separation distance. The angle θ is approximately zero in the case of 3MCP. For 3MCP complete discrimination, $S = 100\%$ can then be achieved at $\varepsilon(\omega_{\mathrm{D}}) \approx 121.5$ (i.e. $n_r \approx 11$) and alternatively but less relevantly for a permittivity of $\varepsilon(\omega_{\mathrm{D}}) = 0.002$ (i.e. $n_r \approx 0.045$), see Fig. 4.8.

In Fig. 4.9 we present the nonretarded and retarded degree of discrimination $S_{r\to 0/\infty}$ as functions of a complex refractive index with trivial permeability $\mu = 1$. In theory, one may achieve a complete inversion of the discriminatory effect in the nonretarded limit for $\mathrm{Im}n_r > \mathrm{Re}n_r$. In the chosen example of 3MCP the same-handed rate vanishes, $\Gamma_{\mathrm{L}} = 0 \Leftrightarrow S_{r\to 0} = -100\%$, for $\mathrm{Im}n_r = 11$ and $\mathrm{Im}n_r = 0.045$. However, the retarded limit does not experience such an inversion of the effect. Here the discrimination simply vanishes with increasing $\mathrm{Im}n_r$. In conclusion, it is in theory possible to find a medium where the direction of discrimination is distance dependent.

Most conventional media may be found around $1 < \mathrm{Re}n_r < 2$ and $0 < \mathrm{Im}n_r \ll 1$. Depending on the transition wavelength liquid solutions with $1.5 < \mathrm{Re}n_r < 2$ are known and commercially available [175–177]. At the transition frequency of 3MCP ($\omega_{\mathrm{D}} = 6.44 \times 10^{15}\ \mathrm{s}^{-1} = 4.3$ eV) some example media are given in table 4.1. If possible, their refractive indices were marked in Fig. 4.9. An interesting and simple, albeit rather academical medium example is mercury where the discrimination is inverted in the nonretarded limit compared to the free-space case. Liquid solutions with resonances at the desired

frequency as well as fluids based on metamaterials may be engineered to cover a larger range of the presented parameter space [178]. The choice of an appropriate medium depends highly on the transition frequency of the chiral molecules of interest.

4.3.3. Discrimination in chiral medium

A medium may enhance the degree of discrimination as shown in the previous section. However, it can also participate actively in the discrimination assuming the medium itself has chiral properties. In this section, the system is placed inside a chiral medium with known handedness, see Fig. 4.5c. We show that the medium can actively discriminate the acceptor and hence we may even choose an achiral donor and still be able to distinguish the acceptor's enantiomers. As shown in the previous section LFCs prove to have a significant effect on the degree of discrimination. The LFC for a chiral medium has been derived in section 4.2 and depends on the chiral property of the medium. In this section, we derive a contribution to the degree of discrimination that stems solely from LFC, i.e. vanishes completely when disregarding LFC effects and show that this contribution even dominates in the nonretarded limit of small donor–acceptor distances.

In case of a surrounding medium with known chirality, the discriminatory part of the rate gains contributions, due to the chiral Green's tensor (4.69). Terms that vanished in the achiral medium as well as in free space lead now to a new finite contribution,

$$\Gamma_{\text{disc2}} = \Gamma_{\text{emee}} + \Gamma_{\text{meee}} + \Gamma_{\text{emmm}} + \Gamma_{\text{memm}}\,, \tag{4.108}$$

which is proportional to the product of the chiral parameters of the medium and the acceptor, $\Gamma_{\text{disc2}} \propto \chi R_{\text{A}}$, and hence changes its sign depending on the acceptor's handedness. As we will see, the sign conventions for the respective chiral parameter for molecules (R_{A}) and media (χ) do not match each other in the intuitive way: a negative χ corresponds to an enhanced energy transfer for a positive R_{A}. We hence switch here to a convention where the signs correspond to each other and define $\overline{\chi} = -\chi$. We first consider an achiral donor $R_{\text{D}} = 0$, such that the discriminatory contributions from the achiral medium study considered in section 4.3.2 vanish,

$$\Gamma_{\text{disc1}} = \Gamma_{\text{emme}} + \Gamma_{\text{meme}} + \Gamma_{\text{emem}} + \Gamma_{\text{meem}} \propto R^{\text{D}} = 0\,. \tag{4.109}$$

The remaining non-vanishing terms give the nondiscriminatory contribution, which are

medium	refractive index	$S_{r\to 0}$	$S_{r\to\infty}$
water	$1.4 + 10^{-8}\mathrm{i}$	5%	10%
biodisel	$1.56 + 8 \times 10^{-6}\mathrm{i}$	6%	11%
ethanol	$1.39 + 3 \times 10^{-6}\mathrm{i}$	5%	10%
methane	$1.44 + 0.07\mathrm{i}$	5%	10%
mercury	$0.52 + 2.39\mathrm{i}$	−7%	1%

Table 4.1.: The asymptotes of the degree of discrimination in simple media. The refractive indices were obtained from [179]. All considered media but mercury show a similar refractive index at $\lambda = 2\pi c/\omega_{01} = 292$ nm.

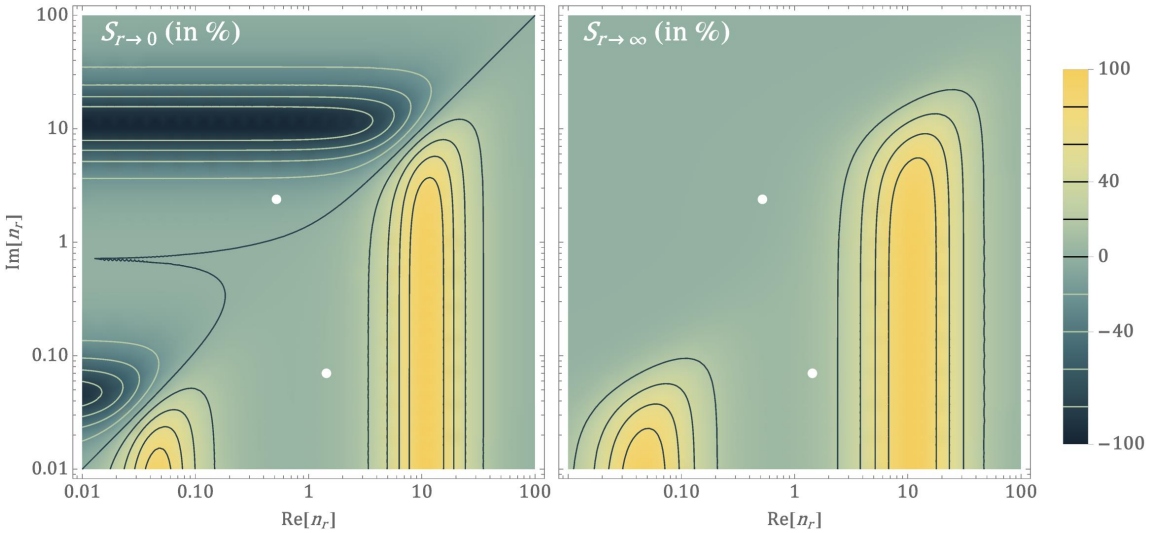

Figure 4.9.: Nonretarded (left plot) and retarded (right plot) degree of discrimination as a function of real and imaginary part of the refractive index (with $\mu = 1$) for the example of 3MCP. We marked simple media with complex n_r: methane at $n_r = 1.44 + 0.04\mathrm{i}$ and mercury at $n_r = 0.52 + 2.39\mathrm{i}$.

the same terms as in the previously discussed cases,

$$\Gamma_{\mathrm{nd}} = \sum_{\lambda_1,\lambda_2} \Gamma_{\lambda_1\lambda_1\lambda_2\lambda_2}\,. \tag{4.110}$$

With this we can calculate the rate contributions in a chiral bulk medium as well as the degree of discrimination analytically. The chiral bulk Green's tensor including local-field corrections is given by Eq. (4.69). Using this Green's tensor to evaluate the rate contributions $\Gamma_{\lambda_1\lambda_2\lambda_3\lambda_4}$ we can calculate the degree of discrimination inside a chiral medium,

$$S = \frac{\Gamma_{\mathrm{disc2}}}{\Gamma_{\mathrm{nd}}}\,. \tag{4.111}$$

The loacl-field correction for chiral media, derived in section 4.2 introduces different correction factors for $\mathbb{G}^{(\mathrm{vv})}_{\lambda\lambda'}$ and $\mathbb{G}^{(\mathrm{ww})}_{\lambda\lambda'}$ in the orginal chiral bulk Green's tensor, see Eq. (4.69). As a consequence they alter the structure of the Green's tensor and the local-field correction does not only give correcting factors to the degree of discrimination but leads to an additional contribution S^{lfc}. Let us only keep the first order of $\chi \ll 1$, such that the local-field correction factors are given by Eqs. (4.49)–(4.50) and read

$$c_{\mathrm{e}v/w} = c_{\mathrm{e}} \mp \overline{\chi} c_{\mathrm{e}\chi} \tag{4.112}$$

$$c_{\mathrm{m}v/w} = c_{\mathrm{m}} \pm \overline{\chi} c_{\mathrm{m}\chi}\,. \tag{4.113}$$

We may then divide the resulting local-field corrected degree of discrimination S inside a chiral medium into two contributions:

$$S = S^{(1)} + S^{\mathrm{lfc}} \tag{4.114}$$

$$S^{(1)} = S\big|_{c_{\mathrm{e}\chi}=c_{\mathrm{m}\chi}=0}\,. \tag{4.115}$$

The two contribution are chosen, such that $S^{(1)}$ stays invariant and the degree of discrimination due to local-field effects S^{lfc} vanishes when neglecting the chiral property of local-field correction, i.e. for $c_{\lambda v} = c_{\lambda w} = c_\lambda$.

In first order of χ, the degrees of discrimination are given in their nonretarded and

	distance limit	achiral medium D discriminates A	chiral medium medium discriminates A
without LFC	nonretarded	$n_r^2 S^{(\mathrm{fs})}_{r\to 0/\infty}$	0
	retarded		$\dfrac{3c\overline{\chi}\lvert\boldsymbol{d}_\mathrm{e}^\mathrm{D}\rvert^2}{2R_\mathrm{D}} S^{(\mathrm{fs})}_{r\to\infty}$
with LFC	nonretarded	$\dfrac{c_\mathrm{m}^2}{c_\mathrm{e}^2} n_r^2 S^{(\mathrm{fs})}_{r\to 0/\infty}$	$-\dfrac{n_r c\lvert\boldsymbol{d}_\mathrm{e}^\mathrm{D}\rvert^2\overline{\chi}}{c_\mathrm{e}^2 R_\mathrm{D}} \left(c_\mathrm{e}c_{\mathrm{m}\chi} - c_\mathrm{m}c_{\mathrm{e}\chi}\right) S^{(\mathrm{fs})}_{r\to 0}$
	retarded		$\dfrac{c\lvert\boldsymbol{d}_\mathrm{e}^\mathrm{D}\rvert^2\overline{\chi}}{2c_\mathrm{e}^2 R_\mathrm{D}} \left(3c_\mathrm{e}c_\mathrm{m} - n_r c_{\mathrm{m}\chi}c_\mathrm{e} + n_r c_{\mathrm{e}\chi}c_\mathrm{m}\right) S^{(\mathrm{fs})}_{r\to\infty}$

Table 4.2.: Asymptotic degree of discrimination $S_{r\to 0/\infty}$ for an achiral medium and a chiral medium relative to the free space degree of discrimination $S^{(\mathrm{fs})}_{r\to 0/\infty}$ in the respective limit, see Eqs. (4.99). We approximated $|\boldsymbol{d}_\mathrm{m}| \ll |\boldsymbol{d}_\mathrm{e}|$, $\overline{\chi} \ll 1$ and assumed that ε, μ, $n_r \in \mathbb{R}$.

retarded limit by

$$S^{(1)}_{r\to 0} = 0\,, \tag{4.116}$$

$$S^{\mathrm{lfc}}_{r\to 0} = \overline{\chi} R_\mathrm{A} \frac{2\mathrm{Re}\left[n_r^*(c_{\mathrm{e}\chi}^* c_\mathrm{m}^* - c_{\mathrm{m}\chi}^* c_\mathrm{e}^*)\left(c_\mathrm{e}^2|\boldsymbol{d}_e^\mathrm{D}|^2 + n_r^2 c_\mathrm{m}^2 |\boldsymbol{d}_\mathrm{m}^\mathrm{D}|^2\right)\right]}{c\left(|c_\mathrm{e}|^4|\boldsymbol{d}_e^\mathrm{A}|^2|\boldsymbol{d}_e^\mathrm{D}|^2 + |c_\mathrm{m}|^4|\boldsymbol{d}_\mathrm{m}^\mathrm{A}|^2|\boldsymbol{d}_\mathrm{m}^\mathrm{D}|^2|n_r|^4\right)}\,, \tag{4.117}$$

$$S^{(1)}_{r\to\infty} = \overline{\chi} R_\mathrm{A} \frac{2\mathrm{Re}\left[|c_\mathrm{e}\boldsymbol{d}_\mathrm{e}^\mathrm{D}|^2 c_\mathrm{e} c_\mathrm{m}^* n_r^*(2n_r + n_r^*) + |n_r c_\mathrm{m}\boldsymbol{d}_\mathrm{m}^\mathrm{D}|^2 c_\mathrm{e} c_\mathrm{m}^* n_r^*(3n_r + 2n_r^*)\right]}{|n_r|^2 D_\infty}\,, \tag{4.118}$$

$$\begin{aligned} S^{\mathrm{lfc}}_{r\to\infty} = \overline{\chi} R_\mathrm{A} \Bigg\{ & \frac{2|\boldsymbol{d}_\mathrm{e}^\mathrm{D}|^2}{D_\infty} \mathrm{Re}\left[n_r c_\mathrm{e}^*(c_{\mathrm{e}\chi} c_\mathrm{e}^* c_\mathrm{m} - 2c_{\mathrm{e}\chi}^* c_\mathrm{e} c_m - c_{\mathrm{m}\chi} c_\mathrm{e} c_\mathrm{e}^*)\right] \\ & + \frac{2|n_r \boldsymbol{d}_\mathrm{m}^\mathrm{D}|^2}{D_\infty} \mathrm{Re}\left[n_r c_\mathrm{m}(c_{\mathrm{e}\chi}^* c_\mathrm{m} c_\mathrm{m}^* - 2c_{\mathrm{m}\chi} c_\mathrm{e}^* c_\mathrm{m}^* - c_{\mathrm{m}\chi}^* c_\mathrm{e}^* c_\mathrm{m})\right] \Bigg\}\,, \end{aligned} \tag{4.119}$$

$$D_\infty = c\left(|c_\mathrm{e}\boldsymbol{d}_\mathrm{e}^\mathrm{A}|^2 + |n_r c_\mathrm{m}\boldsymbol{d}_\mathrm{m}^\mathrm{A}|^2\right)\left(|c_\mathrm{e}\boldsymbol{d}_\mathrm{e}^\mathrm{D}|^2 + |n_r c_\mathrm{m}\boldsymbol{d}_\mathrm{m}^\mathrm{D}|^2\right)\,. \tag{4.120}$$

In the nonretarded regime the discrimination is entirely due to local-field effects, i.e. $S_{r\to 0} = S^{\mathrm{lfc}}_{r\to 0}$. The sign of S^{lfc} depends on the relative magnitude of the correction factors and has for most parameter choices a sign opposite to that of $S^{(1)}$. This is conceptionally different to the behaviour derived in achiral media: which handedness is favoured by RET depends here generally on the intermolecular distance. In an achiral medium we found a similar behaviour only when considering exotic refractive indices n_r, where $\mathrm{Im}\, n_r > \mathrm{Re}\, n_r$,

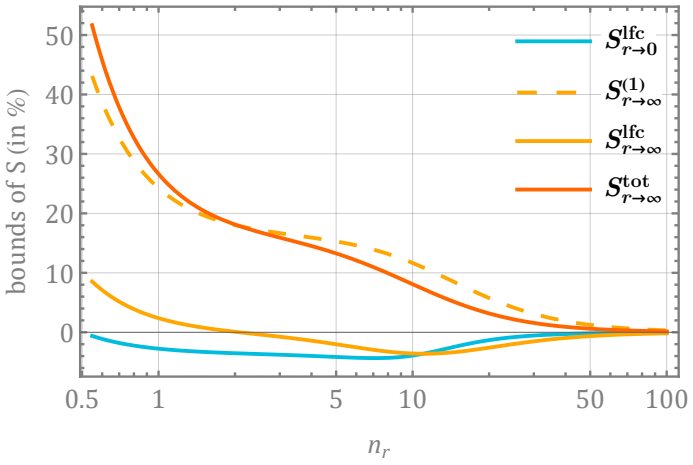

Figure 4.10.: The asymptotes of $S = S^{(1)} + S^{\mathrm{lfc}}$ inside a chiral medium including local-field correction. The contribution S^{lfc} which is due to the local-field correction has usually an opposite to the main contribution $S^{(1)}$ and even dominates in the nonretarded regime.

see Fig. 4.9. This is also shown in table 4.2, here we give the asymptotes of the respective degree of discrimination for real material parameters and in an approximate form in the different limits, with and without local-field corrections and in achiral and chiral media in table 4.2. Within these assumptions, i.e. $|\boldsymbol{d}_{\mathrm{e}}| \gg |\boldsymbol{d}_{\mathrm{m}}|$, $\chi \ll 1$ and $\varepsilon, \mu \in \mathbb{R}$, the degree of discrimination inside achiral media takes a quite simple form, while the expression stays quite involved for the chiral medium.

Let us restrict ourselves to simple cases of chiral media, where the permeability is trivial, $\mu = 1$ and the permittivity is real and positive, $\varepsilon > 0 \Rightarrow n_r = \sqrt{\varepsilon\mu} > 0$. The asymptotes of the degree of discrimination $S_{r\to 0/\infty} = S^{(1)}_{r\to 0/\infty} + S^{\mathrm{lfc}}_{r\to 0/\infty}$ inside a local-field corrected chiral medium are plotted for the example of 3MCP in Fig. 4.10. The nonretarded limit $S_{r\to 0}$ is then proportional to $S^{\mathrm{lfc}}_{r\to 0} \propto -4\overline{\chi}R_{\mathrm{A}}(4n_r^2 - 1)$ and is hence negative for $n_r > 1/2$. While there are choices of parameter where in the retarded limit $S^{\mathrm{lfc}}_{r\to\infty} < 0$ the total retarded asymptote is given by the sum $S_{r\to\infty} = S^{\mathrm{lfc}}_{r\to\infty} + S^{(1)}_{r\to\infty}$ which is usually positive. This means that in this parameter regime if $\Gamma_{\mathrm{L}}(r \to \infty) > \Gamma_{\mathrm{R}}(r \to \infty)$ in one limit of distances then $\Gamma_{\mathrm{R}}(r \to 0) > \Gamma_{\mathrm{L}}(r \to 0)$ in the other due to local-field effects.

An even stronger discrimination may be achieved by additionally considering a chiral donor with known handedness. Then we find a second contribution to the discriminatory rate $\Gamma_{\mathrm{disc1}} \propto R_{\mathrm{D}}R_{\mathrm{A}}$ given by Eq. (4.103) and the nondiscriminatory rate gains a negligible contribution that is proportional to $\overline{\chi}R_{\mathrm{D}}$. The degree of discrimination for known chiral donor and chiral medium behaves therefore approximately additive. This can also be seen in Fig. 4.11, where the degrees of discrimination for all these cases are shown in comparison to each other for the example of 3MCP.

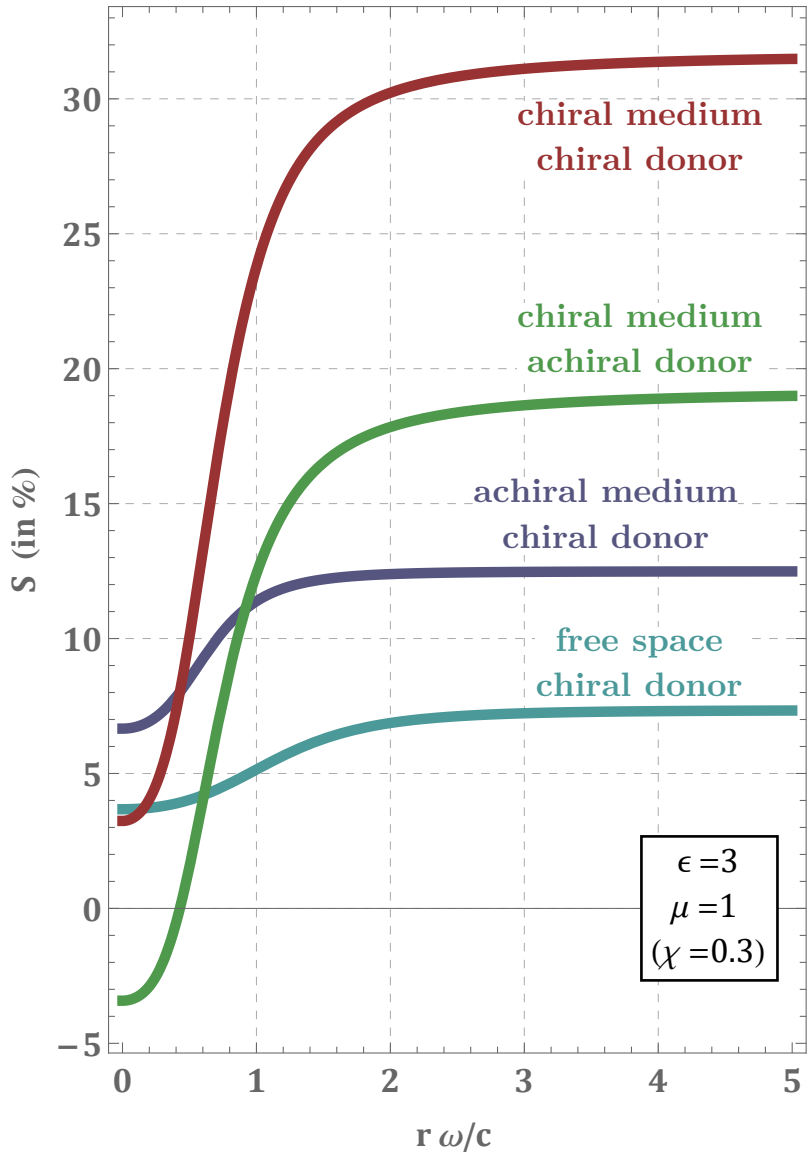

Figure 4.11.: Degree of discrimination in comparison to each other for all cases as a function of the the separation distance. A dielectric medium with conventional properties may enhance the discrimination between chiral donor and acceptor. A chiral medium can actively discriminate the acceptor molecule, even when considering an achiral donor. If both, medium and donor, are chiral the resulting discrimination is approximately given by the sum of the latter two cases.

4.3.4. Discrimination in the presence of a chiral mediator

So far, we have considered dense continuous media surrounding the system that are well described by their macroscopic properties. This model fails in very dilute gaseous media. The environment in the dilute-gas limit is rather modelled by single molecules surrounding the system. In this section, we study chiral discrimination in the presence of a single ground state mediator, see Fig. 4.5d. We consider the mediator to be possibly chiral. On the derived expressions we discuss the results for different combinations of chiral and achiral participants for the degree of discrimination. We show that even a single mediator may have an impact onto the discrimination. The effect is highly position dependent and we show the mediator's impact on the total rate as well as on the discrimination as function of its position for the example of 3MCP.

In the limit of dilute gases the medium is rather modelled by N mediator molecules. Electric mediators can be treated by including them into the Green's tensor, see section 2.3.3 via their electric polarisability. Here, we extend the theory to chiral mediators. We apply from the start some useful assumptions: (1) isotropic transitions of the mediator molecule, (2) the molecule's separation distances larger than their size, such that we may approximate the mediator as point-like and (3) the dilute-gas limit of the Clausius–Mosotti relation as a good approximation.

To find the Green's tensor in the presence of a single chiral mediator we employ the Born–Oppenheimer approximation, see section 2.3.3. The Helmholtz equation inside a chiral medium is given by Eq. (2.72) and reads

$$\left[\nabla\times\frac{1}{\mu}\nabla\times+\frac{\omega}{c}\frac{\overline{\chi}}{\mu}\nabla\times+\frac{\omega}{c}\nabla\times\frac{\overline{\chi}}{\mu}-\frac{\omega^2}{c^2}\left(\varepsilon-\frac{\overline{\chi}^2}{\mu}\right)\right]\mathbb{G}(\boldsymbol{r},\boldsymbol{r}')=\delta(\boldsymbol{r}-\boldsymbol{r}')\mathbb{1}\,. \tag{4.121}$$

Let us assume that the deviation of $\varepsilon = 1+\zeta_{\mathrm{ee}}(\boldsymbol{r})$, $1/\mu = 1+\zeta_{mm}(\boldsymbol{r})$ and $\overline{\chi}/\mu = \mathrm{i}\zeta_{\mathrm{em}}(\boldsymbol{r})$ from their free space values are small, but at this point we allow them to be tensor valued. In free space the solution of the Helmholtz equation is given by the free-space Green's tensor (A.32), such that

$$\left[\nabla\times\nabla\times-\frac{\omega^2}{c^2}\right]\mathbb{G}^{(0)}(\boldsymbol{r},\boldsymbol{r}')=\delta(\boldsymbol{r}-\boldsymbol{r}')\mathbb{1}\,. \tag{4.122}$$

We hence can construct the solution to (4.121) via

$$\begin{aligned}\mathbb{G}(\boldsymbol{r},\boldsymbol{r}') = \mathbb{G}^{(0)}(\boldsymbol{r},\boldsymbol{r}') &- \int \mathrm{d}^3 s\, \mathbb{G}^{(0)}(\boldsymbol{r},\boldsymbol{s}) \cdot [\nabla_s \times \zeta_{\mathrm{mm}}(\boldsymbol{s}) \nabla_s \times]\, \mathbb{G}(\boldsymbol{s},\boldsymbol{r}') \\ &+ \int \mathrm{d}^3 s\, \mathbb{G}^{(0)}(\boldsymbol{r},\boldsymbol{s}) \cdot \left[\frac{\omega^2}{c^2}\zeta_{\mathrm{ee}}(\boldsymbol{s}) + \mathcal{O}(\zeta^2_{\lambda\lambda'})\right] \mathbb{G}(\boldsymbol{s},\boldsymbol{r}') \\ &+ \mathrm{i} \int \mathrm{d}^3 s\, \mathbb{G}^{(0)}(\boldsymbol{r},\boldsymbol{s}) \cdot \left[\frac{\omega}{c}\zeta_{\mathrm{em}}(\boldsymbol{s}) \nabla_s \times + \frac{\omega}{c} \nabla_s \times \zeta_{em}(\boldsymbol{s})\right] \mathbb{G}(\boldsymbol{s},\boldsymbol{r}')\,. \end{aligned} \tag{4.123}$$

In first order of $\zeta_{\lambda\lambda'}$ this can be calculated as a closed expression,

$$\begin{aligned}\mathbb{G}(\boldsymbol{r},\boldsymbol{r}') &= \mathbb{G}^{(0)}(\boldsymbol{r},\boldsymbol{r}') - \int \mathrm{d}^3 s\, \mathbb{G}^{(0)}(\boldsymbol{r},\boldsymbol{s}) \cdot [\nabla_s \times \zeta_{\mathrm{mm}}(\boldsymbol{s}) \nabla_s \times]\, \mathbb{G}^{(0)}(\boldsymbol{s},\boldsymbol{r}') \\ &\quad + \int \mathrm{d}^3 s\, \mathbb{G}^{(0)}(\boldsymbol{r},\boldsymbol{s}) \cdot \left[\frac{\omega^2}{c^2}\zeta_{\mathrm{ee}}(\boldsymbol{s}) + \mathcal{O}(\zeta^2_{\lambda\lambda'})\right] \mathbb{G}^{(0)}(\boldsymbol{s},\boldsymbol{r}') \\ &\quad + \mathrm{i} \int \mathrm{d}^3 s\, \mathbb{G}^{(0)}(\boldsymbol{r},\boldsymbol{s}) \cdot \left[\frac{\omega}{c}\zeta_{\mathrm{em}}(\boldsymbol{s}) \nabla_s \times + \frac{\omega}{c} \nabla_s \times \zeta_{\mathrm{em}}(\boldsymbol{s})\right] \mathbb{G}^{(0)}(\boldsymbol{s},\boldsymbol{r}') \\ &= \mathbb{G}^{(0)}(\boldsymbol{r},\boldsymbol{r}') + \int \mathrm{d}^3 s\, \mathbb{G}^{(0)}(\boldsymbol{r},\boldsymbol{s}) \times \nabla_s \cdot \zeta_{\mathrm{mm}}(\boldsymbol{s}) \cdot \nabla_s \times \mathbb{G}^{(0)}(\boldsymbol{s},\boldsymbol{r}') \\ &\quad + \int \mathrm{d}^3 s\, \frac{\omega^2}{c^2} \mathbb{G}^{(0)}(\boldsymbol{r},\boldsymbol{s}) \cdot \zeta_{\mathrm{ee}}(\boldsymbol{s}) \cdot \mathbb{G}^{(0)}(\boldsymbol{s},\boldsymbol{r}') \\ &\quad + \mathrm{i} \int \mathrm{d}^3 s\, \frac{\omega}{c} \mathbb{G}^{(0)}(\boldsymbol{r},\boldsymbol{s}) \cdot \zeta_{\mathrm{em}}(\boldsymbol{s}) \cdot \nabla_s \times \mathbb{G}^{(0)}(\boldsymbol{s},\boldsymbol{r}') \\ &\quad - \mathrm{i} \int \mathrm{d}^3 s\, \frac{\omega}{c} \mathbb{G}^{(0)}(\boldsymbol{r},\boldsymbol{s}) \times \nabla_s \cdot \zeta_{\mathrm{em}}(\boldsymbol{s}) \cdot \mathbb{G}^{(0)}(\boldsymbol{s},\boldsymbol{r}')\,. \end{aligned} \tag{4.124}$$

The Clausius-Mosotti law in the dilute-gas limit reads

$$\zeta_{\lambda\lambda'}(\boldsymbol{r}) = \frac{\eta(\boldsymbol{r})\boldsymbol{\alpha}_{\lambda\lambda'}}{\varepsilon_0}\,, \tag{4.125}$$

where $\boldsymbol{\alpha}_{\lambda\lambda'}$ is the dual polarisability tensor and $\eta(\boldsymbol{r})$ the number of density of atoms in the gas. We now introduce the remaining assumptions into the expression: the polarisability tensor is isotropic and hence proportional to the identity and each surrounding molecule is at a sharp position that is well approximated by a delta-distribution. We then find in lowest order of the Born-expansion the dual Green's tensor for N mediators to be

$$\mathbb{G}_{\lambda_1\lambda_2}(\boldsymbol{r}_\mathrm{A},\boldsymbol{r}_D) = \mathbb{G}^{(0)}_{\lambda_1\lambda_2}(\boldsymbol{r}_\mathrm{A},\boldsymbol{r}_D) - \sum_i^N \mathbb{G}^{\mathrm{M_i}}_{\lambda_1\lambda_2}(\boldsymbol{r}_\mathrm{A},\boldsymbol{r}_D)\,, \tag{4.126}$$

$$\mathbb{G}^{\mathrm{M}}_{\lambda_1\lambda_2}(\boldsymbol{r}_\mathrm{A},\boldsymbol{r}_D) = \sum_{\lambda,\lambda'} \frac{\alpha_{\lambda\lambda'}}{\varepsilon_0} \mathbb{G}^{(0)}_{\lambda_1\lambda}(\boldsymbol{r}_\mathrm{A},\boldsymbol{r}_\mathrm{M}) \cdot \mathbb{G}^{(0)}_{\lambda'\lambda_2}(\boldsymbol{r}_\mathrm{M},\boldsymbol{r}_\mathrm{D})\,, \tag{4.127}$$

where $\mathbb{G}^{(0)}$ is the free-space Green's tensor and the dual polarisability at the donor's

transition frequency is in analogy to its pure electric version, see Eq. (2.140) given by

$$\alpha_{\lambda\lambda'}(\omega_{\mathrm{D}}) = \frac{1}{3\hbar}\sum_k \Big(\frac{\langle 0|\boldsymbol{d}_\lambda|k\rangle \cdot \langle k|\boldsymbol{d}_{\lambda'}|0\rangle}{\omega_k + \omega_{\mathrm{D}} + \mathrm{i}\gamma_k} + \frac{\langle 0|\boldsymbol{d}_{\lambda'}|k\rangle \cdot \langle k|\boldsymbol{d}_\lambda|0\rangle}{\omega_k - \omega_{\mathrm{D}} + \mathrm{i}\gamma_k} \Big)\,, \tag{4.128}$$

where ω_k are the respective transition frequencies and $1/\gamma_k$ the respective lifetimes. Let us additionally assume that the mediator possesses a transition in resonance with ω_{D}, such that there exists a k with $\omega_k = \omega_{\mathrm{D}}$. The resonance then dominates the polarisability:

$$\alpha_{\lambda\lambda'} = \frac{1}{3\hbar}\Big(\frac{\langle 0|\boldsymbol{d}_\lambda|k\rangle \cdot \langle k|\boldsymbol{d}_{\lambda'}|0\rangle}{2\omega_{\mathrm{D}} + \mathrm{i}\gamma_k} - \mathrm{i}\frac{\langle 0|\boldsymbol{d}_{\lambda'}|k\rangle \cdot \langle k|\boldsymbol{d}_\lambda|0\rangle}{\gamma_k} \Big)\,, \tag{4.129}$$

such that $\alpha_{\mathrm{em}} = -\alpha_{\mathrm{me}} \propto R_{\mathrm{M}}$. The linewidth γ_k is given by the decay rate of state k: $\gamma_k = \sum_\lambda \omega_{\mathrm{D}}^3 |\boldsymbol{d}_\lambda|^2/(3c^3\pi\varepsilon_0\hbar)$. The decay rate γ_k is much smaller than the eigenfrequency $\omega_k = \omega_{\mathrm{D}}$, hence $\mathrm{Re}\alpha_{\lambda\lambda'} \ll \mathrm{Im}\alpha_{\lambda\lambda'}$. We focus on the case of only one mediator molecule. Using the general rate equation (4.17) together with the Green's tensor given by Eq. (4.126) we can calculate the rate and divide it into three different parts, such that

$$\Gamma = \Gamma_{\mathrm{DA}} + \Gamma_{\mathrm{DA-DMA}} + \Gamma_{\mathrm{DMA}}\,, \tag{4.130}$$

$$\Gamma_{\mathrm{DA}} = \sum \Gamma_{\lambda_1\lambda_2\lambda_3\lambda_4}\,, \tag{4.131}$$

$$\Gamma_{\mathrm{DA-DMA}} = \sum \Gamma^{\lambda_a\lambda_b}_{\lambda_1\lambda_2\lambda_3\lambda_4}\,, \tag{4.132}$$

$$\Gamma_{\mathrm{DMA}} = \sum \Gamma^{\lambda_a\lambda_b\lambda_c\lambda_d}_{\lambda_1\lambda_2\lambda_3\lambda_4}\,, \tag{4.133}$$

where Γ_{DA} and Γ_{DMA} are the rates from direct and mediated transfer, respectively, and $\Gamma_{\mathrm{DA-DMA}}$ is their interference term. The individual contributions are given by

$$\Gamma_{\lambda_1\lambda_2\lambda_3\lambda_4} = \frac{2\pi\rho\mu_0^2}{9\hbar^2}(\boldsymbol{d}^{\mathrm{A}}_{\lambda_1}\cdot\boldsymbol{d}^{\mathrm{A}*}_{\lambda_2})(\boldsymbol{d}^{\mathrm{D}*}_{\lambda_3}\cdot\boldsymbol{d}^{\mathrm{D}}_{\lambda_4})\,\mathrm{Tr}\left[\mathbb{G}^{(0)}_{\lambda_1\lambda_4}(\boldsymbol{r}_{\mathrm{A}},\boldsymbol{r}_{\mathrm{D}})\cdot\mathbb{G}^{(0)*T}_{\lambda_2\lambda_3}(\boldsymbol{r}_{\mathrm{A}},\boldsymbol{r}_{\mathrm{D}})\right]\,, \tag{4.134}$$

$$\begin{aligned}\Gamma^{\lambda_a\lambda_b}_{\lambda_1\lambda_2\lambda_3\lambda_4} = {}& \frac{2\pi\rho\mu_0^2}{9\hbar^2}(\boldsymbol{d}^{\mathrm{A}}_{\lambda_1}\cdot\boldsymbol{d}^{\mathrm{A}*}_{\lambda_2})(\boldsymbol{d}^{\mathrm{D}*}_{\lambda_3}\cdot\boldsymbol{d}^{\mathrm{D}}_{\lambda_4})\alpha_{\lambda_a\lambda_b}\\ &\times\mathrm{Tr}\left[\mathbb{G}^{(0)}_{\lambda_1\lambda_4}(\boldsymbol{r}_{\mathrm{A}},\boldsymbol{r}_{\mathrm{D}})\cdot\mathbb{G}^{(0)*T}_{\lambda_a\lambda_3}(\boldsymbol{r}_{\mathrm{M}},\boldsymbol{r}_{\mathrm{D}})\cdot\mathbb{G}^{(0)*T}_{\lambda_2\lambda_b}(\boldsymbol{r}_{\mathrm{A}},\boldsymbol{r}_{\mathrm{M}})\right] + \mathrm{c.c.}\,,\end{aligned} \tag{4.135}$$

$$\begin{aligned}\Gamma^{\lambda_a\lambda_b\lambda_c\lambda_d}_{\lambda_1\lambda_2\lambda_3\lambda_4} = {}& \frac{2\pi\rho\mu_0^2}{9\hbar^2}(\boldsymbol{d}^{\mathrm{A}}_{\lambda_1}\cdot\boldsymbol{d}^{\mathrm{A}*}_{\lambda_2})(\boldsymbol{d}^{\mathrm{D}*}_{\lambda_3}\cdot\boldsymbol{d}^{\mathrm{D}}_{\lambda_4})\alpha_{\lambda_a\lambda_b}\alpha_{\lambda_c\lambda_d}\\ &\times\mathrm{Tr}\left[\mathbb{G}^{(0)}_{\lambda_1\lambda_d}(\boldsymbol{r}_{\mathrm{A}},\boldsymbol{r}_{\mathrm{M}})\cdot\mathbb{G}^{(0)}_{\lambda_c\lambda_4}(\boldsymbol{r}_{\mathrm{M}},\boldsymbol{r}_{\mathrm{D}})\cdot\mathbb{G}^{(0)*T}_{\lambda_a\lambda_3}(\boldsymbol{r}_{\mathrm{M}},\boldsymbol{r}_{\mathrm{D}})\cdot\mathbb{G}^{(0)*T}_{\lambda_2\lambda_b}(\boldsymbol{r}_{\mathrm{A}},\boldsymbol{r}_{\mathrm{M}})\right].\end{aligned} \tag{4.136}$$

We find that several contributions vanish. As in the free-space case, we find that

$$\Gamma_{\mathrm{em}\lambda\lambda} = \Gamma_{\mathrm{me}\lambda\lambda} = \Gamma_{\lambda\lambda\mathrm{em}} = \Gamma_{\lambda\lambda\mathrm{me}} = 0 \tag{4.137}$$

in agreement with the Curie symmetry principle.

In principle we might expect terms that depend on all three handednesses. However, these contributions vanish. This may again be explained via the Curie symmetry principle. We prove this by contradiction: Let us assume that contributions proportional to $R_\mathrm{A} R_\mathrm{D} R_\mathrm{M}$ do not vanish and let us assume we do not know any participant's handedness. Then we would find that the rate involving only left-handed molecules Γ_{LLL} contains a positive term proportional to $R_\mathrm{A} R_\mathrm{D} R_\mathrm{M}$, while Γ_{RRR} contains the same term with opposite sign. Hence one could measure $\Gamma_{\mathrm{LLL}} > \Gamma_{\mathrm{RRR}}$ and would be able to distinguish these two cases without prior knowledge of any handedness. This would be in contradiction to the Curie symmetry principle and we can conclude that these contributions need to vanish for any system.

In case of an unknown acceptor enantiomer we hence obtain two different discriminatory rates, one where the donor discriminates the acceptor $\Gamma^\mathrm{D}_\mathrm{disc} \propto R_\mathrm{A} R_\mathrm{D}$ and one where the mediator discriminates the acceptor $\Gamma^\mathrm{M}_\mathrm{disc} \propto R_\mathrm{A} R_\mathrm{M}$. They are given by

$$\begin{aligned}\Gamma^\mathrm{D}_\mathrm{disc} = \sum \big[&\Gamma_{\mathrm{emem}} + \Gamma_{\mathrm{meem}} + \Gamma_{\mathrm{meme}} + \Gamma_{\mathrm{emme}} \\ &+ \Gamma^{\lambda\lambda}_{\mathrm{emem}} + \Gamma^{\lambda\lambda}_{\mathrm{meem}} + \Gamma^{\lambda\lambda}_{\mathrm{meme}} + \Gamma^{\lambda\lambda}_{\mathrm{emme}} \\ &+ \Gamma^{\lambda\lambda\lambda'\lambda'}_{\mathrm{emem}} + \Gamma^{\lambda\lambda\lambda'\lambda'}_{\mathrm{meem}} + \Gamma^{\lambda\lambda\lambda'\lambda'}_{\mathrm{meme}} + \Gamma^{\lambda\lambda\lambda'\lambda'}_{\mathrm{emme}} + \Gamma^{\lambda_1\lambda_2\lambda_1\lambda_2}_{\mathrm{meme}} + \Gamma^{\lambda_1\lambda_2\lambda_2\lambda_1}_{\mathrm{emme}}\big]\,,\end{aligned} \tag{4.138}$$

with $\lambda_1 \neq \lambda_2$ and

$$\begin{aligned}\Gamma^\mathrm{M}_\mathrm{disc} = \sum \big[&\Gamma^{\mathrm{em}}_{\mathrm{em}\lambda\lambda} + \Gamma^{\mathrm{me}}_{\mathrm{em}\lambda\lambda} + \Gamma^{\mathrm{em}}_{\mathrm{me}\lambda\lambda} + \Gamma^{\mathrm{me}}_{\mathrm{me}\lambda\lambda} \\ &+ \Gamma^{\mathrm{em}\lambda'\lambda'}_{\mathrm{em}\lambda\lambda} + \Gamma^{\mathrm{me}\lambda'\lambda'}_{\mathrm{em}\lambda\lambda} + \Gamma^{\mathrm{em}\lambda'\lambda'}_{\mathrm{me}\lambda\lambda} + \Gamma^{\mathrm{me}\lambda'\lambda'}_{\mathrm{me}\lambda\lambda} \\ &+ \Gamma^{\lambda'\lambda'\mathrm{em}}_{\mathrm{em}\lambda\lambda} + \Gamma^{\lambda'\lambda'\mathrm{me}}_{\mathrm{em}\lambda\lambda} + \Gamma^{\lambda'\lambda'\mathrm{em}}_{\mathrm{me}\lambda\lambda} + \Gamma^{\lambda'\lambda'\mathrm{me}}_{\mathrm{me}\lambda\lambda}\big]\,.\end{aligned} \tag{4.139}$$

The remaining non-vanishing contributions form the nondiscriminatory rate, Γ_{nd}.

In the nonretarded regime ($r_i\omega/c \ll 1$ for all intermolecular distances) the discriminatory and nondiscriminatory rate contributions are dominated by terms of Γ_{DMA}, that are of the form of Eq. (4.136). The degree of discrimination in the this limit is independent

of the specific geometry and reads

$$S_{r\to 0} = S^{\mathrm{M}}_{r\to 0} + S^{\mathrm{D}}_{r\to 0} \tag{4.140}$$

$$S^{\mathrm{M}}_{r\to 0} = \frac{2R_{\mathrm{A}}R_{\mathrm{M}}\left(|\boldsymbol{d}^{\mathrm{D}}_{\mathrm{e}}|^2|\boldsymbol{d}^{\mathrm{M}}_{\mathrm{e}}|^2 + |\boldsymbol{d}^{\mathrm{D}}_{\mathrm{m}}|^2|\boldsymbol{d}^{\mathrm{M}}_{\mathrm{m}}|^2\right)}{D}, \tag{4.141}$$

$$S^{\mathrm{D}}_{r\to 0} = \frac{2R_{\mathrm{A}}R_{\mathrm{D}}\left(|\boldsymbol{d}^{\mathrm{M}}_{\mathrm{e}}|^2|\boldsymbol{d}^{\mathrm{M}}_{\mathrm{m}}|^2 + R^2_{\mathrm{M}}/c^2\right)}{D}, \tag{4.142}$$

$$\begin{aligned} D = {} & c^2|\boldsymbol{d}^{\mathrm{A}}_{\mathrm{e}}|^2|\boldsymbol{d}^{\mathrm{D}}_{\mathrm{e}}|^2|\boldsymbol{d}^{\mathrm{M}}_{\mathrm{e}}|^4 + 2|\boldsymbol{d}^{\mathrm{A}}_{\mathrm{e}}|^2|\boldsymbol{d}^{\mathrm{M}}_{\mathrm{e}}|^2R_{\mathrm{D}}R_{\mathrm{M}} + |\boldsymbol{d}^{\mathrm{A}}_{\mathrm{e}}|^2|\boldsymbol{d}^{\mathrm{D}}_{\mathrm{m}}|^2R^2_{\mathrm{M}} \\ & + |\boldsymbol{d}^{\mathrm{D}}_{\mathrm{e}}|^2|\boldsymbol{d}^{\mathrm{A}}_{\mathrm{m}}|^2R^2_{\mathrm{M}} + 2|\boldsymbol{d}^{\mathrm{A}}_{\mathrm{m}}|^2|\boldsymbol{d}^{\mathrm{M}}_{\mathrm{m}}|^2R_{\mathrm{D}}R_{\mathrm{M}} + c^2|\boldsymbol{d}^{\mathrm{A}}_{\mathrm{m}}|^2|\boldsymbol{d}^{\mathrm{D}}_{\mathrm{m}}|^2|\boldsymbol{d}^{\mathrm{M}}_{\mathrm{m}}|^4, \end{aligned} \tag{4.143}$$

where we defined $S^{\mathrm{M/D}}$ as the degree of discrimination due to the active discrimination by the mediator/donor. Even with an achiral donor molecule ($R_{\mathrm{D}} = 0 \Rightarrow S^{\mathrm{D}} = 0$) the acceptor can be discriminated by the mediator and in the nonretarded limit the degree of discrimination due to the mediator $S^{\mathrm{M}}_{r\to 0}(R_{\mathrm{D}} = 0)$ is the same as the free space degree of discrimination with a chiral donor, see Eq. (4.99). Since usually $|\boldsymbol{d}_{\mathrm{e}}| \gg |\boldsymbol{d}_{\mathrm{m}}|$ the mediator's discrimination $S^{\mathrm{M}}_{r\to 0}$ dominates even if the donor is chiral itself. Hence, the degree of discrimination in the nonretarded limit $S_{r\to 0} \approx S^{\mathrm{M}}_{r\to 0}$ is approximately not affected by the mediator's presence in the nonretarded limit. When the mediator is achiral ($R_{\mathrm{M}} = 0 \Rightarrow S^{\mathrm{M}} = 0$) the degree of discrimination is even suppressed by the mediator in the nonretarded limit as the nondiscriminatory rate is more enhanced than the discriminatory rate. In contrast, in the retarded limit (applied to all distances) the rate is dominated by Γ_{DA}. The degree of discrimination in this limit is therefore approximately the same as without the mediator, see Eq. (4.99).

Between these two distance limits, applied to all intermolecular distances, the impact of the additional mediator onto the system depends on the specific geometry. In general the presence of the mediator has two effects. It influences the total rate of RET as well as the degree of discrimination. In Fig. 4.12 and Fig. 4.13 the impact of the mediator on both are shown for the example of 3MCP. In Fig. 4.12 donor and acceptor are placed at a nonretarded distance to each other, $r_{\mathrm{DA}}\omega_{\mathrm{D}}/c = 0.1$ while in the Fig. 4.13 they are placed at a retarded distance $r_{\mathrm{DA}}\omega/c = 5$. While in the nonretarded geometry any mediator position enhances the total RET rate significantly, the degree of discrimination only changes up to $\pm 3\%$ compared to the free space rate. However, in the retarded geometry a single mediator molecule may enhance the degree of discrimination significantly. A preferable position would be in between donor and acceptor, where the total rate may be enhanced by a factor of 2 while the degree of discrimination gains around 50% compared to the free-space case.

In this section we focussed on the process where the excitation is transferred to the acceptor within the considered order of perturbation. Especially when considering a mediator that is in resonance with the transferred energy, the mediator itself can become

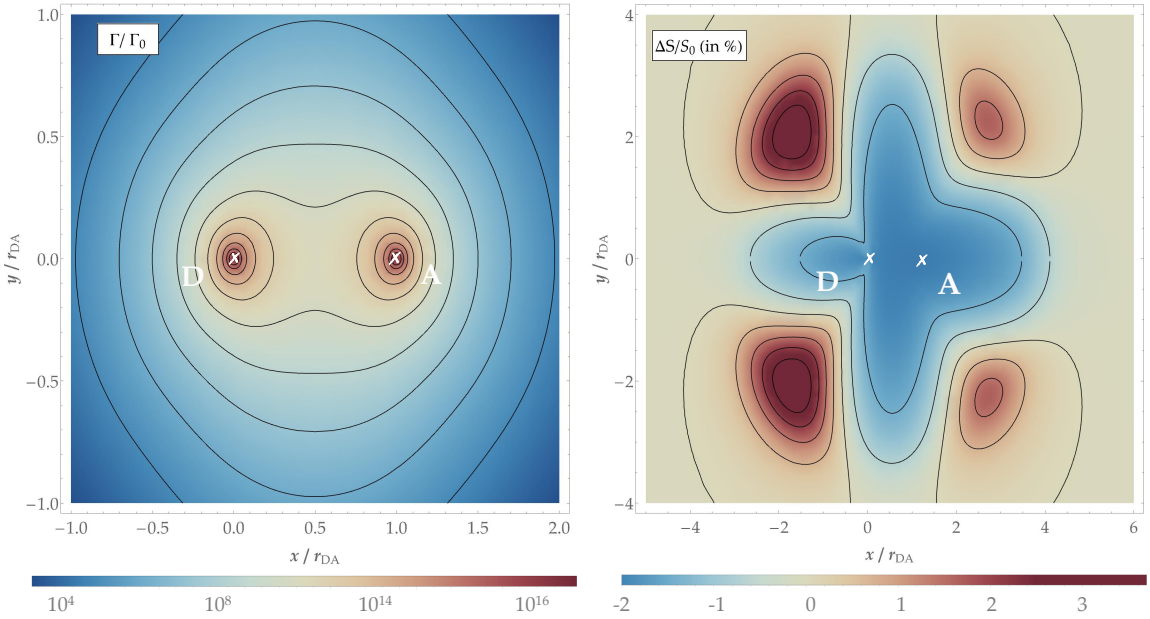

Figure 4.12.: Influence of the mediator in the nonretarded regime as a function of its position for the example of donor, acceptor and mediator being 3MCP. Donor and acceptor are placed on the x-axis at $x_D = 0$ and $x_A = 0.1c/\omega \approx 5$ nm. **Left:** The rate Γ in the presence of the mediator relative to the rate Γ_0 without the mediator as a function of the mediators position. **Right:** The change in the the degree of discrimination $\Delta S = S - S_0$ in the presence of the mediator relative to the degree of discrimination S_0 without the mediator.

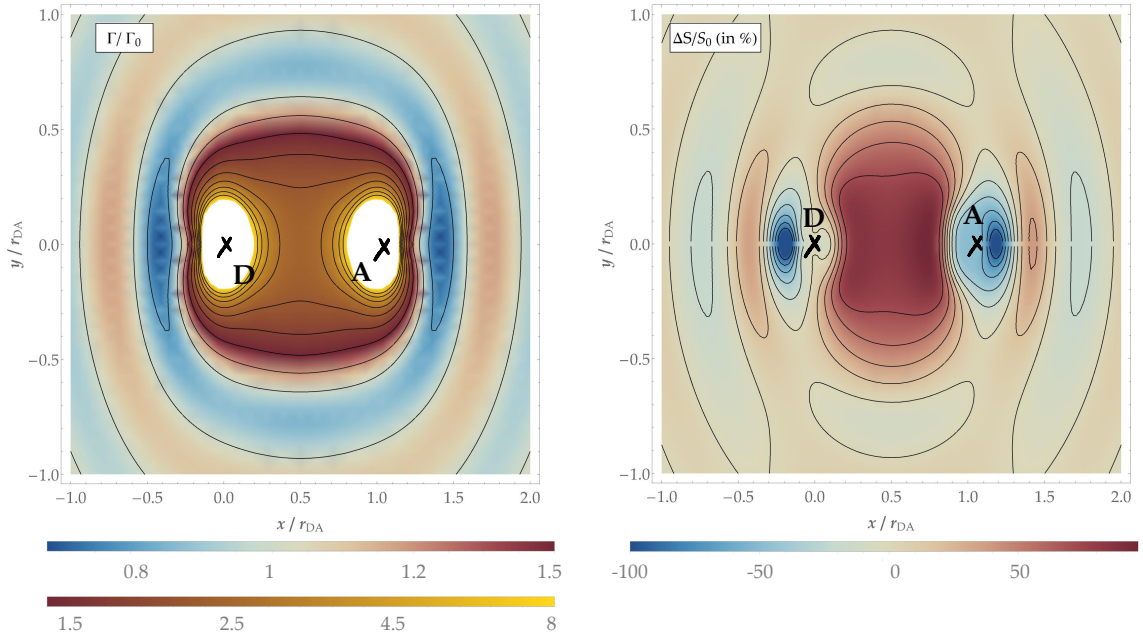

Figure 4.13.: Influence of the mediator in the retarded regime as a function of its position for the example of donor, acceptor and mediator being 3MCP. Donor and acceptor are placed on the x-axis at $x_D = 0$ and $x_A = 5c/\omega \approx 230$ nm. **Left:** The rate Γ in the presence of the mediator relative to the rate Γ_0 without the mediator as a function of the mediators position. **Right:** The change in the the degree of discrimination $\Delta S = S - S_0$ in the presence of the mediator relative to the degree of discrimination S_0 without the mediator.

the acceptor. Additional processes and higher multipoles (such as quadrupoles) have been considered in (chiral) resonance energy transfer in the presence of an achiral mediator [55].

4.4. Conclusion

Resonance energy transfer can be used to discriminate between left- and right-handed molecules, provided that an object with known handedness participates in the process. In our framework, we have recovered the known result that a chiral donor with known handedness can discriminate a chiral acceptor in free space. RET between same-handed molecules is more probable than that between opposite-handed ones. The magnitude of the degree of discrimination depends entirely on the involved electric and magnetic transition dipoles and the intermolecular distance. While the rate itself rapidly decreases with distance, the discrimination itself roughly doubles in the retarded regime of large distances. We derived analytical expressions to consider a continuous medium surrounding the system. We showed that an appropriate medium may enhance the discrimination significantly and discussed the importance of local-field effects onto the correct prediction of the discrimination. We showed that in theory a suitable medium may lead to maximum discrimination, where RET only takes place between same-handed molecules, but also that an appropriate medium can inverse the discriminatory effect in the non-retarded limit, such that the opposite-handed rate is larger than the same-handed one. Since this is only the case for small distances, the discrimination changes its direction as a function of separation distances in such a medium. We worked out the local-field correction in the Onsager real-cavity model for chiral media, in which left- and right-circularly polarised light propagates differently. We showed that a chiral medium with known handedness can itself be used to actively discriminate chiral acceptors, even for achiral donor molecules. The local-field correction of a chiral medium was shown to have a nontrivial impact on the degree of discrimination. The discrimination may change its direction as a function of the separation distance solely because of local-field effects. A similar effect was studied in 2017 by Barcellona et al., where a chiral surface is considered to assist the discriminating Van-der-Waals force between two chiral molecules [180]. Also here, depending on the system–surface distance the chiral medium could result in an either additional attractive or repulsive force, while the sign of the free-space force between the chiral molecules is distance-independent. We discussed a large parameter space of media properties, where recent advances in designing different exotic media based on metamaterials might provide applications with interesting properties in the future [178].

Finally, we have considered the limit of dilute gases where the medium is instead modelled as N surrounding mediator molecules. We calculated the discrimination in the presence of a single chiral mediator molecule as a function of the molecule's positions. In the nonretarded limit, the rate is completely dominated by the mediated transfer. Assuming that donor and mediator are the same chiral molecule with known handedness, the discrimination is approximately unaffected in the nonretarded limit. An achiral mediator even suppresses the discrimination in this limit. In the retarded limit, the mediated transfer becomes negligible and the discrimination is the same as in free space. In between these two limits the discrimination is given by nontrivial position dependent functions. In general, in the distance-regime close to the retarded limit the discrimination is much more affected by the mediator as in its counter regime of small distances. For the example of 3MCP we found that in the regime close to the retarded limit, the discrimination can be roughly doubled by a single mediator, when placing the mediator in the center between the donor and the acceptor molecule.

We have used the Onsager model of the real cavity here to account for local-field effects in chiral media. The effects of the resulting corrections on the discrimination are nontrivial. Future work should investigate other models for local-field correction, such as the virtual cavity model. It would be interesting to see if they lead to similar consequences for the discrimination. While here we have studied the effects of a solvent permeating the molecules, the analysis can be extended to solids separating donor and acceptor molecules. Thanks to metamaterials, such a system, where the solid can have exotic properties, could be quite easily accessible experimentally.

Open quantum systems approach to resonance energy transfer

5

While Fermi's golden rule offers a simple way of obtaining the rate of a given process in its lowest order via perturbation theory, an open quantum systems approach allows in principle for an nonperturbative analysis of the system's dynamics. In this chapter, we derive the transfer rate via open quantum system methods as an alternative to Fermi's golden rule and show how the mixture of both, perturbative methods and open quantum systems, can lead to new insights into the studied dynamics. The work presented here marks the starting point of a study where both frameworks shall be used in conjunction with each other, exploiting each framework's strength, to study energy transfer processes in the presence of macroscopic media.

We start by deriving the elementary spontaneous decay rate and resonance energy transfer (RET) rate first from Fermi's golden rule in section 5.1, then from an open quantum systems approach in section 5.2, where we also employ perturbative calculations for the RET rate. We show that both approaches yield the same result, although based on slightly different assumptions.

In section 5.3.1, we develop an alternative perturbation scheme from the master equation by splitting the master equation in an alternative way into homogeneous and inhomogeneous parts. The incoherent but homogeneous part of the master equation in this scheme is then solved nonperturbatively. We hence call the scheme incoherent perturbation scheme. The incoherent perturbation scheme can then lead to corrections to a variety of quantities by means of energy shifts and damping constants in comparison to the ordinary perturbation scheme.

As an important but simple example, we show in section 5.3.2 the impact of the incoherent perturbation scheme on the polarisability tensor. Similarly, other quantities have been shown to be corrected by the system's incoherent dynamics as well. In particular in the calculation of Van-der-Waals forces between an excited and a ground state particle, it was shown that two different results can be obtained depending on whether damping constants are included or not. These two complementary results derived in several works can be interpreted as one being the force acting on the ground state particle, while one acts on the excited one [181–187]. Due to the additional recoil the excited particle

experiences when spontaneously emitting a photon the force on the two particles is not necessarily symmetric. We show in section 5.3.3 that the full decay rate of a two-particle resonant system shows an analogous behaviour: when considering spontaneous decay explicitly as part of the decay the full decay rate of the donor oscillates as a function of the donor–acceptor distance while the full transition rate of the acceptor behaves monotonically as a function of distance.

To be able to describe incoherent dynamics of the system's state, the open quantum systems approach requires the use of density matrices. Fermi's golden rule however is usually formulated for pure states. In the last section of this chapter we extend Fermi's golden rule to density matrices and hence mixed states and derive from this as an application example superradiant resonance energy transfer as a function of the degree of entanglement between two donor particles sharing one excitation.

5.1. Fermi's golden rule approach

We start this chapter by deriving the RET rate and spontaneous decay rate via Fermi's golden rule. Fermi's golden rule is most commonly used for transition rates of various kinds due to its simplicity and is based on perturbation theory. Its compact form is its strength but also its weakness. It does not allow for a lot of adjustment. As we will see in comparison to the open quantum systems approach that follows thereafter, the method via Fermi's golden rule is much faster. The calculation shown in this section in detail has been outlined in the theoretical background in section 2.3.5 and 2.3.6. In section 5.2, we use the rate expressions obtained here for comparison with the ones obtained via an open quantum systems approach and in section 5.4 we extent Fermi's golden rule to density matrices and employ the results of this section to derive superradiant RET.

A process rate via Fermi's golden rule, see section 2.2.2, is given by

$$\Gamma = \sum_f \frac{2\pi}{\hbar^4} \delta(\omega_f - \omega_i) \left| M_{fi} \right|^2 , \tag{5.1}$$

where M_{fi} is the transition matrix element. Using perturbation theory, see section 2.2.2 we can calculate M_{fi} in different orders. In first and second order it is given by

$$M_{fi}^{(1)} = \left\langle f \left| \hat{H}_{\text{ia}} \right| i \right\rangle , \tag{5.2}$$

$$M_{fi}^{(2)} = \sum_k \frac{\left\langle f \left| \hat{H}_{\text{ia}} \right| k \right\rangle \left\langle k \left| \hat{H}_{\text{ia}} \right| i \right\rangle}{\omega_i - \omega_k} , \tag{5.3}$$

with $|i\rangle$, $|f\rangle$ and $|k\rangle$ being the initial, final and intermediate states, respectively.

We first revisit the derivation of the spontaneous decay rate Γ_s in vacuum in detail, see section 2.3.5. Spontaneous decay is a first-order process on the level of transition matrix elements for a single excited particle. Its initial and final states are given by

$$|i\rangle = |e\rangle_\mathrm{A}\,|\{0\}\rangle_\mathrm{F}\,, \tag{5.4}$$

$$|f\rangle = |g\rangle_\mathrm{A}\,|\mathbf{1}_\lambda(\boldsymbol{r},\omega)\rangle_\mathrm{F}\,, \tag{5.5}$$

where $|\cdot\rangle_{\mathrm{A/F}}$ is the atomic/field state. We only consider electric coupling of the multipolar coupling Hamiltonian in the long-wavelength approximation,

$$\hat{H}_\mathrm{ia} = -\hat{\boldsymbol{d}}\cdot\hat{\boldsymbol{E}}\,. \tag{5.6}$$

In our decomposition the single Fock state $|\mathbf{1}_\lambda(\boldsymbol{r},\omega)\rangle_\mathrm{F}$ is vector-valued in position space. Each vector component of the transition element then reads

$$\begin{aligned}
\langle f|\hat{H}_\mathrm{ia}|i\rangle_l &= -\langle g|\hat{\boldsymbol{d}}|e\rangle\cdot\langle\mathbf{1}_\lambda^{(l)}(\boldsymbol{r},\omega)|\hat{\boldsymbol{E}}(\boldsymbol{r}_\mathrm{A})|\{0\}\rangle\\
&= -\sum_{\lambda'}\int \mathrm{d}^3r'\int \mathrm{d}\omega'\boldsymbol{d}_{ge}^{(i)}\,\mathbb{G}_{\lambda'}^{(ij)*}(\boldsymbol{r}_\mathrm{A},\boldsymbol{r}',\omega')\,\langle\{0\}|\hat{\boldsymbol{f}}_\lambda^{(l)}(\boldsymbol{r},\omega))\hat{\boldsymbol{f}}_{\lambda'}^{(j)\dagger}(\boldsymbol{r}',\omega')|\{0\}\rangle\\
&= -\sum_{\lambda'}\int \mathrm{d}^3r'\int \mathrm{d}\omega'\boldsymbol{d}_{ge}^{(i)}\,\mathbb{G}_{\lambda'}^{(ij)*}(\boldsymbol{r}_\mathrm{A},\boldsymbol{r}',\omega')\,\delta_{lj}\delta(\boldsymbol{r}-\boldsymbol{r}')\delta(\omega-\omega')\delta_{\lambda\lambda'}\\
&= -\left[\boldsymbol{d}_{ge}\cdot\mathbb{G}_\lambda^{T*}(\boldsymbol{r},\boldsymbol{r}_\mathrm{A},\omega)\right]_l\,,
\end{aligned} \tag{5.7}$$

where we have used the properties of the field's fundamental operators, see Eqs. (2.46)–(2.48) and the Onsager reciprocity (2.37). This yields for the spontaneous emission rate

$$\begin{aligned}
\Gamma_\mathrm{s} &= \frac{2\pi}{\hbar^2}\sum_\lambda\int \mathrm{d}^3r\int \mathrm{d}\omega\delta(\omega-\omega_{eg})\boldsymbol{d}_{eg}\cdot\mathbb{G}(\boldsymbol{r}_\mathrm{A},\boldsymbol{r},\omega)\otimes\mathbb{G}^{T*}(\boldsymbol{r},\boldsymbol{r}_\mathrm{A},\omega)\cdot\boldsymbol{d}_{ge}\\
&= \frac{2\mu_0}{\hbar}\omega_{eg}^2\boldsymbol{d}_{eg}\cdot\mathrm{Im}\mathbb{G}(\boldsymbol{r}_\mathrm{A},\boldsymbol{r}_\mathrm{A},\omega_{eg})\cdot\boldsymbol{d}_{ge}\,,
\end{aligned} \tag{5.8}$$

where we have used the Green's tensor's integral relation (2.38). In free space, we recover the usual result, see Eq. (2.160) by substitutiting the free-space Green's tensor (A.32) into the equation,

$$\Gamma_\mathrm{s}^{(0)} = \gamma_{eg} = \frac{\omega_{eg}^3|\boldsymbol{d}_{eg}|^2}{3\pi\varepsilon_0\hbar c^3}\,. \tag{5.9}$$

Next, we revisit the derivation of the RET rate Γ_ret in detail, see section 2.3.6. RET is a second-order process on the level of transition matrix elements and requires two particles

in the field. Its initial, final and intermediate states are given by

$$|i\rangle = |e,0,\{0\}\rangle \ , \tag{5.10}$$

$$|f\rangle = |g,1,\{0\}\rangle \ , \tag{5.11}$$

$$|k\rangle \in \left\{ |g,0,\mathbf{1}_\lambda(\boldsymbol{r},\omega)\rangle \ , |e,1,\mathbf{1}_\lambda(\boldsymbol{r},\omega)\rangle \,\middle|\, \forall\lambda,\boldsymbol{r},\omega \right\} \ , \tag{5.12}$$

where $|n,m,l\rangle = |n\rangle_\mathrm{D}\,|m\rangle_\mathrm{A}\,|l\rangle_\mathrm{F}$ is the product state of donor, acceptor and field state. The transition element then reads in second order

$$\begin{aligned} M_{fi}^{(2)} = -\int\mathrm{d}\omega'\int\mathrm{d}^3r'\Big[\langle g|\hat{\boldsymbol{d}}^\mathrm{D}|e\rangle_\mathrm{D} \cdot \frac{\langle\{0\}|\hat{\boldsymbol{E}}(\boldsymbol{r}_\mathrm{D})|\mathbf{1}'\rangle_\mathrm{F}\,\langle\mathbf{1}'|\hat{\boldsymbol{E}}(\boldsymbol{r}_\mathrm{A})|\{0\}\rangle_\mathrm{F}}{\omega'+\omega_{10}} \cdot \langle 1|\hat{\boldsymbol{d}}^\mathrm{A}|0\rangle_\mathrm{A} \\ + \langle 1|\hat{\boldsymbol{d}}^\mathrm{A}|0\rangle_\mathrm{A} \cdot \frac{\langle\{0\}|\hat{\boldsymbol{E}}(\boldsymbol{r}_\mathrm{A})|\mathbf{1}'\rangle_\mathrm{F}\,\langle\mathbf{1}'|\hat{\boldsymbol{E}}(\boldsymbol{r}_\mathrm{D})|\{0\}\rangle_\mathrm{F}}{\omega'-\omega_{eg}} \cdot \langle g|\hat{\boldsymbol{d}}^\mathrm{D}|e\rangle_\mathrm{D} \Big] , \end{aligned} \tag{5.13}$$

where $|\mathbf{1}'\rangle = |\mathbf{1}_{\lambda'}(\omega',\boldsymbol{r}')\rangle$ and $\omega_{ab} = \omega_a - \omega_b$ and because of the resonance constraint $\omega_i = \omega_f$ in Fermi's golden rule (5.1) it follows that $\omega_{eg} = \omega_{10}$. With the relation (see proof in appendix A.2)

$$\begin{aligned} \int\mathrm{d}\omega'\int\mathrm{d}^3r'\sum_{\lambda'}\frac{\langle\{0\}|\hat{\boldsymbol{E}}(\boldsymbol{r}_\alpha)|\mathbf{1}'\rangle\,\langle\mathbf{1}'|\hat{\boldsymbol{E}}(\boldsymbol{r}_\beta)|\{0\}\rangle}{\omega'+\omega_{10}} \\ = \iint\mathrm{d}\omega_1\mathrm{d}\omega_2\frac{\langle\hat{\boldsymbol{E}}(\omega_1,\boldsymbol{r}_\alpha)\hat{\boldsymbol{E}}^\dagger(\omega_2,\boldsymbol{r}_\beta)\rangle_\mathrm{vac}}{\omega_2+\omega_{10}} \\ = \int\mathrm{d}\omega\frac{\hbar\mu_0}{\pi}\frac{\omega^2}{\omega+\omega_{10}}\mathrm{Im}\mathbb{G}(\boldsymbol{r}_\alpha,\boldsymbol{r}_\beta,\omega) \end{aligned} \tag{5.14}$$

we find

$$\begin{aligned} M_{fi}^{(2)} &= -\iint\mathrm{d}\omega_1\mathrm{d}\omega_2\left(\frac{1}{\omega_2-\omega_{10}}+\frac{1}{\omega_2+\omega_{10}}\right) \\ &\qquad \times\boldsymbol{d}_{10}\cdot\langle\hat{\boldsymbol{E}}_e(\omega_1,\boldsymbol{r}_\mathrm{A})\hat{\boldsymbol{E}}_e^\dagger(\omega_2,\boldsymbol{r}_\mathrm{D})\rangle_\mathrm{vac}\cdot\boldsymbol{d}_{ge} \qquad (5.15) \\ &= -\frac{\hbar\mu_0}{\pi}\int\mathrm{d}\omega\left(\frac{\omega^2}{\omega-\omega_{10}}+\frac{\omega^2}{\omega+\omega_{10}}\right)\boldsymbol{d}_{10}\cdot\mathrm{Im}\mathbb{G}(\boldsymbol{r}_\mathrm{A},\boldsymbol{r}_\mathrm{D},\omega)\cdot\boldsymbol{d}_{ge}\,, \qquad (5.16) \end{aligned}$$

where we have introduced the transition dipole moments $\boldsymbol{d}_{10} = \langle 1|\hat{\boldsymbol{d}}^\mathrm{A}|0\rangle_\mathrm{A}$ and $\boldsymbol{d}_{ge} = \langle g|\hat{\boldsymbol{d}}^\mathrm{D}|e\rangle_\mathrm{D}$ and used the Onsager reciprocity of the fields correlation, i.e. of the Green's tensor. The first term in M_{fi} contains a pole on the real axis and hence diverges, which stems from the time-independent perturbation treatment. Revisiting its derivation, see section 2.2.2, one can regularise the pole accordingly via adiabatic switching and finds

(see proof in appendix A.4)

$$\lim_{\varepsilon\to 0}\int \mathrm{d}\omega \left(\frac{\omega^2}{\omega-(\omega_{10}+\mathrm{i}\epsilon)}+\frac{\omega^2}{\omega+\omega_{10}}\right)\mathrm{Im}\mathbb{G}=\pi\omega_{10}^2\mathbb{G}(\omega_{10})\,. \tag{5.17}$$

And this finally results in the transition matrix element

$$M_{fi}^{(2)}=-\hbar\mu_0\omega_{10}^2\boldsymbol{d}^{\mathrm{A}}\cdot\mathbb{G}(\boldsymbol{r}_{\mathrm{A}},\boldsymbol{r}_{\mathrm{D}},\omega_{10})\cdot\boldsymbol{d}^{\mathrm{D}}\,, \tag{5.18}$$

and hence the rate:

$$\Gamma_{\mathrm{ret}}=\sum_f\delta(\omega_{eg}-\omega_{10})\frac{2\pi\mu_0\omega_{10}^2}{\hbar^2}\left|\boldsymbol{d}_{10}\cdot\mathbb{G}(\boldsymbol{r}_{\mathrm{A}},\boldsymbol{r}_{\mathrm{D}},\omega_{10})\cdot\boldsymbol{d}_{ge}\right|^2\,. \tag{5.19}$$

We may further simplify this result by assuming isotropic dipole moments. The isotropy can be either the result of so-called isotropic averaging, where we assume that the two interacting particle do not have a specific orientation to each other or from isotropic degenerate states in the sum over all final states. In both cases we find that isotropic transition dipoles can be approximated by $\boldsymbol{d}\otimes\boldsymbol{d}=|\boldsymbol{d}|^2\mathbb{I}/3$. With this we can simplify the RET rate further

$$\begin{aligned}\Gamma_{\mathrm{ret}}&=\sum_f\delta(\omega_{eg}-\omega_{10})\frac{2\pi\mu_0\omega_{10}^2}{\hbar^2}\,\mathrm{Tr}\left[\boldsymbol{d}_{10}\cdot\mathbb{G}(\boldsymbol{r}_{\mathrm{A}},\boldsymbol{r}_{\mathrm{D}},\omega_{10})\cdot\boldsymbol{d}_{ge}\otimes\boldsymbol{d}_{eg}\cdot\mathbb{G}^*(\boldsymbol{r}_{\mathrm{D}},\boldsymbol{r}_{\mathrm{A}},\omega_{10})\cdot\boldsymbol{d}_{01}\right]\\&=\sum_f\delta(\omega_{eg}-\omega_{10})\frac{2\pi\mu_0\omega_{10}^2|\boldsymbol{d}_{eg}|^2|\boldsymbol{d}_{10}|^2}{9\hbar^2}\,\mathrm{Tr}\left[\mathbb{G}(\boldsymbol{r}_{\mathrm{A}},\boldsymbol{r}_{\mathrm{D}},\omega_{10})\cdot\mathbb{G}^*(\boldsymbol{r}_{\mathrm{D}},\boldsymbol{r}_{\mathrm{A}},\omega_{10})\right]\,,\end{aligned} \tag{5.20}$$

where we have used the cyclic property of the trace and Onsager reciprocity for the Green's tensor, see Eq. (2.37). Substituting the free-space Green's tensor (A.32) into the equation, yields in free space

$$\Gamma_{\mathrm{ret}}^{(0)}=\frac{\gamma_{eg}\sigma(\omega_{eg})}{4\pi k^4r^6}\left(k^4r^4+k^2r^2+3\right)\,, \tag{5.21}$$

where $r=|r_{\mathrm{A}}-r_{\mathrm{D}}|$ is the donor–acceptor separation distance, σ is here the photoabsorption cross section for the acceptor's ground state, given by Eq. (2.169) and γ_{eg} is the free space spontaneous decay rate (5.85).

5.2. Open quantum systems approach

The goal of this section is the determination of the RET rate via an open quantum systems approach. We employ the Born–Markov approximation, keeping only second-order

correlations of the field and end up with a non-unitary evolution of the reduced atomic system. While the methods of open quantum systems in general enables one to consider the time evolution of a system in a nonperturbative manner, we still apply perturbation theory to determine the RET rate in its lowest order from the master equation. We start by introducing the perturbative ansatz for process rates for an open quantum system. This results into a rate expression that can be determined by the system's Lindblad operator. In the second part of this section we determine this Lindblad operator for our system. We then derive from this the spontaneous decay rate for an isolated atom nonperturbatively and the RET rate from the introduced perturbative ansatz in its lowest order.

5.2.1. General perturbative ansatz

We start by relating the time derivative of the system's density matrix to the process rate. We then derive the master equation for the system in Markov approximation, where we only retain field correlations up to second order. We introduce the Fock–Liouville space for the density matrix to write the master equation in terms of a linear (super)operator. We finally apply perturbation theory to find the transition probability in second order.

The probability to find the reduced atomic system $\rho_S(t) = \mathrm{Tr}_E\left[\rho(t)\right]$ in an (atomic) state ρ_f at time t can be calculated by

$$P_f(t) = \mathrm{Tr}\left\{\rho_f \rho_S(t)\right\} . \tag{5.22}$$

Its process rate Γ can then be determined by the time derivative, such that

$$\Gamma = \frac{\mathrm{d}}{\mathrm{d}t} P_f(t) = \mathrm{Tr}\left\{\rho_f \dot{\rho}_S(t)\right\} . \tag{5.23}$$

We use an open quantum systems approach where we only consider field correlations up to second order via the Born approximation, see section 2.2.4. The system's density matrix in interaction picture $\tilde{\rho}_S(t) = \mathrm{e}^{\mathrm{i}\hat{H}_0 t}\rho_S \mathrm{e}^{-\mathrm{i}\hat{H}_0 t}$ is then given by the Redfield equation (2.130) as

$$\dot{\tilde{\rho}}_S(t) = -\frac{1}{\hbar^2}\int_{t_0}^{t} \mathrm{d}t_1 \,\mathrm{Tr}_F\left\{\left[\hat{V}(t), \left[\hat{V}(t_1), \tilde{\rho}_S(t)\otimes\rho_E\right]\right]\right\} , \tag{5.24}$$

where $\rho_E = \rho_E(t_0)$ is the environment's initial state and the limit $t - t_0 \to \infty$ yields the full Markov approximation. For a coupling Hamiltonian in interaction picture $\hat{V}(t) = \sum_a \hat{S}_a(t)\hat{B}_a(t)$, where $\hat{S}_a$ are system operators and $\hat{B}_a$ act only on the environment, we

obtain for the master equation (5.24) the more explicit form

$$\dot{\tilde{\rho}}_{\mathrm{S}}(t) = -\frac{1}{\hbar^2}\sum_{a,b}\int_{t_0}^{t}\mathrm{d}t_1\Big\{\left[\hat{S}_a(t),\hat{S}_b(t_1)\tilde{\rho}_{\mathrm{S}}(t)\right]C_{ab}(t,t_1) + \left[\tilde{\rho}_{\mathrm{S}}(t)\hat{S}_b(t_1),\hat{S}_a(t)\right]C_{yx}(t_1,t)\Big\}, \tag{5.25}$$

where $C_{ab}(t,t_1) = \left\langle \hat{B}_a(t)\hat{B}_b(t_1)\right\rangle_{\mathrm{E}}$ are the environment's correlation functions. For equilibrium states, where $[H_{\mathrm{E}},\rho_E] = 0$ we may simplify them by $C_{ab}(t,t_1) = C_{ab}(t-t_1) = \langle B_a(t-t_1)B_b\rangle_{\mathrm{E}}$. Next, we transform the equation back to Schrödinger picture and find

$$\begin{aligned}\dot{\rho}_{\mathrm{S}}(t) = -\frac{\mathrm{i}}{\hbar}\left[\hat{H}_{\mathrm{A}},\rho_{\mathrm{S}}(t)\right] - \frac{1}{\hbar^2}\sum_{a,b}\int_{t_0}^{t}\mathrm{d}t_1\Big\{&\left[\hat{S}_a,\hat{S}_b(-\tau)\rho_{\mathrm{S}}(t)\right]C_{ab}(\tau)\\ &+\left[\rho_{\mathrm{S}}(t)\hat{S}_b(-\tau),\hat{S}_a\right]C_{yx}(-\tau)\Big\},\end{aligned} \tag{5.26}$$

where $\tau = t - t_1$. In the limit $t - t_0 \to \infty$ of true Markov processes the master equation can be cast into the form

$$\left|\dot{\rho}_{\mathrm{S}}(t)\right\rangle\!\!\right\rangle = \mathcal{D}_0\cdot\left|\rho_{\mathrm{S}}(t)\right\rangle\!\!\right\rangle + \mathcal{L}\cdot\left|\rho_{\mathrm{S}}(t)\right\rangle\!\!\right\rangle, \tag{5.27}$$

where $\mathcal{D}_0$ and $\mathcal{L}$ are time-independent superoperators acting on the Fock–Liouville vectors of density matrices $|\rho\rangle\!\rangle$ and $\mathcal{D}_0$ is the diagonal superoperator belonging to the uncoupled system. We can write the vectorised density matrix as

$$\rho_{\mathrm{S}}(t) = \sum_{\alpha\beta\gamma\epsilon}\rho_{\alpha\beta\gamma\epsilon}(t)\left|\alpha\right\rangle\left\langle\beta\right|_{\mathrm{D}}\otimes\left|\gamma\right\rangle\left\langle\epsilon\right|_{\mathrm{A}} = \left|\rho_{\mathrm{S}}(t)\right\rangle\!\!\right\rangle = \sum_{\alpha\beta\gamma\epsilon}\rho_{\alpha\beta\gamma\epsilon}(t)\left|\alpha\beta\gamma\epsilon\right\rangle\!\!\right\rangle, \tag{5.28}$$

where $|\alpha\beta\gamma\epsilon\rangle\!\rangle$ denotes a vector in Fock–Liouville space. In this basis the diagonal superoperator $\mathcal{D}_0$ is given by

$$\mathcal{D}_0\cdot\left|\rho_{\mathrm{S}}\right\rangle\!\!\right\rangle = -\frac{\mathrm{i}}{\hbar}\left[\hat{H}_{\mathrm{A}},\rho_{\mathrm{S}}\right] \qquad \Rightarrow \qquad \mathcal{D}_0 = -\mathrm{i}(\omega_{\alpha\beta}+\omega_{\gamma\beta})\left|\alpha\beta\gamma\epsilon\right\rangle\!\!\right\rangle\left\langle\!\!\left\langle\alpha\beta\gamma\epsilon\right|, \tag{5.29}$$

with $\omega_{ij} = \omega_i - \omega_j$. We can formally solve the differential equation

$$\left|\rho_{\mathrm{S}}(t)\right\rangle\!\!\right\rangle = \mathrm{e}^{\mathcal{D}_0(t-t_0)}\cdot\left|\rho_{\mathrm{S},0}\right\rangle\!\!\right\rangle + \int_{t_0}^{t}\mathrm{d}t_1\mathrm{e}^{\mathcal{D}_0(t-t_1)}\cdot\mathcal{L}\cdot\left|\rho_{\mathrm{S}}(t_1)\right\rangle\!\!\right\rangle. \tag{5.30}$$

Using this iteratively by substituting Eq. (5.30) back into Eq. (5.27), we find the second

order of perturbation to be

$$|\rho_S(t)\rangle\!\rangle \approx e^{\mathcal{D}_0(t-t_0)} \cdot |\rho_0\rangle\!\rangle + \int dt_1 e^{\mathcal{D}_0(t-t_1)} \cdot \mathcal{W}^{(1)}(t_1) \cdot |\rho_0\rangle\!\rangle + \int dt_1 e^{\mathcal{D}_0(t-t_1)} \cdot \mathcal{W}^{(2)}(t_1) \cdot |\rho_0\rangle\!\rangle \,, \tag{5.31}$$

$$\mathcal{W}^{(1)}(t_1) = \mathcal{L} \cdot e^{\mathcal{D}_0(t_1-t_0)} \,, \tag{5.32}$$

$$\mathcal{W}^{(2)}(t_1) = \int dt_2 \mathcal{L} \cdot e^{\mathcal{D}_0(t_1-t_2)} \cdot \mathcal{L} \cdot e^{\mathcal{D}_0(t_2-t_0)} \,, \tag{5.33}$$

where we defined the superoperators $\mathcal{W}^{(1)}$ and $\mathcal{W}^{(2)}$, such that we may write the time derivative of the density matrix as

$$|\dot{\rho}_S(t)\rangle\!\rangle \approx \mathcal{D}_0 \cdot |\rho_S(t)\rangle\!\rangle + \mathcal{W}^{(1)} \cdot |\rho_S(t_0)\rangle\!\rangle + \mathcal{W}^{(2)} \cdot |\rho_S(t_0)\rangle\!\rangle \,, \tag{5.34}$$

which will be a convenient notation for the upcoming derivations. Please note, that we did not replace $|\rho_S(t)\rangle\!\rangle$ in the first term of Eq. (5.34) with its approximated form. In the basis of the vectorised density matrix, we can rewrite the master equation, such that

$$|\dot{\rho}_S(t)\rangle\!\rangle = -i\sum(\omega_{st}+\omega_{uv})\rho_{stuv}(t)\,|stuv\rangle\!\rangle + \sum \langle\!\langle stuv|\mathcal{W}^{(1)}|\alpha\beta\gamma\epsilon\rangle\!\rangle\, \rho_{\alpha\beta\gamma\epsilon}(t_0)\,|stuv\rangle\!\rangle + \sum \langle\!\langle stuv|\mathcal{W}^{(2)}|\alpha\beta\gamma\epsilon\rangle\!\rangle\, \rho_{\alpha\beta\gamma\epsilon}(t_0)\,|stuv\rangle\!\rangle \,, \tag{5.35}$$

$$\mathcal{W}^{(2)} \quad = \quad \sum \int_{t_0}^{t} dt_1 e^{-i(\omega_{ij}+\omega_{kl})(t-t_1)}\, \langle\!\langle stuv|\mathcal{L}|ijkl\rangle\!\rangle\, \langle\!\langle ijkl|\mathcal{L}|\alpha\beta\gamma\epsilon\rangle\!\rangle\, |stuv\rangle\!\rangle\, \langle\!\langle \alpha\beta\gamma\epsilon| \,, \tag{5.36}$$

where the sum runs over all state labels.

5.2.2. Determination of the explicit Lindblad operator

In this section we derive the explicit Lindblad operator $\mathcal{L}$ introduced in the master equation (5.27). In Markov approximation the Lindblad operator turns out to be time-independent. We divide the operator $\mathcal{L}$ into three different parts and find a common structure for each coefficient in the Lindblad operator. These coefficients are then evaluated in general in terms of the Green's tensor.

In our case, the coupling Hamiltonian reads

$$\hat{V}(t) = -\sum_{a\in\{D,A\}} \hat{\boldsymbol{d}}_a(t) \cdot \hat{\boldsymbol{E}}_a(\boldsymbol{r}_a, t) \tag{5.37}$$

$$\hat{\boldsymbol{d}}_a(t) = \sum_{mn} \hat{A}^{(a)}_{mn}(t)\boldsymbol{d}^{(a)}_{mn} \,, \tag{5.38}$$

where $\hat{A}^{(a)}_{mn} = |m\rangle\langle n|_a$ denote the atomic flip operators of atom $a \in \{\mathrm{D}, \mathrm{A}\}$. Hence, the correlation functions $C_{ab} = \mathbb{C}_{ab}$ are tensor valued and the system operators $\hat{S}_a = \hat{\boldsymbol{S}}_a$ are vector valued in position space. They are given by:

$$\mathbb{C}_{ab}(t) = \mathrm{Tr}\left[\hat{\boldsymbol{E}}(\boldsymbol{r}_a, t) \otimes \hat{\boldsymbol{E}}(\boldsymbol{r}_b, 0)\rho_\mathrm{F}\right] = \int_0^\infty \mathrm{d}\omega \mathrm{e}^{-\mathrm{i}\omega t} \frac{\hbar\mu_0\omega^2}{\pi} \mathrm{Im}\mathbb{G}(\boldsymbol{r}_a, \boldsymbol{r}_b, \omega) \tag{5.39}$$

$$\hat{\boldsymbol{S}}_a(t) = \sum_{mn} \boldsymbol{d}^{(a)}_{mn} \hat{A}^{(a)}_{mn}(t)\,. \tag{5.40}$$

From this we can conclude some useful properties of $\mathbb{C}_{ab}$, namely Onsager reciprocity and the Schwarz reflection principle:

$$\mathbb{C}_{ab}(-t) = \mathbb{C}^*_{ab}(t)\,, \qquad \mathbb{C}^T_{ab}(t) = \mathbb{C}_{ba}(t)\,. \tag{5.41}$$

By considering the operators' correct contractions with each other in position space we find the fundamental master equation (5.24) to take the form

$$\dot{\rho}_\mathrm{S}(t) = -\mathrm{i}\left[\hat{H}_\mathrm{A}, \rho_S(t)\right] + \sum_{a,b\in\{\mathrm{D},\mathrm{A}\}} \mathcal{L}_{ab} \cdot \rho_\mathrm{S}\,, \tag{5.42}$$

$$\begin{aligned}\mathcal{L}_{ab} \cdot |\rho_\mathrm{S}\rangle\!\rangle = -\frac{1}{\hbar^2} \sum_{m,n,i,j} \int_{t_0}^t \mathrm{d}t_1 \mathrm{e}^{\mathrm{i}\omega_{ij}(t_1-t)} \Big\{ &\left[\hat{A}^{(a)}_{mn}, \hat{A}^{(b)}_{ij}\rho_\mathrm{S}(t)\right] \boldsymbol{d}^{(a)}_{mn} \cdot \mathbb{C}_{xy}(\tau) \cdot \boldsymbol{d}^{(b)}_{ij} \\ &+ \left[\rho_\mathrm{S}(t)\hat{A}^{(b)}_{ij}, \hat{A}^{(a)}_{mn}\right] \boldsymbol{d}^{(a)}_{mn} \cdot \mathbb{C}^*_{ab}(\tau) \cdot \boldsymbol{d}^{(b)}_{ij} \Big\}\,,\end{aligned} \tag{5.43}$$

where we have introduced the explicit time evolution of $\hat{A}$ that is left after transforming back to Schrödinger picture and used the correlation tensor's properties as given by Eqs. (5.41).

Evaluating the commutators and using Eq. (5.28), we can write the Lindblad operator in the basis of the vectorised density matrix as

$$\begin{aligned}\mathcal{L}_\mathrm{DD} = -\frac{1}{\hbar^2} \sum \int_{t_0}^t \mathrm{d}t_1 \Big\{ &\mathrm{e}^{\mathrm{i}\omega_{nm}(t_1-t)} \boldsymbol{d}^\mathrm{D}_{\alpha n} \cdot \mathbb{C}_\mathrm{DD}(\tau) \cdot \boldsymbol{d}^\mathrm{D}_{nm} |\alpha\beta\gamma\epsilon\rangle\!\rangle\langle\!\langle m\beta\gamma\epsilon| \\ &+ \mathrm{e}^{\mathrm{i}\omega_{nm}(t_1-t)} \boldsymbol{d}^\mathrm{D}_{m\beta} \cdot \mathbb{C}^*_\mathrm{DD}(\tau) \cdot \boldsymbol{d}^\mathrm{D}_{nm} |\alpha\beta\gamma\epsilon\rangle\!\rangle\langle\!\langle \alpha n\gamma\epsilon| \\ &+ \Big[\mathrm{e}^{\mathrm{i}\omega_{\alpha n}(t_1-t)} \boldsymbol{d}^\mathrm{D}_{m\beta} \cdot \mathbb{C}_\mathrm{DD}(\tau) \cdot \boldsymbol{d}^\mathrm{D}_{\alpha n} \\ &\qquad + \mathrm{e}^{\mathrm{i}\omega_{m\beta}(t_1-t)} \boldsymbol{d}^\mathrm{D}_{\alpha n} \cdot \mathbb{C}^*_\mathrm{DD}(\tau) \cdot \boldsymbol{d}^\mathrm{D}_{m\beta}\Big] |\alpha\beta\gamma\epsilon\rangle\!\rangle\langle\!\langle nm\gamma\epsilon| \Big\}\,,\end{aligned} \tag{5.44}$$

$$\begin{aligned}\mathcal{L}_{\mathrm{AA}} = -\frac{1}{\hbar^2}\sum\int_{t_0}^{t}\mathrm{d}t_1\Big\{ & \mathrm{e}^{\mathrm{i}\omega_{nm}(t_1-t)}\boldsymbol{d}^{\mathrm{A}}_{\gamma n}\cdot\mathbb{C}_{\mathrm{AA}}(\tau)\cdot\boldsymbol{d}^{\mathrm{A}}_{nm}\,|\alpha\beta\gamma\epsilon\rangle\!\rangle\langle\!\langle\alpha\beta m\epsilon| \\ & + \mathrm{e}^{\mathrm{i}\omega_{nm}(t_1-t)}\boldsymbol{d}^{\mathrm{A}}_{m\epsilon}\cdot\mathbb{C}^{*}_{\mathrm{AA}}(\tau)\cdot\boldsymbol{d}^{\mathrm{A}}_{nm}\,|\alpha\beta\gamma\epsilon\rangle\!\rangle\langle\!\langle\alpha\beta\gamma n| \\ & + \Big[\mathrm{e}^{\mathrm{i}\omega_{\gamma n}(t_1-t)}\boldsymbol{d}^{\mathrm{A}}_{m\epsilon}\cdot\mathbb{C}_{\mathrm{AA}}(\tau)\cdot\boldsymbol{d}^{\mathrm{A}}_{\gamma n} \\ & \qquad + \mathrm{e}^{\mathrm{i}\omega_{m\epsilon}(t_1-t)}\boldsymbol{d}^{\mathrm{A}}_{\gamma n}\cdot\mathbb{C}^{*}_{\mathrm{AA}}(\tau)\cdot\boldsymbol{d}^{\mathrm{A}}_{m\epsilon}\Big]\,|\alpha\beta\gamma\epsilon\rangle\!\rangle\langle\!\langle\alpha\beta nm|\Big\}, \end{aligned} \tag{5.45}$$

$$\begin{aligned}\mathcal{L}_{\mathrm{D,A}} &= \mathcal{L}_{\mathrm{DA}} + \mathcal{L}_{\mathrm{AD}} \\ &= -\frac{1}{\hbar^2}\sum\int_{t_0}^{t}\mathrm{d}t_1\Big\{\Big[\mathrm{e}^{\mathrm{i}\omega_{\alpha n}(t_1-t)} + \mathrm{e}^{\mathrm{i}\omega_{\gamma m}(t_1-t)}\Big]\boldsymbol{d}^{\mathrm{D}}_{\alpha n}\cdot\mathbb{C}_{\mathrm{DA}}(\tau)\cdot\boldsymbol{d}^{\mathrm{A}}_{\gamma m}\,|\alpha\beta\gamma\epsilon\rangle\!\rangle\langle\!\langle n\beta m\epsilon| \\ &\quad + \Big[\mathrm{e}^{\mathrm{i}\omega_{n\beta}(t_1-t)} + \mathrm{e}^{\mathrm{i}\omega_{\gamma m}(t_1-t)}\Big]\boldsymbol{d}^{\mathrm{D}}_{n\beta}\cdot\mathbb{C}^{*}_{\mathrm{DA}}(\tau)\cdot\boldsymbol{d}^{\mathrm{A}}_{\gamma m}\,|\alpha\beta\gamma\epsilon\rangle\!\rangle\langle\!\langle\alpha nm\epsilon| \\ &\quad + \Big[\mathrm{e}^{\mathrm{i}\omega_{m\epsilon}(t_1-t)} + \mathrm{e}^{\mathrm{i}\omega_{m\epsilon}(t_1-t)}\Big]\boldsymbol{d}^{\mathrm{D}}_{n\beta}\cdot\mathbb{C}^{*}_{\mathrm{DA}}(\tau)\cdot\boldsymbol{d}^{\mathrm{A}}_{m\epsilon}\,|\alpha\beta\gamma\epsilon\rangle\!\rangle\langle\!\langle\alpha n\gamma m| \\ &\quad + \Big[\mathrm{e}^{\mathrm{i}\omega_{\alpha n}(t_1-t)} + \mathrm{e}^{\mathrm{i}\omega_{m\epsilon}(t_1-t)}\Big]\boldsymbol{d}^{\mathrm{D}}_{\alpha n}\cdot\mathbb{C}_{\mathrm{DA}}(\tau)\cdot\boldsymbol{d}^{\mathrm{A}}_{m\epsilon}\,|\alpha\beta\gamma\epsilon\rangle\!\rangle\langle\!\langle n\beta\gamma m|\Big\}. \end{aligned} \tag{5.46}$$

The structure of the integrands appearing in $\mathcal{L}_{\mathrm{DD}}$, $\mathcal{L}_{\mathrm{AA}}$ and $\mathcal{L}_{\mathrm{DA}} + \mathcal{L}_{\mathrm{AD}}$ are similar to each other. They can always be cast into a similar form and hence be evaluated in general to become

$$\begin{aligned} -\frac{1}{\hbar^2}\int_{t_0}^{t}\mathrm{d}t_1\mathrm{e}^{\mathrm{i}\omega_i(t-t_1)}\boldsymbol{d}^{(a)}_{k}\cdot\mathbb{C}_{ab}(\tau)\cdot\boldsymbol{d}^{(b)}_{l} & \\ = -\frac{\mu_0}{\hbar}\theta(\omega_i)\omega_i^2\boldsymbol{d}^{(a)}_{j}\cdot\mathrm{Im}\mathbb{G}(\boldsymbol{r}_a,\boldsymbol{r}_b,\omega_i)\cdot\boldsymbol{d}^{(b)}_{k} & \\ + \mathrm{i}\frac{\mu_0}{\hbar\pi}\mathcal{P}\!\int\mathrm{d}\omega\frac{\omega^2}{\omega-\omega_i}\boldsymbol{d}^{(a)}_{j}\cdot\mathrm{Im}\mathrm{G}(\boldsymbol{r}_a,\boldsymbol{r}_b,\omega)\cdot\boldsymbol{d}^{(b)}_{k} & \\ = \mathrm{i}\frac{\mu_0}{\hbar}\theta(\omega_i)\omega_i^2\boldsymbol{d}^{(a)}_{j}\cdot\mathbb{G}(\boldsymbol{r}_a,\boldsymbol{r}_b,\omega_i)\cdot\boldsymbol{d}^{(b)}_{k} & \\ - \mathrm{i}\frac{\mu_0}{\hbar\pi}\mathcal{P}\!\int\mathrm{d}\omega\frac{\omega^2}{\omega+\omega_i}\boldsymbol{d}^{(a)}_{j}\cdot\mathrm{Im}\mathrm{G}(\boldsymbol{r}_a,\boldsymbol{r}_b,\omega)\cdot\boldsymbol{d}^{(b)}_{k}\,, & \end{aligned} \tag{5.47}$$

where $\theta(\omega)$ is the Heaviside step function and we have used the long-time limit $t - t_0 \to \infty$ explicitly to evaluate the time integration

$$\int_{t_0}^{t}\mathrm{d}t_1\mathrm{e}^{-\mathrm{i}(\omega-\omega_{ij})(t-t_1)} \to \int_0^{\infty}\mathrm{d}\tau\mathrm{e}^{-\mathrm{i}(\omega-\omega_{ij})\tau} = \pi\delta(\omega-\omega_{ij}) - \mathrm{i}\frac{\mathcal{P}}{\omega-\omega_{ij}}\,, \tag{5.48}$$

as well as Kramers–Kronig relation, given by

$$\mathcal{P}\!\int_{-\infty}^{\infty}\mathrm{d}\omega\,\frac{\mathrm{Im}f(\omega)}{\omega-\omega_i} = \mathrm{Re}f(\omega_i)\,, \tag{5.49}$$

for any analytic function $f(\omega)$ that vanishes sufficiently fast in the upper half of the

complex plane. For the complex conjugate, we then get

$$
\begin{aligned}
-\frac{1}{\hbar^2}\int_{t_0}^{t} \mathrm{d}t_1 \mathrm{e}^{-\mathrm{i}\omega_i(t-t_1)} \boldsymbol{d}_k^{(a)} \cdot \mathbb{C}_{ab}^*(\tau) \cdot \boldsymbol{d}_l^{(b)} \\
&= -\mathrm{i}\frac{\mu_0}{\hbar}\theta(\omega_i)\omega_i^2 \boldsymbol{d}_j^{(a)} \cdot \mathbb{G}^*(\boldsymbol{r}_a, \boldsymbol{r}_b, \omega_i) \cdot \boldsymbol{d}_k^{(b)} \\
&\quad + \mathrm{i}\frac{\mu_0}{\hbar\pi}\int \mathrm{d}\omega \frac{\omega^2}{\omega+\omega_i} \boldsymbol{d}_j^{(a)} \cdot \mathrm{Im}G(\boldsymbol{r}_a, \boldsymbol{r}_b, \omega) \cdot \boldsymbol{d}_k^{(b)} \,, \qquad (5.50)
\end{aligned}
$$

where it is important to note that the real part vanishes in Eqs. (5.47) and (5.50) for $\omega_i < 0$. Each integral hence yields the time-independent result given either by Eq. (5.47) or Eq. (5.50). We waive giving the full Lindblad operator evaluated in this form, but will use Eqs. (5.47) and (5.50) for explicit derivations later on.

5.2.3. Recovering the spontaneous decay rate

In this section we reduce the derived master equation to the treatment of a single particle in the field and from this derive the spontaneous decay rate. We show that the spontaneous decay rate can be derived nonperturbatively and yields the same result as the one from Fermi's golden rule, see section 5.1.

We have derived the master equation (5.30) for two particles in the field. For the spontaneous decay rate we only need a single particle interacting with the electromagnetic vacuum. We can reduce the master equation to the single-particle case by simply replacing $\mathcal{L}$ with $\mathcal{L}_1 = \mathrm{Tr}_\mathrm{A}\{\mathcal{L}_\mathrm{DD}\}$ in the master equation. The single-particle Lindblad operator is then given by

$$
\begin{aligned}
\mathcal{L}_1 = -\frac{1}{\hbar^2}\sum\int_{t_0}^{t}\mathrm{d}t_1 \Bigg\{ & \mathrm{e}^{\mathrm{i}\omega_{nm}(t_1-t)} \boldsymbol{d}_{\alpha n}^\mathrm{D} \cdot \mathbb{C}_\mathrm{DD}(\tau) \cdot \boldsymbol{d}_{nm}^\mathrm{D} \left|\alpha\beta\right\rangle\!\left\rangle\!\right\langle m\beta\right| \\
& + \mathrm{e}^{\mathrm{i}\omega_{nm}(t_1-t)} \boldsymbol{d}_{m\beta}^\mathrm{D} \cdot \mathbb{C}_\mathrm{DD}^*(\tau) \cdot \boldsymbol{d}_{nm}^\mathrm{D} \left|\alpha\beta\right\rangle\!\left\rangle\!\right\langle \alpha n\right| \\
& + \Big[\mathrm{e}^{\mathrm{i}\omega_{\alpha n}(t_1-t)} \boldsymbol{d}_{m\beta}^\mathrm{D} \cdot \mathbb{C}_\mathrm{DD}(\tau) \cdot \boldsymbol{d}_{\alpha n}^\mathrm{D} \\
& \qquad + \mathrm{e}^{\mathrm{i}\omega_{m\beta}(t_1-t)} \boldsymbol{d}_{\alpha n}^\mathrm{D} \cdot \mathbb{C}_\mathrm{DD}^*(\tau) \cdot \boldsymbol{d}_{m\beta}^\mathrm{D} \Big] \left|\alpha\beta\right\rangle\!\left\rangle\!\right\langle nm\right| \Bigg\} \,, \qquad (5.51)
\end{aligned}
$$

where $|\alpha\beta\rangle\!\rangle$ corresponds to $|\alpha\rangle_\mathrm{D}\langle\beta|_\mathrm{D}$. The spontaneous decay rate can be found in the decay of each state's population $\rho_{\alpha\alpha}(t)$, such that

$$
\rho_{\alpha\alpha}(t) \propto -\Gamma_\mathrm{s}\rho_{\alpha\alpha}(t) \,, \qquad (5.52)
$$

with $\Gamma_\mathrm{s} \in \mathbb{R}$. It can hence be found as a loss term in the diagonal part of the single

particle Lindblad superoperator. The diagonal part of $\mathcal{L}_1$ is given by (see Eq. (5.51))

$$\langle\!\langle \alpha\alpha | \mathcal{L}_1 | \alpha\alpha \rangle\!\rangle = -\frac{1}{\hbar^2} \sum_n \int_{t_0}^{t} \mathrm{d}t_1 \Big\{ \mathrm{e}^{\mathrm{i}\omega_{\alpha n}(t-t_1)} \boldsymbol{d}^{\mathrm{D}}_{\alpha n} \cdot C_{\mathrm{DD}}(\tau) \cdot \boldsymbol{d}^{\mathrm{D}}_{n\alpha} + \mathrm{e}^{-\mathrm{i}\omega_{\alpha n}(t-t_1)} \boldsymbol{d}^{\mathrm{D}}_{n\alpha} \cdot C^{*}_{\mathrm{DD}}(\tau) \cdot \boldsymbol{d}^{\mathrm{D}}_{\alpha n} \Big\}, \quad (5.53)$$

where we used $\omega_{ij} = -\omega_{ji}$. Using Eqs. (5.47) and (5.50) we get

$$\mathrm{Re}\left[\langle\!\langle \alpha\alpha | \mathcal{L}_1 | \alpha\alpha \rangle\!\rangle\right] = -\sum_{n<\alpha} \gamma_{\alpha n} \quad (5.54)$$

$$\gamma_{\alpha n} = \frac{2\mu_0}{\hbar} \omega^2_{\alpha n}\, \boldsymbol{d}_{\alpha n} \cdot \mathrm{Im}\mathbb{G}(\boldsymbol{r}_{\mathrm{D}}, \boldsymbol{r}_{\mathrm{D}}) \cdot \boldsymbol{d}_{n\alpha}\,, \quad (5.55)$$

which for an excited state $|\alpha\rangle = |e\rangle$ and an unpopulated ground state $|n\rangle = |g\rangle$ yields the spontaneous decay rate

$$\Gamma_{\mathrm{s}} = \langle\!\langle ee | \mathcal{L}_1 | ee \rangle\!\rangle = \gamma_{eg} = \frac{2\mu_0}{\hbar} \omega^2_{eg}\, \boldsymbol{d}_{eg} \cdot \mathrm{Im}\mathbb{G}(\boldsymbol{r}_{\mathrm{D}}, \boldsymbol{r}_{\mathrm{D}}) \cdot \boldsymbol{d}_{ge}\,. \quad (5.56)$$

This is the same result as obtained by Fermi's golden rule, see Eq. (5.8).

5.2.4. Recovering the resonance energy transfer rate

So far, we have derived the master equation, approximated it within second-order perturbation theory and derived the explicit form of the Lindblad operator for our system. From this, we next recover the rate for RET obtained via Fermi's golden rule in section 5.1. Although the approximations and assumptions going into both approaches are not equivalent, the resulting rate expression is. We briefly discuss the reason for this at the end of the section.

We are interested in the RET rate in its lowest order, see Eq. (5.58). The rate of a second-order process in its lowest order is given by Eq. (5.23),

$$\Gamma_{\mathrm{ret}} = \mathrm{Tr}\left[\rho_f \dot{\rho}_{\mathrm{S}}(t)\right] \approx \langle\!\langle \rho_f | \cdot \mathcal{D}_0 \cdot |\rho_{\mathrm{S}}(t)\rangle\!\rangle + \left\langle\!\!\left\langle \rho_f | \cdot \mathcal{W}^{(2)} \cdot |\rho_0 \right\rangle\!\!\right\rangle \quad (5.57)$$

$$= \langle\!\langle \rho_f | \mathcal{D}_0 | \rho_f \rangle\!\rangle \langle\!\langle \rho_f | \rho_{\mathrm{S}}(t) \rangle\!\rangle + \left\langle\!\!\left\langle \rho_f | \cdot \mathcal{W}^{(2)} \cdot |\rho_0 \right\rangle\!\!\right\rangle, \quad (5.58)$$

where we have used Eq. (5.34) and that $\mathcal{D}_0$ is a diagonal matrix. Introducing the appropriate initial and final states of interest, this gives the RET rate formula from an open quantum systems approach. In RET the final and initial states are given by $\left|\rho_f\right\rangle\!\rangle = |gg11\rangle\!\rangle$ and $|\rho_0\rangle\!\rangle = |ee00\rangle\!\rangle$. With $\langle\!\langle \rho_f | \mathcal{D}_0 | \rho_f \rangle\!\rangle = \mathrm{i}(\omega_{gg} + \omega_{11}) = 0$, we find for the rate

$$\Gamma_{\mathrm{ret}} = \left\langle\!\!\left\langle gg11 | \mathcal{W}^{(2)} | ee00 \right\rangle\!\!\right\rangle. \quad (5.59)$$

Next, we can determine the intermediate states $|ijkl\rangle\!\rangle$ in Eq. (5.36) that may contribute to the rate. Each superoperator $\mathcal{L}$ in $\mathcal{W}^{(2)}$ can change two state labels of the vectorised density matrix. The intermediate states are hence given by

$$|ijkl\rangle\!\rangle \in \{|ee11\rangle\!\rangle, |gg00\rangle\!\rangle, |ge10\rangle\!\rangle, |eg01\rangle\!\rangle, |eg10\rangle\!\rangle, |ge01\rangle\!\rangle\}. \tag{5.60}$$

As we will see later, only two of them contribute to the rate. The rate is given by the sum over the intermediate states,

$$\Gamma_{\text{ret}} = \sum_{\kappa} W_{\kappa}^{(2)}, \tag{5.61}$$

with

$$W_1^{(2)} = \int_{t_0}^{t} \mathrm{d}t_1 \mathrm{e}^{-\mathrm{i}(\omega_{ee}+\omega_{11})(t-t_1)} \underbrace{\langle\!\langle gg11|\mathcal{L}_{\text{DD}}(t)|ee11\rangle\!\rangle}_{\text{last term in (5.44)}} \underbrace{\langle\!\langle ee11|\mathcal{L}_{\text{AA}}(t_1)|ee00\rangle\!\rangle}_{\text{last term in (5.45)}}, \tag{5.62}$$

$$W_2^{(2)} = \int_{t_0}^{t} \mathrm{d}t_1 \mathrm{e}^{-\mathrm{i}(\omega_{gg}+\omega_{00})(t-t_1)} \underbrace{\langle\!\langle gg11|\mathcal{L}_{\text{AA}}(t)|gg00\rangle\!\rangle}_{\text{last term in (5.45)}} \underbrace{\langle\!\langle gg00|\mathcal{L}_{\text{DD}}(t_1)|ee00\rangle\!\rangle}_{\text{last term in (5.44)}}, \tag{5.63}$$

$$W_3^{(2)} = \int_{t_0}^{t} \mathrm{d}t_1 \mathrm{e}^{-\mathrm{i}(\omega_{ge}+\omega_{10})(t-t_1)} \underbrace{\langle\!\langle gg11|\mathcal{L}_{\text{D,A}}(t)|ge10\rangle\!\rangle}_{\text{third term in (5.46)}} \underbrace{\langle\!\langle ge10|\mathcal{L}_{\text{D,A}}(t_1)|ee00\rangle\!\rangle}_{\text{first term in (5.46)}}, \tag{5.64}$$

$$W_4^{(2)} = \int_{t_0}^{t} \mathrm{d}t_1 \mathrm{e}^{-\mathrm{i}(\omega_{eg}+\omega_{01})(t-t_1)} \underbrace{\langle\!\langle gg11|\mathcal{L}_{\text{D,A}}(t)|eg01\rangle\!\rangle}_{\text{first term in (5.46)}} \underbrace{\langle\!\langle eg01|\mathcal{L}_{\text{D,A}}(t_1)|ee00\rangle\!\rangle}_{\text{third term in (5.46)}}, \tag{5.65}$$

$$W_5^{(2)} = \int_{t_0}^{t} \mathrm{d}t_1 \mathrm{e}^{-\mathrm{i}(\omega_{eg}+\omega_{10})(t-t_1)} \underbrace{\langle\!\langle gg11|\mathcal{L}_{\text{D,A}}(t)|eg10\rangle\!\rangle}_{\text{last term in (5.46)}} \underbrace{\langle\!\langle eg10|\mathcal{L}_{\text{D,A}}(t_1)|ee00\rangle\!\rangle}_{\text{second term in (5.46)}}, \tag{5.66}$$

$$W_6^{(2)} = \int_{t_0}^{t} \mathrm{d}t_1 \mathrm{e}^{-\mathrm{i}(\omega_{ge}+\omega_{01})(t-t_1)} \underbrace{\langle\!\langle gg11|\mathcal{L}_{\text{D,A}}(t)|ge01\rangle\!\rangle}_{\text{second term in (5.46)}} \underbrace{\langle\!\langle ge01|\mathcal{L}_{\text{D,A}}(t_1)|ee00\rangle\!\rangle}_{\text{last term in (5.46)}}, \tag{5.67}$$

where we determined which terms of the respective $\mathcal{L}_{ab}$ are involved for each intermediate state of interest. By using the general evaluation of the coefficients of $\mathcal{L}$, see Eqs. (5.47) and (5.50), we can easily show that the contributions of the first two intermediate states, $W_1^{(2)}$ and $W_2^{(2)}$ vanish. Each of them is proportional to

$$\langle\!\langle nn11|\,\mathcal{L}_{\text{AA}}\,|nn00\rangle\!\rangle = 2\text{Re}\left[\int \mathrm{d}t_1 \{\mathrm{e}^{-\mathrm{i}\omega_{01}(t-t_1)} \boldsymbol{d}_{10} \mathbb{C}_{\text{DD}} \boldsymbol{d}_{01}\}\right] \propto \theta(\omega_{01}) = 0, \tag{5.68}$$

for $n = e, g$. This is a direct consequence of the Markov approximation, where we only take field correlations of lowest order into account. The third and fourth contribution and

the fifth and sixth are complex conjugates of each other, such that

$$W_3^{(2)} + W_4^{(2)} = 2\mathrm{Re}\left[W_3^{(2)}\right], \tag{5.69}$$

$$W_5^{(2)} + W_6^{(2)} = 2\mathrm{Re}\left[W_5^{(2)}\right]. \tag{5.70}$$

We can calculate the transition elements in $W_3^{(2)}$ explicitly, using Eqs. (5.47) and (5.50), and find

$$\begin{aligned}\langle\!\langle ge10|\mathcal{L}_{\mathrm{DA}}|ee00\rangle\!\rangle &= -\frac{1}{\hbar^2}\int_{t_0}^{t} \mathrm{d}t_1 \left[\mathrm{e}^{\mathrm{i}\omega_{eg}(t-t_1)} + \mathrm{e}^{\mathrm{i}\omega_{10}(t-t_1)}\right] \boldsymbol{d}_{ge}\cdot\mathbb{C}_{\mathrm{DA}}\cdot\boldsymbol{d}_{10} \\ &= \mathrm{i}\frac{\mu_0\omega_{eg}^2}{\hbar}\boldsymbol{d}_{ge}\cdot\mathbb{G}(\boldsymbol{r}_{\mathrm{D}},\boldsymbol{r}_{\mathrm{A}},\omega_{eg})\cdot\boldsymbol{d}_{10} + f(\omega_{eg}) - f(\omega_{10}), \end{aligned} \tag{5.71}$$

$$\begin{aligned}\langle\!\langle gg11|\mathcal{L}_{\mathrm{DA}}|ge10\rangle\!\rangle &= -\frac{1}{\hbar^2}\int_{t_0}^{t} \mathrm{d}t_1 \left[\mathrm{e}^{-\mathrm{i}\omega_{eg}(t-t_1)} + \mathrm{e}^{-\mathrm{i}\omega_{10}(t-t_1)}\right] \boldsymbol{d}_{eg}\cdot\mathbb{C}_{\mathrm{DA}}^{*}\cdot\boldsymbol{d}_{01} \\ &= \langle\!\langle ge10|\mathcal{L}_{\mathrm{DA}}|ee00\rangle\!\rangle^{*}, \end{aligned} \tag{5.72}$$

and hence

$$\begin{aligned}W_3^{(2)} + W_4^{(2)} &= \int_{t_0}^{t}\mathrm{d}t_1\, 2\mathrm{Re}\left[e^{-\mathrm{i}(\omega_{10}-\omega_{eg})(t-t_1)}\right] |\langle\!\langle ge10|\mathcal{L}_{\mathrm{DA}}|ee00\rangle\!\rangle|^2 \\ &= 2\lim_{\Delta t\to\infty}\frac{\sin\left[(\omega_{10}-\omega_{eg})\Delta t\right]}{\omega_{10}-\omega_{eg}} |\langle\!\langle ge10|\mathcal{L}_{\mathrm{DA}}|ee00\rangle\!\rangle|^2 \\ &= 2\pi\delta(\omega_{eg}-\omega_{10})\,|\langle\!\langle ge10|\mathcal{L}_{\mathrm{DA}}|ee00\rangle\!\rangle|^2, \end{aligned} \tag{5.73}$$

where $\Delta t = t - t_0$ and we have recovered the resonance constraint of the long-time limit found in Fermi's golden rule, see Eq. (2.119). With the resonance constraint and the integrated expressions of $\mathcal{L}$, see Eqs. (5.47) and (5.50), we can simplify Eq. (5.73) to be

$$W_3^{(2)} + W_4^{(2)} = 2\pi\frac{\mu_0^2\omega_{eg}^4}{\hbar^2}\delta(\omega_{eg}-\omega_{10})\left|\boldsymbol{d}_{ge}\cdot\mathbb{G}(\boldsymbol{r}_{\mathrm{D}},\boldsymbol{r}_{\mathrm{A}},\omega_{eg})\cdot\boldsymbol{d}_{10}\right|^2. \tag{5.74}$$

Similarly we find that

$$W_5^{(2)} + W_6^{(2)} \propto \delta(\omega_{eg}+\omega_{10}), \tag{5.75}$$

and since $\omega_{eg}, \omega_{10} > 0$ conclude that these transition elements vanish. With this we have finally derived the RET rate in its lowest order from an open quantum systems approach:

$$\Gamma_{\mathrm{ret}} = W_3^{(2)} + W_4^{(2)} = 2\pi\frac{\mu_0^2\omega_{eg}^4}{\hbar^2}\delta(\omega_{eg}-\omega_{10})\left|\boldsymbol{d}_{ge}\cdot\mathbb{G}(\boldsymbol{r}_{\mathrm{D}},\boldsymbol{r}_{\mathrm{A}},\omega_{eg})\cdot\boldsymbol{d}_{10}\right|^2. \tag{5.76}$$

This is the same result as the one derived from Fermi's golden rule, see Eq. (5.19).

In both approaches, we apply the long-time limit, which leads to the appearance of the delta distribution. We also use perturbation theory in both approaches to obtain the rate in its lowest order. The main difference between the approaches is the treatment of the environment. In the open quantum systems approach we explicitly neglect any higher-order correlations in the Markov approximation. While we do not explicitly exclude higher-order correlations in the approach via Fermi's golden rule, we implicitly neglected them by determining the initial and final states completely, leading to a result which also only includes second-order correlations. In general, RET also depends on fourth-order correlation functions of the field. However, it has been shown that the neglected correlations only play a role for times smaller than r/c, where r is the separation distance between donor and acceptor [31].

5.3. Incoherent perturbation scheme in the open quantum systems approach

We have shown that an open quantum systems approach where only field correlations of lowest order are taken into account leads to the same result as Fermi's golden rule. The obvious advantage of Fermi's golden rule is its simplicity. However, the open quantum systems approach offers some advantages as well. By approximating the order of field correlations independently of the order of system–field interactions the open quantum systems approach is in general able to treat the dynamics due to the system–field interaction nonperturbatively.

In this section, we show that on the level of the master equation there exists dynamics from the system–field interaction that effectively acts as homogeneous evolution of the system's density matrix. Splitting the master equation into homogeneous and inhomogeneous coupling then leads to an alternative perturbation scheme where the homogeneous evolution includes incoherent dynamics, leading to effective energy-level shifts and decay rates.

Revisiting perturbative calculations in this alternative perturbation scheme then adds self-consistent corrections to them. As an important but simple example we derive the corrections to the polarisability tensor. It was shown in previous works that the inclusion of damping constants in the calculation of Van-der-Waals forces between an excited and a ground state particle lead to an interesting result. The force acting on the ground state particle monotonically decreases with increasing separation distance r, while the force on the excited particle additionally oscillates as a function of r. While we do not revisit its derivation, we derive an analogous behaviour for the transition rates of donor and

acceptor in RET by including the spontaneous emission rate in the presence of a second particle explicitly.

5.3.1. Incoherent perturbation scheme

In this section, we introduce the incoherent perturbation scheme. We identify any homogenous evolution in our master equation, split it off the Lindblad superoperator that is treated perturbatively and redefine them into the bare evolution. The full master equation is not altered by this process, however the perturbation scheme differs in this splitting.

The Lindblad operator given by Eqs. (5.44)–(5.46) still includes diagonal terms that couple an element of the reduced density matrix ρ_S to itself via the master equation (5.27), describing homogeneous dynamics. We can identify these terms and split $\mathcal{L} = \mathcal{D} + \mathcal{M}$ into its diagonal part $\mathcal{D}$ and its hollow part $\mathcal{M}$. We may then write

$$\left|\dot{\rho}(t)\right\rangle\!\!\right\rangle = (\mathcal{D}_0 + \mathcal{D}) \cdot |\rho_S(t)\rangle\!\!\rangle + \mathcal{M} \cdot |\rho_S(t)\rangle\!\!\rangle \,, \tag{5.77}$$

which leads to a new splitting into homogeneous and inhomogeneous solution of the differential equation compared to Eq. (5.34), such that

$$\rho_S(t) = \mathrm{e}^{(\mathcal{D}_0+\mathcal{D})(t-t_0)}\rho_{S,0} + \int_{t_0}^{t} \mathrm{d}t_1 \mathrm{e}^{(\mathcal{D}_0+\mathcal{D})(t-t_1)} \cdot \mathcal{M} \cdot \rho_S(t_1)\,. \tag{5.78}$$

We may use this new splitting to redefine the perturbative expansion in section 5.2.1. Using Eq. (5.78) iteratively, we find the second order of perturbation to be

$$\begin{aligned} |\rho_S(t)\rangle\!\!\rangle \approx \mathrm{e}^{(\mathcal{D}_0+\mathcal{D})(t-t_0)} \cdot |\rho_0\rangle\!\!\rangle + \int \mathrm{d}t_1 \mathrm{e}^{(\mathcal{D}_0+\mathcal{D})(t-t_1)} \cdot \widetilde{\mathcal{W}}^{(1)}(t_1) \cdot |\rho_0\rangle\!\!\rangle \\ + \int \mathrm{d}t_1 \mathrm{e}^{(\mathcal{D}_0+\mathcal{D})(t-t_1)} \cdot \widetilde{\mathcal{W}}^{(2)}(t_1) \cdot |\rho_0\rangle\!\!\rangle \,, \end{aligned} \tag{5.79}$$

$$\widetilde{\mathcal{W}}^{(1)}(t_1) = \mathcal{M} \cdot \mathrm{e}^{(\mathcal{D}_0+\mathcal{D})(t_1-t_0)}\,, \tag{5.80}$$

$$\widetilde{\mathcal{W}}^{(2)}(t_1) = \int \mathrm{d}t_2 \mathcal{M} \cdot \mathrm{e}^{(\mathcal{D}_0+\mathcal{D})(t_1-t_2)} \cdot \mathcal{M} \cdot \mathrm{e}^{(\mathcal{D}_0+\mathcal{D})(t_2-t_0)}\,, \tag{5.81}$$

where we defined the superoperators $\widetilde{\mathcal{W}}^{(1)}$ and $\widetilde{\mathcal{W}}^{(2)}$ in analogy to $\mathcal{W}^{(1)}$ and $\mathcal{W}^{(2)}$ of section 5.2.1. The time derivative of the density matrix is then given by

$$\left|\dot{\rho}_S(t)\right\rangle\!\!\right\rangle \approx (\mathcal{D}_0 + \mathcal{D}) \cdot |\rho_S(t)\rangle\!\!\rangle + \widetilde{\mathcal{W}}^{(1)}(t) \cdot |\rho_S(t_0)\rangle\!\!\rangle + \widetilde{\mathcal{W}}^{(2)}(t_1) \cdot |\rho_S(t_0)\rangle\!\!\rangle \,. \tag{5.82}$$

Again, we did not replace $|\rho_S(t)\rangle\!\!\rangle$ in the first term of Eq. (5.82) with its approximated form. We call this alternative perturbation scheme incoherent perturbation scheme, since the additional homogeneous evolution, given by $\exp[\mathcal{D}t]$ includes incoherent dynamics of the reduced system. Thus, the incoherent perturbation scheme may be obtained from

the ordinary perturbation scheme introduced in section 5.2.1 by replacing $\mathcal{D}_0 \to \mathcal{D}_0 + \mathcal{D}$ and $\mathcal{L} \to \mathcal{M}$.

Next, we determine the diagonal part $\mathcal{D}$ of our explicit Lindblad operator. We have already derived the explicit expression of the Lindblad operator, $\mathcal{L} = \mathcal{L}_{\mathrm{DD}} + \mathcal{L}_{\mathrm{AA}} + \mathcal{L}_{\mathrm{DA}}$ in section 5.2.2. Only $\mathcal{L}_{\mathrm{DD}}$ and $\mathcal{L}_{\mathrm{AA}}$ contain diagonal elements in Fock–Liouvillespace. They are given by

$$\begin{aligned}\mathcal{D} = -\frac{1}{\hbar^2}\sum\int \mathrm{d}t_1 \Big\{ & \mathrm{e}^{\mathrm{i}\omega_{\alpha n}(t-t_1)} \boldsymbol{d}^{\mathrm{D}}_{\alpha n} \cdot C_{\mathrm{DD}}(\tau) \cdot \boldsymbol{d}^{\mathrm{D}}_{n\alpha} + \mathrm{e}^{-\mathrm{i}\omega_{\beta m}(t-t_1)} \boldsymbol{d}^{\mathrm{D}}_{m\beta} \cdot C^*_{\mathrm{DD}}(\tau) \cdot \boldsymbol{d}^{\mathrm{D}}_{\beta m} \\ & + \mathrm{e}^{\mathrm{i}\omega_{\gamma n}(t-t_1)} \boldsymbol{d}^{\mathrm{A}}_{\gamma n} \cdot C_{\mathrm{AA}}(\tau) \cdot \boldsymbol{d}^{\mathrm{A}}_{n\gamma} + \mathrm{e}^{-\mathrm{i}\omega_{\epsilon m}(t-t_1)} \boldsymbol{d}^{\mathrm{A}}_{m\epsilon} \cdot C^*_{\mathrm{AA}}(\tau) \cdot \boldsymbol{d}^{\mathrm{A}}_{\epsilon m} \Big\} \\ & \times |\alpha\beta\gamma\epsilon\rangle\!\rangle\langle\!\langle \alpha\beta\gamma\epsilon| \,, \end{aligned} \tag{5.83}$$

where we have used $\omega_{ij} = -\omega_{ji}$. The superoperator $\mathcal{M}$ is then simply given by the remaining terms of the Lindblad operator, $\mathcal{M} = \mathcal{L} - \mathcal{D}$. Using Eqs. (5.47) and (5.50), we get

$$\begin{aligned}\mathcal{D} \cdot |\rho_{\mathrm{S}}(t)\rangle\!\rangle = \Bigg[& \mathrm{i}\sum_n \Big(\delta\omega_{\alpha n} - \delta\omega_{\beta n}\Big) - \sum_{n<\alpha} \frac{\gamma_{\alpha n}}{2} - \sum_{n<\beta} \frac{\gamma_{\beta n}}{2} \\ & \mathrm{i}\sum_n \big(\delta\omega_{\gamma n} - \delta\omega_{\epsilon n}\big) - \sum_{n<\gamma} \frac{\gamma_{\gamma n}}{2} - \sum_{n<\epsilon} \frac{\gamma_{\epsilon n}}{2} \Bigg] \rho_{\alpha\beta\gamma\epsilon}(t)\, |\alpha\beta\gamma\epsilon\rangle\!\rangle\langle\!\langle \alpha\beta\gamma\epsilon| \,, \end{aligned} \tag{5.84}$$

$$\gamma_{ij} = \frac{2\mu_0}{\hbar}\omega_{ij}^2 \boldsymbol{d}_{ij} \cdot \mathrm{Im}\mathbb{G}(\boldsymbol{r}_a, \boldsymbol{r}_a, \omega_{ij}) \cdot \boldsymbol{d}_{ji} \,, \tag{5.85}$$

$$\delta\omega_{ij} = -\frac{\mu_0}{\hbar\pi}\mathcal{P}\int_0^\infty \mathrm{d}\omega\, \frac{\omega^2}{\omega - \omega_{ij}} \boldsymbol{d}_{ij} \cdot \mathrm{Im}\mathbb{G}(\boldsymbol{r}_a, \boldsymbol{r}_a, \omega_{ij}) \cdot \boldsymbol{d}_{ji} \,, \tag{5.86}$$

where we have introduced the decay rates γ_{ij}, see section 5.2.3 and Lamb shifts $\delta\omega_{ij}$ and used that for all $j < i$ one has $\omega_{ij} > 0$. It should be noted that the symbol γ is used for the decay rates as well as for level labelling, their respective meaning however is unambiguous in the context of each instance. Here, we are not interested in the Lamb shifts. They lead to small corrections of the bare atomic eigenfrequencies which are typically negligible: $\sum_n(\delta\omega_{\alpha n} - \delta\omega_{\beta n}) \ll \omega_{\alpha\beta}$. However, the decay rates γ_{ij} may influence the calculation significantly, despite being small compared to the eigenfrequencies. The diagonal part of the Lindblad superoperator can then be written as

$$\mathcal{D} = -\sum \gamma_{ijkl}\, |ijkl\rangle\!\rangle\langle\!\langle ijkl| \,, \tag{5.87}$$

with $\gamma_{ijkl} = \frac{1}{2}(\gamma_i + \gamma_j + \gamma_k + \gamma_l)$ and $\gamma_i = \sum_{j<i} \gamma_{ij}$ and we neglected the Lamb shifts. And

the homogeneous solution of the master equation is given by

$$\mathrm{e}^{(\mathcal{D}_0+\mathcal{D})(t-t_0)} = \sum \mathrm{e}^{-[\mathrm{i}(\omega_{ij}+\omega_{kl})+\gamma_{ijkl}](t-t_0)} \left|ijkl\right\rangle\!\left\rangle\langle\!\langle ijkl\right| , \tag{5.88}$$

which now includes the incoherent dynamics of the reduced system.

Using the definition of the diagonal matrices $\mathcal{D}_0$ and $\mathcal{D}$, see Eqs. (5.29) and (5.88), we may give the approximated master equation (5.82) in the basis of the vectorised density matrix as

$$\begin{aligned}\left|\dot{\rho}_S(t)\right\rangle\!\left\rangle = &-\left[\mathrm{i}\sum(\omega_{st}+\omega_{uv})+\gamma_{stuv}\right]\rho_{stuv}(t)\left|stuv\right\rangle\!\left\rangle \\ &+\sum\left\langle\!\left\langle stuv|\widetilde{\mathcal{W}}^{(1)}|\alpha\beta\gamma\epsilon\right\rangle\!\right\rangle\rho_{\alpha\beta\gamma\epsilon}(t_0)\left|stuv\right\rangle\!\left\rangle \right. \\ &\left.+\sum\left\langle\!\left\langle stuv|\widetilde{\mathcal{W}}^{(2)}|\alpha\beta\gamma\epsilon\right\rangle\!\right\rangle\rho_{\alpha\beta\gamma\epsilon}(t_0)\left|stuv\right\rangle\!\left\rangle\right. , \end{aligned} \tag{5.89}$$

$$\begin{aligned}\widetilde{\mathcal{W}}^{(2)} = \sum\int_{t_0}^{t}\mathrm{d}t_1\mathrm{e}^{-(\mathrm{i}\omega_{ij}+\mathrm{i}\omega_{kl}+\gamma_{ijkl})(t-t_1)}\mathrm{e}^{-(\mathrm{i}\omega_{\alpha\beta}+\mathrm{i}\omega_{\gamma\epsilon}+\gamma_{\alpha\beta\gamma\epsilon})(t_1-t)} \\ \times\left\langle\!\left\langle stuv|\mathcal{M}|ijkl\right\rangle\!\right\rangle\left\langle\!\left\langle ijkl|\mathcal{M}|\alpha\beta\gamma\epsilon\right\rangle\!\right\rangle\left|stuv\right\rangle\!\left\rangle\left\langle\!\left\langle\alpha\beta\gamma\epsilon\right|\right. , \end{aligned} \tag{5.90}$$

where the sum runs over all state labels.

5.3.2. Polarisability tensor with finite linewidth

We have derived the homogeneous incoherent evolution of an atomic system in the electromagnetic vacuum and based on this introduced an incoherent perturbation scheme. As we will see here, the incoherent perturbation scheme introduces linewidths explicitly into perturbative calculations and may be used to derive corrections to various quantities derived from the ordinary perturbation scheme introduced in section 5.2.1. A rather important example for such corrections is the polarisability tensor, see section 2.3.2. Here, we apply the incoherent perturbation scheme on the example of the polarisability tensor to find corrections due to the finite linewidths of the atomic transitions. The calculation of the polarisability requires only a single atom and first-order perturbation. In addition, we need to consider an external field. Thus, we need to adapt the master equation accordingly.

The polarisability tensor $\boldsymbol{\alpha}_n$ of a particle in state n is defined via the induced dipole moment by an external field in Fourier space:

$$\mathcal{FT}\left[\langle\hat{\boldsymbol{d}}(t)\rangle_n\right] = \langle\hat{\boldsymbol{d}}(\omega)\rangle_n = \boldsymbol{\alpha}_n(\boldsymbol{r},\omega)\cdot\boldsymbol{E}(\boldsymbol{r},\omega)\,, \tag{5.91}$$

$$\hat{\boldsymbol{d}} = \sum_{ij}\boldsymbol{d}_{ij}\hat{A}_{ij} \tag{5.92}$$

where $\boldsymbol{E}(\boldsymbol{r},\omega) = \langle \hat{\boldsymbol{E}}(\boldsymbol{r},\omega)\rangle$ is the Fourier component of the external electric field, $\hat{A}_{ij}$ are again the atomic flip operators and we assumed that the particle does not possess an intrinsic polarisation, i.e. $\boldsymbol{d}_{ii} = \boldsymbol{0}$. In section 2.3.2 we derived the polarisability tensor via ordinary perturbation theory. Here, we repeat the calculation in the incoherent perturbation scheme. For simplicity, we focus on the ground state polarisability $\boldsymbol{\alpha}_0$.

The system that needs to be considered for deriving $\boldsymbol{\alpha}_0$ is given by a single atom in an external field. For only one particle in the field, we find that $\mathcal{L} = \mathcal{L}_1 = \mathrm{Tr}_\mathrm{A}\{\mathcal{L}_\mathrm{DD}\}$, see Eq. (5.51). The diagonal part of the Lindblad operator is then given by

$$\begin{aligned}\mathcal{D} &= -\sum \int \mathrm{d}t_1 \Big\{ \mathrm{e}^{\mathrm{i}\omega_{\alpha n}(t-t_1)} \boldsymbol{d}^\mathrm{D}_{\alpha n} \cdot \mathrm{C}_\mathrm{DD}(\tau) \cdot \boldsymbol{d}^\mathrm{D}_{n\alpha} \\ &\qquad + \mathrm{e}^{-\mathrm{i}\omega_{\beta m}(t-t_1)} \boldsymbol{d}^\mathrm{D}_{m\beta} \cdot \mathrm{C}^*_\mathrm{DD}(\tau) \cdot \boldsymbol{d}^\mathrm{D}_{\beta m} \Big\} \, |\alpha\beta\rangle\!\rangle\langle\!\langle \alpha\beta| \\ &= -\Big(\mathrm{i}\delta\omega_\alpha - \mathrm{i}\delta\omega_\beta + \gamma_\alpha + \gamma_\beta\Big) \, |\alpha\beta\rangle\!\rangle\langle\!\langle \alpha\beta| \ , \end{aligned} \tag{5.93}$$

where the decay rates $\gamma_{\alpha/\beta}$ and the Lamb shifts $\delta\omega_{\alpha/\beta} \ll \omega_{\alpha\beta}$ are given by Eqs. (5.85) and (5.86). We will neglect the Lamb shifts here again. The full homogeneous evolution, see Eq. (5.88) is then governed by

$$\mathrm{e}^{(\mathcal{D}_0+\mathcal{D})(t-t_0)} = \sum \mathrm{e}^{-[\mathrm{i}\omega_{\alpha\beta}+\gamma_\alpha+\gamma_\beta](t-t_0)} \, |\alpha\beta\rangle\!\rangle\langle\!\langle \alpha\beta| \ . \tag{5.94}$$

Additionally, in the presence of an external field our master equation (5.24) needs to be adapted accordingly. We assumed in our derivation for Eq. (5.27) that $\mathrm{Tr}_\mathrm{F}\{[H,\rho_\mathrm{S}\rho_\mathrm{F}]\}$ vanishes, which is not true for an external electric field. The master equation (5.77) hence gains an extra term, such that

$$|\dot{\rho}_\mathrm{S}(t)\rangle\!\rangle = (\mathcal{D}_0 + \mathcal{D}) \cdot |\rho_S(t)\rangle\!\rangle + (\mathcal{M} + \mathcal{M}_\mathrm{ext}) \cdot |\rho_S(t)\rangle\!\rangle \ , \tag{5.95}$$

$$\mathcal{M}_\mathrm{ext} \cdot |\rho_S(t)\rangle\!\rangle = -\frac{\mathrm{i}}{\hbar} \mathrm{Tr}_\mathrm{F} \left\{ \left[\hat{V}(t), \rho_\mathrm{S}(t) \otimes \rho_\mathrm{F}\right]\right\} = \frac{\mathrm{i}}{\hbar} \left[\hat{\boldsymbol{d}} \cdot \boldsymbol{E}(\boldsymbol{r},t), \rho_\mathrm{S}(t)\right] \ , \tag{5.96}$$

where $\mathcal{M}_\mathrm{ext}$ is linear in $\boldsymbol{E}(\boldsymbol{r},t)$, while $\mathcal{M}$ depends on the correlation function $\mathbb{C}$, i.e. depends on quadratic expressions of the external field, see Eq. (5.39). Using the incoherent perturbation scheme for the density matrix up to first order, see Eq. (5.79), we then find

$$\begin{aligned}\rho_\mathrm{S}(t) = \mathrm{e}^{(\mathcal{D}_0+\mathcal{D})(t-t_0)} \, |\rho_S(t_0)\rangle\!\rangle &+ \int \mathrm{d}t_1 \mathrm{e}^{(\mathcal{D}_0+\mathcal{D})(t-t_1)} \cdot \mathcal{M} \cdot \mathrm{e}^{(\mathcal{D}_0+\mathcal{D})(t_1-t_0)} \cdot |\rho_\mathrm{S}(t_0)\rangle\!\rangle \\ &+ \int \mathrm{d}t_1 \mathrm{e}^{(\mathcal{D}_0+\mathcal{D})(t-t_1)} \cdot \mathcal{M}_\mathrm{ext} \cdot \mathrm{e}^{(\mathcal{D}_0+\mathcal{D})(t_1-t_0)} \cdot |\rho_\mathrm{S}(t_0)\rangle\!\rangle \ , \end{aligned} \tag{5.97}$$

where only the last term is proportional to $\boldsymbol{E}(\boldsymbol{r},t)$. The ground state expectation value

of the induced dipole in its lowest order is then given only by the last term:

$$\langle \hat{\boldsymbol{d}}(t)\rangle_0 = \mathrm{Tr}\{\hat{\boldsymbol{d}}\rho_\mathrm{S}(t)\} \approx \mathrm{Tr}\{\hat{\boldsymbol{d}}\rho_\mathrm{S}^\mathrm{ext}(t)\}\,, \tag{5.98}$$

$$\left|\rho_\mathrm{S}^\mathrm{ext}(t)\right\rangle\!\!\right\rangle = \int \mathrm{d}t_1 \mathrm{e}^{(\mathcal{D}_0+\mathcal{D})(t-t_1)} \cdot \mathcal{M}_\mathrm{ext} \cdot \mathrm{e}^{(\mathcal{D}_0+\mathcal{D})(t_1-t_0)} \cdot |\rho_\mathrm{S}(t_0)\rangle\!\!\rangle \tag{5.99}$$

So let us hence focus on calculating $\rho_\mathrm{S}^\mathrm{ext}(t)$. We first derive $\mathcal{M}_\mathrm{ext}$ as a superoperator:

$$\mathcal{M}_\mathrm{ext} \cdot |\rho_\mathrm{S}(t)\rangle\!\!\rangle = -\frac{\mathrm{i}}{\hbar}\left[\hat{\boldsymbol{d}}\cdot\boldsymbol{E}(\boldsymbol{r},t), \rho_\mathrm{S}(t)\right] \tag{5.100}$$

$$= \frac{\mathrm{i}}{\hbar}\sum\left\{\boldsymbol{d}_{k\alpha}\cdot\boldsymbol{E}(\boldsymbol{r},t)\,|k\rangle\,\langle\beta|\,\rho_{\alpha\beta}(t) - \boldsymbol{d}_{\beta k}\cdot\boldsymbol{E}(\boldsymbol{r},t)\,|\alpha\rangle\,\langle k|\,\rho_{\alpha\beta}(t)\right\} \tag{5.101}$$

$$= \frac{\mathrm{i}}{\hbar}\sum\left\{\boldsymbol{d}_{k\alpha}\cdot\boldsymbol{E}(\boldsymbol{r},t)\,|k\beta\rangle\!\!\rangle\langle\!\langle\alpha\beta| - \boldsymbol{d}_{\beta k}\cdot\boldsymbol{E}(\boldsymbol{r},t)\,|\alpha k\rangle\!\!\rangle\langle\!\langle\alpha\beta|\right\}\rho_{\alpha\beta}(t)\,|\alpha\beta\rangle\!\!\rangle\,, \tag{5.102}$$

where $\rho_{\alpha\beta}(t)\,|\alpha\beta\rangle\!\!\rangle = |\rho_\mathrm{S}(t)\rangle\!\!\rangle_{\alpha\beta}$ are the components of the density matrix vector. The superoperator $\mathcal{M}_\mathrm{ext}$ is thus given by

$$\mathcal{M}_\mathrm{ext} = \frac{\mathrm{i}}{\hbar}\sum\left\{\boldsymbol{d}_{k\alpha}\cdot\boldsymbol{E}(\boldsymbol{r},t)\,|k\beta\rangle\!\!\rangle\langle\!\langle\alpha\beta| - \boldsymbol{d}_{\beta k}\cdot\boldsymbol{E}(\boldsymbol{r},t)\,|\alpha k\rangle\!\!\rangle\langle\!\langle\alpha\beta|\right\}\,, \tag{5.103}$$

with this and $|\rho_\mathrm{S}(t_0)\rangle\!\!\rangle = |00\rangle\!\!\rangle$, we may calculate $\rho_\mathrm{S}^\mathrm{ext}(t)$ via Eq. (5.99),

$$\left|\rho_\mathrm{S}^\mathrm{ext}(t)\right\rangle\!\!\right\rangle = \frac{\mathrm{i}}{\hbar}\sum_k\int \mathrm{d}t_1\Big\{\mathrm{e}^{(-\mathrm{i}\omega_{k0}-\gamma_k)(t-t_1)}\boldsymbol{d}_{kn}\cdot\boldsymbol{E}(\boldsymbol{r},t_1)\,|k0\rangle\!\!\rangle - \mathrm{e}^{(\mathrm{i}\omega_{k0}-\gamma_k)(t-t_1)}\boldsymbol{d}_{nk}\cdot\boldsymbol{E}(\boldsymbol{r},t_1)\,|0k\rangle\!\!\rangle\Big\}\,. \tag{5.104}$$

We can translate the Fock–Liouville vector $\left|\rho_\mathrm{S}^\mathrm{ext}(t)\right\rangle\!\!\right\rangle$ back into a usual density matrix,

$$\rho_\mathrm{S}^\mathrm{ext}(t) = \frac{\mathrm{i}}{\hbar}\sum_k\int \mathrm{d}t_1\mathrm{e}^{(\mathcal{D}_0+\mathcal{D})(t-t_1)}\Big\{\mathrm{e}^{(-\mathrm{i}\omega_{k0}-\gamma_k)(t-t_1)}\boldsymbol{d}_{kn}\cdot\boldsymbol{E}(\boldsymbol{r},t_1)\,|k\rangle\,\langle 0| - \mathrm{e}^{(\mathrm{i}\omega_{k0}-\gamma_k)(t-t_1)}\boldsymbol{d}_{nk}\cdot\boldsymbol{E}(\boldsymbol{r},t_1)\,|0\rangle\,\langle k|\Big\}\,. \tag{5.105}$$

Substituting this into Eq. (5.98) yields

$$\langle\hat{\boldsymbol{d}}(t)\rangle_0 = \frac{\mathrm{i}}{\hbar}\sum_k\int \mathrm{d}t_1\mathrm{e}^{-\gamma_k(t-t_1)}\Big\{\mathrm{e}^{-\mathrm{i}\omega_{0k}(t-t_1)}\boldsymbol{d}_{0k}\otimes\boldsymbol{d}_{k0}\cdot\boldsymbol{E}(\boldsymbol{r},t_1) - \mathrm{e}^{\mathrm{i}\omega_{0k}(t-t_1)}\boldsymbol{d}_{k0}\otimes\boldsymbol{d}_{0k}\cdot\boldsymbol{E}(\boldsymbol{r},t_1)\Big\}\,. \tag{5.106}$$

This is almost the same expression for the expectation value of the dipole moment as we have derived in section 2.3.2, see Eq. (2.137) but includes now an additional expo-

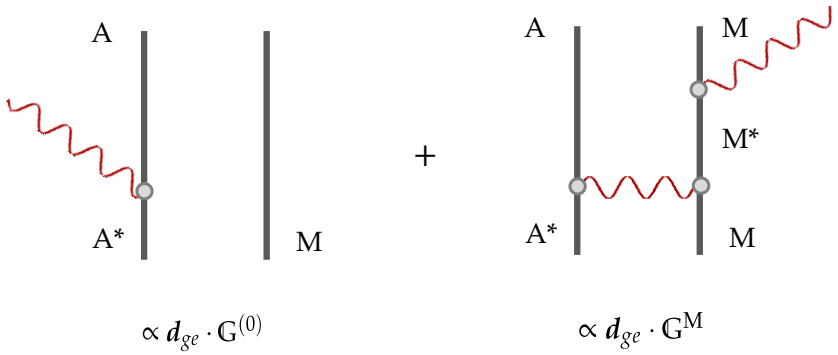

Figure 5.1.: Feynman diagrams for emission rate: In lowest order spontaneous decay is a first order process on the level of transition matrix elements (left diagram). Hence, the transition matrix element is proportional to a single dipole moment $\boldsymbol{d}_{ge}$. The next higher order for the process includes three dipoles and is displayed on the right. Each wavy line represents a field excitation and each intersection represents a transition dipole moment. By introducing the mediator Green's tensor $\mathbb{G}^{\mathrm{M}}$ we can include the higher order Feynman diagram directly into the first order calculation.

nential decay $\mathrm{e}^{-\gamma_{nk}(t-t_1)}$ in the integrand. The remaining calculation follows the same steps as that in section 2.3.2: we substitute the decomposition of the electric field in its Fourier components, perform the integration over t_1, perform the Fourier transform of the expectation value and finally find:

$$\begin{aligned} &\mathcal{FT}\left[\left\langle \hat{\boldsymbol{d}} \right\rangle_n\right] = \boldsymbol{\alpha}(\omega) \cdot \boldsymbol{E}(\boldsymbol{r}, \omega) \\ &\text{with} \quad \boldsymbol{\alpha}(\omega) = \frac{1}{\hbar} \sum_k \left(\frac{\langle k|\boldsymbol{d}|0\rangle \otimes \langle 0|\boldsymbol{d}|k\rangle}{\omega + \omega_{k0} + \mathrm{i}\gamma_k} - \frac{\langle 0|\boldsymbol{d}|k\rangle \otimes \langle k|\boldsymbol{d}|0\rangle}{\omega - \omega_{k0} + \mathrm{i}\gamma_k} \right), \end{aligned} \tag{5.107}$$

which in contrast to the polarisability derived in section 2.3.2 does not diverge for $\omega = \omega_{kn}$ but each transition resonance exhibits a finite width governed by their spontaneous decay rate $\gamma_k = \gamma_{k0}$. They are given by the usual expression Eq. (5.85) when considering the electromagnetic gorund state.

5.3.3. Oscillating transfer rate

When calculating the Van-der-Waals force between an excited and a ground state particle, two different results can be obtained depending on the treatment of the frequency poles appearing in the perturbative calculation. Using an approach comparable to the developed incoherent perturbation scheme, it was shown that both results are legitimate, but have different interpretations. Since the excited particle additionally decays, it experiences a recoil by the emitted photon. In this section we derive an analogous behaviour for the full decay rate of the excited donor atom in contrast to the excitation rate of the

acceptor in RET. We achieve this here by careful consideration of all decay channels via Fermi's golden rule up to the leading perturbation order of RET.

We consider an excited atom in the presence of a second ground state atom. As displayed in Fig. 5.1, the spontaneous decay of the excited atom is in lowest order a first order process. The next correction that has to be taken into account is of third order. In third order we find a correction term to the spontaneous decay rate due to the coupling to the second particle. We circumvent higher-order perturbation theory by including the second atom's interaction with the field into the Green's tensor as a perturbation of the free-space environment.

The Green's tensor in the presence of a mediating atom is given by Eq. (2.146), see section 2.3.3 and reads

$$\mathbb{G}(\boldsymbol{r},\boldsymbol{r}') = \mathbb{G}^{(0)}(\boldsymbol{r},\boldsymbol{r}') + \mathbb{G}^{\mathrm{M}}(\boldsymbol{r},\boldsymbol{r}')\,, \tag{5.108}$$

$$\mathbb{G}^{\mathrm{M}}(\boldsymbol{r},\boldsymbol{r}') = \frac{\omega^2}{c^2}\mathbb{G}^{(0)}(\boldsymbol{r},\boldsymbol{r}_{\mathrm{M}})\cdot\frac{\boldsymbol{\alpha}(\omega)}{\varepsilon_0}\cdot\mathbb{G}^{(0)}(\boldsymbol{r}_{\mathrm{M}},\boldsymbol{r}')\,, \tag{5.109}$$

where $\mathbb{G}^{\mathrm{M}}$ is the mediator Green's tensor and the polarisability is given by

$$\boldsymbol{\alpha}(\omega) = \frac{1}{\hbar}\sum_k\Big(\frac{\langle k|\boldsymbol{d}|0\rangle\otimes\langle 0|\boldsymbol{d}|k\rangle}{\omega+\omega_{k0}+\mathrm{i}\gamma_{k0}} - \frac{\langle 0|\boldsymbol{d}|k\rangle\otimes\langle k|\boldsymbol{d}|0\rangle}{\omega-\omega_{k0}+\mathrm{i}\gamma_{k0}}\Big)\,, \tag{5.110}$$

where γ_{k0} are the damping constants of the k-th level. The damping constant is given by the decay width of the respective level and the damped polarisability tensor is a result obtained from the open quantum systems approach, see section 5.3.2.

By modifying the Green's tensor in this way, we effectively consider the third-order Feynman diagram depicted in Fig. 5.1 as one single order of perturbation. The process is hence included in the first-order rate expression derived via Fermi's golden, see section 5.1,

$$\Gamma = \frac{2\mu_0}{\hbar}\omega_{eg}^2\boldsymbol{d}_{eg}\cdot\mathrm{Im}\mathbb{G}(\boldsymbol{r}_{\mathrm{A}},\boldsymbol{r}_{\mathrm{A}},\omega_{eg})\cdot\boldsymbol{d}_{ge}\,. \tag{5.111}$$

For the Green's tensor including the mediation by a second particle, see Eq. (5.108) we hence get

$$\Gamma = \Gamma_{\mathrm{s}}^{(0)} + \Gamma^{\mathrm{M}}\,, \tag{5.112}$$

$$\Gamma^{\mathrm{M}} = \frac{2\mu_0}{\hbar}\omega_{eg}^2\boldsymbol{d}_{eg}\cdot\mathrm{Im}\mathbb{G}^{\mathrm{M}}(\boldsymbol{r}_{\mathrm{A}},\boldsymbol{r}_{\mathrm{A}},\omega_{eg})\cdot\boldsymbol{d}_{ge}\,, \tag{5.113}$$

where $\Gamma_{\mathrm{s}}^{(0)} = \gamma_{eg}$ is the free space spontaneous decay rate given by Eq. (5.9) and Γ^{M} depends on four dipole moments and results from the interference of both decay channels

depicted in Fig. 5.1. Please note that the absolute squared of the third-order diagram was already implicitly neglected by applying the integral relation for the Born-approximated Green's tensor to obtain Eq. (5.111). The mediator-contribution to the rate Γ^{M} is then given in terms of the polarisability by

$$\begin{aligned}\Gamma^{\mathrm{M}} = \frac{2\mu_0}{\hbar\varepsilon_0 c^2}\omega_{eg}^4 \boldsymbol{d}_{eg}\cdot\Big\{&\mathrm{Im}\mathbb{G}^{(0)}(\boldsymbol{r}_{\mathrm{A}},\boldsymbol{r}_{\mathrm{M}})\cdot\left(\mathrm{Re}\boldsymbol{\alpha}+\mathrm{Re}\boldsymbol{\alpha}^T\right)\cdot\mathrm{Re}\mathbb{G}^{(\mathbf{0})}(\boldsymbol{r}_{\mathrm{M}},\boldsymbol{r}_{\mathrm{A}})\\ &+\mathrm{Re}\mathbb{G}^{(0)}(\boldsymbol{r}_{\mathrm{A}},\boldsymbol{r}_{\mathrm{M}})\cdot\mathrm{Im}\boldsymbol{\alpha}\cdot\mathrm{Re}\mathbb{G}^{(\mathbf{0})}(\boldsymbol{r}_{\mathrm{M}},\boldsymbol{r}_{\mathrm{A}})\\ &-\mathrm{Im}\mathbb{G}^{(0)}(\boldsymbol{r}_{\mathrm{A}},\boldsymbol{r}_{\mathrm{M}})\cdot\mathrm{Im}\boldsymbol{\alpha}\cdot\mathrm{Im}\mathbb{G}^{(\mathbf{0})}(\boldsymbol{r}_{\mathrm{M}},\boldsymbol{r}_{\mathrm{A}})\Big\}\cdot\boldsymbol{d}_{ge}\,. \end{aligned}\tag{5.114}$$

Next, let us apply some assumptions to the polarisability tensor to simplify the derivation. Firstly, we assume that the mediator particle M and the decaying particle A are identical. We then find that there exists a transition such that $\omega_{k0}=\omega_{eg}$ in the polarisability (5.107). In this case the resonant transition dominates and we can approximate

$$\boldsymbol{\alpha}(\omega_{eg})\approx\frac{1}{\hbar}\sum_{\text{degen.}}\left(\frac{\boldsymbol{d}_{eg}\otimes\boldsymbol{d}_{ge}}{\omega_{eg}+(\omega_{eg}+\mathrm{i}\gamma_{eg})}-\frac{\boldsymbol{d}_{ge}\otimes\boldsymbol{d}_{eg}}{\omega_{eg}-(\omega_{eg}-\mathrm{i}\gamma_{eg})}\right), \tag{5.115}$$

where the sum now only includes degeneracies. Secondly, We assume that the transition is isotropic when summing over all its degeneracies, such that $\boldsymbol{d}_{eg}\otimes\boldsymbol{d}_{ge}=|\boldsymbol{d}_{eg}|^2\mathbb{I}/3$. We then get

$$\boldsymbol{\alpha}(\omega_{eg})\approx\frac{2}{3\hbar}\frac{|\boldsymbol{d}_{eg}|^2\omega_{eg}}{\gamma_{eg}^2-2\mathrm{i}\omega_{eg}\gamma_{eg}}\mathbb{I}\approx\frac{\mathrm{i}}{3\hbar}\frac{|\boldsymbol{d}_{eg}|^2}{\gamma_{eg}}\mathbb{I}\,, \tag{5.116}$$

where we have used that the eigen-oscillations are much faster than the decay, $\omega_{eg}\gg\gamma_{eg}$ to approximate $\boldsymbol{\alpha}(\omega_{eg})$ further. Within these approximations the polarisability tensor at the resonance $\boldsymbol{\alpha}(\omega_{eg})$ is hence purely imaginary. With the damping constant given by the spontaneous decay rate in free space, $\gamma_{eg}=\omega_{eg}^3|\boldsymbol{d}_{eg}|^2/3\pi\varepsilon_0\hbar c^3$ we finally get

$$\boldsymbol{\alpha}(\omega_{eg})\approx\frac{\mathrm{i}\pi\varepsilon_0 c^3}{\omega_{eg}^3}\,. \tag{5.117}$$

Substituting this back into Eq. (5.109) we find for the mediated rate (5.113)

$$\begin{aligned}\Gamma^{\mathrm{M}}\approx\frac{2\mu_0\omega_{eg}^4}{\varepsilon_0\hbar c^2}\Big\{&\boldsymbol{d}_{eg}\cdot\mathrm{Re}\mathbb{G}^{(0)}_{\mathrm{AM}}(\omega_{eg})\cdot\mathrm{Im}\boldsymbol{\alpha}(\omega_{eg})\cdot\mathrm{Re}\mathbb{G}^{(0)}_{\mathrm{MA}}(\omega_{eg})\cdot\boldsymbol{d}_{ge}\\ &-\boldsymbol{d}_{eg}\cdot\mathrm{Im}\mathbb{G}^{(0)}_{\mathrm{AM}}(\omega_{eg})\cdot\mathrm{Im}\boldsymbol{\alpha}(\omega_{eg})\cdot\mathrm{Im}\mathbb{G}^{(0)}_{\mathrm{MA}}(\omega_{eg})\cdot\boldsymbol{d}_{ge}\Big\}\,, \end{aligned}\tag{5.118}$$

where we have used the shorthand notation $G_{\mathrm{AM}}(\omega)=\mathbb{G}(\boldsymbol{r}_{\mathrm{A}},\boldsymbol{r}_{\mathrm{M}},\omega)$. We can again employ our assumption that the transition dipole moments are isotropic, i.e. $\boldsymbol{d}_{eg}\otimes\boldsymbol{d}_{ge}=$

$|\boldsymbol{d}_{eg}|^2\mathbb{I}/3$. With $\boldsymbol{v}\cdot\mathbb{T}\cdot\boldsymbol{w} = \mathrm{Tr}[\boldsymbol{w}\otimes\boldsymbol{v}\cdot\mathbb{T}]$ for any vectors $\boldsymbol{v},\boldsymbol{w}$ and tensor $\mathbb{T}$. We then find

$$\Gamma^{\mathrm{M}} \approx \frac{2\pi\omega_{eg}|\boldsymbol{d}_{eg}|^2}{3\hbar\varepsilon_0 c}\Big\{\mathrm{Tr}\left[\mathrm{Re}\mathbb{G}^{(0)}_{\mathrm{AM}}(\omega_{eg})\cdot\mathrm{Re}\mathbb{G}^{(0)}_{\mathrm{MA}}(\omega_{eg})\right] - \mathrm{Tr}\left[\mathrm{Im}\mathbb{G}^{(0)}_{\mathrm{AM}}(\omega_{eg})\cdot\mathrm{Im}\mathbb{G}^{(0)}_{\mathrm{MA}}(\omega_{eg})\right]\Big\}. \tag{5.119}$$

With the free space Green's tensor (A.32) we finally obtain the rate oscillating as a function of the separation distance,

$$\Gamma^{\mathrm{M}} \approx \frac{|\boldsymbol{d}_{eg}|^2}{12\pi\varepsilon_0\hbar k^3 r^6}\left\{\left(3-5k^2r^2+k^4r^4\right)\cos(2kr)+2kr\left(3-k^2r^2\right)\sin(2kr)\right\}, \tag{5.120}$$

where $k = \omega_{eg}/c$ and $r = |\boldsymbol{r}_{\mathrm{M}} - \boldsymbol{r}_{\mathrm{A}}|$. In the nonretarded limit $rk \ll 1$ the mediator contribution Γ^{M} is proportional to $1/r^6$, see Fig. 5.2. Note that Γ^{M} itself can be negative, since it stems from the interference between two decay channels. The decay rate $\Gamma = \Gamma^{(0)} + \Gamma^{\mathrm{M}}$ however is positive.

The full decay rate of an excited (donor) atom in the presence of a ground state (acceptor) atom is hence given up to fourth order by

$$\begin{aligned}\Gamma_{\mathrm{D}} &= \Gamma^{(0)}_{\mathrm{s}} + \Gamma^{\mathrm{M}} + \Gamma^{(0)}_{\mathrm{ret}} \\ &= \Gamma^{(0)}_{\mathrm{s}}\Bigg[1+\frac{1}{4k^6r^6}\left\{\left(3-5k^2r^2+k^4r^4\right)\cos(2kr)+2kr\left(3-k^2r^2\right)\sin(2kr)\right\} \\ &\qquad + \frac{\sigma(\omega_{eg})}{4\pi k^4 r^6}\left(k^4r^4+k^2r^2+3\right)\Bigg],\end{aligned} \tag{5.121}$$

where we have used the explicit form of the isotropic free-space RET rate $\Gamma^{(0)}_{\mathrm{ret}}$, see Eq. (5.21). In contrast, the excitation rate, i.e. the rate at which the acceptor transitions to its excited state is solely given by Γ_{ret},

$$\Gamma_{\mathrm{A}} = \Gamma^{(0)}_{\mathrm{ret}} = \Gamma^{(0)}_{\mathrm{s}}\frac{\sigma(\omega_{eg})}{4\pi k^4 r^6}\left(k^4r^4+k^2r^2+3\right). \tag{5.122}$$

In conclusion, we find that the excited donor exhibits a decay rate that oscillates as a function of the donor–acceptor distance, while the rate at which the acceptor is excited follows the monotonic behaviour predicted by the usual resonance energy transfer rate $\Gamma^{(0)}_{\mathrm{ret}}$.

The difference between these both rates $\Gamma_{\mathrm{D}} - \Gamma_{\mathrm{A}}$ is given by the spontaneous decay rate modified by the presence of the acceptor, $\Gamma_{\mathrm{s}} = \Gamma^{(0)}_{\mathrm{s}} + \Gamma^{\mathrm{M}}$. It is plotted in Fig. 5.2 in the nonretarded and retarded distance regimes. The oscillations are only present in the retarded regime of separations distances larger than the transition wavelength and

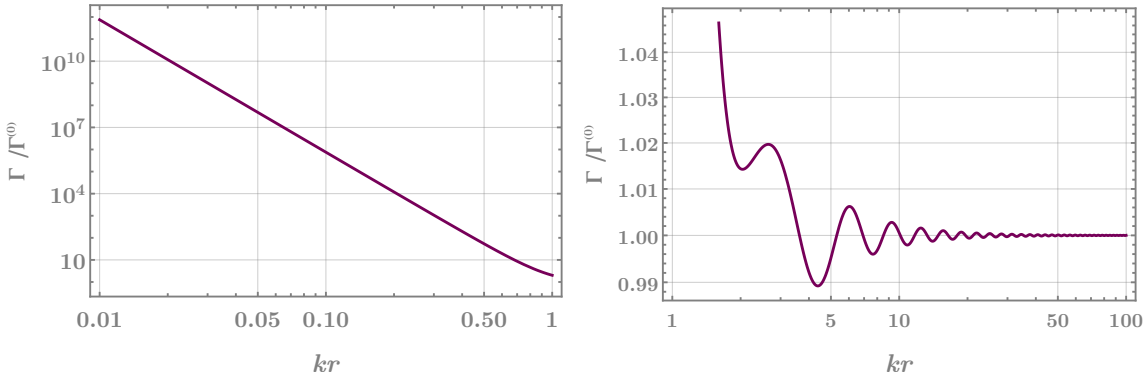

Figure 5.2.: The spontaneous decay rate Γ in the presence of a second identical ground state particle relative to the free space rate $\Gamma^{(0)}$. In the retarded regime we can verify the oscillation as a function of the separation distance r due to the second particle.

are very small in amplitude. This is in analogy with the Van-der-Waals force prediction between an excited and ground state particle [187].

5.4. Superradiance effects via Fermi's golden rule for mixed states

As demonstrated so far in this chapter the open quantum systems approach offers some advantages over purely perturbative methods. However, the respective calculations are much more involved in comparison to calculations via Fermi's golden rule, see section 5.1. So far, we have either considered pure states with the Fermi's golden rule approach or density matrices in the open quantum systems approach. It is however not necessary to discard Fermi's golden rule when considering mixed states. In this last section, we extend Fermi's golden rule to density matrices and thus mixed states. We apply this to show how superradiance effects may emerge when transitioning from a purely mixed state to a purely entangled state of two donors. We show that superradiance emerges due to interference effects and that any deviation from maximum entanglement leads to a decrease of the interference effect.

Fermi's golden rule is derived by calculating the projection of the time-evolved state $|\psi(t)\rangle = \hat{U}(t)\,|i\rangle$ onto some final state of interest $|f\rangle$ and taking the time derivative in the limit of long process times to receive a time-independent rate Γ_f, such that

$$\Gamma_f = \lim_{t\to\infty} \frac{d}{dt} |\langle f|\psi(t)\rangle|^2 . \tag{5.123}$$

Depending on the process we may then expand $|\psi(t)\rangle = \hat{U}(t)\,|i\rangle$ in the perturbation

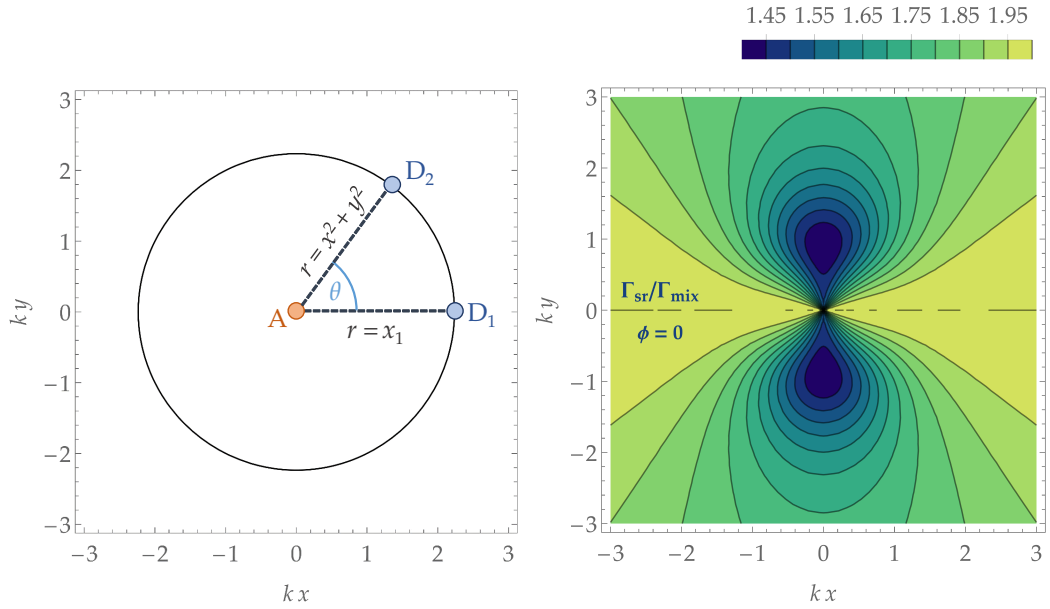

Figure 5.3.: Superradiance effect for two entangled donors with equal distance to the acceptor. The geometry is schematically explained on the left: The acceptor is fixed at the origin. We vary the position of one donor D_2 freely to any position (x, y). The other donor D_1 is fixed at the positive x-axes at $(x_1, 0)$ with $x_1 = r = \sqrt{x^2 + y^2}$. Varying the geometry of the three particles in such a way then leads to the respective relative superradiance rate Γ_{sr}/Γ_{mix} plotted on the right as a function position of D_2 (x, y) for maximum entanglement with complex phase $\phi = 0$.

order of interest which yields the respective transition matrix elements for the process, see section 2.121. Generalising this idea to density matrices yields

$$\Gamma_f = \lim_{t\to\infty} \frac{d}{dt} \mathrm{Tr}\left[\rho_f \rho(t)\right] , \tag{5.124}$$

with $\rho(t) = \hat{U}(t)\rho_i\hat{U}^\dagger(t)$. It is easy to see how pure initial and final states then lead again to the known version of Fermi's golden rule:

$$\begin{aligned}\Gamma_f &= \lim_{t\to\infty} \frac{d}{dt} \mathrm{Tr}\left[|f\rangle\langle f|\,\hat{U}(t)\,|i\rangle\langle i|\,\hat{U}^\dagger(t)\right] \\ &= \lim_{t\to\infty} \frac{d}{dt} \langle f|\,\hat{U}(t)\,|i\rangle\langle i|\,\hat{U}^\dagger(t)\,|f\rangle = \lim_{t\to\infty} \frac{d}{dt} |\langle f|\,\hat{U}(t)\,|i\rangle|^2 .\end{aligned} \tag{5.125}$$

We consider one acceptor A and two donor molecules D_1 and D_2, assuming that the acceptor is initially in its ground state $\rho_A = |0\rangle\langle 0|$, the field in its vacuum state $\rho_F = |\{0\}\rangle\langle\{0\}|$ and that there are no correlations between field and atomic systems. We first consider the two donors to be in a classical mixture $\rho_D = \rho_D^{mix}$, such that they share one

excitation classically. Their density matrix then reads

$$\rho_{\mathrm{D}}^{\mathrm{mix}} = \frac{1}{2}(|eg\rangle\langle eg| + |ge\rangle\langle ge|)\,, \tag{5.126}$$

where we have used the notation $|ij\rangle = |i\rangle_1 |j\rangle_2$ for the product state of the two donor states. Since we assumed the systems A, D and F to be initially uncorrelated we can write the initial state as

$$\rho_i = \rho_{\mathrm{A}}\rho_{\mathrm{D}}\rho_{\mathrm{F}} = \rho_{\mathrm{mix}}\,, \tag{5.127}$$

$$\rho_{\mathrm{mix}} = \frac{1}{2}(|\psi_1\rangle\langle\psi_1| + |\psi_2\rangle\langle\psi_2|)\,, \tag{5.128}$$

$$|\psi_1\rangle = |eg0, \{0\}\rangle\,, \tag{5.129}$$

$$|\psi_2\rangle = |ge0, \{0\}\rangle\,, \tag{5.130}$$

with notations $|ijk, F\rangle = |i\rangle_1 |j\rangle_2 |k\rangle_{\mathrm{A}} |F\rangle_{\mathrm{F}}$ for the product state of the respective states of first donor, second donor, acceptor and field. The final state of interest ρ_f is given by the pure state

$$\rho_f = |f\rangle\langle f| = |gg1, \{0\}\rangle\langle gg1, \{0\}|_{\mathrm{A}}\,, \tag{5.131}$$

where the excitation has been transferred to the acceptor.

In the case of such a classical mixture we can show that the respective RET rate Γ_{mix} is given by the average of two rates, one where only the first donor D_1 is excited and the other where only the second one D_2 is excited:

$$\begin{aligned}
\Gamma_{\mathrm{mix}} &= \lim_{t\to\infty}\frac{d}{dt}\,\mathrm{Tr}\left[\rho_f\rho(t)\right] \\
&= \frac{1}{2}\lim_{t\to\infty}\frac{d}{dt}\left[\langle f|U^{(2)}(t)\,|\psi_1\rangle\langle\psi_1|\,U^{(2)\dagger}(t)|f\rangle + \langle f|U^{(2)}(t)\,|\psi_2\rangle\langle\psi_2|\,U^{(2)\dagger}(t)|f\rangle\right] \\
&= \frac{1}{2}\left(\Gamma_1 + \Gamma_2\right)\,, \qquad (5.132)\\
\Gamma_1 &= \lim_{t\to\infty}\frac{d}{dt}|\,\langle f|\,U^{(2)}(t)\,|\psi_1\rangle\,|^2\,, \qquad (5.133)\\
\Gamma_2 &= \lim_{t\to\infty}\frac{d}{dt}|\,\langle f|\,U^{(2)}(t)\,|\psi_2\rangle\,|^2\,, \qquad (5.134)
\end{aligned}$$

as one would classically expect. The weight of each rate in the average is determined by the weights between ψ_1 and ψ_2 in the mixed initial state (5.127) and there are no additional interference effects. We should mention here that in general the second-order evolution for a density matrix is given by $\rho^{(2)}(t) \propto \left[\hat{H}, \left[\hat{H}, \rho_0\right]\right]$ which leads to more terms than $\hat{U}^{(2)}(t)\rho_0\hat{U}^{(2)}(t)$. However, in our specific case of initial and final states of interest, these additional terms do not contribute and we chose to simplify the derivation to account for this directly. We can calculate the two rates with the help of the Dyson series, Eq. (2.108)

and the subsequent derivation shown in section (2.2.2). The rates are given by

$$\Gamma_{1/2} = \frac{2\pi}{\hbar^4}\delta(\omega_f - \omega_i)|M_{f\psi_{1/2}}|^2\,, \tag{5.135}$$

$$M_{f\psi_{1/2}} = -\hbar\mu_0\omega_{10}^2\,\boldsymbol{d}^{\mathrm{A}}\cdot\mathbb{G}(\boldsymbol{r}_{\mathrm{A}},\boldsymbol{r}_{D_{1/2}},\omega_{10})\cdot\boldsymbol{d}^{\mathrm{D}_{1/2}}\,, \tag{5.136}$$

where the matrix element was derived in section 5.1, see Eq. (5.18). The non-excited donor does not affect the transition to the acceptor in the considered order.

The classical additivity for the total rate, see Eq. (5.132) breaks down if we consider the opposite scenario where the donors are highly entangled and share an excitation. In this case the initial state is again a pure state, given by

$$|i\rangle = \frac{1}{\sqrt{2}}(|\psi_1\rangle + \mathrm{e}^{\mathrm{i}\phi}\,|\psi_2\rangle)\,, \tag{5.137}$$

with $|\psi_{1/2}\rangle$ given by Eqs. (5.129) and (5.130) and where we left the complex phase $\phi \in \mathbb{R}$ between the super imposed states arbitrary. The rate according to Fermi's golden rule is then given by

$$\begin{aligned}\Gamma_{\mathrm{sr}} &= \lim_{t\to\infty}\frac{d}{dt}\frac{1}{2}|\,\langle f|\,U^{(2)}(t)(|\psi_1\rangle + |\psi_2\rangle)|^2 \\ &= \frac{1}{2}(\Gamma_1+\Gamma_2) + \Gamma_{\mathrm{intf}}\end{aligned} \tag{5.138}$$

$$\Gamma_{\mathrm{intf}} = \lim_{t\to\infty}\frac{d}{dt}\mathrm{Re}\left[\mathrm{e}^{-\mathrm{i}\phi}\,\langle f|\,U^{(2)}(t)\,|\psi_1\rangle\,\langle\psi_2|\,U^{(2)\dagger}(t)\,|f\rangle\right]\,, \tag{5.139}$$

where $\Gamma_{1/2}$ are given by Eq. (5.135) and we now find an additional interference term contributing to the rate compared to the RET rate with a mixed initial state, see Eq. (5.132). The interference depends on the particles' positions relative to each other and the complex phase ϕ. Following again the derivation of section 2.2.2 with the Dyson series for the time evolution operator Eq. (2.108), we find for the interference term

$$\Gamma_{\mathrm{intf}} = \frac{2\pi}{\hbar^4}\delta(\omega_f-\omega_i)\mathrm{Re}\left[M_{f\psi_1}M^*_{f\psi_2}\right]\,. \tag{5.140}$$

Let us assume that the involved dipoles have no preferred direction, such that isotropic averaging yields $\boldsymbol{d}_1\otimes\boldsymbol{d}_2 = \boldsymbol{d}_1\cdot\boldsymbol{d}_2\mathbb{I}/3$. With this we may simplify the rates further

$$\Gamma_{1/2} = \frac{2\pi\mu_0^2}{9\hbar^2}\delta(\omega_f-\omega_i)\omega_{10}^4|\boldsymbol{d}^{\mathrm{A}}|^2|\boldsymbol{d}^{\mathrm{D}}|^2\,\mathrm{Tr}\left\{\mathbb{G}_{\mathrm{AD}_{1/2}}(\omega_{10})\cdot\mathbb{G}^*_{\mathrm{D}_{1/2}\mathrm{A}}(\omega_{10})\right\}\,, \tag{5.141}$$

$$\Gamma_{\mathrm{intf}} = \frac{2\pi\mu^2\omega_{10}^2}{9\hbar^2}\delta(\omega_i-\omega_f)|\boldsymbol{d}^{\mathrm{A}}|^2|\boldsymbol{d}^{\mathrm{D}}|^2\mathrm{Re}\left[\mathrm{e}^{-\mathrm{i}\phi}\,\mathrm{Tr}\left\{\mathbb{G}^{(0)}_{\mathrm{AD}_1}(\omega_{10})\cdot\mathbb{G}^{(0)*}_{\mathrm{D}_2\mathrm{A}}(\omega_{10})\right\}\right]\,, \tag{5.142}$$

where we used the Onsager reciprocity for the Green's tensor and that the donors' transition dipoles are the same $\boldsymbol{d}^{\mathrm{D}_1} = \boldsymbol{d}^{\mathrm{D}_2} = \boldsymbol{d}^{\mathrm{D}}$.

In isotropic environment, in particular free space, the Green's tensor and hence the rates $\Gamma_{1/2}$ only depend on the distance between the respective donor and acceptor. Let us assume for simplicity that both donors have the same separation distance to the acceptor in free space, such that $\Gamma_1 = \Gamma_2$. The free-space Green's tensor (A.32) can be written as

$$\mathbb{G}^{(0)}(\boldsymbol{r}_b, \boldsymbol{r}_a, \omega) = -f_i(r_{ab})\mathbb{I} - f_r(r_{ab})\boldsymbol{e}_{ab} \otimes \boldsymbol{e}_{ab}\,, \tag{5.143}$$

$$f_i(r_{ab}) = \frac{c^2 \mathrm{e}^{\mathrm{i}\omega r_{ab}/c}}{4\pi\omega^2 r_{ab}^3}\left(1 - \mathrm{i}\frac{\omega r_{ab}}{c} - \frac{\omega^2 r_{ab}^2}{c^2}\right), \tag{5.144}$$

$$f_r(r_{ab}) = \frac{c^2 \mathrm{e}^{\mathrm{i}\omega r_{ab}/c}}{4\pi\omega^2 r_{ab}^3}\left(3 - 3\mathrm{i}\frac{\omega r_{ab}}{c} - \frac{\omega^2 r_{ab}^2}{c^2}\right), \tag{5.145}$$

where $\boldsymbol{r}_{ab} = \boldsymbol{r}_b - \boldsymbol{r}_a$ and $\boldsymbol{e}_{ab} = \boldsymbol{r}_{ab}/r_{ab}$ and we excluded the case of $\boldsymbol{r}_a = \boldsymbol{r}_b$. With this we find for the pure and interference rate contributions,

$$\Gamma_{1/2} = \frac{\Gamma_{\mathrm{mix}}}{2} = \delta(\omega_f - \omega_i)\frac{|\boldsymbol{d}^{\mathrm{A}}|^2|\boldsymbol{d}^{\mathrm{D}}|^2}{4\pi\varepsilon_0^2\hbar^2 r^6}\left(9 - \frac{\omega_{10}^2 r^2}{c^2} + 3\frac{\omega_{10}^4 r^4}{c^4}\right), \tag{5.146}$$

$$\begin{aligned}\Gamma_{\mathrm{intf}} = \frac{2\pi\mu^2\omega_{10}^2}{\hbar^2}\delta(\omega_i - \omega_f)|\boldsymbol{d}^{\mathrm{A}}|^2|\boldsymbol{d}^{\mathrm{D}}|^2 \mathrm{Re}\Big[\mathrm{e}^{-\mathrm{i}\phi}\,\mathrm{Tr}\left\{|f_i(r)|^2\mathbb{I} + f_r(r)f_i(r)^*\boldsymbol{e}_1 \otimes \boldsymbol{e}_1\right.\\ \left. + f_i(r)f_r(r)^*\boldsymbol{e}_2 \otimes \boldsymbol{e}_2 + |f_r(r)|^2(\boldsymbol{e}_1 \cdot \boldsymbol{e}_2)\boldsymbol{e}_1 \otimes \boldsymbol{e}_2\right\}\Big]\\ = \cos\phi\,\Gamma_{\mathrm{mix}}\left[1 - \sin^2\theta\frac{9 + 3r^2k^2 + r^4k^4}{18 - 2r^2k^2 + 6r^2k^4}\right],\end{aligned} \tag{5.147}$$

where $r = |\boldsymbol{r}_{1/2}| = |\boldsymbol{r}_{\mathrm{A}} - \boldsymbol{r}_{\mathrm{D}_1/\mathrm{D}_2}|$, $\boldsymbol{e}_{1/2} = \boldsymbol{r}_{1/2}/r$, ϕ is the complex phase between the super imposed product states, see Eq. (5.137), we have introduced θ as the angle between $\boldsymbol{r}_1$ and $\boldsymbol{r}_2$ and Γ_{mix} is given by Eq. (5.132). Substituting this back into Eq. (5.138) yields,

$$\Gamma_{\mathrm{sr}} = \Gamma_{\mathrm{mix}}\left(1 + \cos\phi\left[1 - \sin^2\theta\frac{9 + 3r^2k^2 + r^4k^4}{18 - 2r^2k^2 + 6r^2k^4}\right]\right), \tag{5.148}$$

where $k = \omega_{10}/c$. For $\phi = 0$ and $\theta = \pi$ we find maximum superradiance for the entangled pair

$$\Gamma_{\mathrm{sr}}^{\mathrm{max}} = 2\Gamma_{1/2} = 2\Gamma_{\mathrm{mix}}\,. \tag{5.149}$$

Varying the phase ϕ or the donors' relative position to each other can diminish the superradiant effect and even invert it up to complete suppression of the energy transfer $\Gamma_{\mathrm{sr}}^{\mathrm{min}} = 0$ at $\phi = \theta = \pi$.

Next, we want to study systems between these two extreme cases of fully mixed and fully entangled donors. Again we will consider two different cases. First, we only consider mixed states where both possible donor states are equally probable, i.e. $\langle eg|\rho_i|eg\rangle = \langle ge|\rho_i|ge\rangle = 1/2$, while the correlations can be varied. Such a state can always be com-

posed as a classical mixture of a fully entangled and a fully mixed state:

$$\rho_{\mathrm{D}} = (1-p)\rho_{\mathrm{mix}} + p\rho_{\mathrm{ent}}\,, \tag{5.150}$$

with $0 \leq p \leq 1$. Our considerations from before then reveal instantly the RET rate Γ as a classical average of the previously obtained rates:

$$\begin{aligned}\Gamma &= (1-p)\Gamma_{\mathrm{mix}} + p\Gamma_{\mathrm{sr}} \\ &= \Gamma_{\mathrm{mix}} + p\Gamma_{\mathrm{intf}} \\ &= \Gamma_{\mathrm{mix}}\left[1 + p\cos\phi\left(1 - \sin^2\theta\frac{9+3r^2k^2+r^4k^4}{18-2r^2k^2+6r^2k^4}\right)\right]\,. \end{aligned} \tag{5.151}$$

Next, we do not restrict ourselves to equally probable preparation for the excitation. However, for simplicity we keep the restriction that each donor has the same separation distance r to the acceptor. We then may just consider a completely arbitrary mixed initial donor state with one excitation. Such a state can always be written as

$$\rho_{\mathrm{D}} = a\left|eg\right\rangle\left\langle eg\right| + (1-a)\left|ge\right\rangle\left\langle ge\right| + \mathrm{e}^{\mathrm{i}\phi}b\left|eg\right\rangle\left\langle ge\right| + \mathrm{e}^{-\mathrm{i}\phi}b\left|ge\right\rangle\left\langle eg\right|\,, \tag{5.152}$$

with $0 \leq a \leq 1$ and $0 \leq b \leq 1/2$, such that the eigenvalues of ρ_{D} are positive. The full initial state hence reads

$$\rho_i = a\left|\psi_1\right\rangle\left\langle\psi_1\right| + (1-a)\left|\psi_2\right\rangle\left\langle\psi_2\right| + \mathrm{e}^{\mathrm{i}\phi}b\left|\psi_1\right\rangle\left\langle\psi_2\right| + \mathrm{e}^{-\mathrm{i}\phi}b\left|\psi_2\right\rangle\left\langle\psi_1\right|\,. \tag{5.153}$$

Substituting this into Eq. (5.124) yields the rate

$$\begin{aligned}\Gamma &= \lim_{t\to\infty}\frac{d}{dt}\,\mathrm{Tr}\{\rho_f\hat{U}^{(2)}(t)\rho_i\hat{U}^{(2)\dagger}(t)\} \\ &= a\Gamma_1 + (1-a)\Gamma_2 + 2b\Gamma_{\mathrm{intf}} \qquad (5.154) \\ &= \Gamma_{\mathrm{mix}}\left(1 + 2b\cos\phi\left[1 - \sin^2\theta\frac{9+3r^2k^2+r^4k^4}{18-2r^2k^2+6r^2k^4}\right]\right)\,. \qquad (5.155)\end{aligned}$$

The two scenarios described by Eq. (5.151) and Eq. (5.155) yield the same rate for $2b = p$. This is partially due to the chosen simplification of $r_1 = r_2 = r \Rightarrow \Gamma_1 = \Gamma_2$. Even more so, when comparing the fully entangled result Eq. (5.148), the equal-probability restricted mixed state result Eq. (5.151) and finally the arbitrary mixed state result Eq. (5.155), we see that the rate formulas all have the same structure and by measuring the rate we would not be able to distinguish these three cases.

For the rate (5.155) with arbitrary initial donor state, the complex phase ϕ as well as the absolute value of the donors' initial correlations b can again be chosen to either obtain

maximum superradiance, $\phi = 2n\pi$ and $b = 1/2$, maximum suppression $\phi = (2n+1)\pi$ and $b = 1/2$ or anything in between, including no interference effects despite correlations at $\phi = nPi/2$. The interference effect as a function of the donors' relative angle θ and their distance $r_1 = r_2 = r$ to the acceptor is shown in Fig. 5.3. While we have restricted ourselves here for simplification to cases where $r_1 = r_2 = r$, it is straightforward to apply the presented formulas to study any geometries of the three particles.

5.5. Conclusion

In this chapter, we studied the advantages of mixing an open quantum systems approach with perturbation theory. We have derived the spontaneous decay rate from Fermi's golden rule, i.e. via perturbation theory as well as nonperturbatively from open quantum systems approach. Considering only second-order field correlations in the Markov-approximation for open quantum systems we obtained the same result as via second-order Fermi's golden rule. Similarly, the RET rate was derived, first from Fermi's golden rule and second from an open quantum systems approach including perturbation theory.

In the second part of this chapter, we have developed an alternative perturbation scheme in the open quantum systems approach, the incoherent perturbation scheme. In this scheme the homogeneous but incoherent dynamics of the reduced system is solved nonperturbatively. This potentially yields corrections to results obtained from the ordinary perturbation scheme. We derived these corrections for the polarisability tensor explicitly. In a similar way corrections to the Van-der-Waals forces between excited and ground state particles were obtained in other works that suggested an interesting interpretation: the excited particle experiences an additional net force due to the recoil of the emitted photon during spontaneous decay. We have shown an analogous behaviour for the RET rate, where when additionally considering spontaneous decay the donor's decay rate shows an oscillating behaviour as a function of donor–acceptor distance, while the acceptor's transition rate behaves monotonically.

Lastly, we have shown that also Fermi's golden rule is able to take mixed states into consideration and derived as an example superradiant RET for two identical donor particles as a function of their entanglement. It was shown that any deviation of the initial state from the fully entangled one with optimal phase difference leads to a decreased superradiant effect and while entanglement is a necessary condition to observe superradiant RET, it is not a sufficient one. In conclusion superradiant RET may not serve as an entanglement witness.

The groundwork done in this chapter will enable us to treat various problems in the future. By understanding the limitations of the different approaches and their connections to each other we will be able to revisit some previous results and correct them analogously to the polarisability tensor as well as tackle new problems where we need to consider mixed states and incoherent decay while applying perturbation theory in the framework of macroscopic QED.

6 Conclusion and outlook

The goal of this work was on the one hand the modelling of different excitation energy transfer processes in realistic macroscopic environments and on the other to gain control over these atomic processes by modifying their environment. Established methods to investigate excitation transfer were extended to more exotic systems, including high-energy and inner-atomic processes and chiral molecules. In addition we developed an alternative perturbation scheme based on an open quantum systems approach to account for finite linewidths. The obtained results were in all cases presented in a general form that may be applied to various set-ups of interest and were discussed in detail on some carefully chosen examples. In particular, we used the framework of macroscopic quantum electrodynamics (QED) to study Auger decay, interatomic Coulombic decay (ICD), their competition with each other and resonance energy transfer (RET) between chiral molecules with a focus on its discriminatory power. These transfer processes are closely related to each other in view of the underlying quantum mechanical processes but differ in their energy and hence time and length scale regimes. This makes them appear in nature as well as in the lab as very different processes. We conclude the thesis here with a summary of the most important results and by outlining possible future projects built upon the presented results and theory.

In chapter 3 we have studied Auger and interatomic Coulombic decay as competing processes. For this purpose, we developed a novel model for Auger decay that allows the dipole approximation and results in a closed expression for the process rate. In doing so, we introduced a new parameter for the characterisation of a given Auger process, the Auger radius. Via comparison with available numerical data, we verified that the Auger radius behaves like a radius as a function of proton number, that its magnitude can be estimated by that of the vacancy orbital and that the Auger decay rate itself depends on the introduced Auger radius a as predicted with $1/a^6$. This dependency is comparable to the usual dependency of an excitation transfer rate to the transfer distance, as is known for example for ICD and RET. The developed model for Auger decay allowed us to study Auger decay and ICD in a joint framework, namely macroscopic QED in dipole approximation, with the focus on the impact of macroscopic environments.

The introduced Auger radius determines the characteristic length scale of Auger decay

and is usually of the order of the Bohr radius and as such much smaller than the characteristic length scale of the competing ICD process (which is given by the donor–acceptor separation distance). This is in agreement with the fact, that Auger decay is the fastest of the decays studied here and governs the highest energy regime. In a two-atom system, such as a dimer, there exists an energy regime where Auger decay as well as ICD need to be considered as decay channels. We have shown by comparison of the characteristic length scales of each process that in this overlapping energy regime, Auger decay usually dominates over ICD and spontaneous or radiative decay may be neglected as a decay channel. In this comparison we additionally considered the modification of the single-atomic decays, i.e. Auger decay and spontaneous decay, by the presence of the second atom. As it turns out, the additional contribution to the Auger decay rate due to the presence of the second particle may be on the same order of magnitude as the spontaneous decay rate, depending on the properties of the second atom.

As in free space, ICD is usually dominated by Auger decay, we focussed on the goal of enhancing ICD relative to Auger decay via their macroscopic environment. We illustrated how a simple close-by surface may have a significant impact onto the competition of Auger decay and ICD. Depending on the geometry of the system, a surface with a nonretarded reflection coefficient of $|r_{\mathrm{NR}}(E)| = 2$ at the transition energy E may enhance the ICD rate compared to the Auger decay rate already by a factor of roughly 3.5. We have kept the presented study as general as possible and offered a detailed discussion on what kind of enhancement can be expected in which atomic system: for successful enhancement of ICD in comparison to Auger decay via a close-by surface, it is preferrable to use a system where (1) the photoionisation cross section that plays a part in the Auger decay rate is much smaller than the one that is part of the ICD rate, (2) the Auger radius is rather large compared to the Bohr radius, (3) the surface is parallel to the interatomic separation, (4) the involved transitions are anisotropic, and (5) the nonretarded reflection coefficient of the surface at the transition energy is large. Conditions (1) and (2) lead to a small Auger decay rate compared to the ICD rate already in free space, while conditions (3), (4) and (5) optimise the impact of the surface.

The applied framework of macroscopic QED is also suited to consider atomic processes inside a cavity. As cavities for the high energy regime become more and more available, we have studied the impact of a cavity onto Auger decay and ICD. A general estimation was given for the expected enhancement of the Auger decay rate and ICD rate, respectively, in a given cavity as characterised by its Q-factor. The derived expressions can vice versa be used to predict the properties of an appropriate cavity for a specific atomic system. We have shown that a cavity which is suited to enhance ICD will have only little impact on the Auger decay rate. Such a cavity hence supports ICD compared to Auger decay. While we have kept the cavity estimation general by only referring to its Q-factor, the presented formalism is in general able to quantitatively analyse the decay rates inside

specific cavities.

We closed the chapter by demonstrating the applicability of the presented theory to a specific system by considering a He–Ne dimer. Here, we could verify the consistency of our formalism with the results from established *ab initio* quantum chemistry methods by comparison of the free-space limit of our results to rates reported in other works.

The presented study makes it clear that further investigation of Auger decay and ICD would profit from a collaboration with the *ab initio* quantum chemistry community. The distances at which a macroscopic surface has the most impact usually overlap with the distance regime where wave function overlap needs to be considered. For instance, ICD in the presence of a third close-by atom was successfully analysed in such a collaboration and the different frameworks were able to carefully consider different effects due to the third atom in a joint work [97]. The novel treatment of Auger decay should be further investigated. A predictive model for the Auger radius has yet to be developed. We successfully fitted a radius model to a specific isoelectronic sequence of Auger decay undergoing ions. The model works well, but for quantitative predictions in unrelated atomic systems the two parameters of the Auger radius model (namely an overall factor and a screening parameter) need to be related to the electronic structure at hand. For such a study a collaboration with the *ab initio* quantum chemistry community would also be fruitful.

The presented formalism can be used to predict Auger decay and ICD in biological tissue, where the atomic system is not isolated from its macroscopic environment. An additional advantage of our formalism, aside from the possible treatment of macroscopic environment, is its simplicity: each process is described by a closed expression that can be evaluated via tabulated data or data obtained from standard *ab initio* calculations. Hence, the complexity of the formalism scales well for more complex systems and events, such as cascade-like events. In such cascades, ICD decay possibly follows Auger decay and vice-versa and all available decay channels quantum-mechanically interfere with each other. These events play a significant role in the aim for development of radiation therapy techniques based on the emitted electron in the ICD process.

In chapter 4 we studied excitation transfer via RET between two chiral molecules. The transfer rate is sensitive to the handedness of the involved molecules and can hence be used in principle to discriminate between different enantiomers. To this end, the handedness of one participating molecule needs to be known in general. We assumed without loss generality that the donor molecule is known to be left-handed and the acceptor molecule could be either enantiomer. The donor molecule then actively discriminates the different acceptor enantiomers via the transfer. The transfer rate is larger for donor–acceptor pairs with same handedness than for opposite handed pairs. We have studied

the resulting degree of discrimination due to RET in free space, immersed in magneto-electric medium, chiral medium and in the presence of a single chiral mediator molecule. In general, we could show that while the rate itself decreases as a function of the intermolecular distance, the discrimination increases and is largest in the far zone or retarded limit.

The discrimination in free space is usually expected to be small and its magnitude is entirely determined by the involved molecules. We have shown that immersing the molecules inside some medium, such as a liquid or gas, which is well described by its macroscopic properties, can enhance the discrimination. While commercially available solutions may already have a significant impact onto the discrimination, we have predicted that an appropriate medium can even lead to complete discrimination, where the excitation transfer to one of the enantiomers vanishes entirely. We have discussed a large parameter space of dielectric media, finding that dielectrics that are highly absorbing compared to their refraction, i.e. the imaginary part of their refractive index is larger than its real part, result in an interesting effect on the discrimination: in such media, the degree of discrimination does not only change its magnitude as a function of the intermolecular distance but changes its direction. This means that if one enantiomer is favoured by RET in one distance regime, the opposite enantiomer is favoured in the complimentary one.

Starting with the case of magneto-electric media, we have demonstrated the significance of so-called local-field effects for the correct predictions of the degree of discrimination. These can be taken into account by different models leading to local-field corrections. We have used in this work the Onsager real cavity model to describe these effects and subsequently worked out the local-field corrections for chiral media which proved to be much more involved than those for magneto-electric media. The complexity of these corrections stems from the different propagation of left- and right-circularly polarised light inside the chiral medium. For the derivation of the local-field corrections of a chiral medium via the Onsager real cavity model we have developed a matrix-method for dealing with Green's tensors transmitting through and reflecting at different interfaces.

The derived local-field correction was then used to treat chiral RET inside a chiral medium. We have shown that a chiral medium can actively discriminate the different acceptor enantiomers, such that it is sufficient to know the handedness of the medium and the donor molecule could even be achiral. Surprisingly, the local-field correction itself did not only change the magnitude of the derived degree of discrimination but also lead to an additional contribution, which completely vanishes when chiral local-field effects are dismissed. The contribution due to local-field effects to the degree of discrimination even dominates in general in the nonretarded regime or near-zone and its sign is usually opposite to the degree of discrimination due to the bulk medium. This means that in a chiral medium the discrimination due to the medium in general changes

its direction when going from the nonretarded to the retarded distance regime, entirely due to local-field effects.

We closed the chapter by considering the dilute gas limit as a medium. In this limit we may model the system-surrounding gas by its individual molecular constituents. We focussed on the impact of a single close-by molecule onto the degree of discrimination due to RET between two chiral molecules, the extension to several molecules is then straightforward in the presented framework. This additional mediator molecule was considered to be possibly chiral itself. A chiral mediator can again induce the discrimination while an achiral mediator can only passively enhance or suppress the discrimination due to the donor molecule. We have shown that taking the nonretarded limit for all intermolecular distances the degree of discrimination is unchanged by the presence of an identical chiral mediator molecule and usually suppressed in the presence of an achiral mediator. When fixing the donor–acceptor distance at either a nonretarded or retarded distance and varying the position of an identical mediator we found that in the nonretarded geometry the rate itself can be strongly enhanced, while the discrimination is approximately unchanged by the mediator. In the retarded geometry on the other hand we could show that while the RET rate is less modified by the mediator's presence, the discrimination can be significantly enhanced depending on the mediator's position.

The expressions presented for the chiral discrimination via RET are valid for general set-ups and can be hence applied to different systems and problems. A collaboration with an appropriate experimental group could verify the presented predictions, especially concerning the predicted distance-dependent discrimination direction in chiral media and strongly absorbing dielectrics, such that complete discrimination via RET might be accomplished in the lab. While we focussed here on the liquid or gaseous phase of media, the presented analysis can be easily extended in future works to solids, where various metamaterials can be designed to fulfil specific properties, which makes the process more experimentally accessible. In solids, we would expect a similar behaviour as presented here for liquid media.

The developed matrix-method for calculating Green's tensors in the presence of different polarisation-mixing boundaries can be further exploited to not only derive local-field correction via the Onsager real cavity model but also via alternative models, such as the virtual cavity one. The local-field correction via Onsager real cavity model showed a surprising influence on the discrimination. A natural next step is to verify whether this is a model-independent behaviour, i.e. the discrimination direction change due to local-field effects sustains even when using alternative local-field models.

Chapter 5 presents the first step to studying atomic dynamics in a joint framework of open quantum systems and perturbation theory where macroscopic QED is applicable. We verified the consistency between the predictions from open quantum system in

Markov approximation and the standard approach based on Fermi's golden rule within the framework of macroscopic QED. From the master equation of the reduced system, we have developed an alternative to the ordinary perturbation scheme, the incoherent perturbation scheme. In the incoherent perturbation scheme the incoherent but homogeneous evolution of the system is treated nonperturbatively. This is in contrast to the ordinary perturbation scheme.

Using the example of the polarisability tensor, we showed how the incoherent perturbation scheme can be used to derive corrections to quantities originally derived from the ordinary perturbation scheme. Similar methods were used to derive the asymmetric Van-der-Waals forces between an excited and ground-state particle. We have shown via ordinary perturbation theory that in RET, an analogous asymmetric behaviour can be derived for the donor and acceptor rates: while the decay rate of the donor oscillates as a function of the donor–acceptor distance, the transition rate of the acceptor only monotonically decreases with the distance.

Lastly, we considered Fermi's golden rule for mixed states. The extension to mixed states allowed us to study superradiant RET arising from entanglement of two donor particles. The study presented on superradiance is mainly meant to demonstrate the applicability of Fermi's golden rule to density matrices. However, we could demonstrate that superradiance arises from interference effects that vanish in a similar manner for any deviation from the fully entangled initial state with optimum phase. As a consequence, we have shown that superradiant RET cannot serve as an entanglement witness.

With the work done in this last chapter we have closed some gaps when considering collective effects and incoherent dynamics of an atomic system via its reduced density matrix by carefully studying the interplay between perturbation theory and master equations. The developed incoherent perturbation scheme in the framework of macroscopic QED can be applied to a variety of problems and might offer some new insight on one hand to the as closed regarded discussion concerning the correct treatment of the frequency poles in the RET rate calculation and on the other hand to the ongoing discussion on the role of the local density of photon states in RET. For consistency, the asymmetric Van-der-Waals forces as well as the asymmetric RET rate should be rederived from the developed perturbation scheme.

References

1. Purcell, E. M. "Spontaneous emission probabilities at radio frequencies". *Phys. Rev.* **69,** 674–674 (1946).
2. Haroche, S. & Kleppner, D. "Cavity quantum electrodynamics". *Phys. Today* **42,** 24–30 (1989).
3. Dung, H. T., Knöll, L. & Welsch, D.-G. "Spontaneous decay in the presence of dispersing and absorbing bodies: general theory and application to a spherical cavity". *Phys. Rev. A* **62,** 053804 (2000).
4. Vahala, K. J. "Optical microcavities". *Nature* **424,** 839–846 (2003).
5. Raimond, J. M., Brune, M. & Haroche, S. "Manipulating quantum entanglement with atoms and photons in a cavity". *Rev. Mod. Phys.* **73,** 565–582 (2001).
6. Benson, O. "Assembly of hybrid photonic architectures from nanophotonic constituents". *Nature* **480,** 193–199 (2011).
7. Jacob, Z. & Shalaev, V. M. "Plasmonics goes quantum". *Science* **334,** 463–464 (2011).
8. Sauvan, C., Hugonin, J. P., Maksymov, I. S. & Lalanne, P. "Theory of the spontaneous optical emission of nanosize photonic and plasmon resonators". *Phys. Rev. Lett.* **110** (2013).
9. Westerberg, N., Messinger, A. & Barnett, S. M. "Duality, decay rates, and local-field models in macroscopic QED". *Phys. Rev. A* **105,** 053704 (2022).
10. Scheel, S. "Single-photon sources–an introduction". *J. Mod. Opt.* **56,** 141–160 (2009).
11. Qian, Z. *et al.* "Spontaneous emission in micro- or nanophotonic structures". *PhotoniX* **2** (2021).
12. Rustomji, K., Abdeddaim, R., de Sterke, C. M., Kuhlmey, B. & Enoch, S. "Measurement and simulation of the polarization-dependent Purcell factor in a microwave fishnet metamaterial". *Phys. Rev. B* **95,** 035156 (2017).
13. Rustomji, K. *et al.* "Complete electromagnetic dyadic green function characterization in a complex environment—resonant dipole-dipole interaction and cooperative effects". *Phys. Rev. X* **11,** 021004 (2021).
14. García de Abajo, F. J. & Kociak, M. "Probing the photonic local density of states with electron energy loss spectroscopy". *Phys. Rev. Lett.* **100,** 106804 (2008).

15. Krachmalnicoff, V. *et al.* "Towards a full characterization of a plasmonic nanostructure with a fluorescent near-field probe". *Opt. Express* **21,** 11536 (2013).

16. Cao, D. *et al.* "Mapping the radiative and the apparent nonradiative local density of states in the near field of a metallic nanoantenna". *ACS Photonics* **2,** 189–193 (2015).

17. Förster, T. "Energiewanderung und Fluoreszenz". *Sci. Nat.* **33,** 166–175 (1946).

18. Förster, T. "Zwischenmolekulare Energiewanderung und Fluoreszenz". *Ann. Phys.* **437,** 55–75 (1948).

19. Avery, J. S. "The retarded dipole-dipole interaction in exciton theory". *Phys. Rev. B* **89,** 677–682 (1966).

20. Gomberoff, L. & Power, E. A. "The resonance transfer of excitation". *Proc. Phys. Soc* **88,** 281–284 (1966).

21. Craig, D. & Thirunamachandran, T. "Radiation–molecule interactions in chemical physics". *Adv. Quantum Chem.* **16,** 97–160 (1982).

22. Daniels, G. J., Jenkins, R. D., Bradshaw, D. S. & Andrews, D. L. "Resonance energy transfer: the unified theory revisited". *J. Chem. Phys.* **119,** 2264–2274 (2003).

23. Jenkins, R. D., Daniels, G. J. & Andrews, D. L. "Quantum pathways for resonance energy transfer". *J. Chem. Phys.* **120,** 11442–11448 (2004).

24. Power, E. A. & Thirunamachandran, T. "Quantum electrodynamics with nonrelativistic sources. i. transformation to the multipolar formalism for second-quantized electron and Maxwell interacting fields". *Phys. Rev. A* **28,** 2649–2662 (1983).

25. Power, E. A. & Thirunamachandran, T. "Quantum electrodynamics with nonrelativistic sources. ii. Maxwell fields in the vicinity of a molecule". *Phys. Rev. A* **28,** 2663–2670 (1983).

26. Power, E. A. & Thirunamachandran, T. "Quantum electrodynamics with nonrelativistic sources. iii. intermolecular interactions". *Phys. Rev. A* **28,** 2671–2675 (1983).

27. Andrews, D. L. & Sherborne, B. S. "Resonant excitation transfer: a quantum electrodynamical study". *J. Chem. Phys.* **86,** 4011–4017 (1987).

28. Andrews, D. L. "A unified theory of radiative and radiationless molecular energy transfer". *Chem. Phys.* **135,** 195–201 (1989).

29. Craig, D. & Thirunamachandran, T. "An analysis of models for resonant transer of excitation using quantum electrodynamics". *Chem. Phys.* **167,** 229–240 (1992).

30. Andrews, D. L. & Juzeliūnas, G. "Intermolecular energy transfer: retardation effects". *J. Chem. Phys.* **96,** 6606–6612 (1992).

31. Power, E. A. & Thirunamachandran, T. "Analysis of the causal behavior in energy transfer between atoms". *Phys. Rev. A* **56,** 3395–3408 (1997).

32. Jones, G. A. & Bradshaw, D. S. "Resonance energy transfer: from fundamental theory to recent applications". *Front. Phys.* **7,** 100 (2019).

33. Cortes, C. L. & Jacob, Z. "Fundamental figures of merit for engineering Förster resonance energy transfer". *Opt. Express* **26,** 19371 (2018).

34. Stryer, L. & Haugland, R. P. "Energy transfer: a spectroscopic ruler.". *Proc. Natl. Acad. Sci. U.S.A.* **58,** 719–726 (1967).

35. Sahoo, H. "Förster resonance energy transfer – a spectroscopic nanoruler: principle and applications". *J. Photochem. Photobiol. C* **12,** 20–30 (2011).

36. Medintz, I. L. & Mattoussi, H. "Quantum dot-based resonance energy transfer and its growing application in biology". *Phys. Chem. Chem. Phys.* **11,** 17–45 (2009).

37. Willard, D. M. & Orden, A. V. "Resonant energy-transfer sensor". *Nat. Mater.* **2,** 575–576 (2003).

38. Li, L. *et al.* "Quantum dot-aluminum phthalocyanine conjugates perform photodynamic reactions to kill cancer cells via fluorescence resonance energy transfer". *Nanoscale Res. Lett.* **7** (2012).

39. Baldo, M. A., Thompson, M. E. & Forrest, S. R. "High-efficiency fluorescent organic light-emitting devices using a phosphorescent sensitizer". *Nature* **403,** 750–753 (2000).

40. Itskos, G., Othonos, A., Choulis, S. A. & Iliopoulos, E. "Förster resonant energy transfer from an inorganic quantum well to a molecular material: unexplored aspects, losses, and implications to applications". *J. Chem. Phys.* **143,** 214701 (2015).

41. John, S. & Wang, J. "Quantum optics of localized light in a photonic band gap". *Phys. Rev. B* **43,** 12772–12789 (1991).

42. Unold, T., Mueller, K., Lienau, C., Elsaesser, T. & Wieck, A. D. "Optical control of excitons in a pair of quantum dots coupled by the dipole-dipole interaction". *Phys. Rev. Lett.* **94,** 137404 (2005).

43. Weeraddana, D., Premaratne, M. & Andrews, D. L. "Quantum electrodynamics of resonance energy transfer in nanowire systems". *Phys. Rev. B* **93** (2016).

44. Martín-Cano, D., Martín-Moreno, L., García-Vidal, F. J. & Moreno, E. "Resonance energy transfer and superradiance mediated by plasmonic nanowaveguides". *Nano Lett.* **10,** 3129–3134 (2010).

45. Faessler, V. *et al.* "Accelerating fluorescence resonance energy transfer with plasmonic nanoresonators". *Chem. Phys. Lett.* **508,** 67–70 (2011).

46. Bidault, S. *et al.* "Competition between Förster resonance energy transfer and donor photodynamics in plasmonic dimer nanoantennas". *ACS Photonics* **3,** 895–903 (2016).

47. Tumkur, T. U. *et al.* "Control of Förster energy transfer in the vicinity of metallic surfaces and hyperbolic metamaterials". *Faraday Discuss.* **178,** 395–412 (2015).

48. Roth, D. J. *et al.* "Förster resonance energy transfer inside hyperbolic metamaterials". *ACS Photonics* **5,** 4594–4603 (2018).

49. Olivo, J., Zapata-Rodríguez, C. J. & Cuevas, M. "Spatial modulation of the electromagnetic energy transfer by excitation of graphene waveguide surface plasmons". *Journal of Optics* **21,** 045002 (2019).

50. Konrad, A., Metzger, M., Kern, A. M., Brecht, M. & Meixner, A. J. "Controlling the dynamics of Förster resonance energy transfer inside a tunable sub-wavelength Fabry–Pérot-resonator". *Nanoscale* **7,** 10204–10209 (2015).

51. Zurita-Sánchez, J. R. & Méndez-Villanueva, J. "Förster energy transfer in the vicinity of two metallic nanospheres (dimer)". *Plasmonics* **13,** 873–883 (2017).

52. Choi, Y., Park, Y., Kang, T. & Lee, L. P. "Selective and sensitive detection of metal ions by plasmonic resonance energy transfer-based nanospectroscopy". *Nat. Nanotechnol.* **4,** 742–746 (2009).

53. Cushing, S. K. *et al.* "Photocatalytic activity enhanced by plasmonic resonant energy transfer from metal to semiconductor". *J. Am. Chem. Soc.* **134,** 15033–15041 (2012).

54. Li, J. *et al.* "Plasmon-induced resonance energy transfer for solar energy conversion". *Nat. Photonics* **9,** 601–607 (2015).

55. Salam, A. "On the effect of a radiation field in modifying the intermolecular interaction between two chiral molecules". *J. Chem. Phys.* **124,** 014302 (2006).

56. Salam, A. "The unified theory of resonance energy transfer according to molecular quantum electrodynamics". *Atoms* **6** (2018).

57. Ford, J. S., Salam, A. & Jones, G. A. "A quantum electrodynamics description of quantum coherence and damping in condensed-phase energy transfer". *J. Phys. Chem. Lett.* **10,** 5654–5661 (2019).

58. Green, D., Jones, G. A. & Salam, A. "Polariton mediated resonance energy transfer in a fluid". *J. Chem. Phys.* **153,** 034111 (2020).

59. Salam, A. "RET in a dielectric medium: insights from molecular QED theory". *Mol. Phys.* **118,** e1770882 (2020).

60. Salam, A. "Resonance energy transfer mediated by a chiral molecule". *J. Chem. Phys.* **154,** 074111 (2021).

61. Feist, J. & Garcia-Vidal, F. J. "Extraordinary exciton conductance induced by strong coupling". *Phys. Rev. Lett.* **114** (2015).

62. Schachenmayer, J., Genes, C., Tignone, E. & Pupillo, G. "Cavity-enhanced transport of excitons". *Phys. Rev. Lett.* **114** (2015).

63. Zhong, X. *et al.* "Non-radiative energy transfer mediated by hybrid light-matter states". *Angew. Chem. Int. Ed.* **55,** 6202–6206 (2016).

64. Georgiou, K. *et al.* "Control over energy transfer between fluorescent BODIPY dyes in a strongly coupled microcavity". *ACS Photonics* **5,** 258–266 (2017).

65. Juzeliūnas, G. & Andrews, D. L. "Quantum electrodynamics of resonant energy transfer in condensed matter". *Phys. Rev. B* **49,** 8751–8763 (1994).

66. Dung, H. T., Knöll, L. & Welsch, D.-G. "Intermolecular energy transfer in the presence of dispersing and absorbing media". *Phys. Rev. A* **65,** 043813 (2002).

67. Wei, Y.-C. *et al.* "Can nanocavities significantly enhance resonance energy transfer in a single donor–acceptor pair?". *J. Phys. Chem. C* **125,** 18119–18128 (2021).

68. Poudel, A., Chen, X. & Ratner, M. A. "Enhancement of resonant energy transfer due to an evanescent wave from the metal". *J. Phys. Chem. Lett.* **7,** 955–960 (2016).

69. Rustomji, K. *et al.* "Direct imaging of the energy-transfer enhancement between two dipoles in a photonic cavity". *Phys. Rev. X* **9** (2019).

70. Cederbaum, L. S., Zobeley, J. & Tarantelli, F. "Giant intermolecular decay and fragmentation of clusters". *Phys. Rev. Lett.* **79,** 4778–4781 (1997).

71. Marburger, S., Kugeler, O., Hergenhahn, U. & Möller, T. "Experimental evidence for interatomic coulombic decay in Ne clusters". *Phys. Rev. Lett.* **90,** 203401 (2003).

72. Ouchi, T. *et al.* "Three-electron interatomic coulombic decay from the inner-valence double-vacancy states in near". *Phys. Rev. Lett.* **107,** 053401 (2011).

73. Barth, S. *et al.* "Interface identification by non-local autoionization transitions". *Phys. Chem. Chem. Phys.* **8,** 3218–3222 (2006).

74. Barth, S. *et al.* "Observation of resonant interatomic coulombic decay in Ne clusters". *J. Chem. Phys.* **122,** 241102 (2005).

75. Aoto, T. *et al.* "Properties of resonant interatomic coulombic decay in Ne dimers". *Phys. Rev. Lett.* **97,** 243401 (2006).

76. Joshi, S., Barth, S., Marburger, S., Ulrich, V. & Hergenhahn, U. "$2p$ Correlation satellites in neon clusters investigated by photoemission". *Phys. Rev. B* **73,** 235404 (2006).

77. Lablanquie, P. *et al.* "Appearance of interatomic coulombic decay in Ar, Kr, and Xe homonuclear dimers". *J. Chem. Phys.* **127,** 154323 (2007).

78. Sisourat, N. *et al.* "Ultralong-range energy transfer by interatomic coulombic decay in an extreme quantum system". *Nat. Phys.* **6,** 508–511 (2010).

79. Harbach, P. H. P., Schneider, M., Faraji, S. & Dreuw, A. "Intermolecular coulombic decay in biology: the initial electron detachment from $FADH^-$ in DNA photolyases". *J. Phys. Phys. Lett.* **4,** 943–949 (2013).

80. Dreuw, A. & Faraji, S. "A quantum chemical perspective on (6-4) photolesion repair by photolyases". *Phys. Chem. Chem. Phys.* **15,** 19957–19969 (2013).

81. Zobeley, J., Cederbaum, L. S. & Tarantelli, F. "Intermolecular coulombic decay of molecular clusters: identification of the decay mechanism using a new hole-population analysis". *J. Phys. Phys. A* **103,** 11145–11160 (1999).

82. Aziz, E. F., Ottosson, N., Faubel, M., Hertel, I. V. & Winter, B. "Interaction between liquid water and hydroxide revealed by core-hole de-excitation". *Nature* **455,** 89–91 (2008).

83. Cherkes, I. & Moiseyev, N. "Electron relaxation in quantum dots by the interatomic coulombic decay mechanism". *Phys. Rev. B* **83,** 113303 (2011).

84. Bande, A., Gokhberg, K. & Cederbaum, L. S. "Dynamics of interatomic coulombic decay in quantum dots". *J. Chem. Phys.* **135,** 144112 (2011).

85. Bande, Annika, Pont, Federico M., Dolbundalchok, Praphasiri, Gokhberg, Kirill & Cederbaum, Lorenz S. "Electron dynamics of interatomic coulombic decay in quantum dots: singlet initial state". *EPJ Web Conf.* **41,** 04031 (2013).

86. Meitner, L. "Über den Zusammenhang zwischen β- und γ-Strahlen". *Z. Phys.* **9,** 145–152 (1922).

87. Auger, P. "Sur les rayons β secondaires produits dans un gaz par des rayons x.". *CR Acad. Sci. (F)* **177,** 169 (1923).

88. Doschek, G. A. in *Autoionization: recent developments and applications* (ed Temkin, A.) 171–256 (Springer US, Boston, MA, 1985).

89. Gokhberg, K., Kolorenč, P., Kuleff, A. I. & Cederbaum, L. S. "Site- and energy-selective slow-electron production through intermolecular coulombic decay". *Nature* **505,** 661–663 (2013).

90. Kimura, M. *et al.* "Efficient site-specific low-energy electron production via interatomic coulombic decay following resonant Auger decay in argon dimers". *Phys. Rev. A* **87,** 043414 (2013).

91. O'Keeffe, P. *et al.* "The role of the partner atom and resonant excitation energy in interatomic coulombic decay in rare gas dimers". *J. Phys. Phys. Lett.* **4,** 1797–1801 (2013).

92. Kimura, M. *et al.* "Controlling low-energy electron emission via resonant-Auger-induced interatomic coulombic decay". *J. Phys. Chem. Lett.* **4,** 1838–1842 (2013).

93. Miteva, T. *et al.* "Interatomic coulombic decay following resonant core excitation of Ar in argon dimer". *J. Chem. Phys.* **141,** 064307 (2014).

94. Schwartz, C. P., Fatehi, S., Saykally, R. J. & Prendergast, D. "Importance of electronic relaxation for inter-coulombic decay in aqueous systems". *Phys. Rev. Lett.* **105** (2010).

95. Martin, R. F. & Feinendegen, L. E. "The quest to exploit the Auger effect in cancer radiotherapy – a reflective review". *Int. J. Radiat. Biol.* **92,** 617–632 (2016).

96. Hemmerich, J. L., Bennett, R. & Buhmann, S. Y. "The influence of retardation and dielectric environments on interatomic coulombic decay". *Nat. Comm.* **9,** 2934 (2018).

97. Bennett, R. *et al.* "Virtual photon approximation for three-body interatomic coulombic decay". *Phys. Rev. Lett.* **122,** 153401 (2019).

98. Arago, F. *Mémoire sur une modification remarquable qu' éprouvent les rayons lumineux dans leur passage à travers certains corps diaphanes, & sur quelques autres phénomènes d'optique* (1811).

99. Biot, J. B. "Sur les rotations que certaines substances impriment aux axes de polarisation des rayons lumineux". *Mem. Acad. Sci.* **2,** 41–136 (1817).

100. Fresnel, A. J. "Considérations theoriques sur la polarisation de la lumière". *Bull. Sci. Soc. Philomath.,* 147–158 (1824).

101. Pasteur, L. "Sur les relations qui peuvent exister entre la forme crystalline, la composition chimique et le sens de la polarization rotatoire". *Ann. Chim. Phys.* **24,** 442–459 (1848).

102. Pasteur, L. "Mémoire sur la relation qui peut exister entre la forme cristalline et la composition chimique, et sur la cause de la polarisation rotatoire". *C. R. Hebd. Seances Acad. Sci.* **26,** 535–538 (1848).

103. Bel, J. A. L. "Sur les relations qui existent entre les formules atomique des corps organiques et le pouvoir rotatoire de leurs dissolutions". *Bull. Soc. Bot. Fr.* **22,** 337–347 (1874).

104. Van't Hoff, J. H. "Les formules de structure dans l'espace". *Arch. Neerl. Sci. Exactes Nat.* **9,** 445–454 (1874).

105. Van't Hoff, J. H. *Die Lagerung der Atome im Raum* (Vieweg, Braunschweig, 1908).

106. Quack, M., Seyfang, G. & Wichmann, G. "Perspectives on parity violation in chiral molecules: theory, spectroscopic experiment and biomolecular homochirality". *Chemical Science* **13,** 10598–10643 (2022).

107. Córdova, A., Engqvist, M., Ibrahem, I., Casas, J. & Sundén, H. "Plausible origins of homochirality in the amino acid catalyzed neogenesis of carbohydrates". *Chem. Commun.,* 2047–2049 (2005).

108. Blackmond, D. G. & Klussmann, M. "Spoilt for choice: assessing phase behavior models for the evolution of homochirality". *Chem. Commun.,* 3990 (2007).

109. Fletcher, S. P., Jagt, R. B. C. & Feringa, B. L. "An astrophysically-relevant mechanism for amino acid enantiomer enrichment". *Chem. Commun.,* 2578 (2007).

110. Quack, M. "On the measurement of the parity violating energy difference between enantiomers". *Chem. Phys. Lett.* **132,** 147–153 (1986).

111. Albert, S. & Quack, M. "High resolution rovibrational spectroscopy of chiral and aromatic compounds". *ChemPhysChem* **8,** 1271–1281 (2007).

112. Dietiker, P., Miloglyadov, E., Quack, M., Schneider, A. & Seyfang, G. "Infrared laser induced population transfer and parity selection in $^{14}nh_3$: a proof of principle experiment towards detecting parity violation in chiral molecules". *J. Chem. Phys.* **143,** 244305 (2015).

113. Letokhov, V. "On difference of energy levels of left and right molecules due to weak interactions". *Phys. Lett. A* **53,** 275–276 (1975).

114. Daussy, C. *et al.* "Limit on the parity nonconserving energy difference between the enantiomers of a chiral molecule by laser spectroscopy". *Phys. Rev. Lett.* **83,** 1554–1557 (1999).

115. Cournol, A. *et al.* "A new experiment to test parity symmetry in cold chiral molecules using vibrational spectroscopy". *Quantum Electron.* **49,** 288–292 (2019).

116. Nguyen, L. A., He, H. & Pham-Huy, C. "Chiral drugs: an overview". en. *Int. J. Biomed. Sci.* **2,** 85–100 (2006).

117. Curie, P. "Sur la symétrie dans les phénomènes physiques, symétrie d'un champ électrique et d'un champ magnétique". *J. Phys. Theor. Appl.* **3,** 393–415 (1894).

118. Craig, D. P. & Thirunamachandran, T. "Chiral discrimination in molecular excitation transfer". *J. Chem. Phys.* **109,** 1259–1263 (1998).

119. Andrews, D. L. "Chirality in fluorescence and energy transfer". *Methods Appl. Fluoresc.* **7,** 032001 (2019).

120. Jackson, J. D. *Classical electrodynamics* (Wiley, New York, 1975).

121. Buhmann, S. Y. *Dispersion forces I: macroscopic quantum electrodynamics and ground-state Casimir, Casimir–Polder and van der Waals forces* (Springer Berlin, Heidelberg, 2012).

122. Callen, H. B. & Welton, T. A. "Irreversibility and generalized noise". *Phys. Rev.* **83,** 34–40 (1951).

123. Kubo, R. "The fluctuation-dissipation theorem". *Rep. Prog. Phys.* **29,** 255–284 (1966).

124. Dung, H. T. *et al.* "Electromagnetic-field quantization and spontaneous decay in left-handed media". *Phys. Rev. A* **68,** 043816 (2003).

125. Buhmann, S. Y. & Welsch, D.-G. "Dispersion forces in macroscopic quantum electrodynamics". *Prog. Quantum. Electron.* **31,** 51–130 (2007).

126. Scheel, S. & Buhmann, S. Y. "Macroscopic quantum electrodynamics - concepts and applications". *Acta Phys. Slovaca* **58,** 675–809 (2008).

127. Rytov, S. M., Kravtsov, Y. A. & Tatarskii, V. I. *Priniciples of statistical radiophysics 3: elements of random fields* (Springer Berlin, Heidelberg, 1989).

128. Lishitz, E. & Hamermesh, M. in *Perspectives in theoretical physics* (ed Pitaevski, L.) 329–349 (Pergamon, Amsterdam, 1992).

129. Buhmann, S. Y., Butcher, D. T. & Scheel, S. "Macroscopic quantum electrodynamics in nonlocal and nonreciprocal media". *New J. Phys.* **14,** 083034 (2012).

130. Misner, C. W. & Wheeler, J. A. "Classical physics as geometry". *Ann. Phys.* **2,** 525–603 (1957).

131. Gaillard, M. K. & Zumino, B. "Duality rotations for interacting fields". *Nucl. Phys. B* **193,** 221–244 (1981).

132. Power, E. A. & Zienau, S. "Coulomb gauge in non-relativistic quantum electrodynamics and the shape of spectral lines". *Philos. Trans. Royal Soc. A* **251,** 427–454 (1959).

133. Woolley, R. G. & Coulson, C. A. "Molecular quantum electrodynamics". *Proc. Math. Phys. Eng. Sci.* **321,** 557–572 (1971).

134. Cohen-Tannoudji, C., Dupont-Roc, J. & Grynberg, G. *Photons and atoms* (Wiley, New York, 1997).

135. Fiedler, J. *et al.* "Effective polarizability models". *J. Phys. Phys. A* **121,** 9742–9751 (2017).

136. Duan, C.-K., Reid, M. F. & Wang, Z. "Local field effects on the radiative lifetime of emitters in surrounding media: virtual- or real-cavity model?". *Phys. Lett. A* **343,** 474–480 (2005).

137. Onsager, L. "Electric moments of molecules in liquids". *J. Am. Chem. Soc.* **58,** 1486–1493 (1936).

138. Li, L.-W., Kooi, P.-S., Leong, M.-S. & Yee, T.-S. "Electromagnetic dyadic green's function in spherically multilayered media". *IEEE Trans. Microw. Theory Tech.* **42,** 2302–2310 (1994).

139. Tomaš, M. S. "Local-field corrections to the decay rate of excited molecules in absorbing cavities: the onsager model". *Phys. Rev. A* **63,** 053811 (2001).

140. Mott, N. & Massey, H. S. W. *The theory of atomic collisions* (Oxford University Press, Oxford, 1965).

141. Echenique, P. & Alonso, J. L. "A mathematical and computational review of Hartree–fock SCF methods in quantum chemistry". *Mol. Phys.* **105,** 3057–3098 (2007).

142. Friesner, R. A. "*Ab initio* quantum chemistry: methodology and applications". *Proc. Natl. Acad. Sci. U.S.A* **102,** 6648–6653 (2005).

143. Townsend, J., Kirkland, J. K. & Vogiatzis, K. D. in *Mathematical physics in theoretical chemistry* (eds Blinder, S. & House, J.) 63–117 (Elsevier, 2019).

144. Redfield, A. G. "On the theory of relaxation processes". *IBM Journal of Research and Development* **1,** 19–31 (1957).

145. Blum, K. *Density matrix theory and applications* (Plenum Press, New York, London, 1981).

146. Breuer, H. P. & Petruccione, F. *The theory of open quantum systems* (Oxford University Press, Oxford, 2002).

147. Hilborn, R. C. "Einstein coefficients, cross sections, f values, dipole moments, and all that". *Am. J. Phys.* **50,** 982–986 (1982).

148. Chattarji, D. *Theory of the Auger process* (Academic Press, London, 1976).

149. Møller, C. "Über den Stoß zweier Teilchen unter Berücksichtigung der Retardation der Kräfte". *Z. Phys.* **70,** 786–795 (1931).

150. Thomas, W. "Über die Zahl der Dispersionselektronen, die einem stationären Zustande zugeordnet sind". *Sci. Nat.* **13,** 627 (1925).

151. Reiche, F. & Thomas, W. "Über die Zahl der Dispersionselektronen, die einem stationären Zustand zugeordnet sind". *Z. Phys.* **34,** 510 (1925).

152. Kuhn, W. "Über die Gesamtstärke der von einem Zustande ausgehenden Absorptionslinien". *Z. Phys.* **33,** 408 (1925).

153. Craig, D. P. & Tirunamachandran, T. *Molecular quantum electrodynamics* (Dover, New York, 1998).

154. Matthew, J. & Komninos, Y. "Transition rates for interatomic Auger processes". *Surf. Sci.* **53,** 716–725 (1975).

155. Palmeri, P. *et al.* "Radiative and Auger decay of K-vacancy levels in the Ne, Mg, Si, S, Ar, and Ca isonuclear sequences". *Astrophys. J., Suppl. Ser.* **177,** 408–416 (2008).

156. Palmeri, P. *et al.* "Atomic decay data for modeling k lines of iron peak and light odd-z elements". *Astron. Astrophys.* **543,** A44 (2012).

157. Crasemann, B., Chen, M. H. & Kostroun, V. O. "Auger and Coster-Kronig transition probabilities to the atomic 2*s* state and theoretical L_1 fluorescence yields". *Phys. Rev. A* **4,** 2161–2164 (1971).

158. Verner, D. A. & Yakovlev, D. G. "Analytic fits for partial photoionization cross sections.". *Astron. Astrophys., Suppl. Ser.* **109,** 125–133 (1995).

159. Verner, D. A., Ferland, G. J., Korista, K. T. & Yakovlev, D. G. "Atomic data for astrophysics. ii. new analytic fits for photoionization cross sections of atoms and ions". *Amer. J. Phys.* **465,** 487 (1996).

160. Drukarev, E. G. & Mikhailov, A. I. "Asymptotic behavior of photoionization cross section in a central field. ionization of the p states". *Eur. Phys. J. D* **73,** 165 (2019).

161. Jabbari, G., Gokhberg, K. & Cederbaum, L. S. "Competition between interatomic Coulombic decay and autoionization of doubly-excited atoms". *Chem. Phys. Lett.* **754,** 137571 (2020).

162. Sisourat, N. *Private communication.* 2021.

163. Liu, C.-N., Chen, M.-K. & Lin, C. D. "Radiative decay of helium doubly excited states". *Phys. Rev. A* **64,** 010501 (2001).

164. Rubensson, J.-E. *et al.* "Influence of the radiative decay on the cross section for double excitations in helium". *Phys. Rev. Lett.* **83,** 947–950 (1999).

165. Odling-Smee, M. K., Sokell, E., Hammond, P. & MacDonald, M. A. "Radiative decay of doubly excited states in helium below the He^+ $(N = 2)$ ionization threshold". *Phys. Rev. Lett.* **84,** 2598–2601 (2000).

166. CXRO. *X-ray database.* `https://henke.lbl.gov/optical_constants/`. 2020.

167. Gokhberg, K. *Private communication.* 2021.

168. Stumpf, V., Brunken, C. & Gokhberg, K. "Impact of metal ion's charge on the interatomic coulombic decay widths in microsolvated clusters". *J. Chem. Phys.* **145,** 104306 (2016).

169. Engheta, N. & Kowarz, M. W. "Antenna radiation in the presence of a chiral sphere". *J. Appl. Phys.* **67,** 639–647 (1990).

170. Tomaš, M. S. "Green function for multilayers: light scattering in planar cavities". *Phys. Rev. A* **51,** 2545–2559 (1995).

171. Kröner, D. "Laser-driven electron dynamics for circular dichroism in mass spectrometry: from one-photon excitations to multiphoton ionization". *Phys. Chem. Chem. Phys.* **17,** 19643–19655 (2015).

172. Horsch, P., Urbasch, G., Weitzel, K.-M. & Kröner, D. "Circular dichroism in ion yields employing femtosecond laser ionization—the role of laser pulse duration". *Phys. Chem. Chem. Phys.* **13,** 2378–2386 (2011).

173. Kröner, D. "Chiral distinction by ultrashort laser pulses: electron wavepacket dynamics incorporating magnetic interactions.". *J. Phys. Chem. A* **115 50,** 14510–8 (2011).

174. Suzuki, F., Momose, T. & Buhmann, S. Y. "Stern-Gerlach separator of chiral enantiomers based on the Casimir-Polder potential". *Phys. Rev. A* **99,** 012513 (2019).

175. Anderson, B. W. & Payne, C. J. "Liquids of high refractive index". *Nature* **133,** 66–67 (1934).

176. Donaldson, A. & Caplin, A. D. "The optical properties of liquid bromine and iodine". *Philos. Mag. B* **54,** 231–239 (1986).

177. Laskar, J. M., Kumar, P. S., Herminghaus, S., Daniels, K. E. & Schröter, M. "High refractive index immersion liquid for superresolution 3d imaging using sapphire-based aplanatic numerical aperture increasing lens optics". *Appl. Opt.* **55,** 3165 (2016).

178. Zhang, W. *et al.* "Metafluidic metamaterial: a review". *Adv. Phys.: X* **3,** 1417055 (2018).

179. Polyanskiy, M. N. *Refractive index database.* `https://refractiveindex.info`. 2022.

180. Barcellona, P., Safari, H., Salam, A. & Buhmann, S. Y. "Enhanced chiral discriminatory van der Waals interactions mediated by chiral surfaces". *Phys. Rev. Lett.* **118,** 193401 (2017).

181. McLone, R. R. & Power, E. A. "The long range van der Waals forces between non-identical systems". *Proc. Math. Phys. Eng. Sci.* **286,** 573–587 (1965).

182. Power, E. A. & Thirunamachandran, T. "Quantum electrodynamics with nonrelativistic sources. v. electromagnetic field correlations and intermolecular interactions between molecules in either ground or excited states". *Phys. Rev. A* **47,** 2539–2551 (1993).

183. Power, E. A. & Thirunamachandran, T. "Dispersion forces between molecules with one or both molecules excited". *Phys. Rev. A* **51,** 3660–3666 (1995).

184. Sherkunov, Y. "Casimir-Polder interaction between an excited atom and a gas dielectric medium". *Phys. Rev. A* **75,** 012705 (2007).

185. Milonni, P. W. & Rafsanjani, S. M. H. "Distance dependence of two-atom dipole interactions with one atom in an excited state". *Phys. Rev. A* **92,** 062711 (2015).

186. Donaire, M. "Two-atom interaction energies with one atom in an excited state: van der Waals potentials versus level shifts". *Phys. Rev. A* **93,** 052706 (2016).

187. Barcellona, P., Passante, R., Rizzuto, L. & Buhmann, S. Y. "Van der Waals interactions between excited atoms in generic environments". *Phys. Rev. A* **94,** 012705 (2016).

List of publications

JF1. Franz, J., Bennett, R. & Buhmann, S. Y. "Auger decay in dispersing and absorbing environments". *Phys. Rev. A* **104,** 013103 (2021).

JF2. Franz, J. & Buhmann, S. Y. "Purcell modification of auger and interatomic coulombic decay". *New J. Phys.* **24,** 043002 (2022).

JF3. Franz, J. C., Buhmann, S. Y. & Salam, A. *Macroscopic quantum electrodynamics theory of resonance energy transfer involving chiral molecules.* arxiv:2209.15400[quant-phys] (2022).

Appendix

The appendix includes some technical derivations that were left out in the main text to optimise the reading flow. We start by relating the electromagnetic fields as well as their correlation functions of interest to the Green's tensor. We then show that some algebraic manipulation reveal the vacuum correlation function in Fermi's golden rule in second order. The Green's function or bulk media, in particular free space, is then derived, as well as the scattering Green's function. The scattering Green's function is then given analytically for some special cases of interest. Especially spherical layered systems play a major role in the derivations presented in chapter 4. Some more involved expressions and derivation steps of this chapter were moved into the appendix. Finally, all second order rate derivations presented in this work involved some complex contour integration in the frequency domain. The evaluation of these integrals are presented in the last section of the appendix.

A.1. Electromagnetic fields in terms of the Green's tensor

In this section, we relate the electromagnetic fields to the Green's tensor. We introduce shorthand notations for the magnetic and electric Green's tensor as well as define longitudinal and transverse components of vector and tensor fields.

As derived in section 2.1the electric field in terms of the Green's tensor is given by Eq. (2.59)[121],

$$\hat{\boldsymbol{E}}(\boldsymbol{r}) = \int_0^\infty \mathrm{d}\omega \hat{\boldsymbol{E}}(\boldsymbol{r},\omega) + \mathrm{h.c.} \tag{A.1}$$

$$\hat{\boldsymbol{E}}(\boldsymbol{r},\omega) = \sum_{\lambda=e,m} \int \mathrm{d}^3 r' \mathrm{G}_\lambda(\boldsymbol{r},\boldsymbol{r}',\omega) \cdot \hat{\boldsymbol{f}}_\lambda(\boldsymbol{r}',\omega)\,, \tag{A.2}$$

with the electric and magnetic Green's tensor given by

$$\mathbb{G}_e(\boldsymbol{r}_2, \boldsymbol{r}_1, \omega) = \mathrm{i}\frac{\omega^2}{c^2}\sqrt{\frac{\hbar \mathrm{Im}\varepsilon(\boldsymbol{r}_1, \omega)}{\pi\varepsilon_0}}\mathbb{G}(\boldsymbol{r}_2, \boldsymbol{r}_1, \omega)\,, \tag{A.3}$$

$$\mathbb{G}_m(\boldsymbol{r}_2, \boldsymbol{r}_1, \omega) = -\mathrm{i}\frac{\omega^2}{c^2}\sqrt{\frac{\hbar \mathrm{Im}\mu(\boldsymbol{r}_1, \omega)}{\pi\varepsilon_0|\mu(r_1, \omega)|^2}}\mathbb{G}(\boldsymbol{r}_2, \boldsymbol{r}_1, \omega) \times \nabla_1\,. \tag{A.4}$$

The magnetic field is then given by the Faraday law (2.54),

$$\hat{\boldsymbol{B}}(\boldsymbol{r}) = \int_0^\infty \mathrm{d}\omega \hat{\boldsymbol{B}}(\boldsymbol{r}, \omega) + \mathrm{h.c.} \tag{A.5}$$

$$\hat{\boldsymbol{B}}(\boldsymbol{r}, \omega) = \sum_{\lambda=e,m}\int \mathrm{d}^3r' \frac{1}{\mathrm{i}\omega}\nabla \times \mathbb{G}_\lambda(\boldsymbol{r}, \boldsymbol{r}', \omega) \cdot \hat{\boldsymbol{f}}_\lambda(\boldsymbol{r}', \omega)\,. \tag{A.6}$$

In Coulomb gauge, $\nabla \cdot \hat{\boldsymbol{A}} = 0$ the scalar and vector potential (in Fourier space) are given by

$$\nabla\phi(\boldsymbol{r}, \omega) = -\hat{\boldsymbol{E}}^{\parallel}(\boldsymbol{r}, \omega)\,, \qquad \hat{\boldsymbol{A}}(\boldsymbol{r}, \omega) = \frac{\mathrm{i}}{\omega}\hat{\boldsymbol{E}}^{\perp}(\boldsymbol{r}, \omega)\,. \tag{A.7}$$

The superscripts denote the longitudinal and transverse part of the electric field, defined by

$$\boldsymbol{F}^{\parallel/\perp}(\boldsymbol{r}) = \int \mathrm{d}^3r' \boldsymbol{\delta}^{\parallel/\perp}(\boldsymbol{r}' - \boldsymbol{r}) \cdot \boldsymbol{F}(\boldsymbol{r}')\,, \tag{A.8}$$

$$\boldsymbol{\delta}^{\parallel} = -\nabla \otimes \nabla \frac{1}{4\pi r}\,, \tag{A.9}$$

$$\boldsymbol{\delta}^{\perp} = -\nabla \times (\nabla \times \mathbb{I})\frac{1}{4\pi r}\,, \tag{A.10}$$

such that $\boldsymbol{\delta}^{\perp} + \boldsymbol{\delta}^{\parallel} = \boldsymbol{\delta}$. And the vector potential can be decomposed in terms of the Green's tensor,

$$\hat{\boldsymbol{A}}(\boldsymbol{r}, \omega) = \sum_{\lambda=e,m}\int \mathrm{d}^3r' \frac{\mathrm{i}}{\omega}{}^{\perp}\mathbb{G}_\lambda(\boldsymbol{r}, \boldsymbol{r}', \omega) \cdot \hat{\boldsymbol{f}}_\lambda(\boldsymbol{r}', \omega)\,. \tag{A.11}$$

Similarly the longitudinal component of the electric field is simply given by

$$\hat{\boldsymbol{E}}^{\parallel}(\boldsymbol{r}, \omega) = \sum_{\lambda=e,m}\int \mathrm{d}^3r' {}^{\parallel}\mathbb{G}_\lambda(\boldsymbol{r}, \boldsymbol{r}', \omega) \cdot \hat{\boldsymbol{f}}_\lambda(\boldsymbol{r}', \omega)\,. \tag{A.12}$$

The transverse and longitudinal superscript for a tensor $\mathbb{T}(\boldsymbol{r}_1, \boldsymbol{r}_2)$ can be either on its left or right and is defined by

$${}^{\perp/\parallel}\mathbb{T}^{\perp/\parallel}(\boldsymbol{r}_1, \boldsymbol{r}_2) = \iint \mathrm{d}^3r' \mathrm{d}^3r'' \boldsymbol{\delta}^{\perp/\parallel}(\boldsymbol{r}' - \boldsymbol{r}_1) \cdot \mathbb{T}(\boldsymbol{r}', \boldsymbol{r}'') \cdot \delta^{\perp/\parallel}(\boldsymbol{r}' - \boldsymbol{r}_2)\,. \tag{A.13}$$

A.2. Correlation functions in terms of the Green's tensor

Throughout this thesis we relate several quantities to different correlation functions of the field. By using the respective field's expansion in terms of the fundamental creation an annihilation operators it is straightforward to calculate them.

The correlation functions appearing in the derivation of Auger decay are given by

$$\begin{aligned}\langle\hat{\boldsymbol{A}}(\boldsymbol{r}_a,t_a)\otimes\hat{\boldsymbol{A}}(\boldsymbol{r}_b,t_b)\rangle &= \int_0^\infty\int_0^\infty \mathrm{d}\omega_a\mathrm{d}\omega_b \mathrm{e}^{-\mathrm{i}\omega_a t_a}\mathrm{e}^{\mathrm{i}\omega_b t_b}\,\langle\hat{\boldsymbol{A}}(\boldsymbol{r}_a,\omega_a)\otimes\hat{\boldsymbol{A}}^\dagger(\boldsymbol{r}_b,\omega_b)\rangle \\ &= \sum_{\lambda,\lambda'=\mathrm{e,m}}\iint \mathrm{d}^3r'_a\mathrm{d}^3r'_b\iint_0^\infty \mathrm{d}\omega_a\mathrm{d}\omega_b\Big\{\frac{\mathrm{e}^{-\mathrm{i}\omega_a t_a}\mathrm{e}^{\mathrm{i}\omega_b t_b}}{\omega_a\omega_b}\,{}^{\perp}\mathbb{G}_\lambda(\boldsymbol{r}_a,\boldsymbol{r}'_a,\omega_a) \\ &\qquad\cdot\langle\hat{\boldsymbol{f}}(\boldsymbol{r}'_a,\omega_a)\otimes\hat{\boldsymbol{f}}^\dagger(\boldsymbol{r}'_b,\omega_b)\rangle\cdot\mathbb{G}^{\perp *}_{\lambda'}(\boldsymbol{r}'_b,\boldsymbol{r}_b,\omega_b)\Big\} \\ &= \sum_\lambda\int\mathrm{d}^3r'\int_0^\infty\mathrm{d}\omega\frac{\mathrm{e}^{-\mathrm{i}\omega(t_a-t_b)}}{\omega^2}\,{}^{\perp}\mathbb{G}_\lambda(\boldsymbol{r}_a,\boldsymbol{r}',\omega)\cdot\mathbb{G}^{\perp *}_\lambda(\boldsymbol{r}',\boldsymbol{r}_b,\omega) \\ &= \int_0^\infty\mathrm{d}\omega\frac{\hbar}{\pi c^2\varepsilon_0}\mathrm{e}^{-\mathrm{i}\omega(t_a-t_b)}\mathrm{Im}\,{}^{\perp}\mathbb{G}^{\perp}(\boldsymbol{r}_a,\boldsymbol{r}_b,\omega)\,, \end{aligned}\tag{A.14}$$

$$\begin{aligned}\langle\hat{\boldsymbol{E}}^{\parallel}(\boldsymbol{r}_a,t_a)\otimes\hat{\boldsymbol{E}}^{\parallel}(\boldsymbol{r}_b,t_b)\rangle &= \iint_0^\infty \mathrm{d}\omega_a\mathrm{d}\omega_b\mathrm{e}^{-\mathrm{i}\omega_a t_a}\mathrm{e}^{\mathrm{i}\omega_b t_b}\,\langle\hat{\boldsymbol{E}}^{\parallel}(\boldsymbol{r}_a,\omega_a)\otimes\hat{\boldsymbol{E}}^{\parallel\dagger}(\boldsymbol{r}_b,\omega_b)\rangle \\ &= \sum_{\lambda,\lambda'=\mathrm{e,m}}\iint \mathrm{d}^3r'_a\mathrm{d}^3r'_b\iint_0^\infty \mathrm{d}\omega_a\mathrm{d}\omega_b\Big\{\mathrm{e}^{-\mathrm{i}\omega_a t_a}\mathrm{e}^{\mathrm{i}\omega_b t_b}\,{}^{\parallel}\mathbb{G}_\lambda(\boldsymbol{r}_a,\boldsymbol{r}'_a,\omega_a) \\ &\qquad\cdot\langle\hat{\boldsymbol{f}}(\boldsymbol{r}'_a,\omega_a)\otimes\hat{\boldsymbol{f}}^\dagger(\boldsymbol{r}'_b,\omega_b)\rangle\cdot\mathbb{G}^{\parallel *}_{\lambda'}(\boldsymbol{r}'_b,\boldsymbol{r}_b,\omega_b)\Big\} \\ &= \int_0^\infty\mathrm{d}\omega\frac{\hbar\omega^2}{\pi c^2\varepsilon_0}\mathrm{e}^{-\mathrm{i}\omega(t_a-t_b)}\mathrm{Im}\,{}^{\parallel}\mathbb{G}^{\parallel}(\boldsymbol{r}_a,\boldsymbol{r}_b,\omega)\,, \end{aligned}\tag{A.15}$$

$$\begin{aligned}\langle\hat{\boldsymbol{E}}^{\parallel}(\boldsymbol{r}_a,t_a)\otimes\hat{\boldsymbol{A}}(\boldsymbol{r}_b,t_b)\rangle &= \iint_0^\infty \mathrm{d}\omega_a\mathrm{d}\omega_b\mathrm{e}^{-\mathrm{i}\omega_a t_a}\mathrm{e}^{\mathrm{i}\omega_b t_b}\,\langle\hat{\boldsymbol{E}}^{\parallel}(\boldsymbol{r}_a,\omega_a)\otimes\hat{\boldsymbol{A}}^\dagger(\boldsymbol{r}_b,\omega_b)\rangle \\ &= \mathrm{i}\int_0^\infty\mathrm{d}\omega\frac{\hbar\omega}{\pi c^2\varepsilon_0}\mathrm{e}^{-\mathrm{i}\omega(t_a-t_b)}\mathrm{Im}\,{}^{\parallel}\mathbb{G}^{\perp}(\boldsymbol{r}_a,\boldsymbol{r}_b,\omega)\,, \end{aligned}\tag{A.16}$$

$$\begin{aligned}\langle\hat{\boldsymbol{A}}(\boldsymbol{r}_a,t_a)\otimes\hat{\boldsymbol{E}}^{\parallel}(\boldsymbol{r}_b,t_b)\rangle &= \langle\Big[\hat{\boldsymbol{E}}^{\parallel}(\boldsymbol{r}_a,t_a)\otimes\hat{\boldsymbol{A}}(\boldsymbol{r}_b,t_b)\Big]^\dagger\rangle = \langle\hat{\boldsymbol{E}}^{\parallel}(\boldsymbol{r}_b,t_b)\otimes\hat{\boldsymbol{A}}(\boldsymbol{r}_a,t_a)\rangle^{*T} \\ &= -\mathrm{i}\int_0^\infty\mathrm{d}\omega\frac{\hbar\omega}{\pi c^2\varepsilon_0}\mathrm{e}^{-\mathrm{i}\omega(t_a-t_b)}\mathrm{Im}\,{}^{\perp}\mathbb{G}^{\parallel}(\boldsymbol{r}_a,\boldsymbol{r}_b,\omega)\,. \end{aligned}\tag{A.17}$$

The correlation functions of the dual fields appearing in the derivation of the chiral

RET rate in chapter 4 are given by

$$\langle \hat{\boldsymbol{E}}_e(\boldsymbol{r}_1,\omega) \otimes \hat{\boldsymbol{E}}_e^\dagger(\boldsymbol{r}_2,\omega')\rangle = \frac{\hbar\mu_0}{\pi}\omega^2\delta(\omega-\omega')\mathrm{Im}\mathbb{G}(\boldsymbol{r}_1,\boldsymbol{r}_2,\omega)\,, \tag{A.18}$$

$$\begin{aligned}\langle \hat{\boldsymbol{E}}_m(\boldsymbol{r}_1,\omega) \otimes \hat{\boldsymbol{E}}_m^\dagger(\boldsymbol{r}_2,\omega')\rangle &= c^2\,\langle \hat{\boldsymbol{B}}(\boldsymbol{r}_1,\omega) \otimes \hat{\boldsymbol{B}}^\dagger(\boldsymbol{r}_2,\omega')\rangle \\ &= -\frac{\hbar\mu_0 c^2}{\pi}\delta(\omega-\omega')\boldsymbol{\nabla}_A \times \mathrm{Im}\mathbb{G}(\boldsymbol{r}_{1,2},\omega) \times \boldsymbol{\nabla}_B\,,\end{aligned} \tag{A.19}$$

$$\begin{aligned}\langle \hat{\boldsymbol{E}}_m(\boldsymbol{r}_1,\omega) \otimes \hat{\boldsymbol{E}}_e^\dagger(\boldsymbol{r}_2,\omega')\rangle &= c\,\langle \hat{\boldsymbol{B}}(\boldsymbol{r}_1,\omega) \otimes \hat{\boldsymbol{E}}^\dagger(\boldsymbol{r}_2,\omega')\rangle \\ &= -\mathrm{i}\frac{\hbar\mu_0 c\omega}{\pi}\delta(\omega-\omega')\boldsymbol{\nabla}_1 \times \mathrm{Im}\mathbb{G}(\boldsymbol{r}_1,\boldsymbol{r}_2,\omega)\,,\end{aligned} \tag{A.20}$$

$$\begin{aligned}\langle \hat{\boldsymbol{E}}_e(\boldsymbol{r}_1,\omega) \otimes \hat{\boldsymbol{E}}_m^\dagger(\boldsymbol{r}_2,\omega')\rangle &= \langle \hat{\boldsymbol{E}}_m(\boldsymbol{r}_1,\omega) \otimes \hat{\boldsymbol{E}}_e^\dagger(\boldsymbol{r}_2,\omega')\rangle^{*T} \\ &= -\mathrm{i}\frac{\hbar\mu_0 c\omega}{\pi}\delta(\omega-\omega')\mathrm{Im}\mathbb{G}(\boldsymbol{r}_1,\boldsymbol{r}_2,\omega) \times \boldsymbol{\nabla}_2\,.\end{aligned} \tag{A.21}$$

We should mention how to evaluate the curl from the right, since there exist multiple conventions. Here we define:

$$\mathbb{T}(\boldsymbol{r}_1,\boldsymbol{r}_2) \times \boldsymbol{\nabla}_2 = -\boldsymbol{\nabla}_2 \times \mathbb{T}^T(\boldsymbol{r}_1,\boldsymbol{r}_2) \tag{A.22}$$

and the subscript on the nabla denotes with respect to which which position argument the derivative is taken.

A.2.1. Relating the Fermi's golden rule approach to correlation functions

While the correlation functions in the derivation of Auger decay emerge naturally, the derivation of the RET rate via Fermi's golden rule as done in chapter 4 and 5 needs some algebraic manipulation to reveal its relation to the vacuum correlation functions.

We can show the relation by introducing the projection onto the frequency subspace,

$$\hat{P}(\omega) = \sum_{n,\lambda}\int \mathrm{d}^3 r\, |\boldsymbol{n}_\lambda(\boldsymbol{r},\omega)\rangle\,\langle \boldsymbol{n}_\lambda(\boldsymbol{r},\omega)|\,, \tag{A.23}$$

such that

$$\hat{P}(\omega)\hat{\boldsymbol{E}}^{(\dagger)}(\boldsymbol{r},\omega') = \delta(\omega-\omega')\hat{\boldsymbol{E}}^{(\dagger)}(\boldsymbol{r},\omega')\,, \tag{A.24}$$

and $\int \mathrm{d}\omega \hat{P}(\omega)$ is the identity on the fields Hilbert space. Since the fields expectation value is executed in its vacuum state we may introduce the projector into the expression

without changing it,

$$\begin{aligned}
&\int_0^\infty \mathrm{d}\omega' \int \mathrm{d}^3 r' \sum_{\lambda'} \frac{\langle\{0\}|\hat{\boldsymbol{E}}_{\lambda_1}(\boldsymbol{r}_\alpha)|\mathbf{1}'\rangle\,\langle\mathbf{1}'|\hat{\boldsymbol{E}}_{\lambda_2}(\boldsymbol{r}_\beta)|\{0\}\rangle}{\hbar\omega' + \hbar\omega_{eg}^A} \\
&\qquad = \int_0^\infty \mathrm{d}\omega' \int \mathrm{d}^3 r' \sum_{\lambda'} \sum_{n} \frac{\langle\{0\}|\hat{\boldsymbol{E}}_{\lambda_1}(\boldsymbol{r}_\alpha)|\boldsymbol{n}'\rangle\,\langle\boldsymbol{n}'|\hat{\boldsymbol{E}}_{\lambda_2}(\boldsymbol{r}_\beta)|\{0\}\rangle}{\hbar\omega' + \hbar\omega_{eg}^A} \\
&\qquad = \int_0^\infty \mathrm{d}\omega' \frac{\langle\{0\}|\hat{\boldsymbol{E}}_{\lambda_1}(\boldsymbol{r}_\alpha)\hat{P}(\omega')\hat{\boldsymbol{E}}_{\lambda_2}(\boldsymbol{r}_\beta)|\{0\}\rangle}{\hbar\omega' + \hbar\omega_{eg}^A} \\
&\qquad = \int_0^\infty \mathrm{d}\omega_1 \int_0^\infty \mathrm{d}\omega_2 \frac{\langle\hat{\boldsymbol{E}}_{\lambda_1}(\boldsymbol{r}_\alpha,\omega_1)\hat{\boldsymbol{E}}^\dagger_{\lambda_2}(\boldsymbol{r}_\beta,\omega_2)\rangle_{\mathrm{vac}}}{\hbar\omega_2 + \hbar\omega_{eg}^A}\,,
\end{aligned} \tag{A.25}$$

where we have now related the transition matrix element appearing via FGR to (dual) correlation functions.

A.3. The Green's tensor

In this section, we derive the Green's tensor in free space as well as in the presence of different media. The Green's tensor is an essential tool in macroscopic QED and can be separated into two parts, the bulk and scattering Green's tensor. It is defined via its respective Helmholtz equation and can be interpreted as propagator for field excitations. The presented derivations follow the ones found in Ref. [121].

For magnetoelectric media the Helmholtz equation is given by

$$\left[\nabla \times \frac{1}{\boldsymbol{\mu}(\boldsymbol{r},\omega)} \nabla \times - \frac{\omega^2}{c^2}\boldsymbol{\varepsilon}(\boldsymbol{r},\omega)\right] \mathbb{G}(\boldsymbol{r},\boldsymbol{r}',\omega) = \boldsymbol{\delta}(\boldsymbol{r}-\boldsymbol{r}')\,, \tag{A.26}$$

and the Green's tensor needs to fulfil the boundary condition $\mathbb{G}(\boldsymbol{r},\boldsymbol{r}',\omega) \to 0$ for $|\boldsymbol{r}-\boldsymbol{r}'| \to \infty$. Let us first consider a homogenous isotropic magnetoelectric medium, i.e. . Its Helmholtz equation takes the simplified form

$$\left[\nabla \times \nabla \times - k^2\right] \mathbb{G}(\boldsymbol{r},\boldsymbol{r}',\omega) = \mu(\omega)\boldsymbol{\delta}(\boldsymbol{r}-\boldsymbol{r}')\,, \tag{A.27}$$

where $k^2 = \varepsilon(\omega)\mu(\omega)\omega^2/c^2$ is the square of the wave vector inside the medium. It can be solved by

$$\mathbb{G}(\boldsymbol{r},\boldsymbol{r}',\omega) = \mu(\omega)\left[\mathbb{I} + \frac{1}{k^2}\nabla \otimes \nabla\right] g(\boldsymbol{r},\boldsymbol{r}',\omega) \tag{A.28}$$

with the scalar Green's function g fulfilling the scalar Helmholtz equation

$$\left[\Delta + k^2\right] g(\boldsymbol{r}, \boldsymbol{r}', \omega) = -\delta(\boldsymbol{r} - \boldsymbol{r}')\,. \tag{A.29}$$

It is given by

$$g(\boldsymbol{r}, \boldsymbol{r}', \omega) = \frac{\mathrm{e}^{\mathrm{i}k|\boldsymbol{r}_a - \boldsymbol{r}_b|}}{4\pi|\boldsymbol{r} - \boldsymbol{r}'|}\,. \tag{A.30}$$

This underlines the fact that in an isotropic bulk medium the scalar Helmholtz equation is sufficient and hence the scalar Green's function is sufficient to describe the excitation's propagation. The bulk Green's tensor can then be explcitily calculated to be

$$\begin{aligned}\mathbb{G}^{(0)}(\boldsymbol{r}_a, \boldsymbol{r}_b, \omega) &= \frac{\mu(\omega)}{4\pi}\left(\mathbb{I} + \frac{1}{k^2}\nabla_a \otimes \nabla_a\right)\frac{\mathrm{e}^{\mathrm{i}k|\boldsymbol{r}_a - \boldsymbol{r}_b|}}{|\boldsymbol{r}_a - \boldsymbol{r}_b|} \\ &= \frac{\mu(\omega)}{3k^2}\boldsymbol{\delta}(\boldsymbol{r}_{ab}) - \frac{\mu(\omega)\mathrm{e}^{\mathrm{i}kr_{ab}}}{4\pi k^2 r_{ab}^2}\Bigg\{\left[1 - \mathrm{i}kr_{ab} - k^2 r_{ab}^2\right]\mathbb{I} \\ &\qquad - \left[3 - 3\mathrm{i}kr_{ab} - k^2 r_{ab}^2\right]\boldsymbol{e}_{ab} \otimes \boldsymbol{e}_{ab}\Bigg\}\,,\end{aligned} \tag{A.31}$$

where ∇_a is the Nabla-operator with respect to $\boldsymbol{r}_a$, $\boldsymbol{r}_{ab} = \boldsymbol{r}_a - \boldsymbol{r}_b$, $r_{ab} = |\boldsymbol{r}_{ab}|$ and $\boldsymbol{e}_{ab} = \boldsymbol{r}_{ab}/r_{ab}$. In the special case of free space, $\varepsilon = \mu = 1$, the free space Green's tensor is then given by

$$\begin{aligned}\mathbb{G}^{(0)}(\boldsymbol{r}_a, \boldsymbol{r}_b, \omega) &= \frac{1}{4\pi}\left(\mathbb{I} + \frac{c^2}{\omega^2}\nabla_a \otimes \nabla_a\right)\frac{\mathrm{e}^{\mathrm{i}\omega|\boldsymbol{r}_a - \boldsymbol{r}_b|/c}}{|\boldsymbol{r}_a - \boldsymbol{r}_b|} \\ &= \frac{c^2}{3\omega^2}\boldsymbol{\delta}(\boldsymbol{r}_{ab}) - \frac{c^2\mathrm{e}^{\mathrm{i}\omega r_{ab}/c}}{4\pi\omega^2 r_{ab}^2}\Bigg\{\left[1 - \mathrm{i}\frac{\omega r_{ab}}{c} - \frac{\omega^2 r_{ab}^2}{c^2}\right]\mathbb{I} \\ &\qquad - \left[3 - 3\mathrm{i}\frac{\omega r_{ab}}{c} - \frac{\omega^2 r_{ab}^2}{c^2}\right]\boldsymbol{e}_{ab} \otimes \boldsymbol{e}_{ab}\Bigg\}\,.\end{aligned} \tag{A.32}$$

The Green's tensor $\mathbb{G}(\boldsymbol{r}, \boldsymbol{r}', \omega)$ is related to the probability of a field excitation with energy $\hbar\omega$ to propagate from a source point $\boldsymbol{r}'$ to an absorption point $\boldsymbol{r}$, thus we may call the Green's tensor the propagator for field excitations.

Next, let us consider a secondary homogeneous medium with a definite boundary to the first. We assume that the first homogeneous medium with permittivity ε_1 and permeability μ_1 occupies a volume V_1 and the second medium with permittivity ε_2 and permeability μ_2 the complementary volume V_2. From the boundary conditions that must hold for the electromagnetic field, we can deduce the boundary conditions for the Green's

tensor. The electric field $\boldsymbol{E}$ and magnetic excitation field $\boldsymbol{H}$ must fulfil

$$\boldsymbol{e}_{\parallel} \cdot [\boldsymbol{E}(\boldsymbol{r}+\boldsymbol{s}) - \boldsymbol{E}(\boldsymbol{r}-\boldsymbol{s})] = 0\,, \tag{A.33}$$

$$\boldsymbol{e}_{\perp} \cdot [\boldsymbol{B}(\boldsymbol{r}+\boldsymbol{s}) - \boldsymbol{B}(\boldsymbol{r}-\boldsymbol{s})] = 0\,, \tag{A.34}$$

$$\boldsymbol{e}_{\perp} \cdot [\boldsymbol{D}(\boldsymbol{r}+\boldsymbol{s}) - \boldsymbol{D}(\boldsymbol{r}-\boldsymbol{s})] = \rho(\boldsymbol{r}) \tag{A.35}$$

$$\boldsymbol{e}_{\parallel} \cdot [\boldsymbol{H}(\boldsymbol{r}+\boldsymbol{s}) - \boldsymbol{H}(\boldsymbol{r}-\boldsymbol{s})] = \boldsymbol{e}_{\perp} \times \boldsymbol{e}_{\parallel} \cdot \boldsymbol{j}(\boldsymbol{r})\,, \tag{A.36}$$

where $\boldsymbol{e}_{\parallel/perp}$ denotes a unit vector parallel/perpendicular to the boundary surface, $\boldsymbol{r}$ is a position on the boundary surface and $\boldsymbol{s} = s\boldsymbol{e}_{\perp}$ is a vector perpendicular to the boundary surface, such that $\boldsymbol{r} \pm \boldsymbol{s}$ lies in Volume V_1/V_2 and $\rho(\boldsymbol{r})$, $\boldsymbol{j}(\boldsymbol{r})$ are the surface charge and surface current densities, respectively.

In the limit $\lim_{s\to 0}(\boldsymbol{r} \pm \boldsymbol{s}) = \boldsymbol{r}_{+/-}$ we then find for the Green's tensor

$$\boldsymbol{e}_{\parallel} \cdot \left[\mathbb{G}(\boldsymbol{r}_{+}, \boldsymbol{r}', \omega) - \mathbb{G}(\boldsymbol{r}_{-}, \boldsymbol{r}', \omega)\right] = \boldsymbol{0} \tag{A.37}$$

$$\boldsymbol{e}_{\perp} \cdot \left[\nabla \times \mathbb{G}(\boldsymbol{r}_{+}, \boldsymbol{r}', \omega) - \nabla \times \mathbb{G}(\boldsymbol{r}_{-}, \boldsymbol{r}', \omega)\right] = \boldsymbol{0}\,, \tag{A.38}$$

from the homogenous boundary conditions, Eqs. (A.33) and (A.34). The inhomogeneous boundary conditions Eqs. (A.35) and (A.36) yields for the Green's tensor,

$$\begin{aligned}
&\boldsymbol{e}_{\perp} \cdot \left[\varepsilon_1(\omega)\mathbb{G}(\boldsymbol{r}_{+}, \boldsymbol{r}', \omega) - \varepsilon_1(\omega)\mathbb{G}(\boldsymbol{r}_{-}, \boldsymbol{r}', \omega)\right] \\
&\qquad = -\frac{c^2}{\omega^2} \lim_{s\to 0} \int_{-s/2}^{s/2} \mathrm{d}s' \boldsymbol{\nabla} \delta(\boldsymbol{r} - \boldsymbol{r}' + s'\boldsymbol{e}_{\perp})\,, \qquad \text{(A.39)} \\
&\boldsymbol{e}_{\parallel} \cdot \left[\frac{1}{\mu_1(\omega)} \boldsymbol{\nabla} \times \mathbb{G}(\boldsymbol{r}_{+}, \boldsymbol{r}', \omega) - \frac{1}{\mu_2(\omega)} \boldsymbol{\nabla} \times \mathbb{G}(\boldsymbol{r}_{-}, \boldsymbol{r}', \omega)\right] \\
&\qquad = \boldsymbol{e}_{\perp} \times \boldsymbol{e}_{\parallel} \lim_{s\to 0} \int_{-s/2}^{s/2} \mathrm{d}s' \delta(\boldsymbol{r} - \boldsymbol{r}' + s'\boldsymbol{e}_{\perp})\,, \qquad \text{(A.40)}
\end{aligned}$$

where the right hand side of each equation vanishes for all positions but $\boldsymbol{r} = \boldsymbol{r}'$. Using these boundary conditions together with the respective Helmholtz equation enables us to find the Green's tensor.

Let us first assume that source and absorption are located within the same medium, i.e. within the same volume V_1. The bulk Green's tensor (A.31) gives then a particular solution to the inhomogeneous Helmholtz equation, such that

$$\left[\boldsymbol{\nabla} \times \boldsymbol{\nabla} \times -k_1^2\right] \mathbb{G}^{(0)}(\boldsymbol{r}, \boldsymbol{r}', \omega) = \mu_1(\omega) \boldsymbol{\delta}(\boldsymbol{r} - \boldsymbol{r}')\,, \tag{A.41}$$

with $\boldsymbol{r}, \boldsymbol{r}' \in V_1$ and $k_1 = \sqrt{\varepsilon_1 \mu_1}\omega/c$. And we define the scattering Green's tensor $\mathbb{G}^{(1)}$ as a solution for the homogeneous Helmholtz equation,

$$\left[\boldsymbol{\nabla} \times \boldsymbol{\nabla} \times -k_1^2\right] \mathbb{G}^{(1)}(\boldsymbol{r}, \boldsymbol{r}', \omega) = 0\,. \tag{A.42}$$

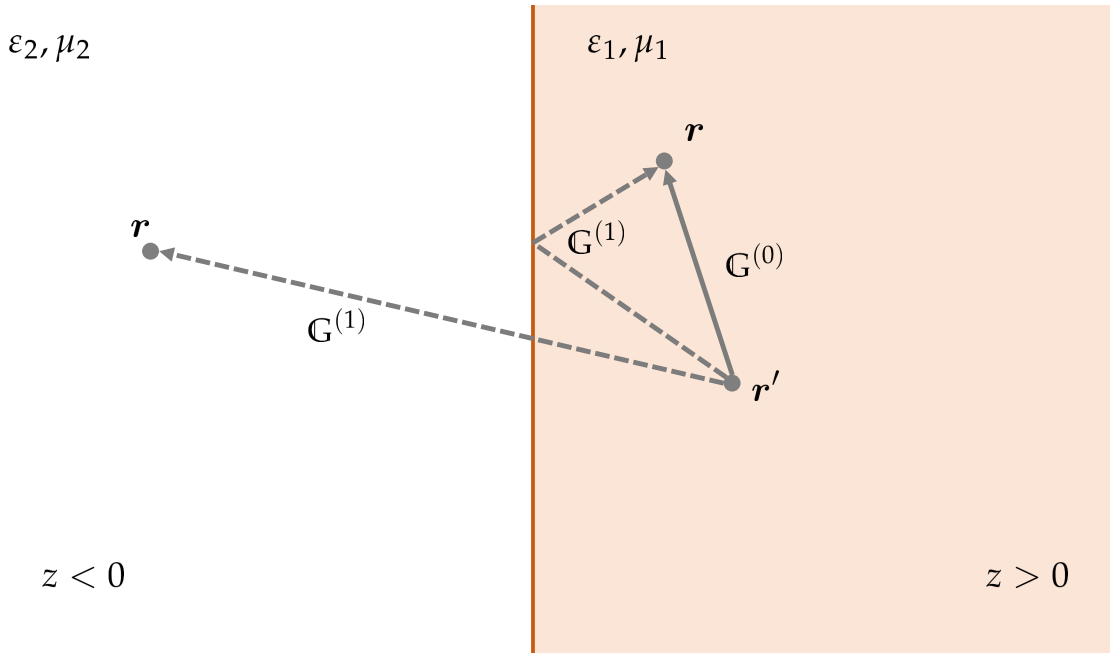

Figure A.1.: Scheme of a planar two-layer system.

For the source and absorption point in different volumes, i.e. $\boldsymbol{r} \in V_2$ and $\boldsymbol{r}' \in V_1$, the respective Helmholtz equation is homogeneous and the Green's tensor is solely given by the scattering Green's tensor. The scattering Green's tensor is then determined by the boundary conditions.

A.3.1. Planar two-layer system

Let us consider a planar two-layer system, see Fig. A.1 where the boundary surface is in the $z = 0$ plane. A basis set of vector wave functions fulfilling the homogeneous Helmholtz equation is then given by

$$\boldsymbol{a}^{(j)}_{\sigma\pm}(\boldsymbol{k}^{\parallel}, \boldsymbol{r}) = \boldsymbol{e}^{(j)}_{\sigma\pm} \mathrm{e}^{\mathrm{i}(\boldsymbol{k}^{\parallel}\cdot\boldsymbol{r} \pm k_j^{\perp} z)} , \tag{A.43}$$

where $k_j^{\perp} = k_j^{\perp}(k^{\parallel}) = \sqrt{k_j^2 - k^{\parallel 2}}$, $\sigma \in \{s, p\}$ and the unit vectors depend on the direction of $\boldsymbol{k}^{\parallel}$ and are defined as

$$\boldsymbol{e}^{(j)}_{s\pm} = \boldsymbol{e}_{\parallel} \times \boldsymbol{e}_z \tag{A.44}$$

$$\boldsymbol{e}^{(j)}_{p\pm} = \frac{1}{k_j} \left(k^{\parallel} \boldsymbol{e}_z \mp k_j^{\perp} \boldsymbol{e}_{\parallel} \right) , \tag{A.45}$$

with $\boldsymbol{e}_{\parallel} = \boldsymbol{k}^{\parallel} / k^{\parallel}$.

We may expand the bulk Green's tensor in this basis set. We assume that the source is

located at $\boldsymbol{r}'$ inside volume V_1, i.e. $z' > 0$ and that the absorption point is at a position $\boldsymbol{r}$, such that $z < z'$ and find for the bulk

$$\mathbb{G}^{(0)} = \frac{\mathrm{i}\mu_1}{8\pi^2} \int \frac{\mathrm{d}^2 k^{\parallel}}{k_1^{\perp}} \sum_{\sigma} \boldsymbol{a}_{\sigma-}^{(1)}(\boldsymbol{k}^{\parallel}, \boldsymbol{r}) \otimes \boldsymbol{c}_{\sigma-}^{(1)}(\boldsymbol{k}^{\parallel}, \boldsymbol{r}') \,, \tag{A.46}$$

with

$$\boldsymbol{c}_{\sigma\pm}^{(j)}(\boldsymbol{k}^{\parallel}, \boldsymbol{r}') = \boldsymbol{e}_{\sigma\pm}^{(j)} \mathrm{e}^{-\mathrm{i}(\boldsymbol{k}^{\parallel} \cdot \boldsymbol{r}' \pm k_j^{\perp} z')} \,. \tag{A.47}$$

Similarly we can expand the scattering Green's tensor in this basis. For absorption within volume V_1, i.e. $z > 0$ we get

$$\mathbb{G}^{(1)}(\boldsymbol{r}, \boldsymbol{r}', \omega) = \frac{\mathrm{i}\mu_1}{8\pi^2} \int \frac{\mathrm{d}^2 k^{\parallel}}{k_1^{\perp}} \sum_{\sigma} r_{\sigma}(k^{\parallel}, \omega) \boldsymbol{a}_{\sigma+}^{(1)}(\boldsymbol{k}^{\parallel}, \boldsymbol{r}) \otimes \boldsymbol{c}_{\sigma-}^{(1)}(\boldsymbol{k}^{\parallel}, \boldsymbol{r}') \,, \tag{A.48}$$

and for absorption within volume V_2, i.e. $z < 0$,

$$\mathbb{G}^{(1)}(\boldsymbol{r}, \boldsymbol{r}', \omega) = \frac{\mathrm{i}\mu_1}{8\pi^2} \int \frac{\mathrm{d}^2 k^{\parallel}}{k_1^{\perp}} \sum_{\sigma} t_{\sigma}(k^{\parallel}, \omega) \boldsymbol{a}_{\sigma-}^{(2)}(\boldsymbol{k}^{\parallel}, \boldsymbol{r}) \otimes \boldsymbol{c}_{\sigma-}^{(1)}(\boldsymbol{k}^{\parallel}, \boldsymbol{r}') \,. \tag{A.49}$$

Solving the boundary conditions Eqs. (A.33)–(A.36) with this ansatz for the Green's tensor then yields for the reflection and transmission coefficients r_σ and t_σ,

$$r_s(k^{\parallel}, \omega) = \frac{\mu_2 k_1^{\perp} - \mu_1 k_2^{\perp}}{\mu_2 k_1^{\perp} + \mu_1 k_2^{\perp}} \,, \tag{A.50}$$

$$r_p(k^{\parallel}, \omega) = \frac{\varepsilon_2 k_1^{\perp} - \varepsilon_1 k_2^{\perp}}{\varepsilon_2 k_1^{\perp} + \varepsilon_1 k_2^{\perp}} \,, \tag{A.51}$$

$$t_s(k^{\parallel}, \omega) = \frac{2\mu_2 k_1^{\perp}}{\mu_2 k_1^{\perp} + \mu_1 k_2^{\perp}} \,, \tag{A.52}$$

$$t_p(k^{\parallel}, \omega) = \frac{k_2}{k_1} \frac{2\varepsilon_2 k_1^{\perp}}{\varepsilon_2 k_1^{\perp} + \varepsilon_1 k_2^{\perp}} \,. \tag{A.53}$$

In general the respective integral, Eq. (A.48) or Eq. (A.49) must be solved numerically for each position $\boldsymbol{r}$ and frequency ω. However, in many cases it is sufficient to know the Green's tensor in the extreme distance limits of non-retarded and retarded limit. In these limits the k-integral can be evaluated and the Green's tensor may be given as a closed expression.

Let us consider the reflection at a dielectric half space, i.e. $\varepsilon_1 = \mu_1 = 1$ and $\mu_2 = 1$ in the nonretarded limit, such that $\omega z/c \ll 1$ and $\omega z'/c \ll 1$. In the integral over $k^{\parallel}$ in Eq. (A.48) the limit of $z^{(\prime)} \ll c/\omega$ leads then effectively to $k^{\perp} c/\omega \gg 1$. In this limit the

reflection coefficients (A.50) and (A.51) assume a simpler form,

$$r_s \to 0\,, \qquad r_p \to r_{\mathrm{NR}} = \frac{\varepsilon_2 - 1}{\varepsilon_2 + 1}\,. \tag{A.54}$$

Using this together with a Taylor expansion for the z-components of the source and absorption point, we may evaluate the k-integral in Eq. (A.48) analytically and find for the scattering Green's tensor close to a dielectric half space:

$$\begin{aligned} \mathbb{G}^{(1)}(\boldsymbol{r}_b, \boldsymbol{r}_a, \omega) &= -\frac{r_{\mathrm{NR}} c^2}{4\pi\omega^2 \bar{r}_{ab}^3}(\mathbb{I} - 3\bar{\boldsymbol{e}}_{ab} \otimes \bar{\boldsymbol{e}}_{ab}) \cdot \mathbb{M}\,, \\ \mathbb{M} &= \mathbb{I} - 2\boldsymbol{e}_{\Delta r} \otimes \boldsymbol{e}_{\Delta r}\,, \\ \bar{\boldsymbol{r}}_{ab} &= \mathbb{M} \cdot \boldsymbol{r}_{ab} - 2\Delta\boldsymbol{r}, \quad \bar{\boldsymbol{e}}_{ab} = \bar{\boldsymbol{r}}_{ab}/\bar{r}_{ab}\,, \end{aligned} \tag{A.55}$$

where $\boldsymbol{r}_{ab} = \boldsymbol{r}_b - \boldsymbol{r}_a$ and $\bar{\boldsymbol{r}}_{ab}$ is its mirror point, behind the surface and $\boldsymbol{e}_x = \boldsymbol{r}_x/|r_x|$ is the respective unit vector.

A.3.2. Spherical layer system

For a spherically layered system the approach for solving the Green's tensor is comparable to the planar layered system. However the geometry shows much more symmetry and the problem is hence easier, as a consequence the scattering Green's tensor can be given as a closed expression for all distances. In the main text, see chapter 4 we derive the Green's tensor for a spherical two-layer system involving chiral media. Magneto-electric medium is then a special case of the Green's tensors derived for the chiral medium. In this section we offer some additional derivations and expressions that are useful to follow the derivations in chapter 4 and finally use the special case of achiral media to derive the scattering Green's tensor for a spherical cavity as we use it as a reference in chapter 3.

Spherical vector wave functions

In chapter 4 we use spherical wave vector functions as a basis to form an ansatz for the Green's tensor inside spherical layered chiral media.

They are given by

$$\boldsymbol{V}_{\substack{\mathrm{e}\\\mathrm{o}}mn}(\boldsymbol{r},k) = \frac{\boldsymbol{M}_{\substack{\mathrm{e}\\\mathrm{o}}mn}(\boldsymbol{r}) + \boldsymbol{N}_{\substack{\mathrm{e}\\\mathrm{o}}mn}(\boldsymbol{r})}{\sqrt{2}} \tag{A.56}$$

$$= \frac{1}{\sqrt{2}}\Bigg[\mp \frac{m}{\sin(\theta)} P_{nm}(\cos(\theta)) \begin{matrix}\sin\\\cos\end{matrix}(m\phi)\left(j_n(kr)\boldsymbol{e}_\theta + \frac{1}{kr}\frac{\partial}{\partial r}[rj_n(kr)]\boldsymbol{e}_\phi\right)$$

$$+ \frac{\partial P_{nm}(\cos(\theta))}{\partial\theta} \begin{matrix}\cos\\\sin\end{matrix}(m\phi)\left(\frac{1}{kr}\frac{\partial}{\partial r}[rj_n(kr)]\boldsymbol{e}_\theta - j_n(kr)\boldsymbol{e}_\phi\right) \tag{A.57}$$

$$+ n(n+1)P_{nm}(\cos(\theta)) \begin{matrix}\cos\\\sin\end{matrix}(m\phi)\frac{j_n(kr)}{kr}\boldsymbol{e}_r\Bigg],$$

$$\boldsymbol{W}_{\substack{\mathrm{e}\\\mathrm{o}}mn}(\boldsymbol{r},k) = \frac{\boldsymbol{M}_{\substack{\mathrm{e}\\\mathrm{o}}mn}(\boldsymbol{r}) - \boldsymbol{N}_{\substack{\mathrm{e}\\\mathrm{o}}mn}(\boldsymbol{r})}{\sqrt{2}} \tag{A.58}$$

$$= \frac{1}{\sqrt{2}}\Bigg[\mp \frac{m}{\sin(\theta)} P_{nm}(\cos(\theta)) \begin{matrix}\sin\\\cos\end{matrix}(m\phi)\left(j_n(kr)\boldsymbol{e}_\theta - \frac{1}{kr}\frac{\partial}{\partial r}[rj_n(kr)]\boldsymbol{e}_\phi\right)$$

$$+ \frac{\partial P_{nm}(\cos(\theta))}{\partial\theta} \begin{matrix}\cos\\\sin\end{matrix}(m\phi)\left(-\frac{1}{kr}\frac{\partial}{\partial r}[rj_n(kr)]\boldsymbol{e}_\theta - j_n(kr)\boldsymbol{e}_\phi\right) \tag{A.59}$$

$$- n(n+1)P_{nm}(\cos(\theta)) \begin{matrix}\cos\\\sin\end{matrix}(m\phi)\frac{j_n(kr)}{kr}\boldsymbol{e}_r\Bigg].$$

Full solution of a vacuum sphere in a chiral medium

In chapter 4, we derive the Green's tensor for a spherically layered system involving chiral media. Here, we give the solution to the boundary problem posed by the set up.

The two boundary conditions, Eqs. (4.32) and (4.33) result in eight different equations that are given by:

$$\mathbb{T}\begin{pmatrix} a_n^v \\ a_n^w \\ c_n^v \\ c_n^w \end{pmatrix} = \begin{pmatrix} k_0^2\partial h \\ k_0^2\partial h \\ k_0^2\partial h \\ k_0^2\partial h \end{pmatrix}, \qquad \mathbb{T}\begin{pmatrix} b_n^v \\ b_n^w \\ d_n^v \\ d_m^w \end{pmatrix} = \begin{pmatrix} -k_0^2\partial h \\ k_0^2\partial h \\ k_0^2\partial h \\ -k_0^2\partial h \end{pmatrix} \tag{A.60}$$

with $k_0 = \omega/c$ and

$$\mathbb{T} = \begin{pmatrix} \partial h_+ & -\partial h_- & -\partial j & \partial j \\ h_+ & h_- & -j & -j \\ l\partial h_+ & l\partial h_- & -\partial j & -\partial j \\ lh_+ & -lh_- & -j & +j \end{pmatrix}, \qquad \text{where } l = \frac{\sqrt{\mu\varepsilon}}{\mu} \tag{A.61}$$

and the shorthand notation:

$$j = j_n(k_0 a) \qquad \partial j = \frac{1}{k_0 a}\frac{\partial}{\partial r}[r j_n(k_0 r)]\Big|_a \tag{A.62}$$

$$h = h_n^{(1)}(k_0 a) \qquad \partial h = \frac{1}{k_0 a}\frac{\partial}{\partial r}[r h_n^{(1)}(k_0 r)]\Big|_a \tag{A.63}$$

$$h_\pm = h_n^{(1)}(k_\pm a) \qquad \partial h_\pm = \frac{1}{k_\pm a}\frac{\partial}{\partial r}[r j_n(k_\pm r)]\Big|_a \tag{A.64}$$

By inverting matrix $\mathbb{T}$ we find for the coefficients of $\mathbb{G}^{21}$:

$$a_n^v = \frac{1}{D_n}\left(2k_0^2(l+1)(\partial j h - \partial h j)(\partial j h_- - \partial h_- j)\right) \tag{A.65}$$

$$a_n^w = \frac{1}{D_n}\left(2k_0^2(l-1)(\partial j h - \partial h j)(\partial j h_+ + \partial h_+ j)\right) \tag{A.66}$$

$$b_n^v = \frac{1}{D_n}\left(2k_0^2(l-1)(\partial j h - \partial h j)(\partial j h_- + \partial h_- j)\right) \tag{A.67}$$

$$b_n^w = \frac{1}{D_n}\left(2k_0^2(l+1)(\partial j h - \partial h j)(\partial j h_+ - \partial h_+ j)\right) \tag{A.68}$$

$$D_n = 2(\partial h_+ j(2\partial h_- j l - h_- \partial j(1+l^2)) + h_+ \partial j(2h_- \partial j l - \partial h_- j(1+l^2))) \tag{A.69}$$

Retarded Green's tensor inside spherical cavity

Let us consider a free space sphere with radius R inside a magneto-electric medium with $\varepsilon, \mu \in \mathbb{R}$. This can be interpreted as a spherical cavity with infinitely thick walls. Using the scattering Green's tensor defined by Eq. (4.34) of the analogue chiral case and setting $\chi = 0$ we find the solution inside magneto-electric media.

In the case of source and absorption point at the center of the sphere, the coefficients for the Green's tensor (4.34) for $\chi = 0$ are given by

$$\begin{aligned} c_v^n = d_w^n = \frac{1}{D_{cd}}\Big\{ &\left(l^2+1\right)\partial h_n(k_1 R) h_n(k_1 R)(\partial h_n(k_0 R) j_n(k_0 R) + \partial j_n(k_0 R) h_n(k_0 R)) \\ &- 2l\partial h_n(k_0 R)\partial j_n(k_0 R) h_n(k_1 R)^2 - 2l\partial h_n^2(k_1 R) h_n(k_0 R) j_n(k_0 R)\Big\}, \end{aligned} \tag{A.70}$$

$$c_w^n = d_v^n = \frac{1}{D_{cd}}\left\{ \left(l^2-1\right)\partial h_n(k_1) h_n(k_1)\left[\partial j_n(k_0 R) h_n(k_0 R) - \partial h_n(k_0 R) j_n(k_0 R)\right]\right\}, \tag{A.71}$$

$$\begin{aligned} D_{cd} = -2\left(l^2+1\right)&\partial h_n(k_1 R)\partial j_n(k_0 R) h_n(k_1 R) j_n(k_0 R) \\ &+ 2l\partial h_n^2(k_1 R) j_n^2(k_0 R) + 2l\partial j_n^2(k_0 R) h_n^2(k_1 R), \end{aligned} \tag{A.72}$$

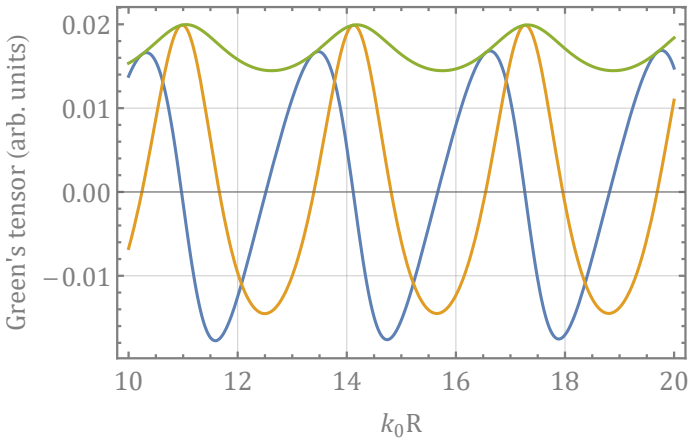

Figure A.2.: Scattering Green's tensor for a cavity in the retarded limit with $n_r = 1.6$. The real part of $\mathbb{G}^{(1)}$ (A.74) is given by the blue curve, the imaginary part by the orange one and the green curve shows the absolute value of $\mathbb{G}$.

with $k_1 = \sqrt{\varepsilon\mu}\omega/c$ and $k_0 = \omega/c$ and we used again the shorthand notation,

$$\partial h_n(kr) = \frac{1}{kr}\frac{\partial}{\partial r}\left[rh_n(kr)\right], \qquad \partial j_n(kr) = \frac{1}{kr}\frac{\partial}{\partial r}\left[rj_n(kr)\right]. \tag{A.73}$$

Substituting this into the scattering Green's tensor defined by Eq. (4.34) and assuming the retarded limit of $\omega R/c \gg 1$ where R is the cavity radius, we find for the scattering Green's tensor:

$$\begin{aligned} \mathbb{G}^{(1)}(0,0,\omega) &= -e^{\mathrm{i}k_0R}\frac{k_0R(n_r^2-n_r)+\mathrm{i}\left(n_r^2-1\right)}{D(k_0R)}\mathbb{I} \\ D(k_0R) &= 6\pi\Big[(\mathrm{i}k_0R(n_r-n_r^2)+n_r^2-1)\cos(k_0R) \\ &\qquad +\mathrm{i}k_0Rn_r^2e^{-\mathrm{i}k_0R}\Big], \end{aligned} \tag{A.74}$$

where $k_0 = \omega/c$ and $n_r = \sqrt{\varepsilon\mu}$ is the refractive index that we assumed to be real here for simplicity.

The retarded scattering Green's tensor (A.74) for a spherical cavity shows oscillations as a function of the radius R. The imaginary and real part of the scattering Green's tensor have then similar amplitudes as shown on the example of $n_r = 1.6$ in Fig. A.2 and we may approximate

$$|\mathbb{G}^{(1)}| \approx \mathrm{Im}\mathbb{G}^{(1)} \approx \mathrm{Re}\mathbb{G}^{(2)}. \tag{A.75}$$

A.4. Complex contour integration

In several derivations throughout this thesis we need to evaluate the same complex contour integration in the frequency domain including a pole. We evaluate this integral here in general.

For $\eta > 0$, $\omega_{nk} > 0$ and $p(\omega) = \omega^n$, with $n \in \{0, 1, 2\}$, we find

$$\begin{aligned}
&\int_0^\infty \mathrm{d}\omega \frac{p(\omega)}{\omega - \omega_{nk} - \mathrm{i}\eta} \mathrm{Im}\mathbb{G}(\omega) \\
&\qquad = -\frac{1}{2} \int_0^\infty \mathrm{d}\omega \left\{ \frac{p(\omega)}{\omega - \omega_{nk} - \mathrm{i}\eta} \mathbb{G}(\omega) - \frac{p(\omega)}{\omega - \omega_{nk} - \mathrm{i}\eta} \overbrace{\mathbb{G}^*(\omega)}^{=\mathbb{G}(-\omega)} \right\} \\
&\qquad = -\frac{1}{2} \left\{ \int_0^\infty \mathrm{d}\omega \frac{p(\omega)}{\omega - (\omega_{nk} + \mathrm{i}\eta)} \mathbb{G}(\omega) - \int_{-\infty}^0 \mathrm{d}\omega \frac{p(-\omega)}{-\omega - (\omega_{nk} + \mathrm{i}\eta)} \mathbb{G}(\omega) \right\} \\
&\qquad = -\frac{1}{2} \left\{ \left[\oint_\gamma - \int_\Gamma - \int_{-\infty}^0 \right] \mathrm{d}\omega \frac{p(\omega)}{\omega - (\omega_{nk} + \mathrm{i}\eta)} \mathbb{G}(\omega) \right. \\
&\qquad\qquad \left. + \left[\oint_\gamma - \int_\Gamma - \int_0^\infty \right] \mathrm{d}\omega \frac{p(-\omega)}{\omega + (\omega_{nk} + \mathrm{i}\eta)} \mathbb{G}(\omega) \right\}
\end{aligned} \tag{A.76}$$

Where we used that the Green's tensor is holomorphic (complex-analytical) in the upper half of the complex plane and we might therefore use the residual theorem. The first closed integral $\oint_\gamma \mathrm{d}\omega$ encloses a pole at $\omega = \omega_{nk} + \mathrm{i}\eta$, while the second does not. The Green's tensor vanishes fast enough on the upper complex plane, so that for radius $R_\Gamma \to \infty$ the integral vanishes. The residue theorem then yields:

$$\begin{aligned}
&-\frac{1}{2} \left\{ \left[\oint_\gamma - \int_\Gamma - \int_{-\infty}^0 \right] \mathrm{d}\omega \frac{p(\omega)}{\omega - (\omega_{nk} + \mathrm{i}\eta)} \mathbb{G}(\omega) + \left[\oint_\gamma - \int_\Gamma - \int_0^\infty \right] \mathrm{d}\omega \frac{p(-\omega)}{\omega + (\omega_{nk} + \mathrm{i}\eta)} \mathbb{G}(\omega) \right\} \\
&\quad = -\frac{1}{2} \left\{ 2\pi \mathrm{i} p(\omega_{nk} + \mathrm{i}\eta) \mathbb{G}(\omega_{nk} + \mathrm{i}\eta) - \int_{-\infty}^0 \mathrm{d}\omega \frac{p(\omega)\mathbb{G}(\omega)}{\omega - (\omega_{nk} + \mathrm{i}\eta)} - \int_0^\infty \mathrm{d}\omega \frac{p(-\omega)\mathbb{G}(\omega)}{\omega + \omega_{nk} + \mathrm{i}\eta} \right\} \\
&\quad = -\frac{1}{2} \left\{ 2\pi \mathrm{i} p(\omega_{nk} + \mathrm{i}\eta) \mathbb{G}(\omega_{nk} + \mathrm{i}\eta) + \int_0^\infty \mathrm{d}\omega \frac{p(-\omega)\mathbb{G}(-\omega)}{\omega + \omega_{nk} + \mathrm{i}\eta} - \int_0^\infty \mathrm{d}\omega \frac{p(-\omega)\mathbb{G}(\omega)}{\omega + \omega_{nk} + \mathrm{i}\eta} \right\} \\
&\quad = -\frac{1}{2} \left\{ 2\pi \mathrm{i} p(\omega_{nk} + \mathrm{i}\eta) \mathbb{G}(\omega_{nk} + \mathrm{i}\eta) - 2\mathrm{i} \int_0^\infty \mathrm{d}\omega \frac{p(-\omega)\mathrm{Im}\mathbb{G}(\omega)}{\omega + \omega_{nk} + \mathrm{i}\eta} \right\} \\
&\quad = -\mathrm{i}\pi p(\omega_{nk}) \mathbb{G}(\omega_{nk}) + \mathrm{i} \int_0^\infty \mathrm{d}\omega \frac{p(-\omega)\mathrm{Im}\mathbb{G}(\omega)}{\omega + \omega_{nk}}
\end{aligned} \tag{A.77}$$

In the limit of $\eta \to 0$ we hence find

$$\int_0^\infty \mathrm{d}\omega \left(\frac{p(\omega)}{\omega - \omega_{nk} - \mathrm{i}\eta} + \frac{p(-\omega)}{\omega + \omega_{nk}} \right) \mathrm{Im}\mathbb{G}(\omega) = \pi p(\omega_{nk}) \mathbb{G}(\omega_{nk}) \tag{A.78}$$